

Ministry of Science and Higher Education of the Russian Federation
ITMO University

ISSN 2220-8054

NANOSYSTEMS:
PHYSICS, CHEMISTRY, MATHEMATICS

2023, volume 14(3)

Наносистемы: физика, химия, математика

2023, том 14, № 3



NANOSYSTEMS:

PHYSICS, CHEMISTRY, MATHEMATICS

ADVISORY BOARD MEMBERS

Chairman: V.N. Vasiliev (*St. Petersburg, Russia*),
V.M. Buznik (*Moscow, Russia*); V.M. Ievlev (*Voronezh, Russia*), P.S. Kop'ev (*St. Petersburg, Russia*), N.F. Morozov (*St. Petersburg, Russia*), V.N. Parmon (*Novosibirsk, Russia*),
A.I. Rusanov (*St. Petersburg, Russia*),

EDITORIAL BOARD

Editor-in-Chief: I.Yu. Popov (*St. Petersburg, Russia*)

Section Co-Editors:

Physics – V.M. Uzdin (*St. Petersburg, Russia*),

Material science – V.V. Gusarov (*St. Petersburg, Russia*); O.V. Al'myasheva (*St. Petersburg, Russia*);

Chemistry – V.K. Ivanov (*Moscow, Russia*),

Mathematics – I.Yu. Popov (*St. Petersburg, Russia*).

Editorial Board Members:

V.M. Adamyan (*Odessa, Ukraine*); A.P. Alodjants (*St. Petersburg, Russia*); S. Bechta (*Stockholm, Sweden*); J. Behrndt (*Graz, Austria*); M.B. Belonenko (*Volgograd, Russia*); A. Chatterjee (*Hyderabad, India*); A.V. Chizhov (*Dubna, Russia*); A.N. Enyashin (*Ekaterinburg, Russia*), P.P. Fedorov (*Moscow, Russia*); E.A. Gudilin (*Moscow, Russia*); H. Jónsson (*Reykjavik, Iceland*); A.A. Kiselev (*Durham, USA*); Yu.S. Kivshar (*Canberra, Australia*); S.A. Kozlov (*St. Petersburg, Russia*); P.A. Kurasov (*Stockholm, Sweden*); A.V. Lukashin (*Moscow, Russia*); I.V. Melikhov (*Moscow, Russia*); G.P. Miroshnichenko (*St. Petersburg, Russia*); I.Ya. Mittova (*Voronezh, Russia*); Nguyen Anh Tien (*Ho Chi Minh, Vietnam*); V.V. Pankov (*Minsk, Belarus*); K. Pankrashkin (*Orsay, France*); A.V. Ragulya (*Kiev, Ukraine*); V. Rajendran (*Tamil Nadu, India*); A.A. Rempel (*Ekaterinburg, Russia*); V.Ya. Rudyak (*Novosibirsk, Russia*); H.M. Sedighi (*Ahvaz, Iran*); D Shoikhet (*Karmiel, Israel*); P Stovicek (*Prague, Czech Republic*); V.M. Talanov (*Novocherkassk, Russia*); A.Ya. Vul' (*St. Petersburg, Russia*); A.V. Yakimansky (*St. Petersburg, Russia*), V.A. Zagrebnov (*Marseille, France*).

Editors:

I.V. Blinova; A.I. Popov; A.I. Trifanov; E.S. Trifanova (*St. Petersburg, Russia*),
R. Simoneaux (*Philadelphia, Pennsylvania, USA*).

Address: ITMO University, Kronverkskiy pr., 49, St. Petersburg 197101, Russia.

Phone: +7(812)607-02-54, **Journal site:** <http://nanojournal.ifmo.ru/>,

E-mail: nanojournal.ifmo@gmail.com

AIM AND SCOPE

The scope of the journal includes all areas of nano-sciences. Papers devoted to basic problems of physics, chemistry, material science and mathematics inspired by nanosystems investigations are welcomed. Both theoretical and experimental works concerning the properties and behavior of nanosystems, problems of its creation and application, mathematical methods of nanosystem studies are considered.

The journal publishes scientific reviews (up to 30 journal pages), research papers (up to 15 pages) and letters (up to 5 pages). All manuscripts are peer-reviewed. Authors are informed about the referee opinion and the Editorial decision.

CONTENT

MATHEMATICS

- M.I. Muminov, A.M. Khurramov, I.N. Bozorov
On eigenvalues and virtual levels of a two-particle Hamiltonian on a d -dimensional lattice 295
- Tulkin Rasulov
The first Schur complement for a lattice spin-boson model with at most two photons 304
- T.K. Yuldashev, A.K. Fayziyev, Sh.Sh. Pulatov
Determination of the coefficient function in a Whitham type nonlinear differential equation with impulse effects 312
- V.D. Lukyanov, L.V. Nosova
Method of reference problems for obtaining approximate analytical solution of multi-parametric Sturm-Liouville problems 321

PHYSICS

- V.A. Lukoshkin, I.E. Sedova, V.K. Kalevich, E.S. Sedov, Z. Hatzopoulos, P.G. Savvidis, A.V. Kavokin
Oscillating vorticity in single ring exciton polariton condensates 328
- I.V. Pleshakov, V.A. Ryzhov, Ya.Yu. Marchenko, A.A. Alekseev, E.K. Karseeva, V.N. Nevedomskiy, A.V. Prokof'ev
Agglomeration of magnetite nanoparticles with citrate shell in an aqueous magnetic fluid 334
- I. Vorontsova, R. Goncharov, S. Kynev, F. Kiselev, V. Egorov
Measurement-device-independent continuous variable quantum key distribution protocol operation in optical transport networks 342
- E.I. Ageev, S.V. Koromyslov, M.A. Gremilov, D.V. Danilov, E.A. Petrova, I.I. Shishkin, D.A. Zuev
Single-step lithography-free fabrication of nanoscale broadband radiation sources 349

CHEMISTRY AND MATERIAL SCIENCE

- O.V. Zaitseva, E.A. Trofimov, V.E. Zhivulin, A. Ostovari Mogaddam, O.V. Samoilova, K.S. Litvinyuk, A.R. Zykova, D.V. Mikhailov, S.A. Gudkova, D.A. Vinnik
Synthesis of $\text{PbFe}_{2.4}\text{X}_{2.4}\text{Y}_{2.4}\text{Ga}_{2.4}\text{In}_{2.4}\text{O}_{19}$ high-entropy oxides with the magnetoplumbite structure 354

O.V. Proskurina, I.D. Chetinel, A.S. Seroglazova, V.V. Gusarov Influence of the composition of the BiPO₄-BiVO₄ system on the phase formation, morphology, and properties of nanocrystalline composites obtained under hydrothermal conditions	363
A.E. Aleksenskii, M.V. Baidakova, A.D. Trofimuk, B.B. Tudupova, A.S. Chizhikova, A.V. Shvidchenko Stable hydrosol prepared by deaggregation from laser synthesis nanodiamond	372
R. Naresh Muthu Synthesis and characterization of one pot electrochemical graphene for supercapacitor applications	380
Information for authors	390

On eigenvalues and virtual levels of a two-particle Hamiltonian on a d -dimensional lattice

Mukhiddin I. Muminov^{1,2,a}, Abdimajid M. Khurramov^{1,b}, Islom N. Bozorov^{1,2,c}

¹Samarkand State University, Samarkand, Uzbekistan

²V. I. Romanovskiy Institute of Mathematics, Uzbekistan Academy of Sciences, Tashkent, Uzbekistan

^ammuminov@mail.ru, ^bxurramov@mail.ru, ^cislomnb@mail.ru

Corresponding author: Mukhiddin I. Muminov, mmuminov@mail.ru

ABSTRACT The two-particle Schrödinger operator $h_\mu(k)$, $k \in \mathbb{T}^d$ (where $\mu > 0$, \mathbb{T}^d is a d -dimensional torus), associated to the Hamiltonian h of the system of two quantum particles moving on a d -dimensional lattice, is considered as a perturbation of free Hamiltonian $h_0(k)$ by the certain 3^d rank potential operator μv . The existence conditions of eigenvalues and virtual levels of $h_\mu(k)$, are investigated in detail with respect to the particle interaction μ and total quasi-momentum $k \in \mathbb{T}^d$.

KEYWORDS two-particle Hamiltonian, invariant subspace, orthogonal projector, eigenvalue, virtual level, multiplicity of virtual level.

ACKNOWLEDGEMENTS The authors expresses gratitude to the referee for valuable remarks. The work was supported by the Fundamental Science Foundation of Uzbekistan, Grant No. FZ–20200929224.

FOR CITATION Muminov M.I., Khurramov A.M., Bozorov I.N. On eigenvalues and virtual levels of a two-particle Hamiltonian on a d -dimensional lattice. *Nanosystems: Phys. Chem. Math.*, 2023, **14** (3), 295–303.

1. Introduction

In quantum modeling of interacting many-body systems for the manipulation of ultracold atoms and unique setting, coherent optical fields provide a strong tool because of their high-degree controllable parameters such as optical lattice geometry, dimension, particle mass, two-body potentials, temperature etc. (See [1–4]). The recent experimental and theoretical results show that integrating plasmonic systems with cold atoms, using optical potential fields formed from the near field scattering of light by an array of plasmonic nanoparticles, allows one to considerably increase the energy scales in the realization of Hubbard models and engineer effective long-range interaction in many body dynamics [5–7]. A several of numerical results for the bound state energies of one and two-particle systems in two adjacent 3D layers, connected through a window were presented in [8] and investigated the relation between the shape of a window and energy levels, as well as the number of eigenfunction's nodal domains. In papers [9] and [10], some spectral properties of the discrete Schrödinger operator with zero-range and short range attractive potentials, respectively, were studied.

In general, the Schrödinger operator $h(k)$, $k \in \mathbb{T}^d$, associated with the lattice Hamiltonian h of two arbitrary particles with some dispersion relation and short range potential interaction acts in $L_2(\mathbb{T}^d)$ as [11]

$$h(k) = h_0(k) - \mathbf{v}, \quad k \in \mathbb{T}^d,$$

where $h_0(k)$ is a multiplication operator by $\mathcal{E}_k(p) = \frac{1}{m_1}\varepsilon(p) + \frac{1}{m_2}\varepsilon(p - k)$ and \mathbf{v} is the integral operator with kernel $v(p, s) = v(p - s)$. In [8], several numerical results for the bound state energies of one and two-particle systems were presented in two adjacent 3D layers, connected through a window. The authors investigated the relation between the shape of the window and the energy levels, as well as the number of eigenfunction's nodal domains.

In [12], the existence conditions and positiveness of eigenvalues of the Schrödinger operator $h(k)$, $k \in \mathbb{T}^d$, were studied with respect to the quasi-momentum k and the virtual level at the lower edge of the essential spectrum.

The existence and absence of eigenvalues of the family $h(k)$ depending on the energy of interaction and quasi-momentum k were investigated in [13] and [14] for the cases $\varepsilon(p) = \sum_{i=1}^3(1 - \cos 2p_i)$, $v(p - s) = \sum_{\alpha=1}^3 \mu_\alpha \cos(p_\alpha - s_\alpha)$

and $\varepsilon(p) = \sum_{i=1}^3(1 - \cos 2np_i)$, $v(p - q) = \sum_{l=1}^N \sum_{i=1}^3 \mu_{li} \cos l(p_i - q_i)$, respectively. The spectral properties of this operator $h(k)$ for the one dimensional case were studied in [15] and more general case in [16]. For general case $\varepsilon(p)$ satisfying some conditions and $v(p - s) = \mu_0 + \sum_{\alpha=1}^d \mu_\alpha \cos(p_\alpha - q_\alpha)$ was investigated in [17]. Detailed spectral properties of the

Hamiltonian $\hat{h}_{\mu\lambda}$, $\mu, \lambda \geq 0$, describing the motion of one quantum particle on a three-dimensional lattice in an external field and more general case were investigated in the papers [18] and [19], respectively. In [20] a class of potentials is found for which the discrete spectrum of the two-particle Schrödinger operator $h(k)$ is preserved when $h(k)$ is perturbed by a potential from this class.

In the recent paper [21], a two particle Schrödinger operator $h_\mu(k)$, $k \in \mathbb{T}^3$, $\mu > 0$, associated to the Hamiltonian h on the three-dimensional lattice is considered. The authors investigated existence conditions of eigenvalues and bound states of $h_\mu(k)$. The investigation is based on the construction of invariant subspaces for the operator $h_\mu(k)$ which allow one to study the compact perturbations of rank one.

This paper is a continuation of the work [21]. We consider a two particle Schrödinger operator $h_\mu(k)$, $k \in \mathbb{T}^3$, $\mu > 0$, associated with the Hamiltonian h for a system of two particles on the d -dimensional lattice \mathbb{Z}^d interacting through *attractive short-range potential* V . We investigate the existence conditions of eigenvalues and virtual levels of the two-particle Schrödinger operator $h_\mu(k)$, where $h_\mu(k)$ is considered as a perturbation of free Hamiltonian $h_0(k)$ by the certain potential operator $\mu\mathbf{v}$ with rank 3^d . The main idea of the investigation is to represent $\mu\mathbf{v}$ via the sum of one rank orthogonal projectors $\mu\mathbf{v}_l$. This allows one to represent the corresponding Birman–Schwinger operator $\mathbf{T}(\mu, k; z)$ via the sum of the one rank projectors $\mathbf{T}_l(\mu, k; z)$, $l = 1, 2, \dots, 3^d$. Moreover, the study of spectral properties of $h_\mu(k)$ reduces to the investigation of 3^d one rank operators $\mathbf{T}_l(\mu, k; z)$. The virtual level of $h_\mu(k)$ is studied as $k = 0$.

2. Statement of the main result

A two-particle Schrödinger operator $h_\mu(k)$, $k \in \mathbb{T}^d$, $\mu > 0$, associated to the Hamiltonian h for a system of two particles on the lattice \mathbb{Z}^d interacting via attractive short-range potential, is a self-adjoint operator and acts in $L_2(\mathbb{T}^d)$ as

$$h_\mu(k) = h_0(k) - \mu\mathbf{v}, \quad k = (k_1, k_2, \dots, k_d) \in \mathbb{T}^d, \quad \mu > 0,$$

where $h_0(k)$ is a multiplication operator by

$$\mathcal{E}_k(p) = \frac{1}{m_1}\varepsilon(p) + \frac{1}{m_2}\varepsilon(p - k), \quad \varepsilon(p) = \sum_{i=1}^d (1 - \cos 2p_i),$$

with \mathbf{v} being an integral operator with kernel

$$v(p - s) = 1 + \sum_{\alpha=1}^d \cos(p_\alpha - s_\alpha) + \sum_{\gamma=1}^d \cos(p_\alpha - s_\alpha) \cos(p_\beta - s_\beta) + \dots + \prod_{\alpha=1}^d \cos(p_\alpha - s_\alpha),$$

$\alpha, \beta, \gamma \in \{1, 2, \dots, d\}$, $\alpha < \beta < \gamma < \alpha$.

Note that by the Weyl theorem [22] the essential spectrum $\sigma_{ess}(h_\mu(k))$ of the operator $h_\mu(k)$ coincides with the spectrum of the unperturbed operator $h_0(k)$

$$\sigma_{ess}(h_\mu(k)) = \sigma(h_0(k)) = [m(k), M(k)],$$

where $m(k) = \min_{p \in \mathbb{T}^d} \mathcal{E}_k(p)$, $M(k) = \max_{p \in \mathbb{T}^d} \mathcal{E}_k(p)$.

Since $\mathbf{v} \geq 0$ for $\mu > 0$,

$$\sup_{\|f\|=1} (h_\mu(k)f, f) \leq \sup_{\|f\|=1} (h_0(k)f, f) = M(k)(f, f), \quad f \in L_2(\mathbb{T}^d).$$

Hence, $h_\mu(k)$ does not have eigenvalues lying to the right of the essential spectrum, i.e.,

$$\sigma(h_\mu(k)) \cap (M(k), +\infty) = \emptyset.$$

Let $\{\varphi_l\}$ be the orthogonal system in $L_2(\mathbb{T}^d)$, where φ_l is defined as

$$\varphi_l(p) = \prod_{\alpha=1}^d \eta_l(p_\alpha), \quad \{\eta_l(p_\alpha)\} \in \{1, \cos p_1, \dots, \cos p_d, \sin p_1, \dots, \sin p_d\}.$$

The number of these orthogonal functions is 3^d .

We numerate the elements of the system $\{\varphi_l\}_{l=1}^{3^d}$ to the following rule.

Consider a set of d -tuples $(\alpha_1, \dots, \alpha_d)$ consisting of 3 digital system. Corresponding for the number zero to 1, 1 to cosine and 2 to sine we construct the following one to one mapping

$$(\alpha_1, \dots, \alpha_d) \leftrightarrow \eta_l(p_{\alpha_1})\eta_l(p_{\alpha_2}) \dots \eta_l(p_{\alpha_d}).$$

For example, for $d = 4$ the tuples $(0, 0, 0, 0)$, $(0, 0, 1, 2)$ and $(1, 2, 2, 1)$ correspond to the functions 1 , $\cos p_3 \sin p_4$ and $\cos p_1 \sin p_2 \sin p_3 \cos p_4$, respectively. We order and numerate the set of d tuples as

$$\begin{array}{ccccccccc} (00 \cdots 00), & (00 \cdots 01), & (00 \cdots 10), & \cdots & (11 \cdots 11), \\ \downarrow & \downarrow & \downarrow & \vdots & \downarrow \\ \varphi_1 & \varphi_2 & \varphi_3 & \cdots & \varphi_{2^d} \\ (00 \cdots 02), & (00 \cdots 12), & (00 \cdots 20), & \cdots & (22 \cdots 22), \\ \downarrow & \downarrow & \downarrow & \vdots & \downarrow \\ \varphi_{2^{d+1}} & \varphi_{2^{d+2}} & \varphi_{2^{d+3}} & \cdots & \varphi_{3^d} \end{array}$$

By construction $\varphi_l(\mathbf{0}) = 1$ for $l = 1, \dots, 2^d$ and $\varphi_l(\mathbf{0}) = 0$ for $l = 2^d + 1, \dots, 3^d$.

The operator \mathbf{v} is expressed via the orthogonal functions $\varphi_l, l = 1, \dots, 3^d$ in the form

$$(\mathbf{v}f)(p) = \sum_{l=1}^{3^d} (\mathbf{v}_l f)(p), \quad (\mathbf{v}_l f)(p) = (\varphi_l, f)\varphi_l(p),$$

where (\cdot, \cdot) is the inner product in $L_2(\mathbb{T}^d)$.

It follows from the nonnegativity of the operator $\mathbf{v} \geq 0$ that the square root $\mathbf{v}^{\frac{1}{2}} \geq 0$ exists. The operator $\mathbf{v}^{\frac{1}{2}}$ acts in $L_2(\mathbb{T}^d)$ as

$$(\mathbf{v}^{\frac{1}{2}}f)(p) = \sum_{l=1}^{3^d} \frac{1}{\|\varphi_l\|} (\mathbf{v}_l f)(p).$$

Let \mathbb{C} be the complex plane, and let $\mathbf{r}_0(k; z), z \in \mathbb{C} \setminus [m(k), M(k)]$ be the resolvent of $h_0(k)$.

Consider the operator $\tilde{h}_\mu(k)$ acting in $L_2(\mathbb{T}^d)$ in accordance with the formula

$$\tilde{h}_\mu(k) = \tilde{h}_0(k) - \mu \mathbf{v},$$

where $\tilde{h}_0(k)$ is the operator of multiplication by the function $\tilde{\mathcal{E}}_k(\cdot)$,

$$\tilde{\mathcal{E}}_k(p) = \sum_{i=1}^d \left(\frac{1}{m_1} + \frac{1}{m_2} - \sqrt{\frac{1}{m_1^2} + \frac{2}{m_1 m_2} \cos 2k_i + \frac{1}{m_2^2} \cos 2p_i} \right).$$

The operator $h_\mu(k)$ is unitary equivalent to the operator $\tilde{h}_\mu(k)$ (See Lemma 2 in [14]). The equivalence is performed by the unitary operator $U : L_2(\mathbb{T}^d) \rightarrow L_2(\mathbb{T}^d)$ as $\tilde{h}_\mu(k) = U^{-1}h_\mu(k)U$, where

$$(Uf)(p) = f\left(p - \frac{1}{2}\theta(k)\right),$$

$$\theta(k) = (\theta_1(k_1), \dots, \theta_d(k_d)), \quad \theta_i(k_i) = \arccos \frac{\frac{1}{m_1} + \frac{1}{m_2} \cos 2k_i}{\sqrt{\frac{1}{m_1^2} + \frac{2}{m_1 m_2} \cos 2k_i + \frac{1}{m_2^2}}}, \quad i = 1, 2, \dots, d.$$

For any $z \in \mathbb{C} \setminus [m(k), M(k)]$, we define a Birman–Schwinger integral operator $\mathbf{T}(\mu, k; z) = \mu \mathbf{v}^{\frac{1}{2}} \mathbf{r}_0(k; z) \mathbf{v}^{\frac{1}{2}}$. The rank of $\mathbf{T}(\mu, k; z)$ is equal to 3^d and it represents via one rank orthogonal projectors $\mathbf{T}_l(\mu, k; z)$ as

$$\mathbf{T}(\mu, k; z)\psi = \sum_{l=1}^{3^d} \mathbf{T}_l(\mu, k; z)\psi,$$

$$\mathbf{T}_l(\mu, k; z)\psi = \frac{\mu}{\|\varphi_l\|^2} (\varphi_l, \mathbf{r}_0(k; z)\varphi_l) (\varphi_l, \psi)\varphi_l,$$

where

$$(\varphi_l, \mathbf{r}_0(k; z)\varphi_l) = \int_{\mathbb{T}^d} \frac{\varphi_l^2(s) ds}{\tilde{\mathcal{E}}_k(s) - z}, \quad l = 1, 2, \dots, 3^d, \quad z \in \mathbb{C} \setminus [m(k), M(k)]. \quad (1)$$

A nonzero eigenvalue of the operator $\mathbf{T}_l(\mu, k; z)$ is $\lambda_l(z) = \mu(\varphi_l, \mathbf{r}_0(k; z)\varphi_l)$, $l = 1, \dots, 3^d$ and φ_l is an eigenfunction corresponding to $\lambda_l(z)$. Moreover,

$$\sigma(\mathbf{T}(\mu, k; z)) = \{0 \cup \lambda_1(z) \cup \dots \cup \lambda_{3^d}(z)\}.$$

For each $z \in \mathbb{C} \setminus [m(k), M(k)]$ and $k \in \mathbb{T}^d$, denote by $\Delta_l(\mu, k; z)$ and $\Delta(\mu, k; z)$ the Fredholm determinants of the operators $I - \mathbf{T}_l(\mu, k; z)$ and $I - \mathbf{T}(\mu, k; z)$, respectively. Then

$$\Delta_l(\mu, k; z) = 1 - \mu \int_{\mathbb{T}^d} \frac{\varphi_l^2(s) ds}{\tilde{\mathcal{E}}_k(s) - z}, \quad l = 1, 2, \dots, 3^d$$

and the equality

$$\Delta(\mu, k; z) = \prod_{l=1}^{3^d} \Delta_l(\mu, k; z).$$

holds.

The following lemma is a consequence of the Fredholm theorem.

Lemma 2.1. A number $z, z \in \mathbb{C} \setminus [m(k), M(k)]$, is an eigenvalue of $h_\mu(k)$ if and only if $\Delta(\mu, k; z) = 0$. Moreover, the multiplicity of a zero of the function $\Delta(\mu, k; \cdot)$ then coincides with the multiplicity of an eigenvalue of the operator $h_\mu(k)$.

Remark 2.1. Clearly, the operator $h_\mu(k)$ has an eigenvalue $z < m(k)$, i.e., $\text{Ker}(h_\mu(k) - zI) \neq 0$ if and only if the compact operator $\mathbf{T}(\mu, k; z)$ in $L_2(\mathbb{T}^d)$ has an eigenvalue equal to 1 and there is a function $\psi \in \text{Ker}(\mathbf{T}(\mu, k; z) - I)$ such that

$$f(\cdot) = \frac{\mu \mathbf{v}^{\frac{1}{2}} \psi(\cdot)}{\tilde{\mathcal{E}}_k(\cdot) - z} \in L_2(\mathbb{T}^d).$$

In this case, $f \in \text{Ker}(h_\mu(k) - zI)$. Moreover, if $z < m(k)$, then

$$\dim \text{Ker}(h_\mu(k) - zI) = \dim \text{Ker}(\mathbf{T}(\mu, k; z) - I),$$

$$\text{Ker}(h_\mu(k) - zI) = \left\{ f : f(\cdot) = \frac{\mu \mathbf{v}^{\frac{1}{2}} \psi(\cdot)}{\tilde{\mathcal{E}}_k(\cdot) - z}, \psi \in \text{Ker}(\mathbf{T}(\mu, k; z) - I) \right\}.$$

Since the minimum points of $\tilde{\mathcal{E}}_k(\cdot)$ are non-degenerate, the operator $\mathbf{T}_l(\mu, k; z)$ in $L_2(\mathbb{T}^d)$ is well defined as $z = m(k)$ for any $d \geq 3$ and $l = 1, \dots, 3^d$. The equality $\varphi_l(\mathbf{0}) = 0, l = 2^d + 1, \dots, 3^d$ provides well defined of $\mathbf{T}_l(\mu, k; z)$ in $L_2(\mathbb{T}^d)$ as $z = m(k)$ for any $d = 1, 2$ and $l = 2^d + 1, \dots, 3^d$. According to (1), the following limits

$$(\varphi_l, \mathbf{r}_0(k; m(k))\varphi_l) := \lim_{z \nearrow m(k)} (\varphi_l, \mathbf{r}_0(k; z)\varphi_l), \quad l = 1, 2, \dots, 3^d,$$

exist (finite or infinite). We set

$$\mu_l(k) := \frac{1}{(\varphi_l, \mathbf{r}_0(k; m(k))\varphi_l)}, \quad l = 1, 2, \dots, 3^d.$$

Assumption 2.1. Assume that $m = m_1 = m_2$ and $k \in \Pi$, where

$$\Pi = \left\{ k = (k_1, k_2, \dots, k_d) \in \mathbb{T}^d : \text{at least } d - 2 (d \geq 3) \text{ coordinates are equal to } -\frac{\pi}{2} \text{ or } \frac{\pi}{2} \right\}.$$

If the Assumption 2.1 is not fulfilled, then $\mu_l(k) = 0$ for $d = 1, 2, l = 1, \dots, 2^d$ and $0 < \mu_l(k) < \infty$ for $d \geq 3, l = 1, \dots, 2^d$ or for $d \geq 1, l = 2^d + 1, \dots, 3^d$.

Definition 2.1. Let $d = 3, 4 (d = 1, 2)$. We say that the operator $h_\mu(\mathbf{0})$ has a virtual level at $z = 0$ (lower edge of the essential spectrum) if 1 is an eigenvalue of $\mathbf{T}(\mu, \mathbf{0}; 0)$ (of $\mathbf{T}_l(\mu, \mathbf{0}; 0)$ for some $l > 2^d$) with some associated eigenfunction ψ satisfying the condition

$$\frac{\mathbf{v}^{\frac{1}{2}} \psi(\cdot)}{\tilde{\mathcal{E}}_{\mathbf{0}}(\cdot)} \notin L_2(\mathbb{T}^d).$$

The number of such linearly independent eigenvectors ψ of the operator $\mathbf{T}(\mu, \mathbf{0}; 0), d \geq 3$ (of all operators $\mathbf{T}_l(\mu, \mathbf{0}; 0)$ for $d = 2$), is called the multiplicity of the virtual level of the operator $h_\mu(\mathbf{0})$.

Note that, if the number 1 is an eigenvalue of the operator $\mathbf{T}(\mu, k; m(k))$, and the corresponding eigenfunction ψ with

$$\frac{\mathbf{v}^{\frac{1}{2}} \psi(\cdot)}{\tilde{\mathcal{E}}_k(\cdot) - m(k)} \in L_2(\mathbb{T}^d), \quad d \geq 3,$$

then the function $\frac{\mathbf{v}^{\frac{1}{2}} \psi(\cdot)}{\tilde{\mathcal{E}}_k(\cdot) - m(k)}$ is the eigenfunction of $h_\mu(k)$ corresponding to the eigenvalue $z = m(k)$.

Theorem 2.1. Suppose that the Assumption 2.1 are not fulfilled. Then for any $k \in \mathbb{T}^d$, the following statements are true

1. Let $d = 1, 2$ and $\mu \in (0, \mu_*(k))$, $\mu_*(k) = \min_{2^d < l \leq 3^d} \mu_l(k)$. Then the operator $h_\mu(k)$ has 2^d eigenvalues (taking into account the multiplicity) lying to the left of the essential spectrum.
2. Let $d \geq 3$ and $\mu \in (0, \mu_*(k))$, $\mu_*(k) = \min_{1 \leq l \leq 3^d} \mu_l(k)$. Then the operator $h_\mu(k)$ has no eigenvalues lying to the left of the essential spectrum.
3. Let $d \geq 1$ and $\mu \in (\mu^*(k), +\infty)$, $\mu^*(k) = \max_{1 \leq l \leq 3^d} \mu_l(k)$. Then the operator $h_\mu(k)$ has 3^d eigenvalues (taking into account the multiplicity) lying to the left of the essential spectrum.

We split the set Π into three subsets Π_n , $n = 0, 1, 2$, of $k \in \Pi$, whose $d - n$ coordinates are only equal to $-\frac{\pi}{2}$ or $\frac{\pi}{2}$.

Theorem 2.2. Let the Assumption 2.1 be fulfilled and let $d \geq 3$. Then for any $\mu > 0$ and $k \in \Pi_n$, $n = 0, 1, 2$ the operator $h_\mu(k)$ has at least

$$s_n = 2^d + \sum_{i=1}^{d-n} 2^{d-i} \cdot 3^{i-1}$$

eigenvalues (taking into account the multiplicity) lying to the left of the essential spectrum. Moreover, if $n = 0$, then $h_\mu(k)$ has $s_0 = 3^d$ eigenvalues (taking into account the multiplicity) lying to the left of the essential spectrum.

Let r_s be a positive integer number defined as

$$r_s = C_d^0 + C_d^1 + \dots + C_d^s, \quad s = 0, 1, \dots, d. \tag{2}$$

We split the numbers $\{1, 2, \dots, 2^d\}$ into $d + 1$ as

$$\{1, 2, \dots, 2^d\} = D_0 \cup \dots \cup D_d,$$

where $D_s = \{1 + r_s - C_d^s, \dots, r_s\}$.

Remark that for any $d \geq 3$ the following assertions

$$\begin{aligned} \mu_{r_s}(\mathbf{0}) &= \mu_r(\mathbf{0}), \quad r \in D_s, \quad s = 0, 1, \dots, d, \\ \mu_{r_0}(\mathbf{0}) &< \mu_{r_1}(\mathbf{0}) < \mu_{r_2}(\mathbf{0}) < \dots < \mu_{r_d}(\mathbf{0}), \\ \mu_{r_d}(\mathbf{0}) &< \mu_l(\mathbf{0}), \quad r_d = 2^d, \quad l = 2^d + 1, \dots, 3^d \end{aligned}$$

hold (see Lemma 4.2 below).

Theorem 2.3. Suppose that the Assumption 2.1 are not fulfilled. Then the following statements are true

1. If $d = 1$ and $\mu = \mu_3(\mathbf{0})$, then $h_\mu(\mathbf{0})$ has a virtual level at $z = 0$ and two simple negative eigenvalues.
2. If $d = 2$ and $\mu = \mu_*(\mathbf{0}) = \min_{4 < l \leq 9} \mu_l(\mathbf{0})$, then $h_\mu(\mathbf{0})$ has three negative eigenvalues, two of them simple and one of them two-fold, and a two-fold virtual level at $z = 0$.
3. Let $d = 3, 4$ ($d > 4$) and $\mu = \mu_{r_s}(\mathbf{0})$ for some $s \in \{0, 1, \dots, d\}$. Then the operator $h_\mu(\mathbf{0})$ has s eigenvalues λ_l , $l = 0, 1, \dots, s - 1$, with multiplicity C_d^l and $\lambda_0 < \dots < \lambda_{s-1} < 0$. Additionally, the operator $h_\mu(\mathbf{0})$ has a virtual level (an eigenvalue) at $z = 0$ with multiplicity C_d^s .
Moreover, if $d \geq 3$ and $\mu_{r_d}(\mathbf{0}) < \mu < \min_{l > 2^d} \mu_l(\mathbf{0})$, then the operator $h_\mu(\mathbf{0})$ has $d + 1$ eigenvalues λ_l , $l = 0, 1, \dots, d$, lying to the left of the essential spectrum, with $\lambda_0 < \dots < \lambda_d < 0$ and $C_d^0 + C_d^1 + \dots + C_d^d = 2^d$, where C_d^r is the multiplicity of λ_r .
4. Let $d \geq 3$ and $\mu = \mu_l(\mathbf{0})$ for some $l \in \{2^d + 1, \dots, 3^d\}$. Then the number $z = 0$ is an eigenvalue of the operator $h_\mu(\mathbf{0})$ and this operator has $2^d + q$ eigenvalues (taking into account the multiplicity) lying to the left of the essential spectrum, where q is the number of elements of the set $\{\mu_n : \mu_n > \mu_l(\mathbf{0}), n > 2^d\}$.

Remark 2.2. A similar Theorems 2.1, 2.2 and 2.3 describe the dependence of the number of eigenvalues and their arrangement on the parameter μ for all $\mu \in \mathbb{R}$. In this case, the eigenvalues of $h_\mu(k)$ are located both to the left and to the right of the essential spectrum. In the case $\mu < 0$, the eigenvalues of $h_\mu(k)$ are only to the right of the essential spectrum.

3. The eigenvalues of $h_\mu(k)$

In this section, we prove Theorems 2.1 and 2.2.

Proof of Theorem 2.1. Remark that the integral

$$\int_{\mathbb{T}^d} \frac{\varphi_l^2(s) ds}{\tilde{\mathcal{E}}_k(s) - m(k)}$$

converges for any $\varphi_l \in \mathcal{H}_l$ for $l = 1, \dots, 3^d$, $d \geq 3$ and for $l = 2^d + 1, \dots, 3^d$, $d = 1, 2$. The function $\Delta_l(\mu, k; \cdot)$ is continuous and monotonically decreasing on $z \in (-\infty, m(k))$ for any fixed $\mu > 0$ and $k \in \mathbb{T}^d$.

1. Let $d = 1, 2$. The following equalities

$$\lim_{z \rightarrow -\infty} \Delta_l(\mu, k; z) = 1,$$

$$\lim_{z \nearrow m(k)} \Delta_l(\mu, k; z) = -\infty \quad \text{for } l = 1, 2, \dots, 2^d$$

hold. Then there is a unique number $z_l(\mu, k) < m(k)$, $l = 1, 2, \dots, 2^d$ such that $\Delta_l(\mu, k; z_l(\mu, k)) = 0$. According to Lemma 2.1, the operator $h_\mu(k)$ has 2^d eigenvalues (taking into account the multiplicity) lying to the left of the essential spectrum.

Since

$$\lim_{z \nearrow m(k)} \Delta_l(\mu, k; z) = \Delta_l(\mu, k; m(k)) < \infty, \quad \text{for } l = 2^d + 1, \dots, 3^d$$

and the function $\Delta_l(\mu, k; \cdot)$ ($\Delta_l(\cdot, k; z)$) is monotonically decreasing on $z \in (-\infty, m(k))$ (on $\mu \in (0, \infty)$) for any fixed $\mu > 0$ ($z \in (-\infty, m(k))$), the inequalities

$$\Delta_l(\mu, k; z) > \Delta_l(\mu, k; m(k)) > \Delta_l(\mu_*(k), k; m(k)) = 0 \quad \text{for all } \mu \in (0, \mu_*(k))$$

hold. Then by the Lemma 2.1 the operator $h_\mu(k)$ has only 2^d eigenvalues (taking into account the multiplicity) lying to the left of the essential spectrum.

2. For the case when $d \geq 3$ by similar way we can show that $\Delta_l(\mu, k; z) > 0$ for all $\mu \in (0, \mu_*(k))$. This proves the required assertion.

3. Note that for the case $d = 1, 2$ and $l = 1, 2, \dots, 2^d$

$$\lim_{z \nearrow m(k)} \Delta_l(\mu, k; z) = -\infty \quad \text{for all } \mu > 0 \tag{3}$$

holds. Let $\mu \in (\mu^*(k), +\infty)$, $\mu^*(k) = \max_{1 \leq l \leq 3^d} \mu_l(k)$. Then for the cases $l = 2^d + 1, \dots, 3^d$, $d = 1, 2$ and $l = 1, 2, \dots, 3^d$, $d \geq 3$ we have

$$\lim_{z \nearrow m(k)} \Delta_l(\mu, k; z) = \Delta_l(\mu, k; m(k)) = 1 - \frac{\mu}{\mu_l(k)} < 0. \tag{4}$$

Since $\Delta_l(\mu, k; \cdot)$ is a continuous monotonic function on $(-\infty, m(k))$ and

$$\lim_{z \rightarrow -\infty} \Delta_l(\mu, k; z) = 1,$$

according to (3), (4), there exists a unique $z_l(\mu, k) \in (-\infty, m(k))$ such that

$$\Delta_l(\mu, k; z_l(\mu, k)) = 0 \quad \text{for all } l = 1, 2, \dots, 3^d.$$

Hence by Lemma 2.1 the operator $h_\mu(k)$ has 3^d eigenvalues (taking into account the multiplicity) lying to the left $m(k)$. □

Proof of Theorem 2.2. The case $n = 0$. Let $k \in \Pi_0$, i.e. $k_i = \pm \frac{\pi}{2}$, $i = 1, 2, \dots, d$. The function $\tilde{\mathcal{E}}_k(\cdot)$ is a constant function. Therefore, we obtain

$$\lim_{z \nearrow m(k)} (\varphi_l, \mathbf{r}_0(k; z)\varphi_l) = \lim_{z \nearrow m(k)} \int_{\mathbb{T}^d} \frac{\varphi_l^2(s) ds}{\tilde{\mathcal{E}}_k(s) - z} = +\infty, \quad l = 1, 2, \dots, 3^d,$$

which implies

$$\lim_{z \nearrow m(k)} \Delta_l(\mu, k; z) = -\infty$$

for any $\mu > 0$. Since

$$\lim_{z \rightarrow -\infty} \Delta_l(\mu, k; z) = 1,$$

there exists unique $z_l(\mu, k) \in (-\infty, m(k))$ such that $\Delta_l(\mu, k; z_l(\mu, k)) = 0$ for any $\mu > 0$ and $l = 1, 2, \dots, 3^d$. Hence by the Lemma 2.1 the operator $h_\mu(k)$ has 3^d eigenvalues (taking into account the multiplicity) lying to the left $m(k)$, $k \in \Pi_0$.

The case $n = 1$. We prove theorem for the case $k \in \Pi_1$ with $k_i = \pm \frac{\pi}{2}$, $i = 1, 2, \dots, d - 1$. The function $\tilde{\mathcal{E}}_k(\cdot)$ does not depend on p_1, p_2, \dots, p_{d-1} and is expressed as

$$\tilde{\mathcal{E}}_k(p) = \frac{2d}{m} - \frac{1}{m} \sqrt{2 + 2 \cos 2k_d \cos 2p_d}.$$

Then there exist n_1 functions $\xi_m(k; \cdot) := (\varphi_{l_m} \mathbf{r}_0(k; \cdot), \varphi_{l_m})$ with $\varphi_{l_m}(p_1, \dots, p_{d-1}, 0) \neq 0$, $m = 1, 2, \dots, n_1$, where

$n_1 = 2^d + \sum_{i=1}^{d-1} 2^{d-i} \cdot 3^{i-1}$. Since $(\tilde{\mathcal{E}}_k(p) - m(k)) = O(p_d^2)$ as $p_d \rightarrow 0$ and $\tilde{\mathcal{E}}_k(\cdot)$ does not depend on p_1, p_2, \dots, p_{d-1} , we have

$$\lim_{z \nearrow m(k)} \xi_{l_r}(k; z) = +\infty.$$

This gives one

$$\lim_{z \nearrow m(k)} \Delta_{l_r}(\mu, k; z) = -\infty, \quad l_r = 1, 2, \dots, n_1.$$

Hence there exists unique $z_{l_r}(\mu, k) \in (-\infty, m(k))$ such that

$$\Delta_l(\mu, k; z_{l_r}(\mu, k)) = 0, \quad l_r = 1, 2, \dots, n_1.$$

According to Lemma 2.1, we obtain the required assertion for the case $k \in \Pi_1$ with $k_i = \pm \frac{\pi}{2}, i = 1, 2, \dots, d - 1$.

The proofs for the remaining cases with $k \in \Pi_1$ can be constructed in a similar way.

The case $n = 2$ can be proven analogously. □

4. Virtual level and eigenvalues of the operator $h_\mu(\mathbf{0})$

In this section, we prove Theorem 2.3. According to the definition of a virtual level of $h_\mu(\mathbf{0})$, we study the equation

$$\mathbf{T}(\mu, \mathbf{0}; 0)\psi = \psi.$$

We note that $\Delta_l(\mu, \mathbf{0}; \cdot)$ is well defined at $z = 0$ for the cases $l = 2^d + 1, \dots, 3^d, d = 1, 2$ and $l = 1, 2, \dots, 3^d, d \geq 3$. According to Lemma 2.1, we can prove the following assertion.

Lemma 4.1. Let $l = 1, 2, \dots, 3^d$ for $d \geq 3$ ($l = 2^d + 1, \dots, 3^d$ for $d = 1, 2$). Then the number $\lambda = 1$ is an eigenvalue of the operator $\mathbf{T}(\mu, \mathbf{0}; 0)$ ($\mathbf{T}_l(\mu, \mathbf{0}; 0)$) if and only if

$$\prod_{l=1}^{3^d} \Delta_l(\mu, \mathbf{0}; 0) = 0, \quad (\Delta_l(\mu, \mathbf{0}; 0) = 0).$$

Lemma 4.2. For any $d \geq 3$, the following assertions are true

$$\begin{aligned} \mu_{r_s}(\mathbf{0}) &= \mu_r(\mathbf{0}), \quad r \in D_s, \quad s = 0, 1, \dots, d, \\ \mu_{r_0}(\mathbf{0}) &< \mu_{r_1}(\mathbf{0}) < \mu_{r_2}(\mathbf{0}) < \dots < \mu_{r_d}(\mathbf{0}), \\ \mu_{r_d}(\mathbf{0}) &< \mu_l(\mathbf{0}), \quad r_d = 2^d, \quad l = 2^d + 1, \dots, 3^d, \end{aligned}$$

where r_0, \dots, r_d are defined by (2).

Proof of lemma 4.2. Since $\tilde{\mathcal{E}}_0(p) = \frac{m_1 + m_2}{m_1 m_2} \sum_{i=1}^d (1 - \cos 2p_i)$ is symmetric under permutations of p_α and p_β , the equality

$$\int_{\mathbb{T}^d} \frac{\cos^2 s_1 \cdots \cos^2 s_r ds}{\tilde{\mathcal{E}}_0(s)} = \int_{\mathbb{T}^d} \frac{\cos^2 s_{j_1} \cdots \cos^2 s_{j_r} ds}{\tilde{\mathcal{E}}_0(s)}, \quad r \leq d$$

holds.

Hence, the following inequalities

$$\int_{\mathbb{T}^d} \frac{\varphi_1^2(s) ds}{\tilde{\mathcal{E}}_0(s)} > \int_{\mathbb{T}^d} \frac{\varphi_{j_1}^2(s) ds}{\tilde{\mathcal{E}}_0(s)} > \int_{\mathbb{T}^d} \frac{\varphi_{j_2}^2(s) ds}{\tilde{\mathcal{E}}_0(s)} > \dots > \int_{\mathbb{T}^d} \frac{\varphi_{j_d}^2(s) ds}{\tilde{\mathcal{E}}_0(s)},$$

hold, where $j_s \in D_s, D_s = \{1 + r_s - C_d^s, \dots, r_s\}, r_s = C_d^0 + C_d^1 + \dots + C_d^s, s = 0, 1, 2, \dots, d$.

Therefore, the following inequalities

$$\mu_{r_0}(\mathbf{0}) < \mu_{r_1}(\mathbf{0}) < \mu_{r_2}(\mathbf{0}) < \dots < \mu_{r_d}(\mathbf{0})$$

hold, where

$$\mu_r(\mathbf{0}) = \left(\int_{\mathbb{T}^d} \frac{\varphi_r^2(s) ds}{\tilde{\mathcal{E}}_0(s)} \right)^{-1}, \quad r = 1, 2, \dots, d + 1.$$

Note that

$$\mu_{r_s}(\mathbf{0}) = \mu_r(\mathbf{0}), \quad r \in D_s, \quad s = 0, 1, 2, \dots, d. \tag{5}$$

We can easily verify the equality (see Lemma 1, [13])

$$\int_{-\pi}^{\pi} \frac{\cos 2s ds}{a - b \cos 2s} = \frac{2\pi}{b} \frac{a - \sqrt{a^2 - b^2}}{\sqrt{a^2 - b^2}}$$

for $0 < b < a$. Therefore,

$$\int_{-\pi}^{\pi} \frac{\cos^2 s ds}{a - b \cos 2s} - \int_{-\pi}^{\pi} \frac{\sin^2 s ds}{a - b \cos 2s} > 0$$

for all $0 < b < a$. Applying this inequality, we obtain

$$\int_{\mathbb{T}^d} \frac{\varphi_m^2(s) ds}{\tilde{\mathcal{E}}_0(s)} > \int_{\mathbb{T}^d} \frac{\varphi_l^2(s) ds}{\tilde{\mathcal{E}}_0(s)} \quad \text{for } m \leq 2^d < l.$$

This gives one $\mu_{r_s}(\mathbf{0}) < \mu_l(\mathbf{0}), l = 2^d + 1, \dots, 3^d$, where $r_d = 2^d$. □

Proof of Theorem 2.3. Let $d = 1$ and $\mu = \mu_3(\mathbf{0})$. Then according to assertion 1 of Theorem 2.1, for any $\mu > 0$, the operator $h_\mu(\mathbf{0})$ has two simple eigenvalues $z_1(\mu, \mathbf{0}) < z_2(\mu, \mathbf{0}) < 0$ and the corresponding eigenfunctions have the form

$$f_1(p) = \frac{1}{\tilde{\mathcal{E}}_0(p) - z_1(\mu, \mathbf{0})} \quad \text{and} \quad f_2(p) = \frac{\cos p}{\tilde{\mathcal{E}}_0(p) - z_2(\mu, \mathbf{0})}$$

respectively.

Since $\mu = \mu_3(\mathbf{0})$, it follows from Lemma 4.1 that $\lambda = 1$ is an eigenvalue of $\mathbf{T}_3(\mu, \mathbf{0}; 0)$ and $\varphi_3(p) = \sin p$ is the corresponding eigenfunction of $\mathbf{T}_3(\mu, \mathbf{0}; 0)$. One can see that $f_3 \notin L_2(\mathbb{T})$, where $f_3(p) = \sin p / \tilde{\mathcal{E}}_0(p)$, i.e., $z = 0$ is a virtual level of the operator $h_\mu(\mathbf{0})$.

2. Let $d = 2$ and $\mu = \min_{4 < l \leq 9} \mu_l(\mathbf{0})$. According to statement 1 of Theorem 2.1, for any $\mu > 0$, the operator $h_\mu(\mathbf{0})$ has four eigenvalues (taking into account the multiplicity) $z_1(\mu, \mathbf{0}) < z_2(\mu, \mathbf{0}) = z_3(\mu, \mathbf{0}) < z_4(\mu, \mathbf{0}) < 0$ and the corresponding eigenfunctions have the form

$$f_1(p) = \frac{1}{\tilde{\mathcal{E}}_0(p) - z_1(\mu, \mathbf{0})}, \quad f_i(p) = \frac{\cos p_i}{\tilde{\mathcal{E}}_0(p) - z_2(\mu, \mathbf{0})}, \quad i = 2, 3, \quad f_4(p) = \frac{\cos p_1 \cos p_2}{\tilde{\mathcal{E}}_0(p) - z_4(\mu, \mathbf{0})},$$

respectively.

Observe that the inequalities

$$\int_{\mathbb{T}^2} \frac{\sin^2 s_i ds}{\tilde{\mathcal{E}}_k(s) - z} > \int_{\mathbb{T}^2} \frac{\cos^2 s_i \sin^2 s_j ds}{\tilde{\mathcal{E}}_k(s) - z} > \int_{\mathbb{T}^2} \frac{\sin^2 s_i \sin^2 s_j ds}{\tilde{\mathcal{E}}_k(s) - z}, \quad i, j = 1, 2$$

show that

$$\min_{4 < l \leq 9} \mu_l(k) = \min_r \left(\int_{\mathbb{T}^2} \frac{\sin^2 s_r ds}{\tilde{\mathcal{E}}_k(s) - m(k)} \right)^{-1}.$$

For the case when $k = \mathbf{0}$ the equalities

$$\int_{\mathbb{T}^2} \frac{\sin^2 s_1 ds}{\tilde{\mathcal{E}}_0(s)} = \int_{\mathbb{T}^2} \frac{\sin^2 s_2 ds}{\tilde{\mathcal{E}}_0(s)}$$

holds.

This gives one

$$\mu = \left(\int_{\mathbb{T}^2} \frac{\sin^2 s_1 ds}{\tilde{\mathcal{E}}_0(s)} \right)^{-1} = \left(\int_{\mathbb{T}^2} \frac{\sin^2 s_2 ds}{\tilde{\mathcal{E}}_0(s)} \right)^{-1}.$$

Hence, by Lemma 4.1, the number $\lambda = 1$ is an eigenvalue of $\mathbf{T}_l(\mu, \mathbf{0}; 0), l = 5, 6$ and $\varphi_5(p) = \sin p_1, \varphi_6(p) = \sin p_2$ are the corresponding eigenfunctions. Since $f_5, f_6 \notin L_2(\mathbb{T}^2)$, where $f_5(p) = \frac{\sin p_1}{\tilde{\mathcal{E}}_0(p)}, f_6(p) = \frac{\sin p_2}{\tilde{\mathcal{E}}_0(p)}$, the number $z = \mathbf{0}$ is a two-fold virtual level of $h_\mu(\mathbf{0})$.

3. Let $d = 3, 4$, and $\mu = \mu_{r_s}(\mathbf{0})$ for some $s \in \{0, 1, \dots, d\}$. Then, as shown in items 1) and 2) of Theorem 2.3, and by lemma 4.2, the operator $h_\mu(\mathbf{0})$ has s eigenvalues $z_l(\mu, \mathbf{0}) < 0, l \in \{0, 1, \dots, s - 1\}$ with multiplicity C_d^s and $z_0(\mu, \mathbf{0}) < \dots < z_{s-1}(\mu, \mathbf{0}) < 0$.

Since $\mu = \mu_{r_s}(\mathbf{0})$, according to the equality (5) and Lemma 4.1 the number $\lambda = 1$ is an eigenvalue of $\mathbf{T}(\mu, \mathbf{0}; 0)$ with multiplicity C_d^s , where $\varphi_l(p), l \in \{1 + r_s - C_d^s, \dots, r_s\}$ are the corresponding eigenfunctions. Since $f_l \notin L_2(\mathbb{T}^d)$, where $f_l(p) = \frac{\varphi_l}{\tilde{\mathcal{E}}_0(p)}$, the number $z = \mathbf{0}$ is virtual level with multiplicity C_d^s of $h_\mu(\mathbf{0})$.

Let $\mu_{r_d}(\mathbf{0}) < \mu < \min_{l > 2^d} \mu_l(\mathbf{0})$. Then, according to Lemma 4.1, the operator $h_\mu(\mathbf{0})$ has $d + 1$ eigenvalues λ_l with multiplicity $C_d^l, l = 0, 1, \dots, d$, lying to the left of the essential spectrum, with $\lambda_0 < \dots < \lambda_d < 0$. Therefore $h_\mu(\mathbf{0})$ has $2^d = C_d^0 + C_d^1 + \dots + C_d^d$ eigenvalues (taking into account the multiplicity).

The prove of the part 4 can be proven similarly. □

5. Conclusion

We investigate the existence conditions for eigenvalues and virtual levels of the two-particle Schrödinger operator $h_\mu(k)$, $k \in \mathbb{T}^d$, $\mu > 0$ corresponding to the Hamiltonian of the two-particle system on the d -dimensional lattice, where $h_\mu(k)$ is considered as a perturbation of free Hamiltonian $h_0(k)$ by the certain potential operator μv with rank 3^d . The main idea of the study was to represent μv via the sum of one-rank orthogonal projectors μv_l . This allowed us to represent the corresponding Birman–Schwinger operator $\mathbf{T}(\mu, k; z)$ via the sum of one-rank projectors $\mathbf{T}_l(\mu, k; z)$, $l = 1, 2, \dots, 3^d$. Moreover, the study of the spectral properties of $h_\mu(k)$ is reduced to the study of 3^d one-rank projectors $\mathbf{T}_l(\mu, k; z)$. The existence conditions of a virtual level of $h_\mu(k)$ is studied at $k = \mathbf{0}$. The study of the virtual levels of $h_\mu(k)$ for the case when $k \neq \mathbf{0}$ is omitted, since analogous results and existence conditions can be described with respect to k .

References

- [1] Bloch I., Dalibard J., and Nascimbene S. Quantum simulations with ultracold quantum gases, *Nature Physics*, 2012, **8**, P. 267–276.
- [2] Jaksch D., Zoller P. The cold atom Hubbard toolbox, *Ann. Phys.*, 2005, **315**, P. 52–79.
- [3] Lewenstein M., Sanpera A., Ahufinger V. *Ultracold Atoms in Optical Lattices: Simulating Quantum Many-body Systems*, Oxford University Press, Oxford, 2012.
- [4] Gullans M., Tiecke T.G., Chang D.E., Feist J., Thompson J.D., Cirac J.I., Zoller P., Lukin M.D. Nanoplasmonic Lattices for Ultracold Atoms. *Phys. Rev. Lett.*, 2012, **109**, P. 235309.
- [5] Hecht E. *Optics*. Addison-Wesley, Reading, MA. 1998.
- [6] Murphy B., Hau L.V. Electro-optical nanotraps for neutral atoms. *Phys. Rev. Lett.*, 2009, **102**, P. 033003.
- [7] N.P. de Leon, Lukin M.D., and Park H. Quantum plasmonic circuits. *IEEE J. Sel. Top. Quantum Electron.*, 2012, **18**, P. 1781–1791.
- [8] Bagmutov A.S., Popov I.Y. Window-coupled nanolayers: window shape influence on one-particle and two-particle eigenstates. *Nanosystems: Physics, Chemistry, Mathematics*, 2020, **11**(6), P. 636–641.
- [9] Hiroshima F., Sasaki I., Shirai T., Suzuki A. Note on the spectrum of discrete Schrödinger operators. *Journal of Math-for-Industry*, 2012, **4**, P. 105–108.
- [10] Higuchi Y., Matsumot T., Ogurisu O. On the spectrum of a discrete Laplacian on \mathbb{Z} with finitely supported potential. *Linear and Multilinear Algebra*, 2011, **8**, P. 917–927.
- [11] Albeverio S., Lakaev S.N., Makarov K.A., Muminov Z.I. The Threshold effects for the two-particle Hamiltonians. *Communications in Mathematical Physics*, 2006, **262**, P. 91–115.
- [12] Muminov M.I. Positivity of the two-particle Hamiltonian on a lattice. *Theoret. and Math. Phys.*, 2007, **153**(3), P. 1671–1676.
- [13] Muminov M.E., Khurramov A.M. Spectral properties of a two-particle Hamiltonian on a lattice. *Theor. Math. Phys.*, 2013, **177**(3), P. 482–496.
- [14] Muminov M.E., Khurramov A.M. Multiplicity of virtual levels at the lower edge of the continuous spectrum of a two-particle Hamiltonian on a lattice. *Theor. Math. Phys.*, 2014, **180**(3), P. 329–341.
- [15] Bozorov I.N., Khurramov A.M. On the number of eigenvalues of the lattice model operator in one-dimensional case. *Lobachevskii Journal of Mathematics*, 2022, **43**(2), P. 353–365.
- [16] Muminov M.E., Khurramov A.M. Spectral properties of two particle Hamiltonian on one-dimensional lattice. *Ufa Math. Jour.*, 2014, **6**(4), P. 99–107.
- [17] Muminov M.I., Khurramov A.M. Spectral properties of a two-particle hamiltonian on a d -dimensional lattice. *Nanosystems: Physics, Chemistry, Mathematics*, 2016, **7**(5), P. 880–887.
- [18] Lakaev S.N., Bozorov I.N. The number of bound states of a one-particle Hamiltonian on a three-dimensional lattice. *Theor. Math. Phys.*, 2009, **158**(3), P. 360–376.
- [19] Bozorov I.N., Khamidov Sh.I., Lakaev S.N. The number and location of eigenvalues of the two particle discrete Schrödinger operators. *Lobachevskii Journal of Mathematics*, 2022, **43**(11), P. 3079–3090.
- [20] Muminov M.I., Khurramov A.M. On compact distribution of two-particle Schrödinger operator on a lattice. *Russian Math. (Iz. VUZ)*, 2015, **59**(6), P. 18–22.
- [21] Muminov M.I., Khurramov A.M., Bozorov I.N. Conditions for the existence of bound states of a two-particle Hamiltonian on a three-dimensional lattice. *Nanosystems: Phys. Chem. Math.*, 2022, **13**(3), P. 237–244.
- [22] Reed M., Simon B. *Methods of modern Mathematical Physics. Vol.4. Analysis of Operators*, Academic Press, London. 1980. 404 p.

Submitted 06 March 2023; revised 26 April 2023; accepted 27 April 2023

Information about the authors:

Mukhiddin I. Muminov – Samarkand State University, University blv., 15, Samarkand, 140104, Uzbekistan; V.I. Romanovskiy Institute of Mathematics, Uzbekistan Academy of Sciences, Tashkent, 100174, Uzbekistan; ORCID 0000-0003-0335-6558; mmuminov@mail.ru

Abdimajid M. Khurramov – Samarkand State University, University blv., 15, Samarkand, 140104, Uzbekistan; ORCID 0000-0001-8565-3702; xurramov@mail.ru

Islom N. Bozorov – Samarkand State University, University blv., 15, Samarkand, 140104, Uzbekistan; V.I. Romanovskiy Institute of Mathematics, Uzbekistan Academy of Sciences, Tashkent, 100174, Uzbekistan; ORCID 0000-0002-0502-8163; islomnb@mail.ru

Conflict of interest: the authors declare no conflict of interest.

The first Schur complement for a lattice spin-boson model with at most two photons

Tulkin Rasulov^a, Elyor Dilmurodov^b

¹Bukhara State University, Bukhara, Uzbekistan

²Bukhara State University, Bukhara branch of the Institute of Mathematics named after V. I. Romanovskiy, Bukhara, Uzbekistan

^at.h.rasulov@buxdu.uz, ^be.b.dilmurodov@buxdu.uz

Corresponding author: Tulkin Rasulov, t.h.rasulov@buxdu.uz

ABSTRACT In the present paper, we consider a lattice spin-boson model \mathcal{A}_2 with a fixed atom and at most two photons. We construct the first Schur complement $S_1(\lambda)$ with spectral parameter λ corresponding to \mathcal{A}_2 . We prove the Birman–Schwinger principle for \mathcal{A}_2 with respect to $S_1(\lambda)$. We investigate an important properties of $S_1(\lambda)$ related to the number of eigenvalues of \mathcal{A}_2 for all dimensions d of the torus \mathbb{T}^d and for any coupling constant $\alpha > 0$.

KEYWORDS lattice spin-boson model, Schur complement, bosonic Fock space, essential spectrum, number of eigenvalues, Birman–Schwinger principle.

ACKNOWLEDGEMENTS The authors thank the anonymous referee for reading the manuscript carefully and for making valuable suggestions.

Dedicated to the memory of Prof. R. A. Minlos and Prof. H. Neidhardt.

FOR CITATION Rasulov T., Dilmurodov E. The first Schur complement for a lattice spin-boson model with at most two photons. *Nanosystems: Phys. Chem. Math.*, 2023, **14** (3), 304–311.

1. Introduction and statement of the problem

The spin-boson model is a well-known quantum-mechanical model which describes the interaction between two-level atom and photon field. We refer to [1] and [2] for excellent reviews respectively from physical and mathematical perspectives. Despite the formal simplicity of the spin-boson model (from the physics viewpoint), its dynamics is rather complicated and rigorous spectral and scattering results are usually very difficult to obtain, especially in the case when the number of photons is unbounded. In this connection, it is natural to consider truncated models [3–6] with at most m ($m \in \mathbb{N}$) photons.

The truncated model in \mathbb{R}^d with $m = 1, 2$ was completely studied in [4] for small values of the parameter α and the case $m = 3$ is considered in [6]. The existence of wave operators and their asymptotic completeness are proven there. In [3, 5], the case of arbitrary m are investigated. It should be mentioned that in these papers the smallness of the coupling constant α is important, in our analysis (in the lattice case) this constant can be arbitrary. A lattice spin-boson model \mathcal{A}_m with $m = 1, 2$ is considered in [7, 8]. In particular, in [7] the location of the essential spectrum of \mathcal{A}_2 is described; for any coupling constant the finiteness of the number of eigenvalues below the bottom of the essential spectrum of \mathcal{A}_2 is established (with a sketch of the proof). The paper [8] is devoted to the study of the geometrical structure of the branches of the essential spectrum of \mathcal{A}_2 .

Let us introduce a lattice spin-boson model with at most two photons. Let \mathbb{T}^d be the d -dimensional torus, $L_2(\mathbb{T}^d)$ be the Hilbert space of square integrable (complex) functions defined on \mathbb{T}^d , \mathbb{C}^2 be the state of the two-level atom and $\mathcal{F}_b(L_2(\mathbb{T}^d))$ be the symmetric Fock space for bosons, that is,

$$\mathcal{F}_b(L_2(\mathbb{T}^d)) := \mathbb{C} \oplus L_2(\mathbb{T}^d) \oplus L_2^{\text{sym}}((\mathbb{T}^d)^2) \oplus \dots$$

Here $L_2^{\text{sym}}((\mathbb{T}^d)^n)$ is the Hilbert space of symmetric functions of $n \geq 2$ variables. For $m = 1, 2$ we denote $\mathcal{L}_m := \mathbb{C}^2 \otimes \mathcal{F}_b^{(m)}(L_2(\mathbb{T}^d))$, where

$$\mathcal{F}_b^{(1)}(L_2(\mathbb{T}^d)) := \mathbb{C} \oplus L_2(\mathbb{T}^d), \quad \mathcal{F}_b^{(2)}(L_2(\mathbb{T}^d)) := \mathbb{C} \oplus L_2(\mathbb{T}^d) \oplus L_2^{\text{sym}}((\mathbb{T}^d)^2).$$

We write elements F of the space \mathcal{L}_2 in the form $F = \{f_0^{(s)}, f_1^{(s)}(k_1), f_2^{(s)}(k_1, k_2); s = \pm\}$. Then the norm in \mathcal{L}_2 is given by

$$\|F\|^2 := \sum_{s=\pm} \left(|f_0^{(s)}|^2 + \int_{\mathbb{T}^d} |f_1^{(s)}(k_1)|^2 dk_1 + \frac{1}{2} \int_{(\mathbb{T}^d)^2} |f_2^{(s)}(k_1, k_2)|^2 dk_1 dk_2 \right). \quad (1.1)$$

We recall that the lattice spin-boson model with at most two photons \mathcal{A}_2 is acting in \mathcal{L}_2 as the 3×3 tridiagonal block operator matrix

$$\mathcal{A}_2 := \begin{pmatrix} A_{00} & A_{01} & 0 \\ A_{01}^* & A_{11} & A_{12} \\ 0 & A_{12}^* & A_{22} \end{pmatrix},$$

where matrix elements A_{ij} are defined by

$$\begin{aligned} A_{00}f_0^{(s)} &= s\varepsilon f_0^{(s)}, & A_{01}f_1^{(s)} &= \alpha \int_{\mathbb{T}^d} v(t)f_1^{(-s)}(t)dt, \\ (A_{11}f_1^{(s)})(k_1) &= (s\varepsilon + w(k_1))f_1^{(s)}(k_1), & (A_{12}f_2^{(s)})(k_1) &= \alpha \int_{\mathbb{T}^d} v(t)f_2^{(-s)}(k_1, t)dt, \\ (A_{22}f_2^{(s)})(k_1, k_2) &= (s\varepsilon + w(k_1) + w(k_2))f_2^{(s)}(k_1, k_2), & f &= \{f_0^{(s)}, f_1^{(s)}, f_2^{(s)}; s = \pm\} \in \mathcal{L}_2. \end{aligned}$$

Here A_{ij}^* denotes the adjoint operator to A_{ij} for $i < j$ with $i, j = 0, 1, 2$; $w(k)$ is the dispersion of the free field, $\alpha v(k)$ is the coupling between the atoms and the field modes, $\alpha > 0$ is a real number, so-called the coupling constant. We assume that $v(\cdot)$ and $w(\cdot)$ are the real-valued continuous functions on \mathbb{T}^d . Under these assumptions the lattice spin-boson model with at most two photons \mathcal{A}_2 is bounded and self-adjoint in the complex Hilbert space \mathcal{L}_2 .

A main goal of the paper is the study of the main spectral properties of \mathcal{A}_2 related to the number of eigenvalues. More precisely, the following results are obtained: using a unitary dilation the lattice model \mathcal{A}_2 of radiative decay with a fixed atom and at most two photons is reduced to the diagonal operator and its spectrum is described; the first Schur complement corresponding to the both diagonal entries of \mathcal{A}_2 is constructed; the relation between the eigenvalues of \mathcal{A}_2 and the first Schur complement (Birman–Schwinger principle) is established.

Throughout the paper, we use the notation $\sigma(\cdot)$, $\sigma_{\text{ess}}(\cdot)$, $\sigma_{\text{p}}(\cdot)$ and $\sigma_{\text{disc}}(\cdot)$, respectively, for the spectrum, the essential spectrum, the point spectrum and the discrete spectrum of bounded self-adjoint operator.

2. The first Schur complement corresponding to \mathcal{A}_2

To study the spectral properties of \mathcal{A}_2 , we introduce the following two bounded self-adjoint operators $\mathcal{A}_2^{(s)}$, $s = \pm$, which act in $\mathcal{F}_{\text{b}}^{(2)}(L_2(\mathbb{T}^d))$ as

$$\mathcal{A}_2^{(s)} := \begin{pmatrix} \widehat{A}_{00}^{(s)} & \widehat{A}_{01} & 0 \\ \widehat{A}_{01}^* & \widehat{A}_{11}^{(s)} & \widehat{A}_{12} \\ 0 & \widehat{A}_{12}^* & \widehat{A}_{22}^{(s)} \end{pmatrix}$$

with the entries

$$\begin{aligned} \widehat{A}_{00}^{(s)}f_0 &= s\varepsilon f_0, & \widehat{A}_{01}f_1 &= \alpha \int_{\mathbb{T}^d} v(t)f_1(t)dt, \\ (\widehat{A}_{11}^{(s)}f_1)(k_1) &= (-s\varepsilon + w(k_1))f_1(k_1), & (\widehat{A}_{12}f_2)(k_1) &= \alpha \int_{\mathbb{T}^d} v(t)f_2(k_1, t)dt, \\ (\widehat{A}_{22}^{(s)}f_2)(k_1, k_2) &= (s\varepsilon + w(k_1) + w(k_2))f_2(k_1, k_2), & (f_0, f_1, f_2) &\in \mathcal{F}_{\text{b}}^{(2)}(L_2(\mathbb{T}^d)). \end{aligned}$$

It is easy to check that

$$\begin{aligned} (\widehat{A}_{01}^*f_0)(k_1) &= \alpha v(k_1)f_0; \\ (\widehat{A}_{12}^*f_1)(k_1, k_2) &= \alpha (v(k_1)f_1(k_2) + v(k_2)f_1(k_1)), & (f_0, f_1) &\in \mathcal{F}_{\text{b}}^{(1)}(L_2(\mathbb{T}^d)). \end{aligned}$$

In order to describe the essential spectrum of \mathcal{A}_2 , we define an analytic function $\Delta^{(s)}(\cdot)$ in $\mathbb{C} \setminus [s\varepsilon + m; s\varepsilon + M]$ by

$$\Delta^{(s)}(\lambda) := -s\varepsilon - \lambda - \alpha^2 \int_{\mathbb{T}^d} \frac{v^2(t)dt}{s\varepsilon + w(t) - \lambda},$$

where the numbers m and M are defined by

$$m := \min_{p \in \mathbb{T}^d} w(p), \quad M := \max_{p \in \mathbb{T}^d} w(p).$$

Let $\sigma^{(s)}$ be the set of all complex numbers $\lambda \in \mathbb{C}$ such that the equality $\Delta^{(s)}(\lambda - w(k_1)) = 0$ holds for some $k_1 \in \mathbb{T}^d$. Then (see [9]) for the essential spectrum of $\mathcal{A}_2^{(s)}$, we have

$$\sigma_{\text{ess}}(\mathcal{A}_2^{(s)}) = \sigma^{(s)} \cup [s\varepsilon + 2m; s\varepsilon + 2M].$$

Consider the permutation operator $\Phi : \mathcal{L}_2 \rightarrow \mathcal{F}_b^{(2)}(L_2(\mathbb{T}^d)) \oplus \mathcal{F}_b^{(2)}(L_2(\mathbb{T}^d))$ defined as

$$\Phi : (f_0^{(+)}, f_0^{(-)}, f_1^{(+)}, f_1^{(-)}, f_2^{(+)}, f_2^{(-)}) \rightarrow (f_0^{(+)}, f_1^{(-)}, f_2^{(+)}, f_0^{(-)}, f_1^{(+)}, f_2^{(-)}).$$

One can trivially verify that the operator Φ is unitary. From the construction of $\mathcal{A}_2, \mathcal{A}_2^{(s)}$ and Φ , it follows that the following equality takes place $\Phi \mathcal{A}_2 \Phi^{-1} = \text{diag}\{\mathcal{A}_2^{(+)}, \mathcal{A}_2^{(-)}\}$. The latter facts mean that the operators \mathcal{A}_2 and $\text{diag}\{\mathcal{A}_2^{(+)}, \mathcal{A}_2^{(-)}\}$ are unitarily equivalent. Therefore, $\sigma(\mathcal{A}_2) = \sigma(\mathcal{A}_2^{(+)}) \cup \sigma(\mathcal{A}_2^{(-)})$. Moreover,

$$\sigma_{\text{ess}}(\mathcal{A}_2) = \sigma_{\text{ess}}(\mathcal{A}_2^{(+)}) \cup \sigma_{\text{ess}}(\mathcal{A}_2^{(-)}); \quad \sigma_p(\mathcal{A}_2) = \sigma_p(\mathcal{A}_2^{(+)}) \cup \sigma_p(\mathcal{A}_2^{(-)}).$$

Since the part of $\sigma_{\text{disc}}(\mathcal{A}_2^{(s)})$ can be located in $\sigma_{\text{ess}}(\mathcal{A}_2^{(-s)})$, we have

$$\sigma_{\text{disc}}(\mathcal{A}_2) \subseteq \sigma_{\text{disc}}(\mathcal{A}_2^{(+)}) \cup \sigma_{\text{disc}}(\mathcal{A}_2^{(-)}).$$

If we set $E_{\min}^{(s)} := \min \sigma_{\text{ess}}(\mathcal{A}_2^{(s)})$ for $s = \pm$ and $E_{\min} := \min \sigma_{\text{ess}}(\mathcal{A}_2) = \min\{E_{\min}^{(+)}, E_{\min}^{(-)}\}$, then

$$\sigma_{\text{disc}}(\mathcal{A}_2) \cap (-\infty; E_{\min}) = \{\sigma_{\text{disc}}(\mathcal{A}_2^{(+)}) \cup \sigma_{\text{disc}}(\mathcal{A}_2^{(-)})\} \cap (-\infty; E_{\min}). \tag{2.1}$$

Next, we represent the space $\mathcal{F}_b^{(2)}(L_2(\mathbb{T}^d))$ as a direct sum of two Hilbert spaces $\mathcal{F}_b^{(1)}(L_2(\mathbb{T}^d))$ and $L_2^{\text{sym}}((\mathbb{T}^d)^2)$, that is, $\mathcal{F}_b^{(2)}(L_2(\mathbb{T}^d)) = \mathcal{F}_b^{(1)}(L_2(\mathbb{T}^d)) \oplus L_2^{\text{sym}}((\mathbb{T}^d)^2)$. Then the first Schur complement of the operator $\mathcal{A}_2^{(s)}$ with respect to this decomposition (see [10]) is defined as

$$S_1^{(s)}(\lambda) : \mathcal{F}_b^{(1)}(L_2(\mathbb{T}^d)) \rightarrow \mathcal{F}_b^{(1)}(L_2(\mathbb{T}^d)), \quad \lambda \in \rho(\widehat{A}_{22}^{(s)});$$

$$S_1^{(s)}(\lambda) := \begin{pmatrix} \widehat{A}_{00}^{(s)} & \widehat{A}_{01} \\ \widehat{A}_{01}^* & \widehat{A}_{11}^{(s)} \end{pmatrix} - \lambda - \begin{pmatrix} 0 \\ \widehat{A}_{12} \end{pmatrix} (\widehat{A}_{22}^{(s)} - \lambda)^{-1} \begin{pmatrix} 0 & \widehat{A}_{12}^* \end{pmatrix}.$$

Define

$$S_{00}^{(s)}(\lambda) := \widehat{A}_{00}^{(s)} - \lambda, \quad S_{01}^{(s)}(\lambda) := \widehat{A}_{01};$$

$$S_{10}^{(s)}(\lambda) := \widehat{A}_{01}^*, \quad S_{11}^{(s)}(\lambda) := \widehat{A}_{11}^{(s)} - \lambda - \widehat{A}_{12}(\widehat{A}_{22}^{(s)} - \lambda)^{-1} \widehat{A}_{12}^*.$$

Then the operator $S_1^{(s)}(\lambda)$ has the form

$$S_1^{(s)}(\lambda) = \begin{pmatrix} S_{00}^{(s)}(\lambda) & S_{01}^{(s)}(\lambda) \\ S_{10}^{(s)}(\lambda) & S_{11}^{(s)}(\lambda) \end{pmatrix}.$$

For convenience, we represent the operator $S_{11}^{(s)}(\lambda)$ as a difference of two operators

$$S_{11}^{(s)}(\lambda) := D^{(s)}(\lambda) - K^{(s)}(\lambda),$$

where the operators $D^{(s)}(\lambda), K^{(s)}(\lambda) : L_2(\mathbb{T}^d) \rightarrow L_2(\mathbb{T}^d)$ are defined by

$$(D^{(s)}(\lambda)f)(k_1) = \Delta^{(s)}(\lambda - w(k_1))f(k_1);$$

$$(K^{(s)}(\lambda)f)(k_1) = \alpha^2 v(k_1) \int_{\mathbb{T}^d} \frac{v(t)f(t)dt}{s\varepsilon + w(k_1) + w(t) - \lambda}.$$

For a fixed $\lambda = \lambda_0 \in \rho(\widehat{A}_{22}^{(s)})$ and $s \in \{-1, 1\}$, we define

$$a := s\varepsilon - \lambda_0, \quad u(k_1) := \Delta^{(s)}(\lambda_0 - w(k_1)), \quad K(k_1, k_2) := \frac{\alpha^2 v(k_1)v(k_2)}{s\varepsilon + w(k_1) + w(k_2) - \lambda_0}.$$

Then the operator matrix $S_1^{(s)}(\lambda_0)$ can be written as

$$S_1^{(s)}(\lambda_0) = \begin{pmatrix} H_{00} & H_{01} \\ H_{01}^* & H_{11}^0 - K \end{pmatrix} \tag{2.2}$$

with

$$H_{00}f_0 = af_0, \quad H_{01} := \widehat{A}_{01}, \quad (H_{11}^0 f_1)(k_1) = u(k_1)f_1(k_1), \quad (Kf_1)(k_1) = \int_{\mathbb{T}^d} K(k_1, t)f_1(t)dt.$$

The operator matrix of the form (2.2) is appeared in a series of problems in analysis, mathematical physics, and probability theory and known as generalized Friedrichs model. This model operator itself was introduced in [11], where its eigenvalues and ‘‘resonances’’ (i.e., the singularities of the analytic continuation of the resolvent) were studied. Note that, the number and location of the eigenvalues of the generalized Friedrichs model in the case where the kernel function $K(\cdot, \cdot)$ is degenerate of rank 1, was studied in [12, 13].

The Schur complement is named after Issai Schur who used it to prove Schur's lemma, although it had been used previously [14]. Haynsworth was the first to call it the Schur complement [15]. The Schur complement is a key tool in the fields of numerical analysis, statistics, and matrix analysis. The general properties of the Schur complement have been studied in many works, for detailed information see [10]. Construction of Schur's complement for exactly solvable models of mathematical physics and proof of important properties that have not been properly studied in general for such special cases, can be considered as one of the actual problems of the operator theory.

3. Main properties of the first Schur complement

In this Section, we will study some important properties of the first Schur complement

$$S_1(\lambda) := \text{diag}\{S_1^{(+)}(\lambda), S_1^{(-)}(\lambda)\}$$

for the lattice spin-boson model with at most two photons \mathcal{A}_2 .

Proposition 3.1. *The number $\lambda \in \mathbb{C} \setminus \sigma_{\text{ess}}(\mathcal{A}_2)$ is an eigenvalue of the operator \mathcal{A}_2 if and only if the operator $S_1(\lambda)$ has an eigenvalue equal to zero. Moreover, the eigenvalues λ and 0 have the same multiplicities.*

Proof. Since $\sigma_{\text{p}}(\mathcal{A}_2) = \sigma_{\text{p}}(\mathcal{A}_2^{(+)}) \cup \sigma_{\text{p}}(\mathcal{A}_2^{(-)})$, it is enough to prove the assertion of the Proposition for the operators $\mathcal{A}_2^{(s)}$ and $S_1^{(s)}(\lambda)$.

Let the number $\lambda \in \mathbb{C} \setminus \sigma_{\text{ess}}(\mathcal{A}_2)$ be an eigenvalue of the operator $\mathcal{A}_2^{(s)}$ and $f = (f_0, f_1, f_2) \in \mathcal{F}_{\text{b}}^{(2)}(L_2(\mathbb{T}^d))$ be the corresponding eigenvector. Then elements f_0, f_1 and f_2 satisfy the system of equations

$$\begin{cases} (\widehat{A}_{00}^{(s)} - \lambda)f_0 + \widehat{A}_{01}f_1 = 0; \\ \widehat{A}_{01}^*f_0 + (\widehat{A}_{11}^{(s)} - \lambda)f_1 + \widehat{A}_{12}f_2 = 0; \\ \widehat{A}_{12}^*f_1 + (\widehat{A}_{22}^{(s)} - \lambda)f_2 = 0. \end{cases} \quad (3.1)$$

Since $\lambda \in \mathbb{C} \setminus \sigma_{\text{ess}}(\mathcal{A}_2)$, from the third equation of system (3.1) for f_2 we have

$$f_2 = -(\widehat{A}_{22}^{(s)} - \lambda)^{-1}\widehat{A}_{12}^*f_1. \quad (3.2)$$

Substituting the expression (3.2) for f_2 into the second equation of system (3.1), we obtain the following system of equations

$$\begin{cases} (\widehat{A}_{00}^{(s)} - \lambda)f_0 + \widehat{A}_{01}f_1 = 0; \\ \widehat{A}_{01}^*f_0 + (\widehat{A}_{11}^{(s)} - \lambda - \widehat{A}_{12}(\widehat{A}_{22}^{(s)} - \lambda)^{-1}\widehat{A}_{12}^*)f_1 = 0. \end{cases} \quad (3.3)$$

System of equations (3.3) has nontrivial solution if and only if the equation

$$S_1^{(s)}(\lambda) \begin{pmatrix} f_0 \\ f_1 \end{pmatrix} = \begin{pmatrix} 0 \\ 0 \end{pmatrix}$$

has nontrivial solution $(f_0, f_1) \in \mathcal{F}_{\text{b}}^{(1)}(L_2(\mathbb{T}^d))$.

Let now the number $\lambda \in \mathbb{C} \setminus \sigma_{\text{ess}}(\mathcal{A}_2^{(s)})$ be an eigenvalue of $\mathcal{A}_2^{(s)}$ with multiplicity n and number 0 be an eigenvalue of $S_1^{(s)}(\lambda)$ with multiplicity m . We will prove that $n = m$.

Assume that $n < m$. Then there exist linearly independent eigenvectors $\tilde{f}^{(i)} = (f_0^{(i)}, f_1^{(i)}) \in \mathcal{F}_{\text{b}}^{(1)}(L_2(\mathbb{T}^d))$, $i = \overline{1, m}$, corresponding to the eigenvalue 0 of the operator $S_1^{(s)}(\lambda)$. For each $i \in \{1, \dots, m\}$ we put $f^{(i)} := (f_0^{(i)}, f_1^{(i)}, f_2^{(i)})$, where the function $f_2^{(i)}$ is determined by formula (3.2), with $f_1^{(i)}$ taken instead of f_1 . Then the vector $f^{(i)}$ satisfies the equation $\mathcal{A}_2^{(s)}f^{(i)} = \lambda f^{(i)}$ for $i = 1, \dots, m$ and hence it is an eigenvector of $\mathcal{A}_2^{(s)}$ corresponding to the eigenvalue λ . Since $n < m$, the eigenvectors $f^{(i)}$, $i = \overline{1, m}$ are linearly dependent. Therefore, there is a non-zero vector $(\alpha_1, \dots, \alpha_m) \in \mathbb{C}^m$ such that $\sum_{i=1}^m \alpha_i f^{(i)} = (0, 0, 0)^t$, but at the same time, it satisfies the inequality $\left(\sum_{i=1}^m \alpha_i f_0^{(i)}, \sum_{i=1}^m \alpha_i f_1^{(i)} \right) \neq (0, 0)^t$ (since $(f_0^{(i)}, f_1^{(i)})$, $i = \overline{1, m}$ are linearly independent). From the last two assertions and the construction of $f^{(i)}$, we have

$$\begin{pmatrix} 0 \\ 0 \\ 0 \end{pmatrix} = \sum_{i=1}^m \alpha_i f^{(i)} = \begin{pmatrix} \sum_{i=1}^m \alpha_i f_0^{(i)} \\ \sum_{i=1}^m \alpha_i f_1^{(i)} \\ -R_{22}^{(s)}(\lambda)\widehat{A}_{12}^* \left(\sum_{i=1}^m \alpha_i f_1^{(i)} \right) \end{pmatrix} \neq \begin{pmatrix} 0 \\ 0 \\ 0 \end{pmatrix}$$

where $R_{22}^{(s)}(\lambda) := (\widehat{A}_{22}^{(s)} - \lambda)^{-1}$. This contradiction shows that the inequality $n < m$ is not true.

Let now $n > m$. In this case, there exist linearly independent eigenvectors $f^{(i)} = (f_0^{(i)}, f_1^{(i)}, f_2^{(i)})$, $i = \overline{1, n}$ corresponding to the eigenvalue λ of the operator $\mathcal{A}_2^{(s)}$. One can easily show that $\widetilde{f}^{(i)} = (f_0^{(i)}, f_1^{(i)})$, $i = \overline{1, n}$ is an eigenvector corresponding to the eigenvalue 0 of the operator $S_1^{(s)}(\lambda)$. Arguing similarly, from the inequality $n > m$, we obtain that there exists nonzero vector $(\beta_1, \dots, \beta_n) \in \mathbb{C}^n$ so that $\sum_{i=1}^n \beta_i \widetilde{f}^{(i)} = (0, 0)^t$. At the same time $\sum_{i=1}^n \beta_i f^{(i)} \neq (0, 0, 0)^t$. From the last two assertions and the construction of $f^{(i)}$, and also linearity of the operators \widehat{A}_{12}^* and $R_{22}^{(s)}(\lambda)$, we have

$$\begin{pmatrix} 0 \\ 0 \\ 0 \end{pmatrix} \neq \sum_{i=1}^n \beta_i f^{(i)} = \begin{pmatrix} \sum_{i=1}^n \beta_i f_0^{(i)} \\ \sum_{i=1}^n \beta_i f_1^{(i)} \\ -R_{22}^{(s)}(\lambda) \widehat{A}_{12}^* \left(\sum_{i=1}^n \beta_i f_1^{(i)} \right) \end{pmatrix} = \begin{pmatrix} 0 \\ 0 \\ 0 \end{pmatrix}.$$

This contradiction shows that the inequality $n > m$ is not valid. Therefore, $n = m$. Proposition 3.1 is proved. \square

Proposition 3.2. $\lambda \in \sigma_{\text{ess}}(\mathcal{A}_2) \setminus \sigma(A_{22})$ if and only if $0 \in \sigma_{\text{ess}}(S_1(\lambda))$.

Proof. We prove that $\lambda \in \sigma_{\text{ess}}(\mathcal{A}_2^{(s)}) \setminus \sigma(\widehat{A}_{22}^{(s)})$ if and only if $0 \in \sigma_{\text{ess}}(S_1^{(s)}(\lambda))$. Let $\text{Ran}(u)$ be the range of the function $u(\cdot)$. Since for any fixed $\lambda \in \mathbb{R} \setminus \sigma(\widehat{A}_{22}^{(s)})$, the kernel of the integral operator $K^{(s)}(\lambda)$ is continuous in $(\mathbb{T}^d)^2$, it is the Hilbert-Schmidt operator. By the Weyl theorem on the invariance of the essential spectrum under compact perturbations and by the continuity of the function $\Delta^{(s)}(\lambda - w(\cdot))$ as $\lambda \in \mathbb{R} \setminus \sigma(\widehat{A}_{22}^{(s)})$ on the compact set \mathbb{T}^d , we obtain

$$\sigma_{\text{ess}}(S_1^{(s)}(\lambda)) = \text{Ran}(\Delta^{(s)}(\lambda - w(\cdot))). \tag{3.4}$$

Let $\lambda_0 \in \sigma_{\text{ess}}(\mathcal{A}_2^{(s)}) \setminus \sigma(\widehat{A}_{22}^{(s)})$. Then $\lambda_0 \in \sigma^{(s)} \setminus \sigma(\widehat{A}_{22}^{(s)})$. From the definition of $\sigma^{(s)}$, it follows that there exists point $p_0 \in \mathbb{T}^d$ such that $\Delta^{(s)}(\lambda_0 - w(k_0)) = 0$. Taking into account equality (3.4), we have $0 \in \sigma_{\text{ess}}(S_1^{(s)}(\lambda_0))$.

Let now $0 \in \sigma_{\text{ess}}(S_1^{(s)}(\lambda_1))$ for some $\lambda_1 \in \mathbb{R} \setminus \sigma(\mathcal{A}_{22}^{(s)})$. Then by virtue of equality (3.4), there exists a point $p_1 \in \mathbb{T}^d$ such that $\Delta^{(s)}(\lambda_1 - w(p_1)) = 0$. Using the construction of $\sigma^{(s)}$, we obtain $\lambda_1 \in \sigma^{(s)} \subset \sigma_{\text{ess}}(\mathcal{A}_2^{(s)})$. \square

From Propositions 3.1 and 3.2, we obtain the following two corollaries.

Corollary 3.3. Let $\lambda \in \mathbb{C} \setminus \sigma_{\text{ess}}(\mathcal{A}_2)$. Then $\lambda \in \rho(\mathcal{A}_2) \iff 0 \in \rho(S_1(\lambda))$.

Corollary 3.4. Let $\lambda_0 \in \mathbb{R} \setminus \sigma_{\text{ess}}(\mathcal{A}_2)$. If $(\lambda_0; \lambda_0 + \gamma) \in \rho(\mathcal{A}_2)$ (resp. $(\lambda_0 - \gamma; \lambda_0) \in \rho(\mathcal{A}_2)$) for some $\gamma > 0$, then there exists a number $\delta = \delta(\gamma) > 0$ such that $(0; \delta) \in \rho(S_1(\lambda_0))$ (resp. $(-\delta; 0) \in \rho(S_1(\lambda_0))$).

The definition of the set $\sigma^{(s)}$ implies that the inequality $\Delta^{(s)}(\lambda - w(k_1)) > 0$ holds for all $k_1 \in \mathbb{T}^d$ and $\lambda < E_{\min}^{(s)}$. Therefore, for such λ , the inclusion $\sigma_{\text{ess}}(S_1^{(s)}(\lambda)) \subset (0; +\infty)$ holds.

For a bounded self-adjoint operator A acting in a Hilbert space \mathcal{H} we denote by $N_{(-\infty; \lambda)}(A)$ the number of eigenvalues of A to the left of λ , $\lambda \leq \min \sigma_{\text{ess}}(A)$.

Theorem 3.5. For any $\lambda < E_{\min}^{(s)}$, the equality

$$N_{(-\infty; \lambda)}(\mathcal{A}_2^{(s)}) = N_{(-\infty; 0)}(S_1^{(s)}(\lambda))$$

holds.

Proof. For any $\lambda < E_{\min}^{(s)}$, the operator $\widehat{A}_{22}^{(s)} - \lambda$ is positive and invertible and hence the square root $(R_{22}^{(s)}(\lambda))^{1/2}$ of the resolvent $R_{22}^{(s)}(\lambda)$ of $\widehat{A}_{22}^{(s)}$ exists.

Let $V^{(s)}(\lambda)$, $\lambda < E_{\min}^{(s)}$ be the 3×3 block operator matrix in $\mathcal{F}_b^{(2)}(L_2(\mathbb{T}^d))$ with entries

$$\begin{aligned} V_{00}^{(s)}(\lambda) &:= \widehat{A}_{00}^{(s)} - \lambda I_0, & V_{01}^{(s)}(\lambda) &:= \widehat{A}_{01}^{(s)}, & V_{02}^{(s)}(\lambda) &:= 0; \\ V_{10}^{(s)}(\lambda) &:= \widehat{A}_{10}^{(s)}, & V_{11}^{(s)}(\lambda) &:= \widehat{A}_{11}^{(s)} - \lambda I_1, & V_{12}(\lambda) &:= \widehat{A}_{12}^{(s)}(R_{22}^{(s)}(\lambda))^{1/2}; \\ V_{20}^{(s)}(\lambda) &:= 0, & V_{21}(\lambda) &:= (R_{22}^{(s)}(\lambda))^{1/2} \widehat{A}_{12}^*, & V_{22}^{(s)}(\lambda) &:= I_2, \end{aligned}$$

where $\text{diag} \{I_0, I_1, I_2\}$ is an identity operator on $\mathcal{F}_b^{(2)}(L_2(\mathbb{T}^d))$. A simple calculation shows that $(\mathcal{A}_2^{(s)} f, f) < \lambda(f, f)$, $f = (f_0, f_1, f_2) \in \mathcal{F}_b^{(2)}(L_2(\mathbb{T}^d))$ if and only if $(V^{(s)}(\lambda)g, g) < 0$, $g = (f_0, f_1, (\widehat{A}_{22}^{(s)} - \lambda I_2)^{1/2} f_2)$. It follows that

$$N_{(-\infty; \lambda)}(\mathcal{A}_2^{(s)}) = N_{(-\infty; 0)}(V^{(s)}(\lambda)). \tag{3.5}$$

For a bounded self-adjoint operator B acting in a Hilbert space \mathcal{H} , let us denote by $\mathcal{H}_B(\lambda) \subset \mathcal{H}$, $\lambda \in \mathbb{R}$, a subspace such that $(Bf, f) > \lambda \|f\|^2$ for any $f \in \mathcal{H}_B(\lambda)$. Assume $\tilde{f} := (f_0, f_1) \in \mathcal{H}_{-S_1^{(s)}(\lambda)}(0)$, i.e., $(S_1^{(s)}(\lambda)\tilde{f}, \tilde{f}) < 0$. Then for any

$$g := (f_0, f_1, -V_{21}^{(s)}(\lambda)f_1) \in \mathcal{F}_b^{(2)}(L_2(\mathbb{T}^d)),$$

we have

$$(V^{(s)}(\lambda)g, g) = (S_1^{(s)}(\lambda)\tilde{f}, \tilde{f}) < 0.$$

Therefore, $g \in \mathcal{H}_{-V^{(s)}(\lambda)}(0)$, and one has

$$N_{(-\infty;0)}(S_1^{(s)}(\lambda)) \leq N_{(-\infty;0)}(V^{(s)}(\lambda)). \quad (3.6)$$

For any $\tilde{f} := (f_0, f_1) \in \mathcal{F}_b^{(1)}(L_2(\mathbb{T}^d))$ and $f = (f_0, f_1, f_2) \in \mathcal{F}_b^{(2)}(L_2(\mathbb{T}^d))$ the equality

$$(S_1^{(s)}(\lambda)\tilde{f}, \tilde{f}) = (V^{(s)}(\lambda)f, f) - (V_{12}^{(s)}(\lambda)V_{21}^{(s)}(\lambda)f_1, f_1) - (V_{21}^{(s)}(\lambda)f_1, f_2) - (V_{12}^{(s)}(\lambda)f_2, f_1) - (f_2, f_2)$$

holds. Then we obtain

$$(S_1^{(s)}(\lambda)\tilde{f}, \tilde{f}) = (V^{(s)}(\lambda)f, f) - \|f_2 + V_{21}^{(s)}f_1\|^2 < 0$$

for all $f = (f_0, f_1, f_2) \in \mathcal{H}_{-V^{(s)}(\lambda)}(0)$, i.e. $\tilde{f} \in \mathcal{H}_{-S_1^{(s)}(\lambda)}(0)$. Consequently,

$$N_{(-\infty;0)}(V^{(s)}(\lambda)) \leq N_{(-\infty;0)}(S_1^{(s)}(\lambda)). \quad (3.7)$$

Now inequalities (3.6), (3.7) and equality (3.5) complete the proof. \square

By Theorem 3.5 and equality (2.1), we obtain

$$N_{(-\infty, E_{\min})}(\mathcal{A}_2) = \sum_{s=\pm} N_{(-\infty,0)}(S_1^{(s)}(E_{\min})). \quad (3.8)$$

Note that the compact part $K^{(s)}(E_{\min})$ of $S_{11}^{(s)}(E_{\min})$ is positive. Indeed, taking into account the identity

$$\frac{\pi}{2x^2y^2(x^2+y^2)} = \int_0^\infty \frac{d\xi}{(x^4+\xi^2)(y^4+\xi^2)}$$

and the inequality

$$w(k_1) + \frac{s\varepsilon - E_{\min}}{2} > 0, \quad k_1 \in \mathbb{T}^d,$$

we represent the kernel $K^{(s)}(\cdot, \cdot)$ of the operator $K^{(s)}(E_{\min})$ in the form

$$\begin{aligned} K^{(s)}(k_1, t) &= \frac{\alpha^2 v(k_1)v(t)}{\pi} \left[w(k_1) + \frac{s\varepsilon - E_{\min}}{2} \right] \left[w(t) + \frac{s\varepsilon - E_{\min}}{2} \right] \\ &\times \int_0^\infty \left(\left[w(k_1) + \frac{s\varepsilon - E_{\min}}{2} \right]^2 + \xi^2 \right)^{-1} \left(\left[w(t) + \frac{s\varepsilon - E_{\min}}{2} \right]^2 + \xi^2 \right)^{-1} d\xi. \end{aligned}$$

Then for any $f_1 \in L_2(\mathbb{T}^d)$, we obtain

$$\langle K^{(s)}(E_{\min})f_1, f_1 \rangle = \frac{\alpha^2}{\pi} \int_0^\infty \int_{\mathbb{T}^d} \frac{v(t) \left[w(t) + \frac{s\varepsilon - E_{\min}}{2} \right]^{3/2} f_1(t) dt}{\left[w(t) + \frac{s\varepsilon - E_{\min}}{2} \right]^2 + \xi^2} \Big|_2^2 d\xi \geq 0.$$

Therefore, $K^{(s)}(E_{\min}) \geq 0$.

Proposition 3.6. *The function $N_{(-\infty;0)}(S_1(\cdot))$ is monotonically increasing in $(-\infty; E_{\min})$.*

Proof. Since $N_{(-\infty;0)}(S_1(\lambda)) = N_{(-\infty;0)}(S_1^{(+)}(\lambda)) + N_{(-\infty;0)}(S_1^{(-)}(\lambda))$ for all $\lambda \in (-\infty; E_{\min})$, we show that the function $N_{(-\infty;0)}(S_1^{(s)}(\cdot))$, $s = \pm$ is monotonically increasing in $(-\infty; E_{\min})$.

Let $\lambda_1, \lambda_2 \in (-\infty; E_{\min})$ be such that $\lambda_1 < \lambda_2$. Since for each $f_2 \in L_2^{\text{sym}}((\mathbb{T}^d)^2)$ the function $(R_{22}^{(s)}(\cdot)f_2, f_2)$ is increasing in $(-\infty; E_{\min})$, we have

$$\begin{aligned} (S_1^{(s)}(\lambda_1)\tilde{f}, \tilde{f}) &= ((\widehat{A}_{00}^{(s)} - \lambda_1)f_0 + \widehat{A}_{01}f_1, f_0) \\ &+ (\widehat{A}_{01}^*f_0 + (\widehat{A}_{11}^{(s)} - \lambda_1 - \widehat{A}_{12}R_{22}^{(s)}(\lambda_1)\widehat{A}_{12}^*)f_1, f_1) = ((\widehat{A}_{00}^{(s)} - \lambda_1)f_0, f_0) \\ &+ (\widehat{A}_{01}f_1, f_0) + (\widehat{A}_{01}^*f_0, f_1) + ((\widehat{A}_{11}^{(s)} - \lambda_1)f_1, f_1) - (R_{22}^{(s)}(\lambda_1)\widehat{A}_{12}^*f_1, \widehat{A}_{12}f_1) \\ &> ((\widehat{A}_{00}^{(s)} - \lambda_2)f_0, f_0) + (\widehat{A}_{01}f_1, f_0) + (\widehat{A}_{01}^*f_0, f_1) \\ &+ ((\widehat{A}_{11}^{(s)} - \lambda_2)f_1, f_1) - (R_{22}^{(s)}(\lambda_2)\widehat{A}_{12}^*f_1, \widehat{A}_{12}f_1) = (S_1^{(s)}(\lambda_2)\tilde{f}, \tilde{f}), \end{aligned}$$

where $\tilde{f} := (f_0, f_1)$. From here, we obtain that if $\tilde{f} \in \mathcal{H}_{S_1^{(s)}(\lambda_1)}(0)$, then $\tilde{f} \in \mathcal{H}_{S_1^{(s)}(\lambda_2)}(0)$, that is, $\mathcal{H}_{S_1^{(s)}(\lambda_1)}(0) \subset \mathcal{H}_{S_1^{(s)}(\lambda_2)}(0)$ and hence, $N_{(-\infty;0)}(S_1^{(s)}(\lambda_1)) \leq N_{(-\infty;0)}(S_1^{(s)}(\lambda_2))$. Proposition 3.6 is completely proved. \square

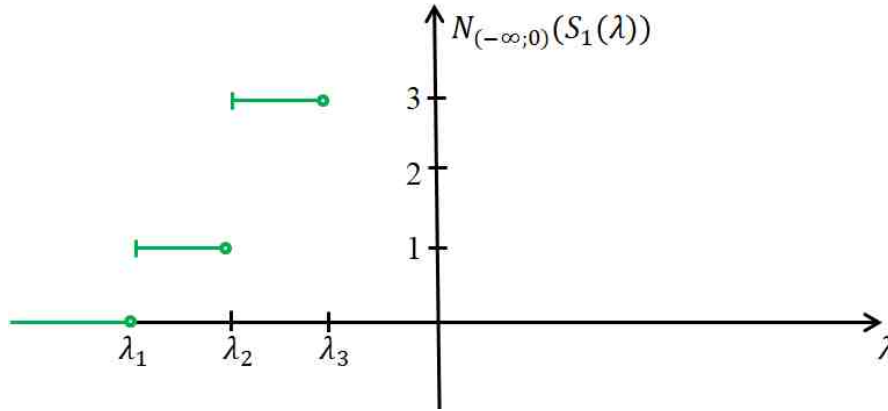


FIG. 1. The graph of $N_{(-\infty;0)}(S_1(\cdot))$ for the case λ_1 is a simple eigenvalue of \mathcal{A}_2 and λ_2 is an eigenvalue of \mathcal{A}_2 with multiplicity two.

Definition 3.7. We denote by $E_m(\cdot)$, $m \in \mathbb{N}$ the positive definite function on the segment $[\alpha; \beta] \subset \mathbb{R} \setminus \sigma_{\text{ess}}(\mathcal{A}_2)$, satisfying the condition: $E_m(\lambda)$ is the m -th eigenvalue (eigenvalues numbered in ascending order, counting their multiplicity) of the operator $S_1(\lambda)$, $\lambda \in [\alpha; \beta]$.

Recall that the operator function $S_1(\cdot)$ is continuous on $[\alpha; \beta]$ in the sense of the uniform operator topology. Therefore for each $m \in \mathbb{N}$, the function $E_m(\cdot)$ is continuous in any segment $[\alpha; \beta] \subset \mathbb{R} \setminus \sigma_{\text{ess}}(\mathcal{A}_2)$.

Theorem 3.8. The number $\lambda_0 < E_{\min}$ is the regular point of the operator \mathcal{A}_2 if and only if the function $N_{(-\infty;0)}(S_1(\cdot))$ is continuous at point $\lambda = \lambda_0$.

Proof. Necessity. Let $\lambda_0 < E_{\min}$ be the regular point of the operator \mathcal{A}_2 . Then from Proposition 3.1, it follows that $E_n(\lambda_0) \neq 0$, $n \in \mathbb{N}$.

Due to the continuity of the function $E_n(\cdot)$, there exists the number $\rho > 0$ such that for all $n \in \mathbb{N}$ and $\lambda \in [\lambda_0 - \rho; \lambda_0 + \rho] \subset (-\infty; E_{\min})$, the inequality $E_n(\lambda) \neq 0$ holds. From here, we obtain

$$\text{card}\{n : E_n(\lambda_0) < 0\} = \text{card}\{n : E_n(\lambda) < 0, \lambda \in [\lambda_0 - \rho; \lambda_0 + \rho]\},$$

where $\text{card}M$ is the cardinality of the set M . Therefore, $N_{(-\infty;0)}(S_1(\lambda_0)) = N_{(-\infty;0)}(S_1(\lambda_0 + \varepsilon))$, $\varepsilon \in [-\rho; \rho]$, that is, the function $N_{(-\infty;0)}(S_1(\cdot))$ is continuous at the point $\lambda = \lambda_0$.

Sufficiency. Let the function $N_{(-\infty;0)}(S_1(\cdot))$ be the continuous one at the point $\lambda = \lambda_0$. Then for some $\varepsilon > 0$, the equalities

$$N_{(-\infty;0)}(S_1(\lambda_0 - \varepsilon)) = N_{(-\infty;0)}(S_1(\lambda_0)) = N_{(-\infty;0)}(S_1(\lambda_0 + \varepsilon)) \tag{3.9}$$

hold.

Taking into account the monotonicity of the quadratic form $(S_1(\lambda)\cdot, \cdot)$ as $\lambda \in (\lambda_0 - \varepsilon; \lambda_0 + \varepsilon)$ and arguing as in the proving of Theorem 2 of the paper [16], one can show that the function $E_1(\cdot), E_2(\cdot), \dots$ monotonically decreases on $(\lambda_0 - \varepsilon; \lambda_0 + \varepsilon)$. From here, we have $E_n(\lambda_0) > E_n(\lambda_0 + \varepsilon)$, $n \in \mathbb{N}$. Thus,

$$E_n(\lambda_0) > E_n(\lambda_0 + \varepsilon) \geq 0, \quad \forall n \in \{n : E_n(\lambda_0 - \varepsilon) \geq 0\}.$$

By virtue of (3.9), the following equality

$$\{n : E_n(\lambda_0 + \varepsilon) < 0\} = \{n : E_n(\lambda_0 - \varepsilon) < 0\}$$

holds. Therefore,

$$E_n(\lambda_0) < E_n(\lambda_0 - \varepsilon) < 0, \quad \forall n \in \{n : E_n(\lambda_0 + \varepsilon) < 0\}.$$

In such a way for every natural $n \in \mathbb{N}$, we obtain the inequality $E_n(\lambda_0) \neq 0$, that is, the number 0 is not an eigenvalue of the operator $S_1(\lambda_0)$. According to Proposition 3.1, the number λ_0 is regular point of the operator \mathcal{A}_2 . Theorem 3.8 is completely proved. \square

References

- [1] Leggett A.J., Chakravarty S., Dorsey A.T., Fisher M.P.A., Garg A., Zwerger W. Dynamics of the dissipative two-state system. *Rev. Mod. Phys.*, **59**, (Jan 1987), P. 1–85.
- [2] Hübner M., Spohn H. Radiative decay: nonperturbative approaches. *Rev. Math. Phys.*, 1995, **7**(3), P. 363–387.
- [3] Huebner M., Spohn H. Spectral properties of spin-boson Hamiltonian. *Ann. Inst. Henri Poincaré*, 1995, **62**(3), P. 289–323.
- [4] Minlos R.A., Spohn H. The three-body problem in radioactive decay: the case of one atom and at most two photons. *Topics in Statistical and Theoretical Physics*, American Mathematical Society Translations–Series 2, 1996, **177**, P. 159–193.
- [5] Spohn H. Ground states of the spin-boson Hamiltonian. *Comm. Math. Phys.*, 1989, **123**, P. 277–304.
- [6] Zhukov Yu., Minlos R. Spectrum and scattering in a “spin-boson” model with not more than three photons. *Theor. Math. Phys.*, 1995, **103**(1), P. 398–411.
- [7] Muminov M., Neidhardt H., Rasulov T. On the spectrum of the lattice spin-boson Hamiltonian for any coupling: 1D case. *Journal of Mathematical Physics*, 2015, **56**, P. 053507.
- [8] Rasulov T.Kh. Branches of the essential spectrum of the lattice spin-boson model with at most two photons. *Theor. Math. Phys.*, 2016, **186**(2), P. 251–267.
- [9] Lakaev S.N., Rasulov T.Kh. A model in the theory of perturbations of the essential spectrum of multi-particle operators. *Math. Notes.*, 2003, **73**(4), P. 521–528.
- [10] Tretter C. *Spectral Theory of Block Operator Matrices and Applications*. Imperial College Press, London, 2008.
- [11] Lakaev S.N. Some spectral properties of the generalized Friedrichs model. *J. Soviet Math.*, 1989, **45**(6), P. 1540–1565.
- [12] Muminov M.I., Rasulov T.H. The Faddeev equation and essential spectrum of a Hamiltonian in Fock space. *Methods Func. Anal. Topology*, 2011, **17**(1), P. 47–57.
- [13] Rasulov T.Kh. Study of the essential spectrum of a matrix operator. *Theor. Math. Phys.*, 2010, **164**(1), P. 883–895.
- [14] Zhang F. *The Schur Complement and Its Applications. Numerical Methods and Algorithms*. Vol. 4. Springer, Berlin, 2005.
- [15] Haynsworth E.V. *On the Schur complement*. Basel Mathematical Notes, BNB 20, 17 pages, 1968.
- [16] Muminov M.I., Rasulov T.Kh. An eigenvalue multiplicity formula for the Schur complement of a 3×3 block operator matrix. *Siberian Math. J.*, 2015, **56**(4), P. 878–895.

Submitted 22 March 2023; revised 24 April 2023; accepted 25 April 2023

Information about the authors:

Tulkin Rasulov – Faculty of Physics and Mathematics, Bukhara State University, M. Ikbol str. 11, 200100 Bukhara, Uzbekistan; ORCID 0000-0002-2868-4390; t.h.rasulov@buxdu.uz

Elyor Dilmurodov – Faculty of Physics and Mathematics, Bukhara State University, Bukhara branch of the Institute of Mathematics named after V. I. Romanovskiy, M. Ikbol str. 11, 200100 Bukhara, Uzbekistan; ORCID 0000-0002-5583-5684; e.b.dilmurodov@buxdu.uz

Conflict of interest: the authors declare no conflict of interest.

Determination of the coefficient function in a Whitham type nonlinear differential equation with impulse effects

Tursun K. Yuldashev^a, Aziz K. Fayziyev^b

Tashkent State University of Economics, Tashkent, Uzbekistan

^at.yuldashev@tsue.uz, ^bfayziyev.a@inbox.ru

Corresponding author: Tursun K. Yuldashev, t.yuldashev@tsue.uz

ABSTRACT In the article, the problems of unique solvability and determination of the redefinition coefficient function in the initial inverse problem for a nonlinear Whitham type partial differential equation with impulse effects are studied. The modified method of characteristics allows partial differential equations of the first order to be represented as ordinary differential equations that describe the change of unknown function along the line of characteristics. The unique solvability of the initial inverse problem is proved by the method of successive approximations and contraction mappings. The determination of the unknown coefficient is reduced to solving the nonlinear integral equation.

KEYWORDS inverse problem, Whitham type equations, determination of the coefficient function, method of successive approximations, unique solvability.

ACKNOWLEDGEMENTS The research of the first author is funded by the Ministry of Innovative development of the Republic of Uzbekistan (Grant F-FA-2021-424).

FOR CITATION Yuldashev T.K., Fayziyev A.K. Determination of the coefficient function in a Whitham type nonlinear differential equation with impulse effects. *Nanosystems: Phys. Chem. Math.*, 2023, **14** (3), 312–320.

1. Problem statement

It is known that the dynamics of evolving processes sometimes undergoes abrupt changes. Often, such short-term perturbations are interpreted as impulses. That is, we actually have a dynamic system with impulse effects, the solutions of which are functions with first kind “discontinuities”. Differential and integro-differential equations with impulse effects have applications in biological, chemical and physical sciences, ecology, biotechnology, industrial robotics, pharmacokinetics, optimal control, etc. [1–5]. In particular, such kind of problems appears in biophysics at micro- and nano-scales [6–10]. A lot of publications of studying the differential equations with impulse effects related to various natural and technical processes are appearing [11–20].

Partial differential equations of the first order can be locally solved by methods of the theory of ordinary differential equations by reducing them to a characteristic system. The application of the method of characteristics to the solution of partial differential equations of the first order makes it possible to reduce the study of wave evolution [21]. In [22, 23], methods for integrating nonlinear partial differential equations of the first order were developed. Further, many papers appeared devoted to the study of questions of the unique solvability of the Cauchy problem for different types of partial differential equations of the first order (see, for example, [24–33]). The issues of determining the coefficient in various inverse problems have been considered by many authors, in particular, in [34–39].

In this paper, we consider the problems of unique solvability and determination of the redefinition coefficient function in the nonlinear inverse problem for a Whitham type partial differential equation with nonlinear initial value and nonlinear impulse conditions. So, in the domain $\Omega \equiv [0; T] \times \mathbb{R}$ for $t \neq t_i, i = 1, 2, \dots, p$, we study the following quasilinear equation

$$\frac{\partial u(t, x)}{\partial t} + u(t, x) \frac{\partial u(t, x)}{\partial x} = \alpha(t) \beta(x) + F(t, x, u(t, x)) \quad (1)$$

with nonlinear initial value condition

$$u(t, x)|_{t=0} = \varphi \left(x, \int_0^T K(\xi) u(\xi, x) d\xi \right), \quad x \in \mathbb{R} \quad (2)$$

and nonlinear impulsive condition

$$u(t_i^+, x) - u(t_i^-, x) = G_i(u(t_i, x)), \quad i = 1, 2, \dots, p, \quad (3)$$

where $u(t, x)$ is the desired function, $\alpha(t)$ is unknown coefficient function, $t \neq t_i, i = 1, 2, \dots, p, 0 = t_0 < t_1 < \dots < t_p < t_{p+1} = T < \infty, 0 \neq \beta(x) \in C^1(\mathbb{R}), \mathbb{R} \equiv (-\infty, \infty), F(t, x, u) \in C^{0,1,0}(\Omega \times \mathbb{R}), \varphi(x, u) \in C^1(\mathbb{R}^2)$,

$K(t) \in C[0, T]$, $u(t_i^+, x) = \lim_{\nu \rightarrow 0^+} u(t_i + \nu, x)$, $u(t_i^-, x) = \lim_{\nu \rightarrow 0^-} u(t_i - \nu, x)$ are the right-hand side and the left-hand side limits of function $u(t, x)$ at the point $t = t_i$, respectively.

We use the following Banach spaces: the space $C(\Omega, \mathbb{R})$ which consists of continuous functions $u(t, x)$ with the norm

$$\|u\|_C = \sup_{(t,x) \in \Omega} |u(t, x)|$$

and the space

$$PC(\Omega, \mathbb{R}) = \{u : \Omega \rightarrow \mathbb{R}; u(t, x) \in C(\Omega_{i,i+1}, \mathbb{R}), i = 1, \dots, p\}$$

with the following norm

$$\|u\|_{PC} = \max \left\{ \|u\|_{C(\Omega_{i,i+1})}, i = 1, 2, \dots, p \right\},$$

where $\Omega_{i,i+1} = (t_i, t_{i+1}] \times \mathbb{R}$, $u(t_i^+, x)$ and $u(t_i^-, x)$ ($i = 0, 1, \dots, p$) exist and are bounded; $u(t_i^-, x) = u(t_i, x)$.

To determine the redefinition coefficient function $\alpha(t)$ in the initial value problem (1)–(3), we use the following nonlinear condition

$$u(t, x_0) = \psi \left(t, \int_0^T \gamma(\xi) \alpha(\xi) d\xi \right), \tag{4}$$

where $x_0 \in \mathbb{R}$, $\psi(t, u) \in C^{1,0}([0; T], \mathbb{R})$, $\gamma(t) \in C[0, T]$,

$$\varphi \left(x_0, \int_0^T K(\xi) \int_0^T \gamma(\theta) \alpha(\theta) d\theta d\xi \right) = \psi \left(0^+, \int_0^T \gamma(\xi) \alpha(\xi) d\xi \right).$$

Direct problem. Find unknown function $u(t, x) \in PC(\Omega, \mathbb{R})$ such that the function $u(t, x)$ for all $(t, x) \in \Omega$, $t \neq t_i$, $i = 1, 2, \dots, p$ satisfies the differential equation (1), initial value condition (2) and for $(t, x) \in \Omega$, $t = t_i$, $i = 1, 2, \dots, p$, satisfies the nonlinear limit condition (3).

Inverse problem. Find a pair of unknown functions $u(t, x) \in PC(\Omega, \mathbb{R})$ and $\alpha(t) \in C([0, T], \mathbb{R})$ such that the function $u(t, x)$ for all $(t, x) \in \Omega$, $t \neq t_i$, $i = 1, 2, \dots, p$ satisfies the differential equation (1), initial value condition (2), for $(t, x) \in \Omega$, $t = t_i$, $i = 1, 2, \dots, p$ satisfies the nonlinear limit condition (3) and nonlinear additional condition (4).

2. Reducing the direct problem to a functional-integral equation

We show that the direct initial value problem (1)–(3) with impulse effects is reduced to solving the following nonlinear functional-integral equation

$$\begin{aligned} u(t, x) = \Theta(t, x; u) \equiv & \varphi \left(p(t, 0, x), \int_0^T K(\xi) u(\xi, p(t, \xi, x)) d\xi \right) + \\ & + \int_0^t [\alpha(s) \beta(p(t, s, x)) + F(s, p(t, s, x), u(s, p(t, s, x)))] ds + \\ & + \sum_{0 < t_i < t} G_i(u(t_i, p(t, t_i, x))), \end{aligned} \tag{5}$$

where $p(t, s, x)$ is defined from the integral equation

$$p(t, s, x) = x - \int_s^t u(\theta, p(t, \theta, x)) d\theta, \quad p(t, t, x) = x, \tag{6}$$

$x \in \mathbb{R}$ plays the role of a parameter.

Let the function $u(t, x) \in PC(\Omega, \mathbb{R})$ be a solution of the direct problem (1)–(3). We present the domain Ω as follows $\Omega = \Omega_{0,1} \cup \Omega_{1,2} \cup \dots \cup \Omega_{p,p+1}$, where $\Omega_{i,i+1} = (t_i, t_{i+1}] \times \mathbb{R}$. On the first domain $\Omega_{0,1}$, the equation (1) is rewritten as

$$D_u[u] = \alpha(t) \beta(x) + F(t, x, u(t, x)), \tag{7}$$

where $D_u = \left(\frac{\partial}{\partial t} + u(t, x) \frac{\partial}{\partial x} \right)$ is the Whitham operator.

Now we introduce the extended characteristics which is defined as follows:

$$p(t, s, x) = x - \int_s^t u(\theta, x) d\theta, \quad p(t, t, x) = x.$$

We introduce a function of three dimensional argument $w(t, s, x) = u(s, p(t, s, x))$, such that for $t = s$, it takes the form $w(t, t, x) = u(t, p(t, t, x)) = u(t, x)$. Let us differentiate the function $w(t, s, x)$ with respect to the new argument s

$$w_s(t, s, x) = u_s(s, p(t, s, x)) + u_p(s, p(t, s, x)) \cdot p_s(t, s, x).$$

Then, taking into account the last relation, we rewrite equation (7) in the following extended form

$$\frac{\partial}{\partial s} w(t, s, x) = \alpha(s) \beta(p(t, s, x)) + F(s, p(t, s, x), w(t, s, x)). \quad (8)$$

Integrating equations (8) along the extended characteristics, we obtain

$$\int_0^{t_1} [\alpha(s) \beta(p(t, s, x)) + F(s, p(t, s, x), w(t, s, x))] ds = w(t, t_1^-, x) - w(t, 0^+, x), \quad t \in (0, t_1], \quad (9)$$

$$\int_{t_1}^{t_2} [\alpha(s) \beta(p(t, s, x)) + F(s, p(t, s, x), w(t, s, x))] ds = w(t, t_2^-, x) - w(t, t_1^+, x), \quad t \in (t_1, t_2], \quad (10)$$

$$\int_{t_p}^{t_{p+1}} [\alpha(s) \beta(p(t, s, x)) + F(s, p(t, s, x), w(t, s, x))] ds = w(t, t_{p+1}^-, x) - w(t, t_p^+, x), \quad t \in (t_p, t_{p+1}], \quad t_{p+1} = T. \quad (11)$$

Taking into account the relations $w(t, 0^+, x) = w(t, 0, x)$, $w(t, t_{p+1}^-, x) = w(t, s, x)$ issued from integral relations (9)–(11) on the interval $(0, T]$, we have

$$\begin{aligned} & \int_0^s [\alpha(\varsigma) \beta(p(t, \varsigma, x)) + F(\varsigma, p(t, \varsigma, x), w(t, \varsigma, x))] d\varsigma = \\ & = [w(t, t_1, x) - w(t, 0^+, x)] + [w(t, t_2, x) - w(t, t_1^+, x)] + \dots + [w(t, s, x) - w(t, t_p^+, x)] = \\ & = -w(t, 0, x) - [w(t, t_1^+, x) - w(t, t_1, x)] - [w(t, t_2^+, x) - w(t, t_2, x)] - \dots - \\ & \quad - [w(t, t_p^+, x) - w(t, t_p, x)] + w(t, s, x). \end{aligned} \quad (12)$$

Taking into account the impulsive condition (3), we rewrite the last equality (12) as follows

$$w(t, s, x) = w(t, 0, x) + \int_0^s [\alpha(\varsigma) \beta(p(t, \varsigma, x)) + F(\varsigma, p(t, \varsigma, x), w(t, \varsigma, x))] d\varsigma + \sum_{0 < t_i < s} G_i(w(t, t_i, x)), \quad (13)$$

where $w(t, 0, x)$ is arbitrary constant along the characteristics, which should be determined. The initial value condition (2) for equation (13) takes the form

$$w(t, 0, x) = \varphi \left(p(t, 0, x), \int_0^T K(\xi) w(t, \xi, x) d\xi \right).$$

Then, taking into account this initial value condition, from (13), we obtain that

$$\begin{aligned} w(t, s, x) &= \varphi \left(p(t, 0, x), \int_0^T K(\xi) w(t, \xi, x) d\xi \right) + \\ &+ \int_0^s [\alpha(\varsigma) \beta(p(t, \varsigma, x)) + F(\varsigma, p(t, \varsigma, x), w(t, \varsigma, x))] d\varsigma + \sum_{0 < t_i < s} G_i(w(t, t_i, x)). \end{aligned} \quad (14)$$

For $t = s$, from (14), we arrive at the nonlinear functional-integral equation (5) together with the integral equation (6).

3. Solvability of the functional-integral equation

For fixed values of redefinition function $\alpha(t)$, we study the functional-integral equation (5).

Theorem 1. Let the following conditions be satisfied:

1. $0 < \sup_{x \in \mathbb{R}} |\varphi(x, 0)| \leq \Delta_\varphi < \infty$;
2. $0 < \sup_{x \in \mathbb{R}} |\beta(x)| \leq \Delta_\beta < \infty$;
3. $\sup_{x \in \mathbb{R}} |F(t, x, 0)| \leq \Delta_f(t)$, $0 < \Delta_f(t) \in C[0; T]$;
4. $0 < |G_i(0)| \leq \Delta_{G_i} < \infty$, $i = 1, 2, \dots, p$;
5. $|\varphi(x_1, u_1) - \varphi(x_2, u_2)| \leq \chi_1 (|x_1 - x_2| + |u_1 - u_2|)$, $0 < \chi_1 = \text{const}$;
6. $|\beta(x_1) - \beta(x_2)| \leq \chi_2 |x_1 - x_2|$, $0 < \chi_2 = \text{const}$;
7. $|G_i(u_1) - G_i(u_2)| \leq \chi_{3i} |u_1 - u_2|$, $0 < \chi_{3i} = \text{const}$;
8. $|F(t, x_1, u_1) - F(t, x_2, u_2)| \leq Q(t) |x_1 - x_2| + P(t) |u_1 - u_2|$;
9. $0 < Q(t), P(t) \in C[0; T]$, $0 < \max_{t \in [0; T]} \int_0^t [Q(s)(t-s) + P(s)] ds < \infty$;
10. $\rho_1 = \max_{t \in [0; T]} \int_0^t H(t, s) ds + \sum_{i=1}^p \chi_{3i} < 1$, where

$$H(t, s) = \chi_1 (1 + |K(s)|) + (Q(s) + \chi_2 |\alpha(s)|) (t - s) + P(s).$$

Then, for fixed values of $\alpha(t)$, the functional-integral equation (5) has unique solution in the domain Ω . This solution can be founded by the following successive approximations:

$$u_0(t, x) = 0, \quad u_{k+1}(t, x) \equiv \Theta(t, x; u_k, p_k), \quad k = 0, 1, 2, \dots, \tag{15}$$

where $p_k(s, t, x)$ is defined from the following iteration

$$p_0(t, t, x) = x, \quad p_k(t, s, x) = x - \int_s^t u_{k-1}(\theta, p_{k-1}(t, \theta, x)) d\theta.$$

Proof. By virtue of the conditions of the theorem, we obtain that the following estimate holds for the first difference of approximation (15):

$$\begin{aligned} |u_1(t, x) - u_0(t, x)| &\leq \sup_{x \in \mathbb{R}} |\varphi(x, 0)| + \sup_{(t, x) \in \Omega} \int_0^t |\alpha(s) \beta(x)| ds + \\ &+ \sum_{0 < t_i < T} |G_i(0)| + \max_{t \in [0; T]} \int_0^t \Delta_f(s) ds \leq \Delta_\varphi + \sum_{i=1}^p \Delta_{G_i} + \Delta_1 + \Delta_2 < \infty, \end{aligned} \tag{16}$$

where

$$\Delta_1 = \max_{t \in [0; T]} \int_0^t \Delta_f(s) ds < \infty, \quad \Delta_2 = \Delta_\beta \max_{t \in [0; T]} \int_0^t |\alpha(s)| ds < \infty.$$

Taking into account estimate (16) and the conditions of the theorem, we obtain that for arbitrary difference of approximation (15), the following estimate holds:

$$\begin{aligned} |u_{k+1}(t, x) - u_k(t, x)| &\leq \left| \varphi \left(p_{k+1}(t, 0, x), \int_0^T K(\xi) u_k(\xi, p_k(t, \xi, x)) d\xi \right) - \right. \\ &\quad \left. - \varphi \left(p_k(t, 0, x), \int_0^T K(\xi) u_{k-1}(\xi, p_{k-1}(t, \xi, x)) d\xi \right) \right| + \\ &\quad + \int_0^t |\alpha(s)| \cdot |\beta(p_{k+1}(t, s, x)) - \beta(p_k(t, s, x))| ds + \\ &\quad + \int_0^t |F(s, p_{k+1}(t, s, x), u_k(s, p_k(t, s, x))) - F(s, p_k(t, s, x), u_{k-1}(s, p_{k-1}(t, s, x)))| ds + \end{aligned}$$

$$\begin{aligned}
 & + \sum_{0 < t_i < t} |G_i(u_k(t_i, p_k(t, t_i, x))) - G_i(u_{k-1}(t_i, p_{k-1}(t, t_i, x)))| \leq \\
 & \leq \chi_1 \left[\int_0^t |u_k(s, x) - u_{k-1}(s, x)| ds + \int_0^T |K(s)| \cdot |u_k(s, x) - u_{k-1}(s, x)| ds \right] + \\
 & + \int_0^t \left[(Q(s) + \chi_2 |\alpha(s)|) \int_s^t |u_k(\theta, x) - u_{k-1}(\theta, x)| d\theta + P(s) |u_k(s, x) - u_{k-1}(s, x)| \right] ds + \\
 & \quad + \sum_{0 < t_i < t} \chi_{3i} |u_k(t_i, x) - u_{k-1}(t_i, x)| \leq \\
 & \leq \max_{t \in [0; T]} \int_0^t H(t, s) |u_k(s, x) - u_{k-1}(s, x)| ds + \sum_{i=1}^p \chi_{3i} |u_k(t, x) - u_{k-1}(t, x)|, \tag{17}
 \end{aligned}$$

where

$$H(t, s) = \chi_1 (1 + |K(s)|) + (Q(s) + \chi_2 |\alpha(s)|) (t - s) + P(s).$$

In estimation (17), we pass to the norm in the space $PC(\Omega, \mathbb{R})$ and arrive at the estimate

$$\|u_{k+1}(t, x) - u_k(t, x)\|_{PC} \leq \rho_1 \cdot \|u_k(t, x) - u_{k-1}(t, x)\|_{PC}, \tag{18}$$

where

$$\rho_1 = \max_{t \in [0; T]} \int_0^t H(t, s) ds + \sum_{i=1}^p \chi_{3i}.$$

Since $\rho_1 < 1$, it follows from estimate (18) that the sequence of functions $\{u_k(t, x)\}_{k=1}^\infty$, defined by formula (15), converges absolutely and uniformly in the domain Ω . In addition, it follows from the existence of the unique fixed point of the operator $\Theta(t, x; u)$ on the right side of (5) that the functional-integral equation (5) has unique solution in the domain Ω . The theorem has been proven.

Corollary. *Let all the conditions of Theorem 1 be satisfied. Then, for fixed values of the function $\alpha(t)$, the direct initial value problem (1)–(3) with impulse effects has unique solution in the domain Ω .*

Remark. *Functional-integral equation (5) contains four nonlinear functions. So, in the formulation of the theorem, we required that for each nonlinear function the boundedness condition and the Lipschitz condition be satisfied.*

4. Determination of the redefinition coefficient function

Using the nonlinear additional condition (4), from the functional-integral equation (5), we obtain the nonlinear integral equation

$$\begin{aligned}
 & \int_0^t \beta(t, s) \alpha(s) ds + \varphi \left(p(t, 0, x_0), \int_0^T K(\xi) \psi \left(\xi, \int_0^T \gamma(\theta) \alpha(\theta) d\theta \right) d\xi \right) + \\
 & \quad + \int_0^t F \left(s, p(t, s, x_0), \psi \left(s, \int_0^T \gamma(\xi) \alpha(\xi) d\xi \right) \right) ds + \\
 & \quad + \sum_{0 < t_i < t} G_i \left(\psi \left(t_i, \int_0^T \gamma(\xi) \alpha(\xi) d\xi \right) \right) = \psi \left(t, \int_0^T \gamma(\xi) \alpha(\xi) d\xi \right), \tag{19}
 \end{aligned}$$

where $\beta(t, s) = \beta(p(t, s, x_0))$. Integral equation (19) is a very complex equation, because $p(t, s, x_0)$ contains redefinition function in the nonlinear form. But, for $t = s$ in $p(t, s, x_0)$, from equation (19), we come to simpler integral equation with respect to redefinition function $\alpha(t)$:

$$\begin{aligned}
 & \beta(x_0) \int_0^t \alpha(s) ds + \varphi \left(x_0, \int_0^T K(\xi) \psi \left(\xi, \int_0^T \gamma(\theta) \alpha(\theta) d\theta \right) d\xi \right) + \\
 & \quad + \int_0^t F \left(s, x_0, \psi \left(s, \int_0^T \gamma(\xi) \alpha(\xi) d\xi \right) \right) ds +
 \end{aligned}$$

$$+ \sum_{0 < t_i < t} G_i \left(\psi \left(t_i, \int_0^T \gamma(\xi) \alpha(\xi) d\xi \right) \right) = \psi \left(t, \int_0^T \gamma(\xi) \alpha(\xi) d\xi \right). \tag{20}$$

Here the following holds true.

Theorem 2. Let all conditions of Theorem 1 be satisfied. Let the following conditions be fulfilled:

1. $\max_{t \in [0; T]} |\psi(t, 0)| \leq \Delta_\psi < \infty$; $0 < \Delta_f(t) \in C[0; T]$;
2. $|\psi(t, u_1) - \psi(t, u_2)| \leq \chi_4 |u_1 - u_2|$, $0 < \chi_4 = \text{const}$;
3. $\rho_2 = \frac{\chi_0}{T |\beta(x_0)|} \int_0^T |\gamma(\xi)| d\xi < 1$, where

$$\chi_0 = \chi_4 \left[1 + \chi_1 \int_0^T |K(\xi)| d\xi + \int_0^t |\Delta_F(s)| ds + \sum_{i=1}^n \chi_{3i} \right].$$

Then the inverse problem (1)–(4) with impulse effects has unique pair of solutions $\{u(t, x), \alpha(t)\}$.

Proof. The method of successive approximations can be applied to equation (20). This equation can be reduced to a functional-integral equation by differentiation. The iteration process for equation (20) can be described as follows

$$\begin{aligned} \alpha_0(t) = 0, \quad \beta(x_0) \int_0^t \alpha_{k+1}(s) ds = \\ = \psi \left(t, \int_0^T \gamma(\xi) \alpha_k(\xi) d\xi \right) - \varphi \left(x_0, \int_0^T K(\xi) \psi \left(\xi, \int_0^T \gamma(\theta) \alpha_k(\theta) d\theta \right) d\xi \right) - \\ - \int_0^t F \left(s, x_0, \psi \left(s, \int_0^T \gamma(\xi) \alpha_k(\xi) d\xi \right) \right) ds - \sum_{0 < t_i < t} G_i \left(\psi \left(t_i, \int_0^T \gamma(\xi) \alpha_k(\xi) d\xi \right) \right). \end{aligned} \tag{21}$$

By virtue of the conditions of the theorem, for the first difference from the approximations (21), we obtain

$$\begin{aligned} |\beta(x_0)| \int_0^t |\alpha_1(s) - \alpha_0(s)| ds \leq \left| \psi \left(t, \int_0^T \gamma(\xi) \alpha_0(\xi) d\xi \right) \right| + \\ + \left| \varphi \left(x_0, \int_0^T K(\xi) \psi \left(\xi, \int_0^T \gamma(\theta) \alpha_0(\theta) d\theta \right) d\xi \right) \right| + \\ + \int_0^t \left| F \left(s, x_0, \psi \left(s, \int_0^T \gamma(\xi) \alpha_0(\xi) d\xi \right) \right) \right| ds + \sum_{0 < t_i < t} \left| G_i \left(\psi \left(t_i, \int_0^T \gamma(\xi) \alpha_0(\xi) d\xi \right) \right) \right| \leq \\ \leq \Delta_\psi + \Delta_\varphi + \Delta_1 + \sum_{i=1}^p \Delta_{G_i} < \infty. \end{aligned} \tag{22}$$

Now for the arbitrary difference from the approximations (21), we obtain

$$\begin{aligned} |\beta(x_0)| \int_0^t |\alpha_{k+1}(s) - \alpha_k(s)| ds \leq \left| \psi \left(t, \int_0^T \gamma(\xi) \alpha_k(\xi) d\xi \right) - \psi \left(t, \int_0^T \gamma(\xi) \alpha_{k-1}(\xi) d\xi \right) \right| + \\ + \left| \varphi \left(x_0, \int_0^T K(\xi) \psi \left(\xi, \int_0^T \gamma(\theta) \alpha_k(\theta) d\theta \right) d\xi \right) - \varphi \left(x_0, \int_0^T K(\xi) \psi \left(\xi, \int_0^T \gamma(\theta) \alpha_{k-1}(\theta) d\theta \right) d\xi \right) \right| + \\ + \int_0^t \left| F \left(s, x_0, \psi \left(s, \int_0^T \gamma(\xi) \alpha_k(\xi) d\xi \right) \right) - F \left(s, x_0, \psi \left(s, \int_0^T \gamma(\xi) \alpha_{k-1}(\xi) d\xi \right) \right) \right| ds + \\ + \sum_{0 < t_i < t} \left| G_i \left(\psi \left(t_i, \int_0^T \gamma(\xi) \alpha_k(\xi) d\xi \right) \right) - G_i \left(\psi \left(t_i, \int_0^T \gamma(\xi) \alpha_{k-1}(\xi) d\xi \right) \right) \right| \leq \end{aligned}$$

$$\begin{aligned} &\leq \chi_4 \int_0^T |\gamma(\xi)| \cdot |\alpha_k(\xi) - \alpha_{k-1}(\xi)| d\xi + \\ &+ \chi_1 \int_0^T |K(\xi)| \cdot \left| \psi \left(\xi, \int_0^T \gamma(\theta) \alpha_k(\theta) d\theta \right) - \psi \left(\xi, \int_0^T \gamma(\theta) \alpha_{k-1}(\theta) d\theta \right) \right| d\xi + \\ &+ \int_0^t |\Delta_F(s)| \cdot \left| \psi \left(s, \int_0^T \gamma(\xi) \alpha_k(\xi) d\xi \right) - \psi \left(s, \int_0^T \gamma(\xi) \alpha_{k-1}(\xi) d\xi \right) \right| ds + \\ &+ \sum_{0 < t_i < t} \chi_{3i} \left| \psi \left(t_i, \int_0^T \gamma(\xi) \alpha_k(\xi) d\xi \right) - \psi \left(t_i, \int_0^T \gamma(\xi) \alpha_{k-1}(\xi) d\xi \right) \right| \leq \\ &\leq \chi_0 \int_0^T |\gamma(\xi)| \cdot |\alpha_k(\xi) - \alpha_{k-1}(\xi)| d\xi, \end{aligned}$$

where

$$\chi_0 = \chi_4 \left[1 + \chi_1 \int_0^T |K(\xi)| d\xi + \int_0^t |\Delta_F(s)| ds + \sum_{i=1}^n \chi_{3i} \right].$$

Hence, we pass to the norm in the space $PC([0; T], \mathbb{R})$ and arrive at the estimate

$$\|\alpha_{k+1}(t) - \alpha_k(t)\|_{PC} \leq \rho_2 \|\alpha_k(t) - \alpha_{k-1}(t)\|_{PC}, \tag{23}$$

where

$$\rho_2 = \frac{\chi_0}{|\beta(x_0)| T} \int_0^T |\gamma(\xi)| d\xi.$$

According to the last condition of the theorem, one has the inequality $\rho_2 < 1$. We take into account that

$$\varphi \left(x_0, \int_0^T K(\xi) \int_0^T \gamma(\theta) \alpha(\theta) d\theta d\xi \right) = \psi \left(0^+, \int_0^T \gamma(\xi) \alpha(\xi) d\xi \right).$$

So, from estimates (22) and (23), it follows that integral equation (20) has the unique solution on the interval $[0; T]$.

We substitute the solution of the nonlinear integral equation (20) into the functional-integral equation (5) and obtain the desired solution $u(t, x)$ by the method of successive approximations. The proof of the second theorem is completed.

5. Conclusion

In this paper, the problems of unique solvability and determination of the redefinition coefficient function $\alpha(t)$ in the initial inverse problem (1)–(4) for a nonlinear Whitham type partial differential equation with impulse effects are studied. The modified method of characteristics allows partial differential equations of the first order to be represented as ordinary differential equations that describe the change of unknown function along the line of characteristics. The nonlinear functional-integral equation (5) is obtained. The unique solvability of the initial inverse problem (1)–(4) is proved by the method of successive approximations and contraction mappings. The determination of the unknown coefficient function $\alpha(t)$ is reduced to solving the integral equation (20). After solving nonlinear integral equation (20) by iteration process, we substitute its solution into the functional-integral equation (5) and obtain the desired solution $u(t, x)$ by the method of successive approximations.

The results of this work allows one to investigate other type partial differential equations of the first order with impulse effects. In our present work, we studied the given differential equation (1) with initial value condition with respect to first argument t . Next step is that we will study this equation (1) with initial value condition with respect to the second argument x . Moreover, we would like to study inverse problem with redefinition function, which is part of the initial condition. So, we hope that our work will stimulate the study of various kind of inverse boundary value problems for impulsive partial differential and integro-differential equations with many redefinition functions and results of investigations find applications in mechanics, technology and in nanotechnology.

References

- [1] Benchohra M., Henderson J., Ntouyas S.K. *Impulsive differential equations and inclusions. Contemporary Mathematics and its Application*. Hindawi Publishing Corporation, New York, 2006.
- [2] Halanay A., Veksler D. *Qualitative Theory of Impulsive Systems*. Mir, Moscow, 1971, 309 p. (in Russian).
- [3] Lakshmikantham V., Bainov D.D., Simeonov P.S. *Theory of Impulsive Differential Equations*. World Scientific, Singapore, 1989, 434 p.
- [4] Perestyk N.A., Plotnikov V.A., Samoilenko A.M., Skripnik N.V. *Differential Equations with Impulse Effect: Multivalued Right-hand DSides with Discontinuities*. DeGruyter Stud. 40, Mathematics. Walter de Gruyter Co., Berlin, 2011.
- [5] Samoilenko A.M., Perestyk N.A. *Impulsive Differential Equations*. World Scientific, Singapore, 1995.
- [6] Stamova I., Stamov, G. Impulsive Biological Models. In: *Applied Impulsive Mathematical Models. CMS Books in Mathematics*. Springer, Cham., 2016.
- [7] Catlla J., Schaeffer D.G., Witelski Th.P., Monson E.E., Lin A.L. On spiking models for synaptic activity and impulsive differential equations. *SIAM Review*, 2008, **50**(3), P. 553–569.
- [8] Fedorov E.G., Popov I.Yu. Analysis of the limiting behavior of a biological neurons system with delay. *Journal of Physics: Conf. Series*, 2021, **2086**, 012109.
- [9] Fedorov E.G., Popov I.Yu. Hopf bifurcations in a network of Fitzhigh-Nagumo biological neurons. *International Journal of Nonlinear Sciences and Numerical Simulation*, 2021.
- [10] Fedorov E.G. Properties of an oriented ring of neurons with the FitzHugh-Nagumo model. *Nanosystems: Phys. Chem. Mathematics*, 2021, **12**(5), P. 553–562.
- [11] Anguraj A., Arjunan M.M. Existence and uniqueness of mild and classical solutions of impulsive evolution equations. *Elect. Journal of Differential Equations*, 2005, **2005**(111), P. 1–8.
- [12] Ashyralyev A., Sharifov Y.A. Existence and uniqueness of solutions for nonlinear impulsive differential equations with two-point and integral boundary conditions. *Advances in Difference Equations*, 2013, **2013**(173).
- [13] Bai Ch., Yang D. Existence of solutions for second-order nonlinear impulsive differential equations with periodic boundary value conditions. *Boundary Value Problems (Hindawi Publishing Corporation)*, 2007, **2007**(41589), P. 1–13.
- [14] Bin L., Xinzhi L., Xiaoxin L. Robust global exponential stability of uncertain impulsive systems. *Acta Mathematica Scientia*, 2005, **25**(1), P. 161–169.
- [15] Mardanov M.J., Sharifov Ya. A., Habib M. H. Existence and uniqueness of solutions for first-order nonlinear differential equations with two-point and integral boundary conditions. *Electr. Journal of Differential Equations*, 2014, **2014**(259), P. 1–8.
- [16] Yuldashev T.K. Periodic solutions for an impulsive system of nonlinear differential equations with maxima. *Nanosystems: Phys. Chem. Mathematics*, 2022, **13**(2), P. 135–141.
- [17] Yuldashev T.K. Periodic solutions for an impulsive system of integro-differential equations with maxima. *Vestnik Sam. Gos. Universiteta. Seria: Fiziko.-Matem. Nauki*, 2022, **26**(2), P. 368–379.
- [18] Yuldashev T.K., Fayziev A.K. On a nonlinear impulsive system of integro-differential equations with degenerate kernel and maxima. *Nanosystems: Phys. Chem. Mathematics*, 2022, **13**(1), P. 36–44.
- [19] Yuldashev T.K., Fayziev A.K. Integral condition with nonlinear kernel for an impulsive system of differential equations with maxima and redefinition vector. *Lobachevskii Journal of Mathematics*, 2022, **43**(8), P. 2332–2340.
- [20] Yuldashev T.K., Ergashev T.G., Abduvahobov T.A. Nonlinear system of impulsive integro-differential equations with Hilfer fractional operator and mixed maxima. *Chelyab. Physical Math. Journal*, 2022, **7**(3), P. 312–325.
- [21] Goritskiy A.Yu., Kruzhkov S.N., Chechkin G.A. *Partial Differential Equations of the First Order*. Mekhmat MGU, Moscow, 1999. 95 p. (in Russian).
- [22] Imanaliev M.I., Ved Yu.A. On a partial differential equation of the first order with an integral coefficient. *Differential equations*, 1989, **23**(3), P. 325–335.
- [23] Imanaliev M.I., Alekseenko S.N. On the theory of systems of nonlinear integro-differential partial differential equations of the Whitham type. *Doklady Mathematics*, 1993, **46**(1), P. 169–173.
- [24] Alekseenko S.N., Dontsova M.V. Study of the solvability of a system of equations describing the distribution of electrons in the electric field of a sprite. *Matematicheskii vestnik pedvuzov i universitetov Volgo-Vyatskogo regiona*, 2012, **14**, P. 34–41 (in Russian).
- [25] Alekseenko S.N., Dontsova M.V. Local existence of a bounded solution of a system of equations describing the distribution of electrons in a weakly ionized plasma in the electric field of a sprite. *Matematicheskii vestnik pedvuzov i universitetov Volgo-Vyatskogo regiona*, 2013, **15**, P. 52–59 (in Russian).
- [26] Alekseenko S.N., Dontsova M.V. Solvability conditions for a system of equations describing long waves in a rectangular water channel whose depth varies along the axis. *Zhurnal Srednevolzhskogo matematicheskogo obshchestva*, 2016, **18**(2), P. 115–124 (in Russian).
- [27] Alekseenko S.N., Dontsova M.V., Pelinovsky D.E. Global solutions to the shallow water system with a method of an additional argument. *Applicable Analysis*, 2017, **96**(9), P. 1444–1465.
- [28] Dontsova M.V. Nonlocal solvability conditions for the Cauchy problem for a system of partial differential equations of the first order with continuous and bounded right-hand sides. *Vestnik Voronezh Gos. Universiteta. Ser. Fizika. Matematika*, 2014, **4**, P. 116–130 (in Russian).
- [29] Dontsova M.V. Nonlocal solvability conditions for Cauchy problem for a system of first order partial differential equations with special right-hand sides. *Ufa Mathematical Journal*, 2014, **6**(4), P. 68–80.
- [30] Imanaliev M.I., Alekseenko S.N. To the problem of the existence of a smooth bounded solution for a system of two nonlinear partial differential equations of the first order. *Doklady Mathematics*, 2001, **64**(1), P. 10–15.
- [31] Yuldashev T.K. On the inverse problem for a quasilinear partial differential equation of the first order. *Vestnik Tomsk. Gos. Universiteta. Matematika i mekhanika*, 2012, **2**(18), P. 56–62 (in Russian).
- [32] Yuldashev T.K. Initial problem for a quasilinear partial integro-differential equation of higher order with a degenerate kernel. *Izvestia Instituta Matematiki i Informatiki Udmurt. Gos. Universiteta*, 2018, **52**, P. 116–130 (in Russian).
- [33] Yuldashev T.K., Shabadikov K.Kh. Initial-value problem for a higher-order quasilinear partial differential equation. *Journal of Mathematical Sciences*, 2021, **254**(6), P. 811–822.
- [34] Aliev F.A., Ismailov N.A., Namazov A.A., Magarramov I.A. Asymptotic method for determining the coefficient of hydraulic resistance in different sections of the pipeline during oil production. *Proceedings of IAM*, 2017, **6**(1), P. 3–15 (in Russian).
- [35] Gamzaev Kh.M. Numerical method for solving the coefficient inverse problem for the diffusion-convection-reaction equation. *Vestnik Tomsk. Gos. Universiteta. Matematika i Mekhanika*, 2017, **50**, P. 67–78 (in Russian).

- [36] Kostin A.B. Recovery of the coefficient of u_t in the heat equation from the condition of nonlocal observation in time. *Computational Mathem. and Math. Physics*, 2015, **55**(1), P. 85–100.
- [37] Romanov V.G. On the determination of the coefficients in the viscoelasticity equations. *Siberian Math. J.*, 2014, **55**(3), P. 503–510.
- [38] Yuldashev T.K. Determination of the coefficient and boundary regime in boundary value problem for integro-differential equation with degenerate kernel. *Lobachevskii Journal of Mathematics*, 2017, **38**(3), P. 547–553.
- [39] Yuldashev T.K. On inverse boundary value problem for a Fredholm integro-differential equation with degenerate kernel and spectral parameter. *Lobachevskii Journal of Mathematics*, 2019, **40**(2), P. 230–239.

Submitted 17 January 2023; revised 19 March 2023; accepted 20 March 2023

Information about the authors:

Tursun K. Yuldashev – Tashkent State University of Economics, Karimov street, 49, TSUE, Tashkent, 100066, Uzbekistan; ORCID 0000-0002-9346-5362; t.yuldashev@tsue.uz

Aziz K. Fayziyev – Tashkent State University of Economics, Karimov street, 49, TSUE, Tashkent, 100066, Uzbekistan; ORCID 0000-0001-6798-3265; fayziyev.a@inbox.ru

Conflict of interest: the authors declare no conflict of interest.

Method of reference problems for obtaining approximate analytical solution of multi-parametric Sturm–Liouville problems

Valeriy D. Lukyanov^{1,a}, Lyudmila V. Nosova^{2,b}

¹Joint-Stock Company “Avangard”, St. Petersburg, Russia

²Mozhaisky Military Space Academy, St. Petersburg, Russia

^alukyanovvd@rambler.ru, ^bvka@mil.ru

Corresponding author: Valeriy D. Lukyanov, lukyanovvd@rambler.ru

PACS 02.60.Lj, 47.61.Fg, 62.25.-g

ABSTRACT Approximate analytical formulas are obtained for the eigenfrequencies of longitudinal oscillations of an elastic rod with different mechanical fixings of the ends. The eigenfrequencies are found by solving Sturm–Liouville problems with the third kind boundary conditions as roots of transcendental equations. Homogeneous boundary conditions contain one or more parameters whose values are calculated through the indices of mechanical system. Approximate expression for analytical dependencies of the eigenfrequencies on the single parameter are obtained for one-parametric problems, which are called reference ones. We propose a method for obtaining approximate analytical expression for dependencies of the eigenfrequencies on several parameters in boundary conditions by sequentially solving the reference problems. The two-parametric Sturm–Liouville problem is solved by the proposed method.

KEYWORDS Sturm–Liouville problem, elastic rod, longitudinal oscillations, eigenfrequencies, approximation, least-squares method.

FOR CITATION Lukyanov V.D., Nosova L.V. Method of reference problems for obtaining approximate analytical solution of multi-parametric Sturm–Liouville problems. *Nanosystems: Phys. Chem. Math.*, 2023, **14** (3), 321–327.

1. Introduction

For the time being high-precision measuring instruments which use resonant microelectromechanical systems (MEMS) and nanoelectromechanical systems (NEMS) are of theoretical and practical interests [1–11]. Simple elastic constructions with resonance properties are used as primary converters of physical quantities in MEMS and NEMS [1, 6, 11]. The main characteristic parameters of such systems are their resonant frequencies. Mathematical modeling of time-harmonic oscillations of one-dimensional distributed elastic constructions such as strings, rods, beams, supported by elastic elements leads to the Sturm–Liouville problems. The Sturm–Liouville problem is the boundary value problem for an ordinary linear homogeneous differential equation with homogeneous boundary conditions at the ends of the interval [12–19].

The Sturm–Liouville problem for the second-order differential equation with boundary conditions of the third kind is of practical interest [20, 21]. The boundary condition at each edge of the interval has the form of annihilation of the linear combination of the function value and its derivative calculated at the end point of the interval. The coefficients of the linear combination in the boundary condition are the parameters of the problem. We call the Sturm–Liouville problem containing n parameters n -parametric. The Sturm–Liouville problem eigenvalues are roots of a transcendental equation which depend on the problem parameters.

We have proposed earlier (in [22–24]) an analytical method for obtaining approximate values for the eigenfrequencies of the one-parametric Sturm–Liouville problem. Using the proposed method, we obtain approximate analytical solutions of two one-parametric Sturm–Liouville problems, which will be called the reference ones. We extend this method to solving of the n -parametric Sturm–Liouville problem. As an example, we solve the two-parametric Sturm–Liouville problem.

2. Reference one-parametric Sturm–Liouville problems

Let the elastic homogeneous rod of length l be located on the interval $[0, l]$ along the axis OX . The cross-sectional area of the rectangular rod is F . The Young’s modulus and the linear rod density are E and ρ , respectively.

Small longitudinal displacements $U = U(X, t)$ of the cross section of the rod with coordinate X from the equilibrium position at time moment t satisfy to the following equation

$$\rho F \frac{\partial^2 U(X, t)}{\partial t^2} = EF \frac{\partial^2 U(X, t)}{\partial X^2}, \quad 0 < X < l. \quad (1)$$

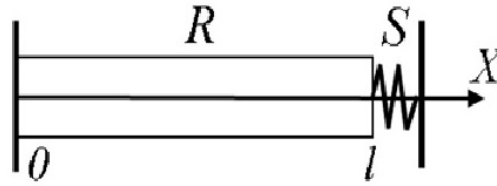


FIG. 1. Choice of the coordinate system for the first reference one-parametric problem. R is an elastic rod, the left end of the rod at $X = 0$ is rigidly embedded into the wall, the right end at $X = l$ is supported by a spring S

The left end of the rod at $X = 0$ is rigidly embedded into the wall. It is described by the boundary condition

$$U(0, t) = 0. \quad (2)$$

The right end of the rod at $X = l$ is supported by an elastic spring with the stiffness K . Correspondingly, one has the following boundary condition [13]:

$$-EF \frac{\partial U(l, t)}{\partial X} = K U(l, t). \quad (3)$$

To find the eigenfrequencies of the rod oscillations, we assume that the dependence of longitudinal displacement on time is harmonic, $U(X, t) = Y(X)e^{-i\omega t}$, where ω is the circular frequency, and $Y(X)$ is the amplitude of the longitudinal displacement of the cross section at the point with coordinate X .

Let's transform the boundary value problem (1)–(3) to the dimensionless form. We introduce the dimensionless coordinate x , $x = X/l$, $0 \leq x \leq 1$ and the dimensionless amplitude of the longitudinal displacement of the cross-section $y(x) = Y(X)/l$. We also introduce the following dimensionless quantities: eigenfrequency $\lambda = \omega l \sqrt{\rho/E}$ and stiffness of the spring $k = K/(EF l)$.

Taking into account the introduced dimensionless quantities, we have the first reference one-parametric Sturm–Liouville problem for finding the set of eigenfunctions $y(x)$ and dimensionless eigenfrequencies λ , $\lambda > 0$:

$$y''(x) = -\lambda^2 y(x), \quad 0 < x < 1 \quad (4)$$

With the boundary conditions:

$$y(0) = 0, \quad y'(1) + k y(1) = 0. \quad (5)$$

The general solution of equation (4) is as follows

$$y = y(x) = C_1 \sin \lambda x + C_2 \cos \lambda x, \quad (6)$$

where C_1, C_2 are arbitrary constants.

Let's find a particular solution of the differential equation (4) satisfying boundary conditions (5). It follows from the boundary condition $y(0) = 0$ that $C_2 = 0$ in the representation (6). Correspondingly, the general solution transforms to the form $y = C_1 \sin \lambda x$. The second boundary condition at $x = 1$ gives one $\Delta(\lambda, k) = 0$, where $\Delta(\lambda, k) = \lambda \cos \lambda + k \sin \lambda$. Keeping in mind that $\lambda \neq \pi n$, $n \in \mathbb{Z}$, we transform this equation to the form

$$\lambda \operatorname{ctg} \lambda + k = 0. \quad (7)$$

The spectral equation (7) gives the dependence of eigenfrequencies on the parameter k

$$\lambda = \Lambda(k), \quad (8)$$

where Λ is a multivalued function implicitly specified by equation (7). The equation is transcendental with respect to the frequency λ and does not allow one to find an analytical solution of the form (8) in elementary functions.

Graphical, numerical and analytical solutions of the spectral equations similar to (7) are considered in [25, 27]. To obtain an approximate analytical solution of the spectral equation (7), we apply the method proposed in [24]. For this purpose, we note that this equation is linear in respect to the parameter k . Therefore, at the first stage of solving the spectral equation we find the dependence of the parameter k on the eigenfrequency λ :

$$k = \Lambda^{-1}(\lambda) = -\lambda \operatorname{ctg} \lambda.$$

This dependence is an elementary function, and is the inverse of the required dependence (8).

The function $k = \Lambda^{-1}(\lambda)$ is a meromorphic function which is defined for those values of $\lambda > 0$ for which the values of function are nonnegative. The behavior of the function $k = -\lambda \operatorname{ctg} \lambda$ is determined by its zeros $w_n = \pi(n - 0.5)$ and by its poles $v_n = \pi n$. We assume here and elsewhere below that $n \in \mathbb{N}$. The function takes nonnegative values for $w_n \leq \lambda < v_n$. On each interval of such type, the function has the positive derivative and is monotonically increasing.

We denote the function $\Lambda^{-1}(\lambda)$ for $\lambda \in [w_n, v_n)$ as $\Lambda_n^{-1}(\lambda)$. Note that each function $\Lambda_n^{-1}(\lambda)$ is continuous and monotonically increasing in the domain of $\lambda \in [w_n, v_n)$. As for the values of these functions at the ends of the intervals, one has $\Lambda_n^{-1}(w_n) = 0$ and $\Lambda_n^{-1}(\lambda) \rightarrow +\infty$ as $\lambda \rightarrow v_n - 0$. The functions $\Lambda_n^{-1}(\lambda)$ have inverse functions with the range of

values $\lambda \in [w_n, v_n)$. Let's denote these inverse functions by Λ_n so that $\lambda = \Lambda_n(k)$. Graphs of the functions $\lambda = \Lambda_n(k)$ are shown in Fig. 2. In constructing the graphs, we used the fact that the functions $k = \Lambda^{-1}(\lambda)$ and $\lambda = \Lambda_n(k)$ are inverse functions. The points on the graphs have coordinates $(\Lambda^{-1}(\lambda), \lambda)$, $\lambda \in [w_n, v_n)$.

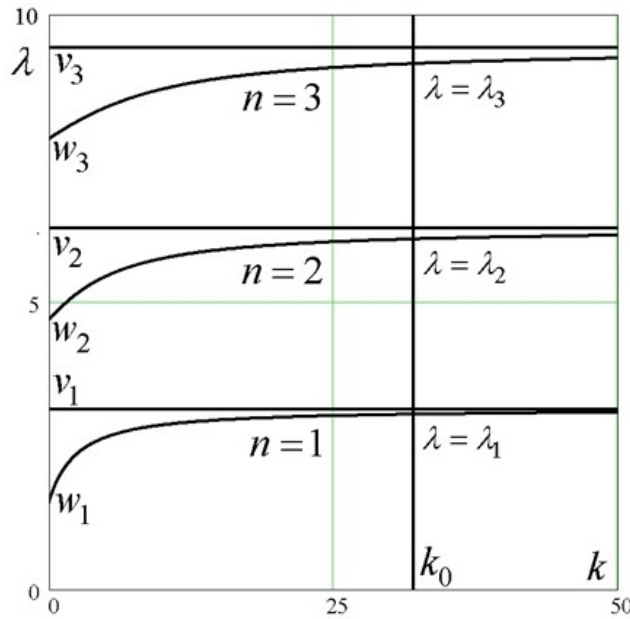


FIG. 2. Graphs of the functions $\lambda = \Lambda_n(k)$ for $n=1, 2, 3$. Graphical finding of eigenfrequencies $\lambda_1, \lambda_2, \lambda_3$ is presented

As the first step of the Sturm–Liouville problem solving, we find graphically (Fig. 2) the values $\lambda_n = \lambda_n(k_0)$ as ordinates of the intersection points of function graphs $\lambda = \Lambda_n(k)$ with the vertical straight line $k = k_0$. The disadvantage of the graphical solution is the impossibility of using the eigenfrequencies found graphically in the subsequent computer modeling of the physical problem.

To obtain approximate analytical expressions for the eigenfrequencies, we use the method proposed in [24]. We choose the approximation of functions $\Lambda_n^{-1}(\lambda)$ by functions $G_n(\lambda)$, following the conditions listed below:

- the functions $G_n(\lambda)$ should be elementary functions with elementary inverse functions G_n^{-1} , i.e. analytic representations of $G_n(\lambda)$ and G_n^{-1} functions should contain only basic elementary functions;
- the functions $G_n(\lambda)$ should provide sufficient approximation accuracy $G_n(\lambda) \approx \Lambda_n^{-1}(\lambda)$, $\lambda \in [w_n, v_n)$.

As in [28], we use the interpolation method and the approximation by the method of least-squares (LSM) in combination to find the $G_n(\lambda)$ functions.

To interpolate the functions $G_n(\lambda)$, $\lambda \in [w_n, v_n)$, we choose the ends of intervals $\lambda = v_n$ and $\lambda = w_n$, and the middle of the intervals $\lambda = \gamma_n = 0.5(v_n + w_n)$ as interpolation nodes. We look for the functions in the form

$$G_n(\lambda) = A_n \left(\frac{\lambda - w_n}{v_n - \lambda} \right)^{r_n}, \quad (9)$$

where A_n and r_n are some positive constants. The choice of the representation (9) ensures the equality of the functions $G_n(\lambda)$ and $\Lambda_n^{-1}(\lambda)$ at $\lambda = w_n$: $G_n(w_n) = \Lambda_n^{-1}(w_n) = 0$. The choice of the representation (9) also ensures that both functions $G_n(\lambda)$ and $\Lambda_n^{-1}(\lambda)$ tend to $+\infty$ as $\lambda \rightarrow v_n - 0$.

Let's choose the constants A_n so that the values of the functions $G_n(\lambda)$ and $\Lambda_n^{-1}(\lambda)$ are equal in the centers of the intervals (w_n, v_n) i.e. at $\lambda = \gamma_n = 0.5(v_n + w_n)$:

$$G_n(\gamma_n) = \Lambda_n^{-1}(\gamma_n). \quad (10)$$

Substitution the values of $\lambda = \gamma_n$ into formula (9) gives one the equalities $G_n(\gamma_n) = A_n$. Given equality (10), we obtain

$$A_n = \Lambda_n^{-1}(\gamma_n) = -\gamma_n \operatorname{ctg} \gamma_n. \quad (11)$$

To find the constants r_n , we use the LSM. Taking logarithm of the left and the right hand sides of equation (9), we obtain

$$\psi_n(\lambda) = r_n \varphi_n(\lambda), \quad w_n < \lambda < v_n. \quad (12)$$

TABLE 1. Values of approximation constants r_n for the selected intervals

j	1	2	3	4	5	6	7	8	9	$J = 10$
n_j	1	2	3	4	5	7	10	15	30	$N = n_J = 50$
r_{n_j}	0.961	0.878	0.864	0.854	0.849	0.843	0.838	0.834	0.832	$r_J = r_{50} = 0.831$

Here $\psi_n(\lambda) = \ln(G_n(\lambda)/A_n)$ and $\varphi_n(\lambda) = \ln((\lambda - w_n)/(v_n - \lambda))$. According to the LSM, on each interval (w_n, v_n) , we choose M points $\lambda_{nm} \in (w_n, v_n)$, where m is the ordinal number of the chosen argument λ_{nm} and pick the coefficients r_n to minimize the residual sum of squares

$$\varepsilon_n(r_n) = \frac{1}{M} \sum_{m=1}^M (\psi_n(\lambda_{nm}) - r_n \varphi_n(\lambda_{nm}))^2. \tag{13}$$

Differentiating with respect to r_n , one obtains

$$\frac{d\varepsilon_n(r_n)}{dr_n} = \frac{2}{M} \sum_{m=1}^M \psi_n(\lambda_{nm}) \varphi_n(\lambda_{nm}) - \frac{2r_n}{M} \sum_{m=1}^M (\varphi_n(\lambda_{nm}))^2 = 0. \tag{14}$$

The solution of equation (14) gives one the values of the constants r_n

$$r_n = \frac{\sum_{m=1}^M \psi_n(\lambda_{nm}) \varphi_n(\lambda_{nm})}{\sum_{m=1}^M (\varphi_n(\lambda_{nm}))^2}. \tag{15}$$

Let's find an *approximate analytical* dependence of the constant r_n on the interval number n . We calculate r_n for J intervals with ordinal numbers $n_1, n_2, \dots, n_j, \dots, n_J = N$. On each interval n_j , we choose M points $\lambda_{n_j m} = w_{n_j} + m \Delta_{n_j}$, where $\Delta_{n_j} = (v_{n_j} - w_{n_j})/(M + 1)$, and calculate the values of r_n by formula (15). Table 1 gives one the values of r_{n_j} for $J = 10, M = 20, N = 50$.

Keeping in mind the obtained values r_{n_j} , we can suggest the following approximate analytical dependence of the constant r_n on the number n :

$$r_n \approx \hat{r}_n = \psi(n, \alpha) = r_N + \frac{r_1 - r_N}{n^\alpha}, \tag{16}$$

provided that the approximation parameter α is positive: $\alpha > 0$. The choice of formula (16) ensures that equality $r_1 = \hat{r}_1$ and approximation equality $r_N \approx \hat{r}_N$ are satisfied, since $N = 50 \gg 1$ and the second summand in the right side of formula (16) is small.

To find the value of the parameter α , we use the LSM. Dependence (16) will be reduced to a linear model on the parameter α after elementary transformations:

$$\ln \left(\frac{r_1 - r_N}{\hat{r}_n - r_N} \right) = \alpha \ln n, 2 \leq n \leq N - 1.$$

According to the LSM, by formulas similar to (12)–(15), we obtain the value

$$\alpha = \frac{\sum_{j=2}^{J-1} \ln \left(\frac{r_1 - r_N}{\hat{r}_{n_j} - r_N} \right) \ln n_j}{\sum_{j=2}^{J-1} (\ln n_j)^2}.$$

We find the inverse functions G_n^{-1} for the functions G_n by solving the equations $k = G_n(\lambda)$ with respect to λ . Taking into account that the functions G_n^{-1} are approximations of the functions $\Lambda_n^{-1}(\lambda)$, we find approximate values $\lambda_n \approx \hat{\lambda}_n$ for the eigenfrequencies of the Sturm–Liouville problem

$$\hat{\lambda}_n = \frac{k^{q_n} w_n + (A_n)^{q_n} v_n}{k^{q_n} + (A_n)^{q_n}},$$

where $q_n = 1/\hat{r}_n$.

Table 2 shows the results of solving two reference problems. The first problem ($s = 1$) is solved above; the second problem ($s = 2$) has different boundary condition and was solved similarly to the first problem.

In Table 2, we use the following notations: s is the number of the problem $s = 1, 2, v_n = \pi n, w_n = \pi(n - 0, 5), n \in N$,

$$\hat{r}_n^{(s)} = r_N^{(s)} + \frac{r_1^{(s)} - r_N^{(s)}}{n^{\alpha_s}}, \tag{17}$$

$$\varphi_n^{(s)}(k, a, b) = \frac{a k^{q_n^{(s)}} + b (A_n^{(s)})^{q_n^{(s)}}}{k^{q_n^{(s)}} + (A_n^{(s)})^{q_n^{(s)}}}, \tag{18}$$

TABLE 2. One-parametric reference Sturm–Liouville problems: boundary conditions, intermediate solution results and approximate formulas for eigenfrequencies

s	Boundary conditions	Spectral equation $\Delta^{(s)}(\lambda, k) = 0$	Function $k = (\Lambda^{(s)})^{-1}(\lambda)$, domain of function	Approximate function $k = (\Lambda_n^{(s)})^{-1}(\lambda)$	Eigenfrequencies $\lambda_n^{(s)} = \varphi_n^{(s)}(k, a, b)$	α_s $r_1^{(s)}$ $r_{50}^{(s)}$
1	$y(0) = 0$ $y'(1) + ky(1) = 0$	$\Delta^{(1)}(\lambda, k) = \lambda \cos \lambda + k \sin \lambda = 0$	$k = -\lambda \operatorname{ctg} \lambda$, $\lambda \in [w_n, v_n)$	$k = A_n^{(1)} \left(\frac{\lambda - w_n}{v_n - \lambda} \right)^{\hat{r}_n^{(1)}}$	$\lambda_n^{(1)} = \varphi_n^{(1)}(k, w_n, v_n)$	0.9 0.961 0.831
2	$y'(0) = 0$ $y'(1) + ky(1) = 0$	$\Delta^{(2)}(\lambda, k) = \lambda \sin \lambda - k \cos \lambda = 0$	$k = \lambda \operatorname{tg} \lambda$, $\lambda \in [v_{n-1}, w_n)$	$k = A_n^{(2)} \left(\frac{\lambda - v_{n-1}}{w_n - \lambda} \right)^{\hat{r}_n^{(2)}}$	$\lambda_n^{(2)} = \varphi_n^{(2)}(k, v_{n-1}, w_n)$	0.8 1.100 0.840

where

$$A_n = (\Lambda_n^{(s)})^{-1}(\gamma_n) \tag{19}$$

$$q_n^{(s)} = \frac{1}{\hat{r}_n^{(s)}}. \tag{20}$$

The quality of the problem solution is characterized by the relative errors $\delta_n = \delta_n(k) = |\lambda_n - \hat{\lambda}_n|/\lambda_n$ of the determined values $\hat{\lambda}_n$. The functions $\delta_n = \delta_n(k)$ are determined parametrically using the parameter λ :

$$\begin{cases} k = \Lambda^{-1}(\lambda), \\ \delta_n = \left| 1 - \frac{\hat{\lambda}_n(\Lambda^{-1}(\lambda))}{\lambda_n} \right|. \end{cases}$$

Numerical calculations have shown that the relative errors of the approximate calculation of $\lambda_n \approx \hat{\lambda}_n$ values do not exceed the magnitude of 0.002.

3. The two-parametric Sturm–Liouville problem

In this section, we show how to use the obtained solutions of one-parametric reference problems to solve the *two-parametric* Sturm–Liouville problem.

We consider the problem on longitudinal oscillations of an elastic rod, whose ends are supported by elastic springs S_1 and S_2 with stiffnesses K_1 and K_2 (Fig. 3).

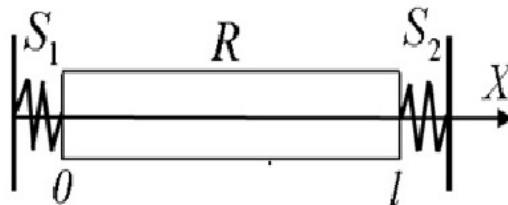


FIG. 3. Coordinate system for the two-parametric problem. The ends of the rod R are supported by springs S_1 and S_2 at $X = 0$ and $X = l$

Introducing the dimensionless quantities, as was done earlier in Section 2, we obtain the Sturm–Liouville problem for finding the set of eigenfunctions $y(x)$ and the set of eigenfrequencies λ : $y''(x) = -\lambda^2 y(x)$ for $0 < x < 1$ with boundary conditions

$$y'(0) - k_1 y(0) = 0, \quad y'(1) + k_2 y(1) = 0, \tag{21}$$

where $k_p = K_p/EF l$, $p = 1, 2$ are dimensionless spring stiffnesses.

We show that the solution of the two-parametric problem is reduced to sequential solving of the one-parametric reference problems. The general solution of the differential equation (4) has the form (6). Substituting it into the boundary conditions (21), we obtain a system of linear algebraic equations for constants C_1 and C_2 .

$$\begin{cases} \lambda C_1 - k_1 C_2 = 0, \\ (\lambda \cos \lambda + k_2 \sin \lambda) C_1 + (k_2 \cos \lambda - \lambda \sin \lambda) C_2 = 0. \end{cases} \tag{22}$$

To obtain the eigenfunctions $y(x)$ we find a nonzero solution of the homogeneous system (22) from the condition that the principal determinant $\Delta(\lambda, k_1, k_2)$ is zero:

$$\Delta(\lambda, k_1, k_2) = k_1 k_2 \sin \lambda + \lambda(k_1 + k_2) \cos \lambda - \lambda^2 \sin \lambda = 0. \tag{23}$$

Equation (23) is the spectral equation for calculating the eigenfrequencies of the two-parametric problem for given values of parameters k_1 and k_2 . Let a function Γ represent the dependence of λ on parameters k_1 and k_2

$$\lambda = \Gamma(k_1, k_2). \tag{24}$$

The function $\Gamma(k_1, k_2)$ is a non-elementary multivalued function of two variables k_1 and k_2 , implicitly given by equation (23). Equation (23) is linear with respect to parameters k_1, k_2 , and their permutation does not change the equation. Let a function Γ^{-1} represent the dependence of k_1 on λ and k_2 .

$$k_1 = \Gamma^{-1}(\lambda, k_2). \tag{25}$$

It follows from equation (23) that the function $\Gamma^{-1}(\lambda, k_2)$ has the following form

$$k_1 = \Gamma^{-1}(\lambda, k_2) = \frac{\lambda(\lambda \sin \lambda - k_2 \cos \lambda)}{(\lambda \cos \lambda + k_2 \sin \lambda)}. \tag{26}$$

The function $\Gamma^{-1}(\lambda, k_2)$ is a meromorphic function of the variable λ . It also depends on a fixed value of the parameter k_2 . The values of roots W_n and poles V_n of the function $\Gamma^{-1}(\lambda, k_2)$ are found from the solutions of the reference problems given in Table 2. We find the positive poles $V_n = V_n(k_2)$ of the function $\Gamma^{-1}(\lambda, k_2)$ from the spectral equation $\lambda \cos \lambda + k_2 \sin \lambda = 0$ of the first reference problem (Table 2, $s = 1$): $V_n(k_2) = \lambda_n^{(1)}$. We find the positive roots $W_n = W_n(k_2)$ of the function $\Gamma^{-1}(\lambda, k_2)$ from the spectral equation $\lambda \sin \lambda - k_2 \cos \lambda = 0$ of the second reference problem (Table 2, $s = 2$): $W_n(k_2) = \lambda_n^{(2)}$. Using Table 2, we obtain formulas for the positive poles and roots of the function $\Gamma^{-1}(\lambda, k_2)$: $\lambda_n^{(1)} = \varphi_n^{(1)}(k_2, w_n, v_n)$ and $\lambda_n^{(2)} = \varphi_n^{(2)}(k_2, v_n, w_n)$. Note that the inequalities $W_n(k_2) < V_n(k_2)$ are satisfied. Graph of the function $\Gamma^{-1}(\lambda, k_2)$ is similar to graph of the function $k = \Lambda^{-1}(\lambda)$ in Fig. 2 if we replace quantities v_n and w_n with quantities V_n and W_n , respectively.

Then the two-parametric problem is solved by the method used above for solving the first reference problem:

1. We introduce the functions $\Gamma_n^{-1}(\lambda, k_2), \lambda \in [W_n, V_n]$.
2. We approximate the functions $k_1 = \Gamma_n^{-1}(\lambda, k_2)$ by the functions $G_n(\lambda, k_2)$,

$$G_n(\lambda, k_2) = A_n(k_2) \left(\frac{\lambda - \lambda_n^{(2)}(k_2)}{\lambda_n^{(1)}(k_2) - \lambda} \right)^{\hat{r}_n(k_2)},$$

where $A_n(k_2)$ and $\hat{r}_n(k_2)$ are approximation constants to be calculated.

3. We calculate the constants $A_n(k_2) = \Gamma_n^{-1}(\gamma_n(k_2), k_2)$, where

$$\gamma_n(k_2) = 0.5(\lambda_n^{(1)}(k_2) + \lambda_n^{(2)}(k_2)),$$

$$\Gamma_n^{-1}(\gamma_n(k_2), k_2) = \frac{\gamma_n(k_2)(\gamma_n(k_2) \sin \gamma_n - k_2 \cos \gamma_n(k_2))}{(\gamma_n(k_2) \cos \gamma_n(k_2) + k_2 \sin \gamma_n(k_2))}.$$

4. We calculate the constants $\hat{r}_n(k_2)$ by formulas similar to formulas (12)–(15).
5. We find the inverse functions G_n^{-1} and calculate approximate analytical dependencies of eigenfrequencies $\hat{\lambda}_n = G_n^{-1}(k_1, k_2)$ on the parameters k_1 and k_2 .

As a result, in the case of the two-parametric problem, we calculate the eigenfrequencies λ_n for the given values of the parameters k_1 and k_2 by the approximate formula

$$\lambda_n \approx \hat{\lambda}_n = \frac{\lambda_n^{(2)}(k_2) k_1^{q_n(k_2)} + (A_n(k_2))^{q_n(k_2)} \lambda_n^{(1)}(k_2)}{k_1^{q_n(k_2)} + (A_n(k_2))^{q_n(k_2)}}, \tag{27}$$

$$q_n(k_2) = 1/\hat{r}_n(k_2), \quad \hat{r}_n = \hat{r}_n(k_2) = r_{50}(k_2) + \frac{r_1(k_2) - r_{50}(k_2)}{n^\alpha}.$$

Numerical calculations using the above algorithm for the two-parameter problem at the values of the parameters $k_1 = 2, k_2 = 1$ gave us the following results: $\alpha = 1.320, r_1(k_2) = 0.947, r_{50}(k_2) = 0.837$. The relative errors δ_n of calculating $\lambda_n \approx \hat{\lambda}_n$ values do not exceed the magnitude of 0.002.

4. Conclusion

Mathematical modeling of applied problems may lead to multi-parameter boundary value problems. This is the case in the problem of longitudinal oscillations of a rod, the ends of which are supported by elastic springs and weighed by masses. Several parameters also appear in the problem of bending oscillations of an elastic beam with elastic springs and masses with given moments of inertia located at its ends [13].

The proposed approach makes it possible to find solutions of multi-parametric problems using the solutions of reference one-parametric problems. We obtain n one-parametric problems from an n -parametric Sturm–Liouville problem assuming that all but one parameter is zero. The one-parametric problems are reference problems for the n -parametric problem. By solving each one-parametric problem, we find an approximate analytical dependence of the eigenfrequencies on the single parameter of the problem. Then we sequentially reduce the n -parametric Sturm–Liouville problem to the solution of n one-parametric problems. As a result, we obtain an approximate analytical dependence of the eigenfrequencies on all parameters of the n -parametric Sturm–Liouville problem.

References

- [1] Lyshevski S.E. *MEMS and NEMS Systems, Devices, and Structures*. CRC Press, New York, 2002, 461 p.
- [2] Nguyen C.T.-C. MEMS technology for timing and frequency control. *IEEE Trans. Ultrason. Ferroelectr. Freq. Control*, 2007, **54**, P. 251–270.
- [3] Basu J. Bhattacharyya, T.K. Microelectromechanical resonators for radio frequency communication applications. *Microsyst. Technol.*, 2011, **17**, P. 1557–1580.
- [4] NEMS/MEMS Technology and Devices. Edited by Lynn Khine and Julius M. Tsai. International Conference on Materials for Advanced Technologies (ICMAT 2011), Symposium G: NEMS/MEMS and microTAS, June 26– July 1, Suntec, Singapore, 2011, 242 p.
- [5] Mukhurov N.I., Efremov G.I. *Electromechanical Micro Devices*. Belarusian Navuka, Minsk, 2012, 257 p. (in Russian).
- [6] Greenberg Y.S., Pashkin Y.A., Ilyichev K.V. Nanomechanical Resonators. *Physics–Uspekhi*, 2012, **55**(4), P. 382–407.
- [7] Vojtovich I.D., Korsunsky V.M. *Intelligent Sensors*. BINOM. Knowledge Laboratory, M., 2012, 624 p (in Russian).
- [8] Van Beek J.T.M., Puers R. A review of MEMS oscillators for frequency reference and timing applications. *J. Micromech. Microeng.*, 2012, **22**, P. 13001.
- [9] Abdolvand R., Bahreyni B., Lee J., Nabki F. Micromachined Resonators: A review. *Micromachines*, 2016, **7**(9), P. 160–213.
- [10] Ali W.R., Prasad M. Piezoelectric MEMS based acoustic sensors: A review. *Sensors and Actuators A*, 2020, **301**, P. 2–31.
- [11] Kolmakov A.G., Barinov S.M., Alymov M.I. *Fundamentals of Tech. and App. of Nanomat*. Fizmatlit M., 2012, 208 p (in Russian).
- [12] Collatz L. *Problems on eigenvalues (with technical applications)*. Science, M., 1968, 504 p.
- [13] *Vibrations in engineering: Handbook. V. 1. Vibrations of linear systems*. Ed. V.V. Bolotin. Mashinostroenie, M., 1978, 352 p (in Russian).
- [14] Zaitsev V.F., Polyaniin A.D. *Handbook of Ordinary Differential Equations. Exact Solutions, Methods, and Problems. 3rd Edition*. Chapman and Hall/CRC, New York, 2017, 1496 p.
- [15] Kandidov V.P., Kapzov L.N., and Kharlamov A.A. *Solution and Analysis of Linear Vibration Theory Problems*. Moscow State Univ. Press, M., 1976, 272 p (in Russian).
- [16] Naimark M.A. *Linear Differential Operators*. Ungar, New York, 1968.
- [17] Titchmarsh E.C. *Eigenfunction Expansions Associated with Second Order Differential Equations. VI*. Oxford Univ. Press, London, 1962, 203 p.
- [18] Shkalikov A.A. Boundary value problems for ordinary differential equations with parameter under boundary conditions. *Works of I.G. Petrovsky Seminar*, 1983, **9**, P. 190–229 (in Russian).
- [19] Charles T. Fulton Two-point boundary value problems with eigenvalue parameter contained in the boundary conditions. *Proceedings of the Royal Society of Edinburgh*, 1977, **77** A, P. 293–308.
- [20] Akhtyamov A.M. *Theory of Identification of Boundary Conditions and Its Applications*. Fizmatlit, M., 2009, 272 p (in Russian).
- [21] Akhtyamov A.M., Ilgamov M.A. Review of research on identification of local defects of rods. *Problems of machine building and reliability*, 2020, **2**, P. 3–15 (in Russian).
- [22] Lukyanov V.D., Nosova L.V. Analytical solution of the Sturm–Liouville problem with complex boundary conditions. Fundamental and applied developments in the field of technical and physical and mathematical sciences. Collection of scientific articles of the final international round table, December 28–30, OOO Envelope, Kazan', 2018, P. 74–77 (in Russian).
- [23] Lukyanov V.D., Nosova L.V., Bogorodsky A.V. et al. Approximate solution of the Sturm–Liouville problem with complex boundary conditions. *Marine intellectual technologies*, 2019, **1**(43), P. 142–146 (in Russian).
- [24] Lukyanov V.D., Bulekbaev D.A., Morozov A.V., Nosova L.V. Approximate analytical method for finding eigenvalues of Sturm–Liouville problem with generalized boundary condition of the third kind. *Nanosystems: physics, chemistry, mathematics*, 2020, **11**(3), P. 275–284.
- [25] Koshlyakov N.S., Gliner E.B., Smirnov M.M. *Differential Equations of Mathematical Physics*. North-Holland Publishing Co., Amsterdam, 1964.
- [26] Smirnov V.I. *A Course of Higher Mathematics. V. 1*. Pergamon, New York, 2013.
- [27] Qjang Luo, Zhidan Wang, Jiurong Han. A Pade approximant approach to two kinds of transcendental equations with applications in physics. *Eur. J. Phys.*, 2015, **36**, P. 035030.
- [28] Lukyanov V.D. On the construction of an interpolation-approximation polynomial. *Nanosystems: physics, chemistry, mathematics*, 2012, **3**(6), P. 5–15 (in Russian).

Submitted 12 April 2023; revised 29 May 2023; accepted 30 May 2023

Information about the authors:

Valeriy D. Lukyanov – Joint-Stock Company “Avangard”, Kondrat’evsky, 72, St. Petersburg, 195271, Russia; ORCID 0009-0009-8184-3264; lukyanovvd@rambler.ru

Lyudmila V. Nosova – Mozhaisky Military Space Academy, Zhdanovskaya, 13, St. Petersburg, 197198, Russia; ORCID 0009-0009-1207-9266; vka@mil.ru

Conflict of interest: the authors declare no conflict of interest.

Oscillating vorticity in single ring exciton polariton condensates

Vladimir A. Lukoshkin^{1,2,a}, Irina E. Sedova^{3,b}, Vladimir K. Kalevich^{1,2,c}, Evgeny S. Sedov^{2,3,d}, Zacharias Hatzopoulos^{4,e}, Pavlos G. Savvidis^{5,6,4,7,f}, Alexey V. Kavokin^{5,6,8,2,g}

¹Ioffe Institute, Russian Academy of Sciences, St. Petersburg, Russia

²Spin Optics Laboratory, St. Petersburg State University, St. Petersburg, Russia

³Stoletov Vladimir State University, Vladimir, Russia

⁴FORTH-IESL, Heraklion, Crete, Greece

⁵Key Laboratory for Quantum Materials of Zhejiang Province, School of Science, Westlake University, Hangzhou, Zhejiang, China

⁶Institute of Natural Sciences, Westlake Institute for Advanced Study, Hangzhou, Zhejiang Province, China

⁷Department of Materials Science and Technology, University of Crete, Heraklion, Crete, Greece

⁸Moscow Institute of Physics and Technology, Dolgoprudnyi, Moscow Region, Russia

^av.lukosh@mail.ioffe.ru, ^biemedvedeva@vlsu.ru, ^ckalevich.solid@mail.ioffe.ru, ^devgeny_sedov@mail.ru,
^echatzop@physics.uoc.gr, ^fp.savvidis@westlake.edu.cn, ^ga.kavokin@westlake.edu.cn

Corresponding author: Evgeny S. Sedov, evgeny_sedov@mail.ru

PACS 71.36.+c, 03.75.Lm

ABSTRACT We study annular flows of exciton polaritons in exciton polariton condensates emerging in cylindrical optical micropillar cavities under the spatially localised non-resonant laser pumping. Annular flows indicate nonzero vorticity of the polariton condensate associated with the appearance of polariton vortices around the center of the micropillar. We report an experimental observation of single ring shaped condensates in the regime of vorticity oscillating in time. We reproduce the vorticity oscillations numerically and reveal possible control parameters for manipulating by the oscillation period.

KEYWORDS polariton, exciton-polariton condensate, persistent current, micropillar, vortex

ACKNOWLEDGEMENTS Work was supported by the Saint Petersburg State University (Grant No. 94030557). Numerical simulations of evolution of the ring-shaped polariton condensate in the regime of oscillating vorticity were supported by the Russian Science Foundation (Grant No. 19-72-20039). Work of V.L., V.K., and A.K. was partially supported by the RFBR (Grant No. 19-52-12032). I.S. acknowledges state assignment in the field of scientific activity of the Ministry of Science and Higher Education of the Russian Federation (theme FZUN-2020-0013, state assignment of VISU). A.K. acknowledges the support of Westlake University, Project 041020100118 and Program 2018R01002 funded by the Leading Innovative and Entrepreneur Team Introduction Program of Zhejiang Province of China. Authors acknowledge Prof. Y. G. Rubo for fruitful discussions.

FOR CITATION Lukoshkin V.A., Sedova I.E., Kalevich V.K., Sedov E.S., Hatzopoulos Z., Savvidis P.G., Kavokin A.V. Oscillating vorticity in single ring exciton polariton condensates. *Nanosystems: Phys. Chem. Math.*, 2023, **14** (3), 328–333.

1. Introduction

Light interacting with matter can considerably change its properties. An essential condition for this is the energy exchange of light radiation and matter excitations, which occurs near their energy resonance. Such exchange can be provided in specially designed structures of microcavities [1]. A microcavity represents a semiconductor or dielectric layer of width of a light wavelength sandwiched between two distributed Bragg reflectors. The central layer contains one or several quantum wells (QWs) embedded in the antinodes of the cavity electric field. Microcavity photons strongly couple to excitons in QWs and form exciton polaritons, new eigenmodes of the microcavity system.

Polaritons inherit bosonic nature from both their constituents and can form a macroscopic coherent state of the Bose-Einstein condensate [2] characterized by a single wave function $\Psi(\mathbf{r})$. Due to the localization of polaritons in the microcavity growth direction, polariton problems are typically two-dimensional, $\mathbf{r} = (x, y)$. Due to the limited quality factor of microcavities, polaritons possess a finite lifetime. The consequence of this is the fact that the polariton condensates are dissipative. Nevertheless, the condensates can exist in microcavities for infinitely long time without losing coherence in the presence of external pumping by laser radiation. Another peculiarity of the polariton condensates, which stems in part from their dissipative nature, is that, as a rule, they are characterized by internal currents (flows) of polaritons [3–5].

In this regard, when describing polariton condensates, one should speak about achieving not stationary states, but steady states. The last definition is more capacious. It describes a system whose parameters do not change in time, while allowing the movement of polaritons in the cavity plane. The polariton current density determined as $\mathbf{J}(\mathbf{r}) = \text{Im}[\Psi^*(\mathbf{r})\nabla\Psi(\mathbf{r})]$ is helpful for characterising polariton currents. By writing the wave function as $\Psi(\mathbf{r}) = \sqrt{\rho(\mathbf{r})}\exp[i\varphi(\mathbf{r})]$, where $\rho(\mathbf{r})$ and $\varphi(\mathbf{r})$ are the density and phase of the polariton condensate, we can reduce the expression to the form $\mathbf{J}(\mathbf{r}) = \rho(\mathbf{r})\nabla\varphi(\mathbf{r})$.

Internal flows are inherent in some topological objects in quantum fluids, including vortices that represent the movement of the fluid along a closed circuit [3, 6]. Since polariton systems are non-conservative, internal polariton currents can be justified by the inhomogeneity of gain and losses within the polariton condensate area, provided that the overall gain-loss balance is maintained. This is especially relevant when spatially localized pumping and microcavity structures with a complex in-plane profile are used for obtaining polariton condensates. Among such structures are, e. g., mesas [7], planar polariton waveguides [8, 9], micropillars [10–12].

A series of our papers is devoted to azimuthal currents of polaritons in polariton condensates excited in cylindrical micropillars by the spatially localised non-resonant optical pump [10–15]. The currents in such condensates are persistent and quantum, characteristic of the corresponding vortex eigenstates of the effective trap for polaritons and quantitatively characterized by the azimuthal quantum number of the vortex topological charge m . At the same time, the currents take place in the spatially inhomogeneous non-conservative system in the presence of external pumping. Herewith the polariton localization area is responsible for the spatial distribution of the polariton current density $\mathbf{J}(\mathbf{r})$ in the microcavity plane. The localization area is generally determined by the geometry of the effective trap, in particular, by the shape of the pillar, as well as by the shape and size of the pump spot [16–19]. The latter acts as a control parameter for polariton currents in our consideration.

For characterizing azimuthal polariton currents, it is convenient to introduce the reduced orbital angular momentum (OAM) of the polariton condensate $\ell = N^{-1} \int [xJ_y(\mathbf{r}) - yJ_x(\mathbf{r})]d\mathbf{r}$ and its winding number $m = (2\pi)^{-1} \int_S d\varphi$, where $N = \int |\Psi(\mathbf{r})|^2 d\mathbf{r}$ is the population of the polariton condensate, S is the closed pass within the condensate around its center of mass [14]. A non-zero value ℓ indicates the presence of azimuthal currents of polaritons in the condensate, while a non-zero value of m indicates vorticity of the condensate. As one has shown in [12], the presence of the former does not necessarily require the presence of the latter. Vorticity implies that the condensate supports closed azimuthal persistent currents of polaritons and is characterized by the integer nonzero winding number m which ensures the phase change by a multiple of 2π for one turn around the pillar, $\phi|_{\theta=2\pi} - \phi|_{\theta=0} = 2\pi m$, θ is the azimuthal angle. In this regime, one can speak about the polariton vortices.

In our papers [10–15], we have reported observation of polariton condensates in the form of concentric rings. We have shown that by changing the size of the micropillar, one can excite polariton current states in the form of single and concentric rings [10, 13, 15]. However, in our studies we dealt with polariton condensates in the steady state regime. As one has mentioned above, in this regime, despite the internal currents, the parameters of the condensate remain unchanged in time, including the population N , OAM ℓ and the winding number m of the condensate, as well as its density and phase distribution.

In the experiment described in our recent paper [14], we have observed for the first time the regime of oscillating vorticity in a double concentric ring condensate excited in cylindrical micropillar. In this regime, the parameters N , ℓ and m of the condensate exhibit oscillations in time with a constant period. We have identified convincing traces of the oscillations in an interference experiment with time averaging of measurements. When considering the manuscript by the reviewers, the following issue arose, which later on repeatedly raised in discussions of the results of the work. Double concentric ring condensates, although of fundamental interest, are rather specific objects of study. At the same time, single ring condensates are more basic, and their application prospects are more obvious [20–22]. In addition, they require lower pump powers, they are better protected from mixing with other both radial and azimuthal modes. However, vorticity oscillations have not yet been observed in such condensates. In this article, we eliminate this omission. We demonstrate the regime of vorticity oscillations in single ring polariton condensates excited by the non-resonant laser pump in a cylindrical micropillar cavity. We investigate the properties of the polariton condensate using interferometry measurements. We support our observations with numerical simulations based on the solution of the generalized Gross-Pitaevskii equation. We estimate the period of vorticity oscillations and show that it can be controlled by changing the shape of the effective trap for polaritons, in particular, the ellipticity of the pump spot.

2. Experimental observation of single ring polariton condensates in the regime of oscillating vorticity

In the experiment, we excited single ring polariton condensates in a cylindrical micropillar of diameter of $25 \mu\text{m}$. The micropillar was etched from a GaAs microcavity of width of $5\lambda/2$ containing a set of embedded quantum wells. The quality factor of the microcavity was measured as about $1.6 \cdot 10^4$. The sample was kept in the helium-flow cryostat at $T = 4 \text{ K}$. The excitation of the condensate was performed by a continuous wave laser beam focused close to the center of the micropillar in the regime of non-resonant pumping (with energy about 110 meV above the bottom of the lower dispersion branch of polaritons). Two types of measurements were performed in the experiment. First, we detected

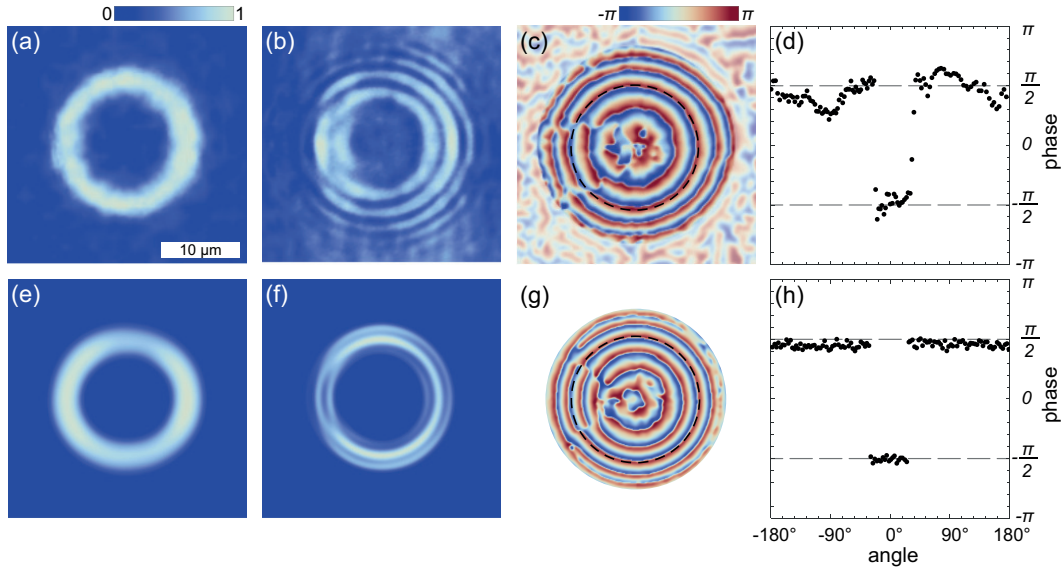


FIG. 1. Observation (top panels) and simulation (bottom panels) of the single ring polariton condensate with oscillating vorticity. (a) Image of the time-averaged PL distribution of the condensate indicating the condensate density distribution in the micropillar, (b) image of interference of PL of the condensate with the reference spherical wave, (c) distribution of the phase of the condensate relative to the phase of the reference wave extracted from panel (b), and (d) the phase variation around the condensate ridge indicated by a black dashed circle in panel (c). Panels (e–h) have the same meaning as (a–d), respectively, but for the simulated data. Dashed lines in (d) and (h) are guides for the eye indicating constant phases $\pm\pi/2$.

photoluminescence (PL) of the polariton condensate to reveal distribution of density of polaritons in the micropillar plane. Second, we detected interference of PL of the condensate with the coherent spherical reference wave using the Mach-Zehnder interferometer. See details of the sample and measurements in Refs. [10, 14].

The results of measurements are shown in Fig. 1(a–d). Photoluminescence of the polariton condensate shown in Fig. 1(a) confirms that under the excitation conditions described above the condensate possesses a single ring shape. The possibility of taking such a shape for the condensate was ensured by the ring shape of the effective potential trap. The latter was composed of two component. The outer wall of the trap was formed by the edge of the cylindrical micropillar. The inner wall was formed by the repulsive reservoir of incoherent excitons emerging within the pump spot under the non-resonant optical excitation. While the stationary potential from the pillar keeps unchanged during the experiment, the shape and height of the optically induced potential is subject to control by controlling the shape of the pump spot and the pump power.

For running azimuthal currents, in our experiments we slightly shifted the pump beam from the center of the pillar [10, 11]. A submicrometer shift is sufficient for this. When the system is chiral, it acquires a preferred direction of the polariton current. Nevertheless, the shift of the pump spot alone is not able to break equivalence between clockwise and counterclockwise directions. In our papers [10–14], we have shown that chirality can be acquired by the polariton system when the shift coexists with another symmetry breaking inclusion, e. g., deformation of the pump beam, defects in the stationary potential landscape. In this case, polariton currents emerge in the condensate manifested as spiral fringes in the images of interference of PL of the condensate and the spherical reference wave. In the absence of polariton currents, spirals degenerate to concentric rings (like Newton’s rings in the textbook optical experiment).

The interferometry image obtained in our experiment is shown in Fig. 1(b). One can see that the interference fringes represent concentric rings, each having two breaks at some points. This considerably differs the image from those in the cases of azimuthal polariton currents and in the absence of currents in the single ring condensate. Figs. 1(c,d) show the extracted from 1(b) distribution of the phase of the condensate relative to the phase of the reference wave, and the azimuthal variation of the phase along the ridge of the condensate (indicated by a black dashed circle in the panel (c)), respectively. One can see that the phase between the fringe breaks remains constant, while at the points of the breaks it undergoes jumps by $\pm\pi$.

The interference fringe breaks indicating the phase jumps are known for polariton condensates with fractional OAM [11, 12]. However, for such states the phase jump coexists with a dip in the density distribution, thus the fractional OAM condensates possess a half-moon shape. This is inconsistent with the azimuthally homogeneous density distribution in our experiment, illustrated in Fig. 1(a). To explain this observation, following [14], we assume that in the experiment we observe not a steady state single ring polariton condensate, but the condensate, whose vorticity oscillates

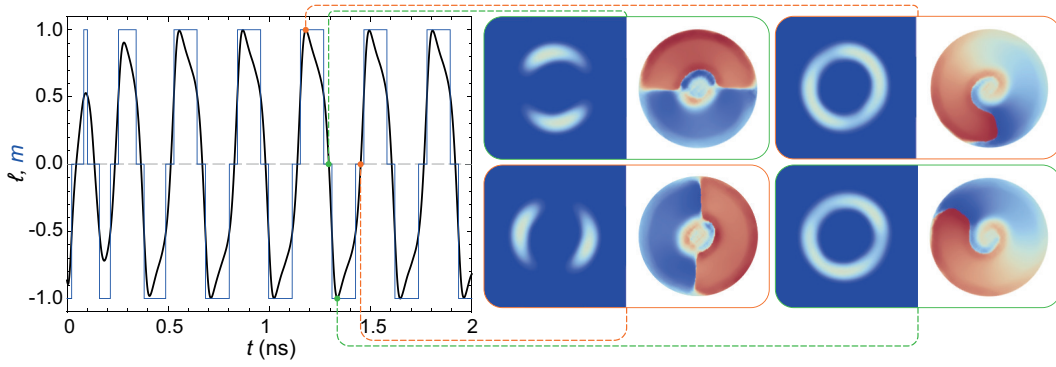


FIG. 2. Simulated evolution of OAM $\ell(t)$ (black curve) and the winding number $m(t)$ (blue curve) of the single ring polariton condensate in the regime of oscillating vorticity. Right panels show spatial distribution of the density and phase of the condensate at time moments indicated by color circles in the left panel.

in time. Thus, the panels 1(a) and 1(b) show averaged in time density distribution and interferometry image of the single ring condensate in the oscillating regime. To confirm the validity of our assumption, we support our observations with the numerical experiment, described in the next section.

3. Numerical simulation of single ring polariton condensates in the regime of oscillating vorticity

To simulate behavior of the polariton condensate in the micropillar, we use the generalized Gross–Pitaevskii equation for the polariton wave function $\Psi(t, \mathbf{r})$ [14, 23, 24]:

$$i\hbar\partial_t\Psi(t, \mathbf{r}) = \left[-\frac{\hbar^2}{2M}\nabla^2 + V(r) + \alpha|\Psi(t, \mathbf{r})|^2 + \alpha_R n_R(t, \mathbf{r}) \right] \Psi(t, \mathbf{r}) + \frac{i\hbar}{2} \left[\frac{\hbar\Lambda_0}{M} n_R(t, \mathbf{r}) \nabla^2 + R n_R(t, \mathbf{r}) - \gamma \right] \Psi(t, \mathbf{r}), \quad (1)$$

where M is the effective mass of polaritons in the microcavity plane, $V(r)$ is the stationary potential of the micropillar taken in the complex form $V(r) = V_R(r) + iV_I(r)$. The real part is taken as $V_R(r) = V_0 \{ \tanh[a(r - d/2)] + 1 \} / 2$, where V_0 and d are the height of the potential and the diameter of the pillar, a is the fitting parameter. The imaginary part responsible for damping due to etching of the pillar [9, 14, 25] can be obtained from the real part by replacing $\eta \rightarrow \eta'$, $\eta = V_0, a, d$. α and α_R are the polariton-polariton interaction constant and the interaction constant of polaritons with optically excited excitons in the reservoir, respectively, $n_R(t, \mathbf{r})$ is the density of the exciton reservoir. The imaginary term in Eq. (1) is responsible for relaxation processes in the polariton condensate. The term proportional to Λ_0 is responsible for the energy relaxation of polaritons [14, 23, 24] with Λ_0 being the relaxation constant. R is the stimulated scattering rate from the exciton reservoir to the condensate, γ is the decay rate of polaritons.

The exciton reservoir density obeys to the following rate equation:

$$\partial_t n_R(t, \mathbf{r}) = P(\mathbf{r}) - (\gamma_R + R|\Psi(t, \mathbf{r})|^2) n_R(t, \mathbf{r}), \quad (2)$$

where $P(\mathbf{r})$ is the pump power taken in the Gaussian form:

$$P(\mathbf{r}) \propto \exp \left[-\frac{x^2 + (y/s)^2}{2w^2} \right]. \quad (3)$$

In (3), w is the width of the beam, s is responsible for the ellipticity of the pump spot. We use s as the control parameter in our consideration. γ_R is the decay rate of excitons in the reservoir.

We use the following values of the parameters for simulations. The effective mass of polaritons is $M = 3 \cdot 10^{-5} m_e$, where m_e is the free electron mass, the polariton and exciton decay rates are $\gamma = 0.025 \text{ ps}^{-1}$ and $\gamma_R = 0.02 \text{ ps}^{-1}$, respectively, the stimulated scattering rate is $\hbar R = 0.1 \text{ meV } \mu\text{m}^2$, the interaction coefficients are $\alpha = \alpha_R/2 = 3 \text{ } \mu\text{eV } \mu\text{m}^2$, the energy relaxation constant is $\Lambda_0 = 0.0063 \text{ } \mu\text{m}^2$, the pump width is $w = 2.9 \text{ } \mu\text{m}$. The parameters of the stationary potential: $V_0 = -3V'_0 = 3 \text{ meV}$, $a = a' = 4 \text{ } \mu\text{m}^{-1}$, $d = 25 \text{ } \mu\text{m}$ and $d' = 25.7 \text{ } \mu\text{m}$.

The results of simulations of the single ring polariton condensate in the regime of oscillating vorticity are illustrated in Fig. 2. In order to achieve the oscillations, we have undertaken the following. We have introduced a weak ellipticity in the pump spot, taking $s = 0.86$. We have also taken the initial conditions as random distribution of the polariton density accompanied by a seed in the form of a vortex with $m = -1$ in the phase component. One can see that the resulting polariton state exhibits oscillations of OAM $\ell(t)$ and the winding number $m(t)$ between -1 and $+1$ with the period estimated as about 300 ps. As a possible drivers of the vorticity oscillations, we distinguish the interplay between

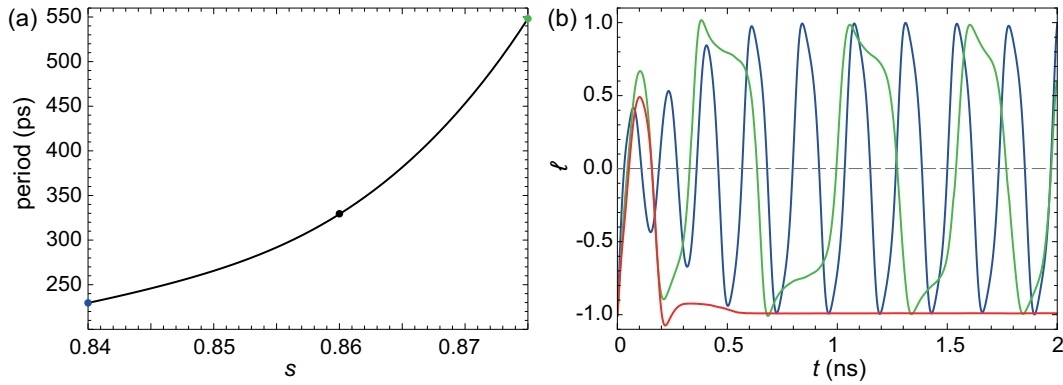


FIG. 3. (a) Simulated dependence of the period of oscillations of the vorticity of the single ring polariton condensate on the ellipticity of the pump spot s for the parameters indicated in the text. (b) Evolution of OAM of the condensates at different ellipticities: $s = 0.84$ (blue), $s = 0.875$ (green) and $s = 0.88$ (red).

interactions of polaritons in the system and the dissipative coupling of the interacting condensate modes, which leads to the creation of the limit cycle state [26–28]

The right panels in Fig. 2 show the intermediate states through which the condensate passes during oscillations. Among them are the states characterized by azimuthally homogeneous density distribution and azimuthal polariton currents in the clockwise or counterclockwise directions as well as the states with the dumbbell-like density distribution and a kink in the distribution of the phase.

The averaged polariton density distribution and the interferometry image reconstructed from the numerical data accompanied by the phase distribution are shown in Figs. 2(e–h) in comparison with the experimental data, cf. Figs 2(a–d). One can see that all peculiarities of the observations are very well qualitatively reproduced by the numerical simulations.

The period of the vorticity oscillations depends on many factors among which is the landscape of the effective trapping potential. In our simulations, the parameter of the system that contributed to the appearance of the oscillations is the ellipticity of the pump spot s . For the used parameters of the system and of the pump, in Fig. 3(a) we show the dependence of the period of oscillations on the ellipticity s . One can see that the period increases with s nearly quadratically. In Fig. 3(b), we show several examples of evolution of OAM $\ell(t)$ in time at different s . One should note that the range of the considered values of s from 0.84 to 0.875 was not chosen arbitrarily. The upper boundary of the range is limited by the computational resources, namely for $s > 0.875$ the period of oscillations, if they are still present, exceeds the considered time range. For s below the lower boundary, the oscillations do not occur. The reason for this may be, e. g., the loss of stability of the oscillating solution or its insufficient pumping to compensate for the losses [13].

4. Conclusion

In this manuscript, we have demonstrated both experimentally and theoretically oscillations of vorticity of the single ring exciton polariton condensate excited in the cylindrical micropillar by the nonresonant laser pump. For observing traces of the oscillations, we used interferometry measurements for detecting averaged in time interference of PL of the condensate with the reference spherical wave. In the numerical experiments, we have shown that ellipticity of the pump spot can act as an effective control tool for manipulating by the period of oscillations. The results of our study are promising for application in the developing new devices for classical and quantum computing with use of polariton flux bits and qubits [22, 29].

References

- [1] Kavokin A., Baumberg J., Malpuech G., Laussy F. *Microcavities*, 2nd ed., Series on Semiconductor Science and Technology, OUP Oxford, Oxford, 2017.
- [2] Kasprzak J., Richard M., Kundermann S., et al., Bose–Einstein condensation of exciton polaritons. *Nature*, 2006, **443** (7110), P. 409–414.
- [3] Ostrovskaya E.A., Abdullaev J., Desyatnikov A.S., Fraser M.D., Kivshar Y.S. Dissipative solitons and vortices in polariton Bose-Einstein condensates. *Physical Review A*, 2012, **86** (1), 013636.
- [4] Li G., Fraser M.D., Yakimenko A., Ostrovskaya E.A. Stability of persistent currents in open dissipative quantum fluids. *Physical Review B*, 2015, **91** (18), 184518.
- [5] Nalitov A.V., Liew T.C.H., Kavokin A.V., Altshuler B.L., Rubo Y.G. Spontaneous Polariton Currents in Periodic Lateral Chains. *Physical Review Letters*, 2017, **119** (6), 067406.
- [6] Lagoudakis K.G., Wouters M., Richard M., et al. Quantized vortices in an exciton–polariton condensate. *Nature Physics*, 2008, **4** (9), 706.
- [7] Kuznetsov A.S., Helgers P.L.J., Biermann K., Santos P.V. Quantum confinement of exciton-polaritons in a structured (Al,Ga)As microcavity. *Physical Review B*, 2018, **97** (19), 195309.
- [8] Sich M., Tapia-Rodríguez L.E., Sigurdsson H., et al. Spin domains in one-dimensional conservative polariton solitons. *ACS Photonics*, 2018, **5** (12), P. 5095–5102.

- [9] Beierlein J., Rozas E., Egorov O.A., et al. Propagative oscillations in codirectional polariton waveguide couplers. *Physical Review Letters*, 2021, **126** (7), P. 075302.
- [10] Lukoshkin V.A., Kalevich V.K., Afanasiev M.M., et al. Persistent circular currents of exciton-polaritons in cylindrical pillar microcavities. *Physical Review B*, 2018, **97** (19), 195149.
- [11] Sedov E., Lukoshkin V., Kalevich V., et al. Persistent Currents in Half-Moon Polariton Condensates. *ACS Photonics*, 2020, **7**, P. 1163–1170.
- [12] Sedov E.S., Lukoshkin V.A., Kalevich V.K., et al. Circular polariton currents with integer and fractional orbital angular momenta. *Physical Review Research*, 2021, **3** (1), 013072.
- [13] Sedov E.S., Lukoshkin V.A., Kalevich V.K., et al. Double ring polariton condensates with polariton vortices. *Nanosystems: Phys. Chem. Math.*, 2022, **13** (6), P. 608–614.
- [14] Lukoshkin V., Sedov E., Kalevich V., et al. Steady state oscillations of circular currents in concentric polariton condensates. *Scientific Reports*, 2023, **13**, 4607.
- [15] Sedov E., Arakelian S., Kavokin A. Spontaneous symmetry breaking in persistent currents of spinor polaritons. *Scientific Reports*, 2021, **11**, 22382.
- [16] Askitopoulos A., Ohadi H., Kavokin A.V., et al. Polariton condensation in an optically induced two-dimensional potential. *Physical Review B*, 2013, **88** (4), 041308.
- [17] Askitopoulos A., Nalitov A.V., Sedov E.S., et al. All-optical quantum fluid spin beam splitter. *Physical Review B*, 2018, **97** (23), 235303.
- [18] Dall R., Fraser M.D., Desyatnikov A.S., et al. Creation of orbital angular momentum states with chiral polaritonic lenses. *Physical Review Letters*, 2014, **113** (20), 200404.
- [19] Aladinskaia E., Cherbunin R., Sedov E., et al. Spatial quantization of exciton-polariton condensates in optically induced traps. *Physical Review B*, 2023, **107** (4), 045302.
- [20] Paschos G.G., Liew T.C.H., et al. An exciton-polariton bolometer for terahertz radiation detection. *Sci. Rep.*, 2018, **8**, 10092.
- [21] Kozin V.K., Shelykh I.A., Nalitov A.V., Iorsh I.V. Topological metamaterials based on polariton rings. *Physical Review B*, 2018, **98** (12), 125115.
- [22] Xue Y., Chestnov I., Sedov E., et al. Split-ring polariton condensates as macroscopic two-level quantum systems. *Physical Review Research*, 2021, **3** (1), 013099.
- [23] Wouters M. Energy relaxation in the mean-field description of polariton condensates. *New Journal of Physics*, 2012, **14**, 075020.
- [24] Wertz E., Amo A., Solnyshkov D.D., et al. Propagation and Amplification Dynamics of 1D Polariton Condensates. *Physical Review Letters*, 2012, **109** (21), 216404.
- [25] Sedova I., Sedov E. Polarization conversion in a polariton three-waveguide coupler. *Results in Optics*, 2021, **4**, 100105.
- [26] Rayanov K., Altshuler B.L., Rubo Y.G., Flach S. Frequency combs with weakly lasing exciton-polariton condensates. *Physical Review Letters*, 2015, **114** (19), 193901.
- [27] Kim S., Rubo Y.G., Liew T.C.H., et al. Emergence of microfrequency comb via limit cycles in dissipatively coupled condensates. *Physical Review B*, 2020, **101** (8), 085302.
- [28] Nalitov A.V., Sigurdsson H., Morina S., et al. Optically trapped polariton condensates as semiclassical time crystals. *Physical Review A*, 2019, **99** (3), 033830.
- [29] Kavokin A., Liew T.C.H., Schneider C., et al. Polariton condensates for classical and quantum computing. *Nature Reviews Physics*, 2022, **4**, P. 435–451.

Submitted 25 April 2023; accepted 12 May 2023

Information about the authors:

Vladimir A. Lukoshkin – Ioffe Institute, Russian Academy of Sciences, 26 Politechnicheskaya, 194021, St. Petersburg, Russia; Spin Optics Laboratory, St. Petersburg State University, Ulyanovskaya 1, St. Petersburg 198504, Russia; ORCID 0000-0002-6565-916X; v.lukosh@mail.ioffe.ru

Irina E. Sedova – Stoletov Vladimir State University, 87 Gorky str. 600000, Vladimir, Russia; iemedvedeva@vlsu.ru

Vladimir K. Kalevich – Ioffe Institute, Russian Academy of Sciences, 26 Politechnicheskaya, 194021, St. Petersburg, Russia; Spin Optics Laboratory, St. Petersburg State University, Ulyanovskaya 1, St. Petersburg 198504, Russia; ORCID 0000-0002-8010-2714; kalevich.solid@mail.ioffe.ru

Evgeny S. Sedov – Spin Optics Laboratory, St. Petersburg State University, Ulyanovskaya 1, St. Petersburg 198504, Russia; Stoletov Vladimir State University, 87 Gorky str. 600000, Vladimir, Russia; ORCID 0000-0001-5684-151X; evgeny_sedov@mail.ru

Zacharias Hatzopoulos – FORTH-IESL, P.O. Box 1527, 71110 Heraklion, Crete, Greece; chatzop@physics.uoc.gr

Pavlos G. Savvidis – Key Laboratory for Quantum Materials of Zhejiang Province, School of Science, Westlake University, 18 Shilongshan Rd., Hangzhou 310024, Zhejiang, China; Institute of Natural Sciences, Westlake Institute for Advanced Study, 18 Shilongshan Rd., Hangzhou, Zhejiang Province 310024, China; FORTH-IESL, P.O. Box 1527, 71110 Heraklion, Crete, Greece; Department of Materials Science and Technology, University of Crete, P.O. Box 2208, 71003 Heraklion, Crete, Greece; ORCID 0000-0002-8186-6679; p.savvidis@westlake.edu.cn

Alexey V. Kavokin – Key Laboratory for Quantum Materials of Zhejiang Province, School of Science, Westlake University, 18 Shilongshan Rd., Hangzhou 310024, Zhejiang, China; Institute of Natural Sciences, Westlake Institute for Advanced Study, 18 Shilongshan Rd., Hangzhou, Zhejiang Province 310024, China; Moscow Institute of Physics and Technology, Institutskiy per., 9, Dolgoprudnyi, Moscow Region, 141701, Russia; Spin Optics Laboratory, St. Petersburg State University, Ulyanovskaya 1, St. Petersburg 198504, Russia; ORCID 0000-0003-2713-1062; a.kavokin@westlake.edu.cn

Conflict of interest: the authors declare no conflict of interest.

Agglomeration of magnetite nanoparticles with citrate shell in an aqueous magnetic fluid

Ivan V. Pleshakov^{1,a}, Vyacheslav A. Ryzhov^{2,b}, Yaroslav Yu. Marchenko^{2,c}, Arseniy A. Alekseev^{3,d}, Elina K. Karseeva^{3,e}, Vladimir N. Nevedomskiy^{1,f}, Andrey V. Prokof'ev^{1,g}

¹Ioffe Institute, St. Petersburg, Russia

²Petersburg Nuclear Physics Institute named by B. P. Konstantinov of National Research Centre “Kurchatov Institute”, Gatchina, Russia

³Peter the Great St. Petersburg Polytechnic University, St. Petersburg, Russia

^aivanple@yandex.ru, ^bvaryzhov@yandex.ru, ^c046_slava@mail.ru, ^darseniy.alekseev98@gmail.com, ^eelina.nep@gmail.com, ^fnevedom@mail.ioffe.ru, ^gAndrey.prokofyev@algo-spb.com

Corresponding author: Ivan V. Pleshakov, ivanple@yandex.ru

PACS 75.50.Mm; 75.50.Tt

ABSTRACT In this work, the aggregation of nanoparticles in an aqueous colloidal solution of magnetite, stabilized by creating a citrate shell on the particle surface is studied. Electron microscopy and laser correlation spectroscopy were used as experimental methods. Optical measurements were carried out both at zero external magnetic field and in the fields differently oriented relative to the probing laser beam. It is shown that the samples tend to form large aggregates even without the application of the field, and in the case of its presence the behavior of these structures has features that distinguish them from other magnetic fluids.

KEYWORDS magnetic fluid, aggregation, citrate stabilization, electron microscopy, laser correlation spectroscopy.

FOR CITATION Pleshakov I.V., Ryzhov V.A., Marchenko Ya.Yu., Alekseev A.A., Karseeva E.K., Nevedomskiy V.N., Prokof'ev A.V. Agglomeration of magnetite nanoparticles with citrate shell in an aqueous magnetic fluid. *Nanosystems: Phys. Chem. Math.*, 2023, **14** (3), 334–341.

1. Introduction

Magnetic fluids, or ferrofluids, are a special type of colloids with magnetic properties [1, 2]. The solid phase of these substances is a magnetically ordered material (very often, magnetite) in a nanodispersed state, and various liquid media are used as carriers, such as kerosene, water, oil, etc. As in many other colloids, when creating these systems, special techniques are used to stabilize them, that is, to prevent the adhesion of magnetic nanoparticles, for example, by coating them with a layer of surfactant. Differently stabilized ferrofluids may differ noticeably in their characteristics.

Being an interesting physical object, magnetic fluids have attracted the attention of researchers for several decades. As a result, a number of novel phenomena associated with their nanostructural nature combined with magnetism were discovered in them. In addition, it was also found quite a large number of applications. Recently, the practical proposals in this area has begun to increase rapidly, which, in turn, has given a rise to new directions, including those focused on fundamental problems.

Photonics and electronics (magnetically controlled elements [3, 4]), as well as biomedical studies considering all possible aspects of the behavior of magnetic nanoparticles embedded in the biological medium can be named as the fields developing ideas pertaining to ferrofluids [5, 6].

Physical, in particular, optical effects in ferrofluids are largely determined by the structures that nanoparticles form in them. It is well known that an external magnetic field usually leads to the appearance of extended aggregates that grow with its increase [7]. However, even without a field, objects consisting of many nanoparticles normally appear in a magnetic fluid due to coagulation. For the areas mentioned above, it is important to study the processes and features of aggregation, which provide the key to understanding the capabilities of magnetic fluids. These studies cannot be considered as complete, since fluids of different compositions and stabilized by different approaches have different properties, and currently are the subject of active investigation. This work is devoted to an aqueous solution of magnetite particles in a citrate shell, demonstrating, as will be seen from the following, significant differences from other aqueous colloids of this material.

2. Samples

Iron oxide nanoparticles were obtained by co-precipitation of iron salts ($\text{Fe}^{2+}/\text{Fe}^{3+} = 2/1$) with an excess of ammonium hydroxide according to the scheme described earlier in [8]. The reaction was carried out in an inert nitrogen atmosphere at a temperature of $80\text{ }^{\circ}\text{C}$. The resulting iron oxide Fe_3O_4 was washed with distilled water to a neutral pH, after which it was separated by a magnet. A sample of 2.3 g wet oxide was suspended in 10 ml of 1 mM aqueous solution of citric acid monohydrate at $\text{pH} = 5$. Then the liquid obtained was subjected to ultrasonic treatment for 60 minutes at $90\text{ }^{\circ}\text{C}$, and after that it was cooled to room temperature [9–11]. The starting point for further experiments was a sample with a solid phase concentration of 6.8 mg/ml, which was stored at $4\text{ }^{\circ}\text{C}$. In the various cases described below, it could be diluted to the desired concentrations and subjected to additional sonification.

3. Experimental techniques

3.1. Electron microscopy

Transmission electron microscopy (TEM) studies were performed at the “Material science and characterization in advanced technology” in the Ioffe Institute by JEM-2100F microscope (JEOL Ltd., Japan) at an accelerating voltage of 200 kV. Sample particles were imaged mainly under two-beam conditions in bright field mode.

Samples were prepared in the traditional way adapted to specific conditions by the following steps: 1) dilution of the initial colloidal solution by approximately 20 times with distilled water, 2) dispersion of the resulting solution with ultrasound for 8–10 min, 3) immersion in the resulting solution of a special mesh for TEM studies with a thin supporting carbon film already applied to it, on which the solution was deposited, 4) drying the obtained sample under normal conditions for 30 minutes.

3.2. Laser correlation spectroscopy

It is known that laser correlation spectroscopy is an effective tool for studying clusters in solutions containing nanoparticles; in particular, it has been successfully used to characterize ferrofluids placed in a magnetic field [12–14]. This method is based on the calculation of the autocorrelation function of the light scattered by the sample, from which, with a known viscosity of the carrier liquid, data on the sizes of particles or their agglomerates d are extracted (a more detailed description of this technique can be found in [14] and references therein).

To implement the method, we used the installation, the block diagram of which is shown in Fig. 1. The laser beam was focused by an optical system on a magnetic fluid placed in a cuvette located in the Helmholtz coils that create a magnetic field H .

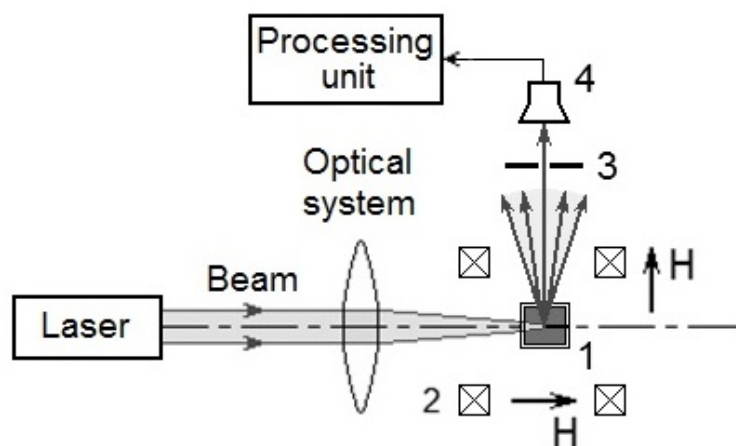


FIG. 1. Experimental setups for laser correlation spectroscopy: 1 – sample (cuvette with magnetic fluid); 2 – Helmholtz coils; 3 – diaphragm; 4 – photomultiplier. Possible orientations of the field H are shown

Scattered radiation that passed through the diaphragm at an angle of 90 ° with respect to the optical axis of the system was recorded by a photomultiplier, and then the electrical signal was digitized and processed on a computer. The results of the analysis were displayed as a normalized scattering intensity versus d . We used a special algorithm for determining the size of scatterers, described in [15], the characteristic time of one measurement procedure, dependent on the time of signal accumulation and processing, was 2–3 min. In the measurements, a He-Ne laser with a wavelength of $\lambda = 632.8\text{ nm}$, high stability and a narrow spectral line was used. Scattered light was detected in a plane perpendicular to the plane of polarization of the incident beam.

To ensure single scattering, in laser correlation spectroscopy experiments the sample was diluted to a particle concentration of 10^{-3} vol. %.

The experimental setup was similar to that used earlier in [14], but in this case, the design of the Helmholtz coils made it possible to orient the magnetic field H created by them both parallel to the optical axis of the system and perpendicular to it (in the direction of scattered light propagation). The field strength could vary within 0–400 Oe.

4. Results of experiments

The microstructure of the sample obtained by the deposition is shown in Fig. 2. By these electron micrographs, one can make an estimate of the average size of nanoparticle, which, as can be seen from Fig. 2a and Fig. 2b is about 10 nm, which does not differ from the data typical for other similar materials [16, 17]. An essential circumstance is that the pattern observed at a different scale (Fig. 2b,c,d) indicates the appearance of large formations of many nanoparticles in the deposited layer, reaching significant dimension of hundreds of nanometers. Most likely, the formation of similar aggregates still occurs in the liquid state (although such factors as surface tension, the effect of the surface on which the deposition occurs, etc. should affect their shape and size after the deposition process is completed). It should be emphasized that the images in Fig. 2 were obtained without applying an external magnetic field.

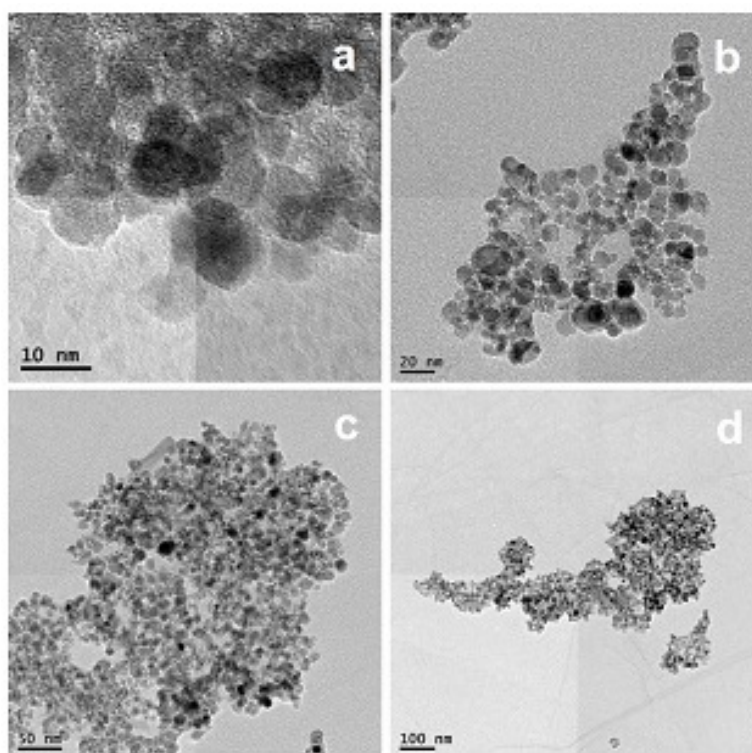


FIG. 2. Electronic micrographs of ferrofluid sediment at different scales (shown in the figure)

In experiments on laser correlation spectroscopy, it was found that the results of measurements performed after the application of the magnetic field depend on time. This reflects the evolution of forming aggregates peculiar to ferrofluids, which occurs rather slowly (with a characteristic time of the order of minutes) [14]. Keeping this in mind, the study of aggregation processes was carried out as follows: first, data were obtained at $H = 0$, then the field was switched on, and after some time, chosen in such a way that the total interval from the moment of the switching on to the end of the measurement was five minutes, the data collection procedure was started. The initial values of the average sizes of scatterers d_0 and, consequently, the distribution functions of d obtained for a nonzero field could depend on the preliminary preparation of the samples, but the qualitative behavior of the system always remained the same. (The value of d_0 is understood further as such a d at which, when $H = 0$, the local maximum in the aggregate size distribution is reached.)

Examples of distribution functions d taken at different times and for different field orientations are shown in Fig. 3 ($H = 380$ Oe). Because of the fact that in these experiments the spread of data was quite large, they were smoothed using the sliding window algorithm with the number of points in the window equal to five. In all measurements, the distribution pattern turned out to be quite complex, containing many peaks, each of which was assigned its own value d_0 .

In the case of measurements with a parallel orientation of the field (Fig. 3a), the solution was subjected to ultrasonic treatment and settled for two days before measurements were taken, and with a perpendicular orientation (Fig. 3b), the difference was that the measurements were carried out after two weeks. As can be seen, the numerical values of d differed

here; in general, we found that the values of d_0 , i.e., those from which every particular measurement began, could vary substantially depending on the prehistory of the sample. Nevertheless, qualitatively the behavior of the system, as well as the data obtained for relative values, was reproduced quite well from experiment to experiment.

From graphs like those shown in Fig. 3, several peaks were distinguished, that assuredly observed in most experiments (it should be noted that at certain points in time some peaks disappeared, and new ones could also appear). Each was described satisfactorily by log-normal distribution:

$$f(d) = \frac{A}{\sqrt{2\pi}\sigma d} \exp \left[-\frac{(\ln \frac{d}{d_0})^2}{2\sigma^2} \right], \quad (1)$$

where A and σ are parameters (along with d_0 used in the fitting). Statistical characteristics of the distributions indicated in Fig. 3 as 1 and 2 are summarized in Tables 1 and 2, which refer to the parallel and perpendicular field orientations, respectively (additional rows reflect the appearance of additional peaks). Here d_0 is the median, $\mu = \ln d_0$.

The time behavior of the relative average size of aggregates d/d_0 belonging to groups 1 and 2 is shown in Fig. 4 (the first and the last points on this graph correspond to $H = 0$). The field had no effect on fine structural elements (at $d \sim 40\text{--}60$ nm).

The dependence of the sizes of large aggregates on H under the conditions of their temporal evolution can be obtained only with a certain degree of conventionality, since along with their growth during the measurement, the opposite process must occur as can be seen from Fig. 4. However, a rough idea of it may be the result of the experiment, which is set as follows: after each increase in the field, a measurement is performed (which, as mentioned above, takes 2–3 min), and then the field is immediately increased and the procedure repeated. The outcome taken in this way for a perpendicular orientation of the magnetic field is shown in Fig. 5.

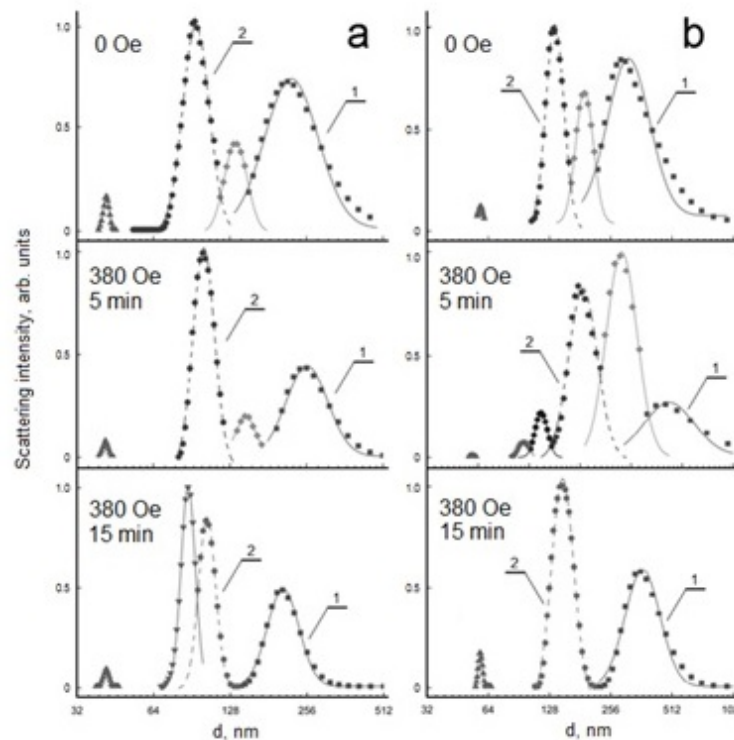


FIG. 3. Examples of size distributions of agglomerates for the cases of: a) parallel orientation of the magnetic field H with the optical axis and b) perpendicular orientation of the magnetic field H with the optical axis ($H = 380$ Oe). 1, 2 – selected groups of agglomerates, for which the dependences of their relative parameters are given further

5. Discussion

The obvious conclusion that follows from the above experimental results is that in the initial state, the nanoparticles of the ferrocolloid under study are mainly belong to large formations, for which the applied magnetic field, at first, has the expected effect, i.e. leads to their growth. Further, the particle size distribution (Fig. 3) begins to evolve, demonstrating, despite the presence of the field, a gradual decrease in the size of these aggregates in the time interval of 5–15 min (Fig. 4). We can approximately assume that at the time of H switching off ($t = 20$ min), the system returns to its original position.

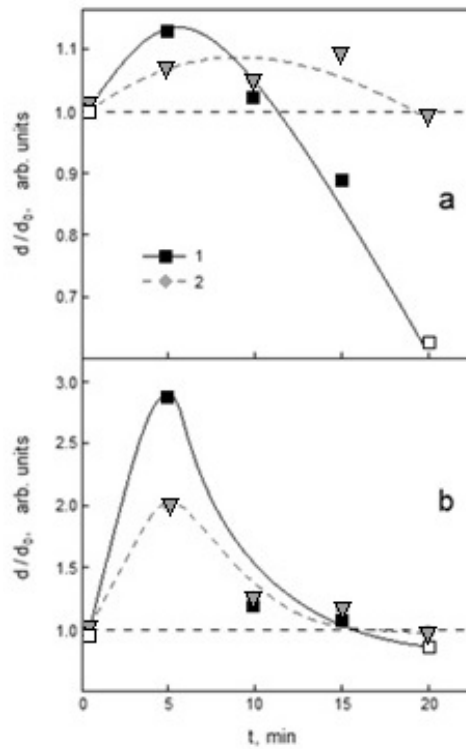


FIG. 4. Time dependences of the relative sizes of agglomerates for a) parallel geometry of experiment and b) perpendicular geometry of experiment ($H = 380$ Oe). 1 – group 1, 2 – group 2 (open symbols correspond to $H = 0$)

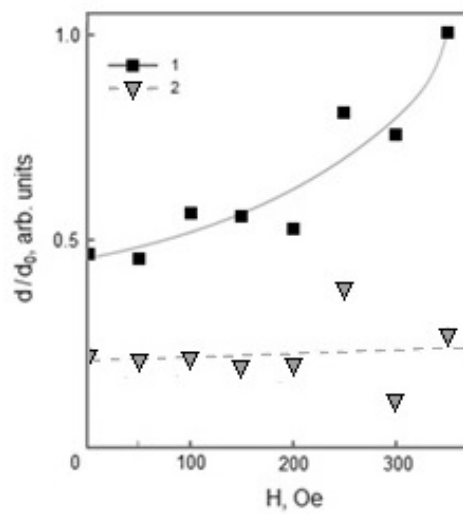


FIG. 5. Field dependences of the relative medium sizes of agglomerates (groups 1 and 2) for perpendicular geometry of experiment (normalized on the medium size d_0 in group 1 at the maximum value of the field).

TABLE 1. Parallel geometry of the experiment

H , Oe	Time of action t , min	d_0 , nm
0	0	237.02
		136.49
		95.49
		41.81
380	5	266.93
		148.83
		102.08
		41.49
380	10	242.06
		99.86
		76.59
		41.36
380	15	210.62
		104.38
		87.82
		41.72
0	20	148.41
		94.56
		73.97
		41.66

The effect of differently orientated fields are markedly distinguished: as can be seen from the comparison of Fig. 4a and Fig. 4b, in perpendicular geometry, at the initial stage a much more significant change in the relative value d/d_0 is recorded. Since the laser correlation spectroscopy is sensitive to the size of scatterers in a plane orthogonal to the optical axis, the registration of this phenomenon reflects the formation of structures elongated parallel to H , which is always observed in such materials. From Fig. 4, it is easy to determine that at $H = 380$ Oe, the longitudinal size of the aggregate increases by 2–3 times, while for the transverse size the enhancement does not exceed 15 %, i.e. an increase in its volume can be estimated as half the order.

The nontrivial fact of a decrease in the value of d/d_0 at the next stage of evolution has not yet found a strict explanation, but most likely it is owing to the dynamics of large objects with many nanoparticles that do not maintain stability even at $H \neq 0$. After reaching the maximum size, aggregates decrease, and the longitudinal size decreases most rapidly. There is no ideal restoration of the initial state (some peaks of the distribution of d are shifted to the region of even slightly smaller values than at $t = 0$).

On the whole, however, it can be stated that the system tends to a certain equilibrium state, in which its structural elements have approximately the same dimensions as those formed in the colloid before external influence. Note that the spread of d values associated with each group of aggregates described by individual functions (1) is comparable with the distance between the peaks, so it is difficult to accurately determine the temporal and field behavior of the aggregates. Thus, the graphs in Fig. 4 and 5 represent only the general nature of those. However, the field dependence (Fig. 5), taken according to the method described above, still reflects the tendency for aggregates to enlarge after the switching on or increase of H , despite the opposing processes of growth and decay of these formations.

Figure 5 does not show data related to very small scatterers ($d \sim 60$ nm), since their sizes are almost independent of the field (Table 2). Perhaps this is due to the fact that they are non-magnetic inclusions that may be presented in samples because of certain peculiarities of their manufacturing.

The specificity associated with the stabilizing method of the magnetic fluid is determined by the peculiarities of the interaction of nanoparticles with a given type of surfactant deposited on their surface, that is, ultimately, from what

TABLE 2. Perpendicular geometry of the experiment

H , Oe	Time of action t , min	d_0 , nm
0	0	331.52
		192.29
		137.48
		58.63
380	5	963.26
		470.61
		276.51
		152.23
		119.72
		59.24
380	10	411.46
		171.12
		58.57
380	15	382.01
		150.89
		58.55
0	20	288.71
		131.89
		59.60

structure begins the formation of a new one after the application of the field. Idealized approach to the analysis of ferrocolloids usually considers a medium with single nanoparticles dispersed in it, which gather into clusters when a magnetic field is applied [17]. This is a simplification, since, as already was mentioned, even at $H = 0$ some amount of large particle associates are almost always presented in such substances [14]. In our case at the initial state practically all particles are already combined into very large aggregates (Fig. 2,3), which, most probably, is determined by the properties of the citrate shell. Further growth of aggregates in the field can continue up to a certain limit and then their fragmentation occurs. (It should be noted that the observed effect of the decrease of the amount of large objects cannot be explained by their sedimentation, since the characteristic time of such a process, estimated by the Stokes formula, significantly exceeds the measurement time.)

Electron microscopy confirms our assumption that nanoparticles in the studied materials tend to assemble into large formations even in the absence of the external action. Despite the fact that these data were obtained under conditions different from those under which the laser correlation spectroscopy experiments were performed, as well as the above-mentioned distortions that occur when a ferrocolloid is deposited on a substrate, the result presented in Fig. 2 provides a fairly convincing illustration of this property of our samples at a qualitative level. In the presence of agglomerates in the liquid state with dimensions of the order of hundreds of nanometers similar to those shown in the figure, after applying a magnetic field to the system, processes associated with their initial growth and subsequent fragmentation will develop.

6. Conclusion

In this paper, it is shown that large-sized aggregates can form in citrate stabilized aqueous magnetite-containing ferrofluid without external magnetic field. Besides, the presence of large formations determines the unusual behavior of the system in the field, which combines their conventional field-induced grows with the decay process. The latter begins at a certain stage, after some limiting volume of aggregate has been reached. This information should be useful in the analysis of colloids with a magnetically ordered substance dispersed in a medium of complex composition.

References

- [1] Socoliuc V., Avdeev M., Kuncser V., Turcu R., Tombácz E., Vekas L. Ferrofluids and bio-ferrofluids: looking back and stepping forward. *Nanoscale*, 2022, **14**, P. 4786–4886.
- [2] Oehlsen O., Cervantes-Ramírez S.I., Cervantes-Avilés P., Medina-Velo I.A. Approaches on ferrofluid synthesis and applications: current status and future perspectives. *ACS Omega*, 2022, **7**, P. 3134–3150.
- [3] Taghizadeh M., Bozorgzadeh F., Ghorbani M. Designing magnetic field sensor based on tapered photonic crystal fibre assisted by a ferrofluid. *Scientific Reports*, 2021, **11**(1), P. 14325.
- [4] Yong Zhao, Yuyan Zhang, R.-Q. Lv, Qi Wang. Novel optical devices based on the tunable refractive index of magnetic fluid and their characteristics. *J. Magn. Magn. Mat.*, 2011, **323**(23), P. 2987–2996.
- [5] Imran M., Alam M.M., Khan A. Advanced biomedical applications of iron oxide nanostructures based ferrofluids. *Nanotechnology*, 2021, **32**(42), P. 422001.
- [6] Pilati V., Gomide G., Cabreira Gomes R., Goya G.F., Depeyrot J. Colloidal stability and concentration effects on nanoparticle heat delivery for magnetic fluid hyperthermia. *Langmuir*, 2021, **37**(3), P. 1129–1140.
- [7] Ivanov A.O., Zubarev A.Yu. Chain formation and phase separation in ferrofluids: the influence on viscous properties. *Materials*, 2020, **13**(18), P. 3956.
- [8] Shevtsov M.A., Nikolaev B.P., Yakovleva L.Y., Marchenko Y.Y., Dobrodumov A.V., Mikhrina A.L., Martynova M.G., Bystrova O.A., Yakovenko I.V., Ischenko A.M. Superparamagnetic iron oxide nanoparticles conjugated with epidermal growth factor (SPION-EGF) for targeting brain tumors. *Int. J. Nanomed.*, 2014, **9**, P. 273.
- [9] Kotsmar C., Ki Youl Yoon, Haiyang Yu, Seung Yup Ryoo, Joseph Barth, Shao S., Prodanović M., Milner T.E., Bryant S.L., Chun Huh, Johnston K.P. Stable citrate-coated iron oxide superparamagnetic nanoclusters at high salinity. *Ind. Eng. Chem. Res.*, 2010, **49**, P. 12435–12443.
- [10] Yusuf M.S., Rahmasari S., Rahmasari R. Synthesis processing condition optimization of citrate stabilized superparamagnetic iron oxide nanoparticles using direct co-precipitation method. *Biomed. Pharmacol. J.*, 2021, **14**(3), P. 1533–1542.
- [11] Arefi M., Kazemi Miraki M., Mostafalu R., Satari M., Heydari A. Citric acid stabilized on the surface of magnetic nanoparticles as an efficient and recyclable catalyst for transamidation of carboxamides, phthalimide, urea and thiourea with amines under neat conditions. *J. Iran. Chem. Soc.*, 2019, **16**, P. 393–400.
- [12] Broillet S., Szlag D., Bouwens A., Maurizi L., Hofmann H., Lasser T., Leutenegger M. Visible light optical coherence correlation spectroscopy. *Opt. Express*, 2014, **22**(18), P. 21944–21957.
- [13] Nepomnyashchaya E., Velichko E., Aksenov E., Bogomaz T. Optoelectronic method for analysis of biomolecular interaction dynamics. *J. Phys. Conf. Ser.*, 2014, **541**(9), P. 01203.
- [14] Nepomnyashchaya E.K., Prokofiev A.V., Velichko E.N., Pleshakov I.V., Kuzmin Yu.I. Investigation of magneto-optical properties of ferrofluids by laser light scattering techniques. *J. Magn. Magn. Mat.*, 2017, **431**, P. 24–26.
- [15] Nepomniashchaia E.K., Velichko E.N., Aksenov E.T. Solution of the laser correlation spectroscopy inverse problem by the regularization method. *Univ. Res. J.*, 2015, **15**, P. 13–21.
- [16] Scherer C., Figueiredo Neto A.M. Ferrofluids: Properties and Applications. *Braz. J. Phys.*, 2005, **35**(3A), P. 718–727.
- [17] Chikazumi S., Taketomi S., Ukita M., Mizukami M., Miyajima H., Setogawa M., Kurihara Y. Physics of magnetic fluids. *J. Magn. Magn. Mat.*, 1987, **65**, P. 245–251.

Submitted 28 May 2023; accepted 5 June 2023

Information about the authors:

Ivan V. Pleshakov – Ioffe Institute, 26 Politechnicheskaya str., St. Petersburg, 194021, Russia; ORCID 0000-0002-6707-6216; ivanple@yandex.ru

Vyacheslav A. Ryzhov – Petersburg Nuclear Physics Institute named by B. P. Konstantinov of National Research Centre “Kurchatov Institute”, Gatchina, 188300, Russia; ORCID 0000-0002-0546-1805; varyzhov@yandex.ru

Yaroslav Yu. Marchenko – Petersburg Nuclear Physics Institute named by B. P. Konstantinov of National Research Centre “Kurchatov Institute”, Gatchina, 188300, Russia; ORCID 0000-0002-7923-2175; 046.slava@mail.ru

Arseniy A. Alekseev – Peter the Great St. Petersburg Polytechnic University, 29 Polytechnicheskaya str., St. Petersburg, 195251, Russia; ORCID: 0009-0000-5368-6788; arseniy.alekseev98@gmail.com

Elina K. Karseeva – Peter the Great St. Petersburg Polytechnic University, 29 Polytechnicheskaya str., St. Petersburg, 195251, Russia; ORCID 0000-0002-4416-9380; elina.nep@gmail.com

Vladimir N. Nevedomskiy – Ioffe Institute, 26 Politechnicheskaya str., St. Petersburg, 194021, Russia; ORCID 0000-0002-7661-9155; nevedom@mail.ioffe.ru

Andrey V. Prokof'ev – Ioffe Institute, 26 Politechnicheskaya str., St. Petersburg, 194021, Russia; ORCID 0009-0009-7894-1947; andrey.prokofyev@algo-spb.com

Conflict of interest: the authors declare no conflict of interest.

Measurement-device-independent continuous variable quantum key distribution protocol operation in optical transport networks

Irina Vorontsova¹, Roman Goncharov¹, Sergey Kynev^{1,2}, Fedor Kiselev^{1,2}, Vladimir Egorov^{1,2}

¹ITMO University, St. Petersburg, Russia

²SMARTS-Quanttelecom LLC, St. Petersburg, Russia

Corresponding author: Irina Vorontsova, iovorontsova@itmo.ru

PACS 03.67.-a, 42.50.-p

ABSTRACT Numerically, a theoretical analysis of the noise impact caused by spontaneous Raman scattering, four-wave mixing, and linear channel crosstalk on the measurement-device-independent continuous variable quantum key distribution systems is conducted. The analysis considers symmetry and asymmetry of system paths, as well as possible channel allocation schemes, for a quantum channel located in C- and O-bands. Mathematical models for MDI CV-QKD system and the contributing noises' description are provided. The secure key generation rate is estimated to state features of protocol operation when integrated with existing DWDM systems in the context of its implementation into telecommunication networks.

KEYWORDS device-independence, quantum key distribution, continuous variables

ACKNOWLEDGEMENTS The work was done by Leading Research Center "National Center for Quantum Internet" of ITMO University by the order of JSCo Russian Railways.

FOR CITATION Vorontsova I., Goncharov R., Kynev S., Kiselev F., Egorov V. Measurement-device-independent continuous variable quantum key distribution protocol operation in optical transport networks. *Nanosystems: Phys. Chem. Math.*, 2023, **14** (3), 342–348.

1. Introduction

Quantum key distribution (QKD) is one of the most rapidly advancing fields of quantum technologies [1, 2]. Its main idea is an opportunity to transport a cryptographically secure key between two and more authenticated users connected to each other through quantum and information channels. Guaranteed by the principles of quantum mechanics [3], the security of QKD to attacks from an eavesdropper ensures safety of the transmitted data from all kinds of hacking and known attacks.

One option to classify QKD protocols is based on them being discrete-variable (DV) or continuous-variable (CV) [4]. Additionally, among many other QKD protocol classifications, there is the one distinguishing between protocols in terms of their device-dependence or (semi-)device-independence [5]. The intersection of these two criteria gives rise to a new class of protocols, that is measurement-device-independent (MDI) CV-QKD protocol. Device-independence features particular practical importance, for it eliminates many side channel attacks, though implies accurate theoretical analysis.

Not only does this work discuss the latter, but also for the first time combines this analysis with the task of simultaneous propagation of information and quantum signals in a single optical fiber [6]. The effects considered as channel loss sources are spontaneous Raman scattering, four-wave mixing, and linear channel crosstalk. A possible realization scheme is discussed, as well as the allocation of classical channels on the standard DWDM grid. The security analysis is carried out numerically, employing the known theoretical security bounds to estimate the performance of the addressed QKD system. The results are quite important in practice to be considered when integrating QKD with the existing telecommunication networks.

2. Measurement-device-independent QKD

Let us discuss main principles underlying MDI QKD protocol operation [5, 7]. The essence of the approach lies in the fact that no assumptions are made about the detectors involved in the protocol, such that they can even be controlled by an eavesdropper (Eve). In a typical single-photon MDI QKD protocol, two legitimate users (Alice and Bob) send quantum signals to an untrusted central relay, often addressed as Charlie. A Bell state measurement is performed then; both signals interfere at a 50:50 beam splitter (BS). Next, output signals go through a polarizing beam splitter (PBS) to be projected into either horizontal (H) or vertical (V) polarization state. The measurement is pronounced successful if two of the four involved detectors click.

2.1. Continuous-variable MDI QKD protocol

Similarly to the conventional MDI QKD, the continuous variable (CV) version of the protocol [8, 9] again implies there are the two senders and an untrusted relay performing the measurements to be used during legitimate users' post-processing to generate the secure key.

The two known approaches to a general protocol description, namely, "prepare-and-measure" (PM) and "entanglement-based" (EB) scenarios, apply to the case of MDI CV-QKD as well. For these scenarios are equivalent in terms of their mathematical description and effectiveness, we will consider a more practically convenient PM version of the protocol. Gaussian modulation [4, 10] (GG02 protocol) is considered, so Alice and Bob are operating with coherent states with a two-dimensional Gaussian distribution. They first generate coherent states $|x_A + ip_A\rangle$ and $|x_B + ip_B\rangle$ with the quadratures x and p featuring variance $V_{A(B)} - 1$ (in shot noise units (SNU)) and then send their states to Charlie via quantum channels. Next, Alice's and Bob's modes interfere at the beam splitter, while Charlie measures the C and D modes' quadratures on homodyne detectors and announces the resulting state $\{X_C, P_D\}$ publicly. It is Bob only who changes his state according to $X_B = x_B + kX_C, P_B = p_B - kP_D$ (with k standing for the gain associated with channel losses), whereas Alice's state remains unchanged. Finally, standard procedures are utilized for parameter estimation, information reconciliation, and privacy amplification.

Since there is equivalency between the CV-QKD EB and PM scenarios' security proof against collective attacks [11, 12], we shall now switch to the well-known covariance matrix formalism.

Implying that Eve has access to the relays, quantum channels, and even Bob's state displacement operation in the EB scheme, further security analysis of the MDI CV-QKD protocol can be seen as a special case of a typical one-way CV-QKD protocol [4, 10].

Then the secure key fraction can be estimated in accordance with the Devetak-Winter bound [13, 14]:

$$r = \beta I(X_A, P_A : X_B, P_B) - \chi(X_B, P_B : E), \quad (1)$$

where $0 \leq \beta \leq 1$ is the reconciliation efficiency (assumed to be ideal in the further numerical simulations), I is the mutual information between Alice and Bob, $\chi(X_B, P_B : E) = S(\hat{\rho}_E) - S(\hat{\rho}_E|X_B, P_B)$ is the Holevo bound, and $S(\hat{\rho}_E)$ denotes the von Neumann entropy of quantum state $\hat{\rho}_E$.

The upper bound $\chi(X_B, P_B : A_1, B'_1)$ is determined only using the corresponding covariance matrix. Supposing the system is under two independent entangling cloner attacks [4], the covariance matrix takes the form of:

$$\Xi = \begin{pmatrix} V_A I_2 & \sqrt{(T(V_A^2 - 1)\sigma_z)} \\ \sqrt{(T(V_A^2 - 1)\sigma_z)} & [(V_A - 1) + 1 + T\xi'] I_2 \end{pmatrix}, \quad (2)$$

$$T = \frac{\eta_A}{2} g^2, \quad (3)$$

$$\xi' = 1 + \frac{1}{\eta_A} [\eta_B(\Xi_B - 1) + \eta_A \Xi_A] + \frac{1}{\eta_A} \left(\frac{\sqrt{2}}{g} \sqrt{V_B - 1} - \sqrt{\eta_B} \sqrt{V_B + 1} \right)^2, \quad (4)$$

$$\Xi_A = \frac{1 - \eta_A}{\eta_A} + \xi_A, \quad \Xi_B = \frac{1 - \eta_B}{\eta_B} + \xi_B, \quad (5)$$

$$\eta_A = 10^{-\alpha L_{AC}/10}, \quad \eta_B = 10^{-\alpha L_{BC}/10}, \quad (6)$$

where η_A (η_B) is a channel (Alice-Charlie or Bob-Charlie) transmittance, ξ_A (ξ_B) is the excess noise, g is the offset factor, I_2 is the identity matrix, and σ_z is the Pauli z -matrix.

To minimize the excess noise, the offset factor is set as

$$g = \sqrt{\frac{2}{\eta_B}} \sqrt{\frac{V_B - 1}{V_B + 1}}. \quad (7)$$

Then, the excess noise is expressed as:

$$\xi' = \xi_A + \frac{1}{\eta_A} [\eta_B(\xi_B - 2) + 2], \quad (8)$$

where the excess noise on Alice's side (Bob's side) $\xi_{A(B)}$ contain the corresponding channel noise converted to SNU. Alice's and Bob's variances are considered equal $V_A = V_B = 40$ in the simulations.

3. Channel Noise Sources and their Mathematical Description

Naturally, losses are inevitable when it comes to signal propagation in any medium, be it fiber-optical communication lines or free space. Regarding QKD, three effects are addressed in terms of noise primarily, which are the spontaneous Raman scattering (SpRS), the four-wave mixing (FWM) nonlinearity, and the linear channel crosstalk (LCXT). Now, we will briefly summarize their physical nature and corresponding mathematical description, then estimate the negative contribution they make to the performance of MDI CV-QKD system under consideration.

3.1. Spontaneous Raman Scattering

Firstly, the main contributor to the overall channel losses in case of QKD integrated with DWDM systems is the SpRS noise [15, 16]. Its impact is minor for classical networks, though the contribution becomes substantial for joint QKD and DWDM systems [15, 16]. The origin of the SpRS is different for the cases of co- and counter-propagation of signals. Thus, two sub-types are distinguished usually, that are forward (for co-propagating signals) and backward (for counter-propagating signals) SpRS noise. When speaking in the context of simultaneous QKD session and information transmission within single optical fiber, the mathematical representation of their contribution is given by [6, 17]:

$$P_{\text{ram},f} = P_{\text{out}} L \sum_{c=1}^{N_{ch}} \rho(\lambda_c, \lambda_q) \Delta\lambda, \quad (9)$$

and

$$P_{\text{ram},b} = P_{\text{out}} \frac{\sinh(\xi L)}{\xi} \sum_{c=1}^{N_{ch}} \rho(\lambda_c, \lambda_q) \Delta\lambda, \quad (10)$$

where P_{out} denotes the output power for a single channel, L is the length of the optical fiber, N_{ch} is the number of classical channels present in a DWDM system, $\rho(\lambda_c, \lambda_q)$ describes the normalized scattering cross-section for the wavelengths of classical (λ_c) and quantum (λ_q) channels, and $\Delta\lambda$ is the bandwidth of the quantum channel filtering system.

For the MDI CV-QKD realization considered here, both forward and backward SpRS occur for different system paths. A detailed description of the configuration will be provided in the following section.

The output power values appear in formulas instead of the input ones, so that to meet the the bit error rate (BER) requirements of a DWDM system directly. Thus, the value of P_{out} can be obtained as follows:

$$P_{\text{out}} \text{ (dBm)} = R_x \text{ (dBm)} + IL \text{ (dBm)}, \quad (11)$$

where R_x is the sensitivity of a receiver and IL denotes the insertion losses of the system.

3.2. Four-wave Mixing

Next channel noise source to consider is FWM. It is a third-order nonlinear process, which sequence is creation of photons at new frequencies as a result of the interaction between the initial ones [18]. These new frequencies might coincide with the one of the quantum channel [19], thus contributing to the overall noise in the band of the quantum channel.

To come up with the mathematical model for the FWM noise contribution consideration, let us consider three pump channels with the frequencies $f_i, f_j,$ and f_k . Then, the value of the resulting FWM noise peak power P_{ijk} featuring the frequency $f_i + f_j - f_k$ can be expressed as [6]:

$$P_{ijk} = \eta \gamma^2 D^2 p^2 e^{-\xi L} \frac{(1 - e^{-\xi L})^2}{9\xi^2} P_s P_l P_h, \quad (12)$$

where the phase-matching efficiency for the FWM η and parameter $\Delta\beta$ are defined as:

$$\eta = \frac{\xi^2}{\xi^2 + \Delta\beta^2} \left[1 + \frac{4e^{-\xi L} \sin^2(\Delta\beta L/2)}{(1 - e^{-\xi L})^2} \right], \quad (13)$$

and

$$\Delta\beta = \frac{2\pi\lambda^2}{c} |f_i - f_k| |f_j - f_k| \cdot \left[D_c + \frac{dD_c}{d\lambda} \left(\frac{\lambda^2}{c} \right) (|f_i - f_k| + |f_j - f_k|) \right], \quad (14)$$

correspondingly. In the above equations, L is the transmission distance of the interacting light fields in the optical fiber, D denotes the degeneracy factor ($D = 6, D = 3$), $P_{i(j,k)}$ and $f_{i(j,k)}$ are the input power and optical frequency of the interacting fields correspondingly, γ stands for the third-order nonlinear coefficient, ξ is the loss coefficient, D_c and $dD_c/d\lambda$ are the dispersion coefficient of an optical fiber and its slope respectively with λ standing for the wavelength of the FWM radiation.

Finally, performing the summation of all the powers of the resulting FWM signals with frequencies coinciding with the frequency of the quantum channel, one obtains:

$$P_{\text{FWM}} = \sum P_{ijk}, \quad f_i + f_j - f_k = f_q. \quad (15)$$

3.3. Linear Channel Crosstalk

It is due to the imperfections of the demultiplexers that any practically implemented DWDM system suffers LCXT losses [20].

Since information signals are orders of magnitude more powerful than quantum ones, the insufficient isolation might cause considerable LCXT noise, that can be estimated in the following way:

$$P_{\text{LCXT}} = P_{\text{out}} (\text{dBm}) - \text{ISOL} (\text{dB}). \quad (16)$$

Once the power values of the contributing to the overall channel noise effects are calculated, it is needed to recalculate them to a photon detection probability. To do so, the following formula can be used:

$$p_{\text{ram,f(b)}/\text{FWM}/\text{LCXT}} = \frac{P_{\text{ram,f(b)}/\text{FWM}/\text{LCXT}}}{hc/\lambda_q} \Delta t \eta_D \eta_B, \quad (17)$$

where η_D denotes the detector efficiency, $\eta_B = 10^{-0.1LL}$ is the transmission coefficient associated with the insertion losses of the detection system, h is the Planck constant, and c is the light speed.

4. MDI CV-QKD scheme and channel allocation

Here, a possible realization scheme of MDI CV-QKD protocol will be addressed to analyze its potential for creating telecommunication optical transport networks integrated with DWDM systems. The notion of maximal achievable distances of MDI CV-QKD systems employed to characterize the latter denotes fiber length corresponding to the case, when the secure key generation rate is non-zero.

The realization of MDI CV-QKD addressed in the work is shown in Fig. 1.

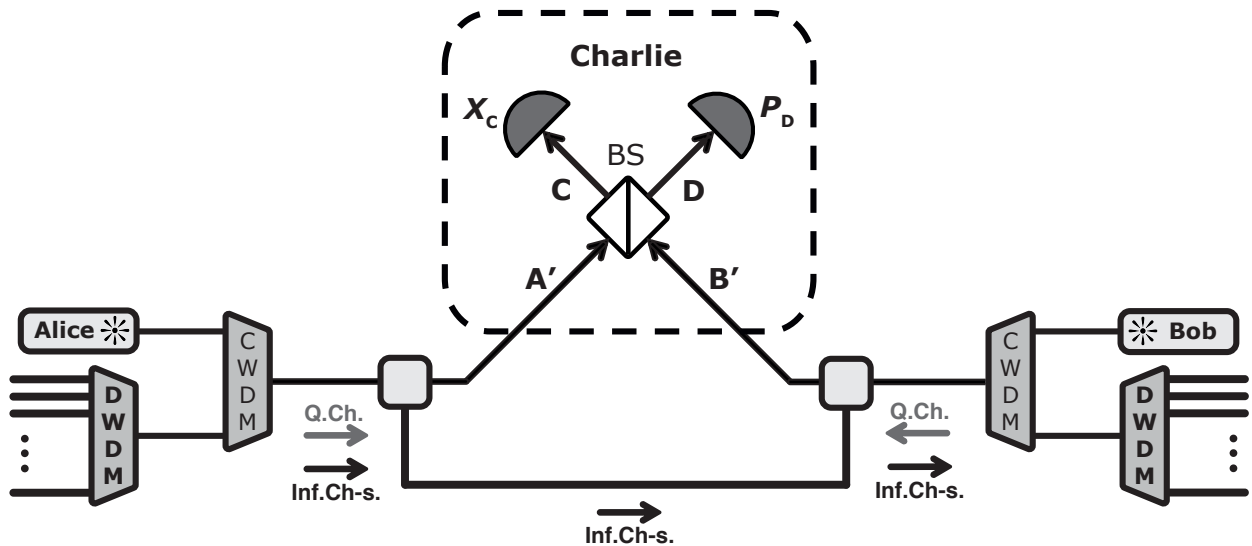


FIG. 1. Schematic illustration for the MDI CV-QKD protocol realization with DWDM: information is transmitted from Alice to Bob via DWDM-information channels; quantum channel is co-propagating with information channels in Alice's path, whereas counter-propagating with them in Bob's path and, thus, which means forward SpRS noise is induced in the Alice-Charlie path and backward SpRS - in the Bob-Charlie path

Here, quantum signals are sent to the untrusted central relay to be homodyned there, whereas the information is transferred from Alice to Bob directly. It means, quantum and information signals are unidirectional in Alice's path (i.e., there is forward SpRS noise in the path) and counter-propagating through the Bob's path, so the SpRS noise features the backward type.

The performance of the MDI CV-QKD realization was then numerically analyzed in terms of the possible channel allocation schemes and asymmetry coefficients between Alice's L_a and Bob's L_b paths $R_{\text{asym}} = L_a/L_b$.

Similarly to the work [21], four allocation schemes for the quantum channel located in C-band and O-band of the telecommunication window were considered. The criterion and complete explanation for such a choice is provided in detail in the works [22,23]. The final choice of the configurations considered in the further numerical simulations is given in Table 1.

The parameters of the DWDM system are the following: $\xi = 0.18$ dB/km, $\Delta\lambda = 15$ GHz, $N_{ch} = 10$ or 40 , $R_x = -32$ dBm and IL = 8 dB.

TABLE 1. Description of the optimal configurations chosen for numerical simulations

Configuration	Number of channels	Quantum channel wavelength, nm
Configuration 1	10	1536.61
Configuration 2	10	1310
Configuration 3	40	1537.40
Configuration 4	40	1310

As for the asymmetry coefficient R_{asym} , three different relations are address here: a symmetric (i.e., $L_a/L_b = 1$) and two asymmetric realizations ($L_a/L_b = 3/2$ and $L_a/L_b = 2/1$).

5. Results and discussion

Using the mathematical models for the MDI CV-QKD secure key generation rate, SpRS, FWM, and LCXT noises, the realization of the system depicted in Fig. 1 was numerically simulated. The results are presented in Fig. 2.

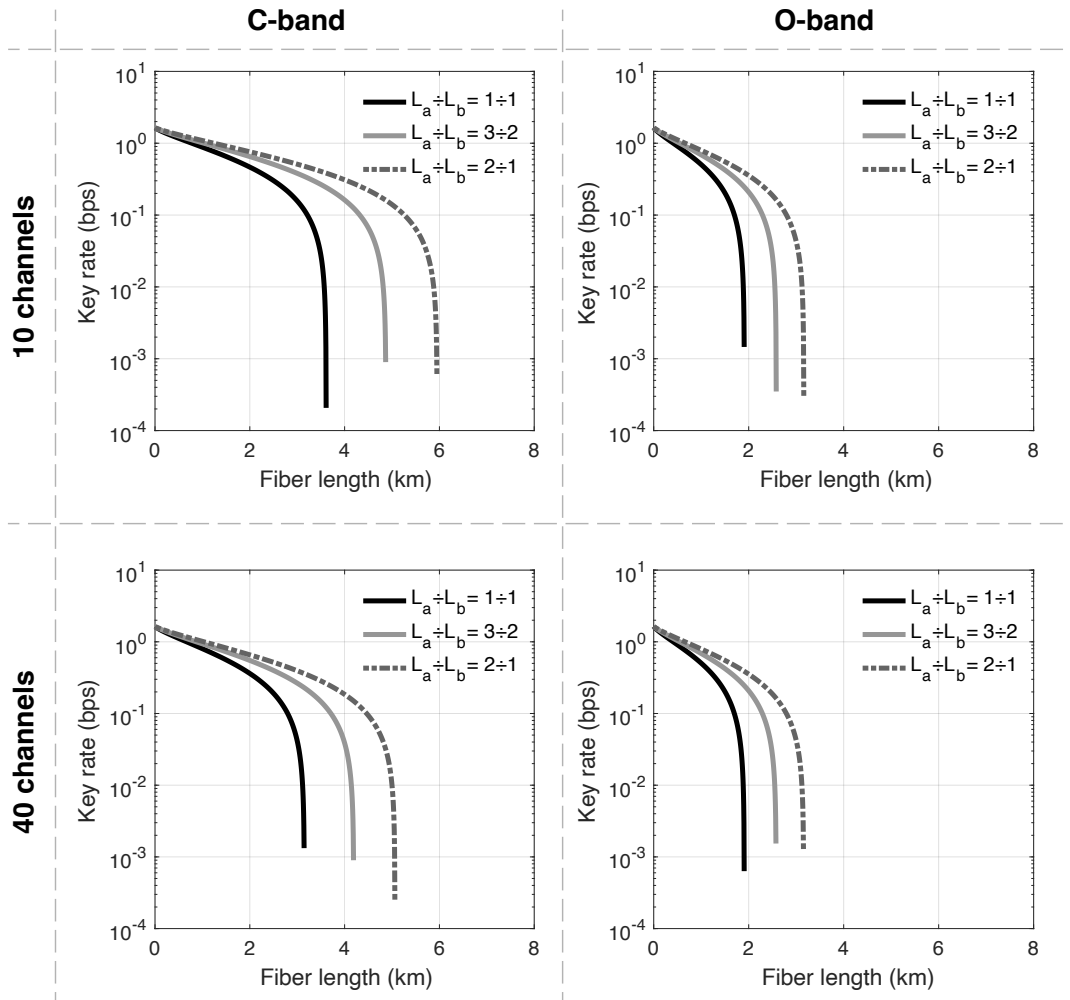


FIG. 2. The dependence of the secure key generation rate on the optical fiber length for MDI CV-QKD system corresponding to the scheme in Fig. 1.

It is a known fact that for MDI CV-QKD systems the secure key generation rate decreases dramatically as the system approaches its symmetry ($L_a = L_b$), with the best result corresponding to the situation when one of the paths equals zero [24].

The results obtained confirm the stated conclusion, as the maximal achievable distance increases together with the system's paths asymmetry.

Interestingly, for the case of MDI CV-QKD, configurations for which the quantum channel is located in the C-band appeared to be more efficient in terms of their maximal achievable distances. For most cases, configurations with O-band-located quantum channel are more beneficial (MDI QKD as well, see [22]), as FWM noise does not contribute to the overall losses. Though the overall contribution of channel noises here is less for such cases too, fiber attenuation for the quantum channel wavelength of 1310 nm surpasses them significantly. It can be seen also that the maximum achievable distances do not exceed 6 km, thus, the secure key distribution over long distances is not possible here. Still, such realizations can be utilized for short-distance communication.

Regarding the number of information channels (10 and 40 in the work), for a larger number of information channels, a decrease in the maximal achievable distances takes place. This is a natural observation, as the more information channels are there in the system, the greater is the value of the overall channel losses. The decrease is substantial for C-band configurations, whereas is quite small in case of O-band.

6. Conclusion

In this work, the MDI CV-QKD protocol was addressed. A theoretical research and numerical simulation of the noise influence caused by SpRS, FWM, and LCXT effects on the performance of the MDI CV-QKD system performance was analyzed for a proposed practical realization scheme, in terms of channel allocation and the paths' asymmetry coefficient. Increasing the number of information channels naturally leads to a decrease in the maximal achievable distances. In addition, the allocation of a wavelength of 1310 nm for a quantum channel results in the shortening of maximal distance values for MDI CV-QKD, regardless of the fact the overall channel noise is less for such configurations. The superior contribution comes from the fiber attenuation, which is larger for the wavelength of 1310 nm. It was confirmed that the more asymmetric are the paths for the MDI CV-QKD scheme, the more efficient is the systems. Moreover, MDI CV-QKD realizations feature significantly shorter maximal achievable distances, that do not exceed several kilometers and can be utilized for short-distance information transmission only. The results obtained can be used in terms of practical implementation of MDI CV-QKD systems, so that to obtain optimal results.

References

- [1] Scarani V., Bechmann-Pasquinucci H., J Cerf N., Dušek M., Lütkenhaus N., Peev M. The security of practical quantum key distribution. *Reviews of Modern Physics*, 2009, **81** (3), P. 1301–1350.
- [2] Pirandola S., Andersen U.L., Banchi L., Berta M., Bunandar D., Colbeck R., Englund D., Gehring T., Lupo C., Ottaviani C., Pereira J.L. Advances in quantum cryptography. *Advances in Optics and Photonics*, 2020, **12** (4), P. 1012–1236.
- [3] Gisin N., Ribordy G.G., Tittel W., Zbinden H. Quantum cryptography. *Reviews of Modern Physics*, 2002, **74** (1), P. 145–196.
- [4] Grosshans F., Van Assche G., Wenger J., Brouri R., Cerf N.J., Grangier P. Quantum key distribution using gaussian-modulated coherent states. *Nature*, 2003, **421** (1), P. 238–241.
- [5] Lo H.-K., Curty M., Qi B. Measurement-Device-Independent Quantum Key Distribution. *Physical Review Letters*, 2012, **108** (3), 130503.
- [6] Mlejnek M., Kaliteevskiy N., Nolan D.A. Reducing spontaneous Raman scattering noise in high quantum bit rate QKD systems over optical fiber, 2017, URL: <https://arxiv.org/ftp/arxiv/papers/1712/1712.05891.pdf>.
- [7] Ma X., Razavi M. Alternative schemes for measurement-device-independent quantum key distribution. *Physical Review A*, 2012, **86** (6), 62319.
- [8] Papanastasiou P., Ottaviani C., Pirandola S. Finite-size analysis of measurement-device-independent quantum cryptography with continuous variables. *Physical Review A*, 2017, **96** (10), 042332.
- [9] Lupo C., Ottaviani C., Papanastasiou P., Pirandola S. Continuous-variable measurement-device-independent quantum key distribution: Composable security against coherent attacks. *Physical Review A*, 2018, **97** (5), P. 1–10.
- [10] Weedbrook C., Lance A.M., Bowen W.P., Symul T., Ralph T.C., Lam P.K. Quantum Cryptography Without Switching. *Physical Review Letters*, 2004, **93** (10), 170504.
- [11] Grosshans F., Cerf N.J., Wenger J., Tualle-Brouri R., Grangier P. Virtual Entanglement and Reconciliation Protocols for Quantum Cryptography with Continuous Variables. *Quantum Information and Computation*, 2003, **3** (7), P. 535–552.
- [12] Laudenbach F., Pacher C., Fung C.-H.F., Poppe A., Peev M., Schrenk B., Hentschel M., Walther P., Übel H. H. Continuous-Variable Quantum Key Distribution with Gaussian Modulation-The Theory of Practical Implementations. *Advanced Quantum Technologies*, 2018, **1** (8), 1800011.
- [13] Devetak I., Winter A. Distillation of secret key and entanglement from quantum states. *Proceedings of the Royal Society A: Mathematical, Physical and Engineering Sciences*, 2005, **461** (1), P. 207–235.
- [14] Pirandola S., Mancini S., Lloyd S., Braunstein S.L. Continuous-variable quantum cryptography using two-way quantum communication. *Nature Physics*, 2008, **4** (9), P. 726–730.
- [15] Lin R., Chen J. Minimizing spontaneous Raman scattering noise for quantum key distribution in WDM network. *Optical Fiber Communication Conference, Optica Publishing Group*, 2021, F4E–6.
- [16] Cai C., Sun Y., Ji Y. Intercore spontaneous raman scattering impact on quantum key distribution in multicore fiber. *New Journal of Physics*, 2020, **22** (8), 083020.
- [17] Eraerds P., Walenta N., Legre M., Gisin N., Zbinden H. Quantum key distribution and 1 Gbps data encryption over a single fibre. *New Journal of Physics*, 2010, **12** (6), 063027.
- [18] Boyd R.W. *Nonlinear Optics*. 4th Edition. Elsevier, Amsterdam, 2019.
- [19] Lin Q., Yaman F., Agrawal G.P. Photon-pair generation in optical fibers through four-wave mixing: Role of Raman scattering and pump polarization. *Physical Review A*, 2007, **75** (1), 023803.
- [20] Hill A.-M., Payne D. B. Linear crosstalk in wavelength-division-multiplexed optical-fiber transmission systems. *Journal of Lightwave Technology*, 1985, **3** (3), P. 643–651.

- [21] Vorontsova I, Goncharov R., Tarabrina A., Kiselev F., Egorov V. Theoretical analysis of quantum key distribution systems when integrated with a DWDM optical transport network. *Journal of the Optical Society of America B*, 2023, **40** (1), P. 63–71.
- [22] Vorontsova I, Goncharov R., Tarabrina A., Tupyakov D., Bolychev E., Smirnov S., Kiselev F., Egorov V. Theoretical analysis of measurement-device-independent quantum key distribution systems integrated into fiber-optic communication lines using dense wavelength division multiplexing. *Journal of Optical Technology*, 2022, **89** (7), P. 424–429.
- [23] Tarabrina A., Tupyakov D., Vorontsova I, Goncharov R., Zinovev A., Smirnov S., Kiselev F., Egorov V. Application of optimization methods to minimize noise in quantum key distribution systems integrated into fiber-optic communication lines using dense wavelength division multiplexing. *Journal of Optical Technology*, 2022, **89** (9), P. 549–554.
- [24] Li Z., Zhang Y.-C., Xu F., Peng X., Guo H. Continuous-variable measurement-device-independent quantum key distribution. *Physical Review A*, 2014, **89** (5), 052301.

Submitted 3 March 2023; revised 11 March 2023; accepted 12 March 2023

Information about the authors:

Irina Vorontsova – ITMO University, Kronverkskiy, 49, St. Petersburg, 197101, Russia; ORCID 0000-0001-9861-0816; iovorontsova@itmo.ru

Roman Goncharov – ITMO University, Kronverkskiy, 49, St. Petersburg, 197101, Russia; ORCID 0000-0002-9081-8900; rkgoncharov@itmo.ru

Sergey Kynev – ITMO University, Kronverkskiy, 49, St. Petersburg, 197101, Russia; SMARTS-Quanttelecom LLC, 6th Vasilyevskogo Ostrova Line, 59, St. Petersburg, 199178, Russia; ORCID 0000-0001-8698-1804; sergey.kynev@itmo.ru

Fedor Kiselev – ITMO University, Kronverkskiy, 49, St. Petersburg, 197101, Russia; SMARTS-Quanttelecom LLC, 6th Vasilyevskogo Ostrova Line, 59, St. Petersburg, 199178, Russia; ORCID 0000-0002-3894-511X; fdkiselev@itmo.ru

Vladimir Egorov – ITMO University, Kronverkskiy, 49, St. Petersburg, 197101, Russia; SMARTS-Quanttelecom LLC, 6th Vasilyevskogo Ostrova Line, 59, St. Petersburg, 199178, Russia; ORCID 0000-0003-0767-0261; viegorov@itmo.ru

Conflict of interest: the authors declare no conflict of interest.

Single-step lithography-free fabrication of nanoscale broadband radiation sources

Eduard I. Ageev¹, Sergej V. Koromyslov¹, Mikhail A. Gremilov², Denis V. Danilov³, Elena A. Petrova¹, Ivan I. Shishkin¹, Dmitry A. Zuev¹

¹ITMO University, St. Petersburg, Russia

²St. Petersburg Polytechnic University of Peter the Great, St. Petersburg, Russia

³St. Petersburg State University, St. Petersburg, Russia

Corresponding author: Eduard I. Ageev, eiageev@itmo.ru

PACS 42.62.-b, 42.79.-e, 78.55.-m, 78.67.-n

ABSTRACT In this paper, we present a one-stage method for fabricating hybrid metal-dielectric nanostructures without the use of complex and expensive lithographic processes. The formation of arrays of nanoparticles occurs in the process of irradiation of a two-layer gold-silicon film with simultaneous mixing of materials. In this work, the internal structure of the obtained nanoparticles was studied using the methods of transmission scanning electron microscopy and energy-dispersive X-ray spectroscopy, and their broadband photoluminescence in the range of 450 – 900 nm was also demonstrated. These structures are promising as a source of radiation for optical measurements in lab-on-a-chip devices, which was shown by measuring the transmission spectrum of the Rhodamine B dye as an example.

KEYWORDS hybrid nanoparticles, broadband photoluminescence, laser-induced nanoparticles, dewetting, bi-layer gold-silicon films

ACKNOWLEDGEMENTS This work was supported by the Russian Science Foundation (Grant No. 19-79-10259, <https://rscf.ru/project/19-79-10259/>). SEM and STEM studies were carried out on the basis of the Interdisciplinary Resource Center for Nanotechnology, Research Park, St. Petersburg State University.

FOR CITATION Ageev E.I., Koromyslov S.V., Gremilov M.A., Danilov D.V., Petrova E.A., Shishkin I.I., Zuev D.A. Single-step lithography-free fabrication of nanoscale broadband radiation sources. *Nanosystems: Phys. Chem. Math.*, 2023, **14** (3), 349–353.

1. Introduction

Hybrid nanostructures consisting of semiconductor materials with a high refractive index and low optical losses and noble metals, in which there are resonant oscillations of free electron plasma, have been actively studied in recent years for various applications in such areas as sensorics, optoelectronics, and nanophotonics [1–5].

Lab-on-a-chip devices [6] are currently being used to diagnose, monitor, and treat chronic diseases that require economically relevant and clinically accurate measurement of various biomarkers, such as IFN- γ -induced protein 10 (IP-10) for the diagnosis of rheumatoid arthritis, serum antibodies for the diagnosis of kidney disease, serum glucose concentrations for the diagnosis and monitoring of diabetes mellitus (type I and II). Currently, such measurements are carried out using enzyme immunoassay, chromatography, mass spectrometry, gel electrophoresis and polymerase chain reaction [8–10]. The disadvantages of such approaches are: a long time for the study, the need to transport the patient to the biomaterial collection point, the high cost of the study, and the need for special skills to conduct the study. The main advantages of lab-on-a-chip technology over traditional analytical detection methods include: lower liquid consumption, which reduces the cost of reagents and sample volume for analysis, faster analysis time due to better controlled liquid transfer and high surface to volume, more compact implementation and higher performance. However, to carry out efficient optical measurements in such devices, a miniature radiation source with characteristic dimensions less than 1 μm and emitting in the visible spectral range is required.

The creation of such a source based on silicon, due to its high compatibility with existing microelectronics technologies, is limited by the indirect gap structure of the material, which does not allow obtaining a quantum yield of emitters above 10^{-4} [11]. Nanoscale sources of gold or silver nanoparticles (NPs) also do not have high efficiency due to heating losses [12].

Obtaining emitters with high efficiency has become possible through the use of hybrid materials consisting of a mixture of gold and silicon. Silicon inclusions in metal structures lead to an increase in the spontaneous emission of a quantum system, which increases the efficiency of nanoscale light sources [13]. In particular, it has recently been demonstrated that optically resonant Au@Si hybrid nanostructures can be used as efficient nanoscale sources of white light and higher harmonics [2, 14, 15], as well as optical nanoantennas, which make it possible to enhance the photoluminescence (PL) of attached quantum emitters due to the Purcell effect [16, 17].

The fabrication of such nanoparticles (NPs) can be implemented using the methods of electron beam lithography [18], the formation of eutectic alloys [19,20], as well as laser printing methods [14,21], due to ablation in various media [22,23], irradiation of suspended particles in a liquid or combined methods, including an additional stage of chemical reduction using HAuCl_4 solution [4].

However, the methods listed above either have a high cost and labor intensiveness, or do not allow control over the size and location of the obtained NPs. In this paper, we present a method for fabricating metal-dielectric nanostructures, study their optical and material properties, and demonstrate the possibility of their use as a microsized emitter with an operating range of 450 – 900 nm.

2. Materials and methods

2.1. Fabrication of hybrid structures

For the fabrication of hybrid structures, two-layer films are used. The production of the film take place in two stages: a silicon layer of 100 nm thickness are deposited on a glass substrate by chemical vapor deposition, then 10 nm gold layer is deposited over the silicon by magnetron sputtering.

To form structures, the film surface was scanned by a laser beam with a wavelength of (790 ± 5) nm, a pulse duration of 100 fs, and a pulse repetition rate of 80 MHz from the silicon side along a circular path with a radius of $1.3 \mu\text{m}$. As a result, a hybrid structure is formed in the center of the irradiated region. The optimal regime for fabrication of ordered arrays was determined during preliminary experiments [15], and corresponds to a scanning speed of 30 mm/s and a laser fluence of 160 mJ/cm^2 for a two-layer Au (10 nm)/Si (100 nm) film, placed on a glass substrate.

2.2. Characterization of obtained structures

The fabricated structures are characterized using scanning electron microscopy (SEM), scanning transmission electron microscopy (STEM), and energy dispersive X-ray spectroscopy (EDS). SEM images are obtained using an Inspect microscope (FEI Company, USA) in the secondary electron recording mode with an accelerating voltage of 20 kV. STEM and EDS studies are carried out on a Libra200FE microscope (Zeiss, Germany) with an accelerating voltage of 200 kV. To study and analyze the resulting hybrid structures using STEM, lamellae is fabricated using a focused ion beam of gallium ions using a Zeiss Auriga Laser dual-beam workstation.

The optical properties of hybrid nanoparticles are also studied by photoluminescent spectroscopy. To excite and record optical responses, we use an experimental setup including a TEMA-150 femtosecond ytterbium laser (Avesta, Russia) and a Horiba LabRAM HR confocal spectrometer with a CCD detector DU 420A-OE 325 (Andor, Great Britain). Thorlabs optical filters are inserted in the optical path of the measuring setup to separate laser radiation from radiation of pump diode (FELH1000) and to block residual laser radiation before the detector (FESH1000). The radiation is focused and the signal was collected using a Mitutoyo NIR M Plan Apo M 50x objective, $\text{NA} = 0.65$.

3. Results and discussion

Figure 1a shows an ordered array of spherical NPs with a characteristic size of about $1 \mu\text{m}$. The results of the analysis of the elemental composition in Fig.1b show that silicon spheroids coated with a gold network and smaller gold NPs with diameters of about 20 – 40 nm appear during fabrication.

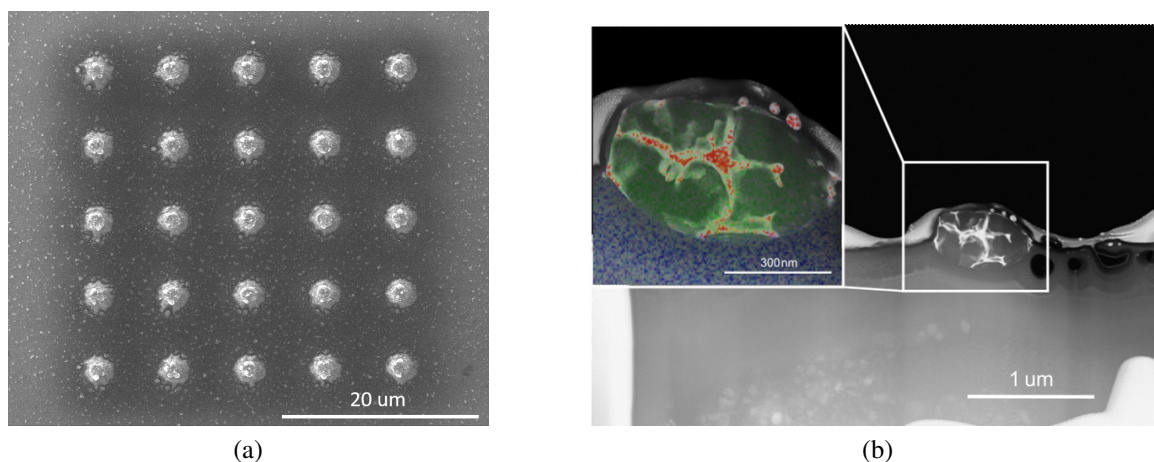


FIG. 1. (a) – SEM image of the array of obtained NPs. (b) – STEM image of a NP cross section; the inset shows a map of the elemental composition of a hybrid NP: red areas correspond to gold, green areas to silicon, blue areas to oxygen, and light gray areas to platinum and gold. Dark cavities in the near-surface region are voids.

The appearance of such hybrid structures presumably occurs when a thin film breaks up into particles as a result of heating in an oven or local exposure to laser radiation [24] with simultaneous mixing of gold and silicon Fig. 1b. Previously, silicon [26] and gold [25] nanoparticles were obtained by this method.

Figure 2 shows the photoluminescence spectrum of a single particle, showing the photoluminescence (PL) in the range from 450 to 900 nm, as well as the spectrum of the original film for comparison. To determine the PL mechanism, we plot the dependence of the PL intensity on the pump fluence (inset in Fig. 2 on a log-log scale. From the slope of the line, one can say that PL occurs as a result of two-photon absorption. Amplification of radiation in hybrid nanostructures consisting of silicon bound to the plasmonic part mainly occurs due to multiphoton absorption in the silicon part, while “hot” charge carriers generated in gold located on the surface of the silicon spheroid can be injected into silicon due to the tunneling effect, providing an increase in the efficiency of PL [27].

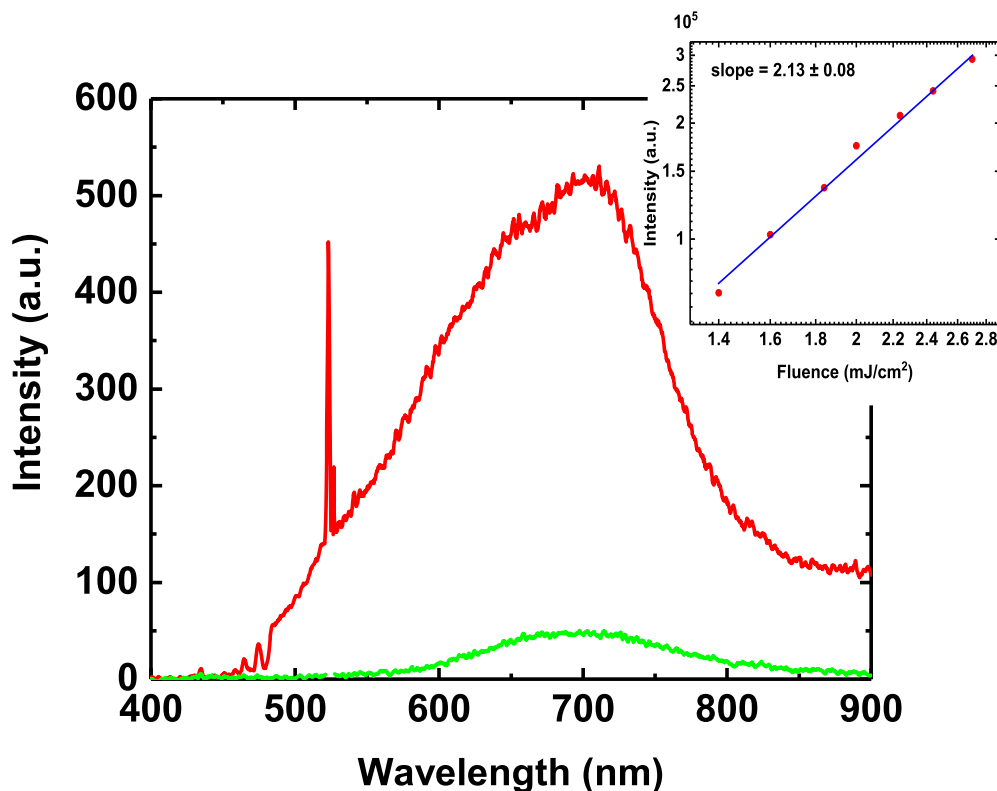


FIG. 2. PL spectra of the hybrid particle (red) and the original film (green). The inset shows the dependence of the broadband PL intensity on the pump fluence.

To demonstrate the possibility of using hybrid particles as a source of broadband radiation, the transmission spectrum of the Rhodamine B dye is measured. In the first case, a compact stabilized halogen light source with a fiber output (Avantes AvaLight-HAL-S-Mini) is used as a radiation source (Fig. 3a), and in the second, the PL emission of the hybrid particle (Fig. 3b). The radiation from the source passed through the cell with the dye and then was detected by the spectrometer.

As can be seen from Figure 3, the obtained transmission spectra are in good agreement, which proves the applicability of hybrid microstructures in the implementation of a nanospectrometer.

4. Conclusion

In this work, using femtosecond laser radiation, we experimentally demonstrate the creation of hybrid metal-dielectric nanostructures without the use of complex and expensive nanolithography methods. The formation of arrays of nanoparticles occurs in the process of irradiation of a two-layer gold-silicon film along a circular trajectory. Using the methods of transmission scanning electron microscopy and energy-dispersive X-ray spectroscopy, the internal structure of the obtained nanoparticles was studied. The obtained nanostructures consist of a mixture of gold and silicon and exhibit broadband photoluminescence in the range of 450 – 900 nm. It is also shown, using the example of measuring the transmission spectrum of the Rhodamine B dye, that such a structure can act as a radiation source for optical measurements in lab-on-a-chip devices.

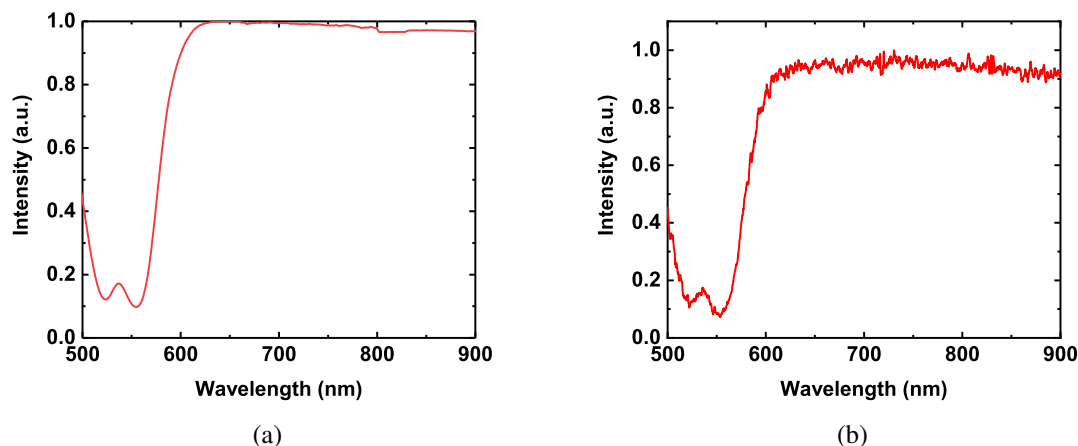


FIG. 3. Transmission spectra of the Rhodamine B dye obtained using a halogen lamp (a) and a hybrid particle (b)

References

- [1] Jiang R., Li B., Fang C., Wang J. Metal/semiconductor hybrid nanostructures for plasmon-enhanced applications. *Advanced materials*, 2014, **26**, P. 5274–5309.
- [2] Makarov S., Sinev I., Milichko V., Komissarenko F., Zuev D., Ushakova E., Mukhin I., Yu Y., Kuznetsov A., Belov P., et al. Nanoscale generation of white light for ultrabroadband nanospectroscopy. *Nano letters*, 2018, **18**, P. 535–539.
- [3] Lebedev D., Shkoldin V., Mozharov A., Larin A., Permyakov D., Samusev A., Petukhov A., Golubok A., Arkhipov A., Mukhin I. Nanoscale Electrically Driven Light Source Based on Hybrid Semiconductor/Metal Nanoantenna. *The Journal of Physical Chemistry Letters*, 2022, **13**, P. 4612–4620.
- [4] Gurbatov S., Puzikov V., Storozhenko D., Modin E., Mitsai E., Cherepakhin A., Shevlyagin A., Gerasimenko A., Kulinich S., Kuchmizhak A. Multigram-Scale Production of Hybrid Au–Si Nanomaterial by Laser Ablation in Liquid (LAL) for Temperature-Feedback Optical Nanosensing, Light-to-Heat Conversion, and Anticounterfeit Labeling. *Appl. Mater. Interfaces*, 2023, **15**, P. 3336–3347.
- [5] Guo H., Hu Q., Zhang C., Liu H., Wu R., Pan S. Strong Plasmon-Mie Resonance in SiPd Core- Ω Shell Nanocavity. *Materials*, 2023, **16**, 1453.
- [6] Wu J., Dong M., Rigatto C., Liu Y., Lin F. Lab-on-chip technology for chronic disease diagnosis. *NPJ Digital Med.*, 2018, **1**, P. 1–11.
- [7] Rezaei S.D., Dong Z., Chan Y.E., Trisno J., Ng R.J.H., Ruan Q., Qiu C.-W., Mortensen N.A., Yang J.K.W. Nanophotonic Structural Colors. *ACS Photonics*, 2020, **8**, P. 18–33.
- [8] De La Rica R., Stevens M. Plasmonic ELISA for the ultrasensitive detection of disease biomarkers with the naked eye. *Nature nanotechnology*, 2012, **7**, P. 821–824.
- [9] Diamandis E.P. Mass Spectrometry as a Diagnostic and a Cancer Biomarker Discovery Tool: Opportunities and Potential Limitations. *Molecular & Cellular Proteomics*, 2004, **3**, P. 367–378.
- [10] Loonen A.J.M., Schuurman R., van den Brule A.J.C. Highlights from the 7th European Meeting on Molecular Diagnostics. *Expert review of molecular diagnostics*, 2012, **12**, P. 17–19.
- [11] Cho C.-H., Aspetti C.O., Park J., Agarwal R. Silicon coupled with plasmon nanocavities generates bright visible hot luminescence. *Nature photonics*, 2013, **7**, P. 285–289.
- [12] Bouhelier A., Beversluis M., Novotny L. Characterization of nanoplasmonic structures by locally excited photoluminescence. *Applied Physics Letters*, 2003, **83**, P. 5041–5043.
- [13] Lepeshov S., Krasnok A., Belov P., Miroshnichenko A. Hybrid nanophotonics *Physics–Uspekhi*, 2019, **61**, 1035.
- [14] Larin A., Nomine A., Ageev E., Ghanbaja J., Kolotova L., Starikov S., Bruy'ere S., Belmonte T., Makarov S., Zuev D. Plasmonic nanosponges filled with silicon for enhanced white light emission. *Nanoscale*, 2020, **12**, P. 1013–1021.
- [15] Koromyslov S., Ageev E., Ponkratova E., Larin A., Shishkin I., Danilov D., Mukhin I., Makarov S., Zuev D. Femtosecond Laser-Assisted Formation of Hybrid Nanoparticles from Bi-Layer Gold-Silicon Films for Microscale White-Light Source. *Nanomaterials*, 2022, **12**, 1756.
- [16] Dmitriev P., Lassalle E., Ding L., Pan Z., Neo D., Valuckas V., Paniagua-Dominguez R., Yang J., Demir H., Kuznetsov A. Hybrid Dielectric-Plasmonic Nanoantenna with Multiresonances for Subwavelength Photon Sources. *ACS Photonics*, 2023, **10**, P. 582–594.
- [17] Tiwari S., Taneja C., Sharma V., Vasista A., Paul D., Kumar G. Dielectric Microsphere Coupled to a Plasmonic Nanowire: A Self-Assembled Hybrid Optical Antenna. *Adv. Opt. Mater.*, 2020, **8**, 1901672.
- [18] Zuev D., Makarov S., Mukhin I., Milichko V., Starikov S., Morozov I., Shishkin I., Krasnok A., Belov P. Fabrication of Hybrid Nanostructures via Nanoscale Laser-Induced Reshaping for Advanced Light Manipulation. *Advanced Materials*, 2016, **28**, P. 3087–3093.
- [19] Adachi N.N. Eutectic reaction of gold thin-films deposited on silicon surface. *Surface science*, 2002, **506**, P. 305–312.
- [20] Ruffino F., Pugliara A., Carria E., Romano L., Bongiorno C., Spinella C., Grimaldi M. Novel approach to the fabrication of Au/silica core-shell nanostructures based on nanosecond laser irradiation of thin Au films on Si. *Nanotechnology*, 2012, **23**, 045601.
- [21] Zhigunov D., Evlyukhin A., Shalin A., Zywieta U., Chichkov B. Femtosecond Laser Printing of Single Ge and SiGe Nanoparticles with Electric and Magnetic Optical Resonances. *ACS Photonics*, 2018, **5**, P. 977–983.
- [22] Kucherik A., Kutrovskaya S., Osipov A., Gerke M., Chestnov I., Arakelian S., Shalin A., Evlyukhin A., Kavokin A. Nano-Antennas Based on Silicon-Gold Nanostructures. *Scientific Reports*, 2019, **9**, P. 1–6.
- [23] Al-Kattan A., Tselikov G., Metwally K., Popov A., Mensah S., Kabashin A. Laser Ablation-Assisted Synthesis of Plasmonic Si@Au Core-Satellite Nanocomposites for Biomedical Applications. *Nanomaterials*, 2021, **11**, 592.
- [24] Ye J., Zuev D., Makarov S. Dewetting mechanisms and their exploitation for the large-scale fabrication of advanced nanophotonic systems. *Int. Materials Reviews*, 2019, **64**, P. 439–477.

- [25] Makarov S.V., Milichko V.A., Mukhin I.S., Shishkin I.I., Zuev D.A., Mozharov A.M., Krasnok A.E., Belov P.A. Controllable femtosecond laser-induced dewetting for plasmonic applications. *Laser Photonics Rev.*, 2016, **10**, P. 91–99.
- [26] Syubaev S., Mitsai E., Starikov S., Kuchmizhak A. Laser-printed hemispherical silicon Mie resonators. *Optics Letters*, 2021, **46**, P. 2304–2307.
- [27] Zhang C., Xu Y., Liu J., Li J., Xiang J., Li H., Li J., Dai Q., Lan S., Miroshnichenko A.E. Lighting up silicon nanoparticles with Mie resonances. *Nat. Commun.*, 2018, **9**, P. 1–7.

Submitted 5 April 2023; revised 23 April 2023; accepted 24 April 2023

Information about the authors:

Eduard I. Ageev – ITMO University, Kronverkskiy, 49, St. Petersburg, 197101, Russia; ORCID 0000-0001-5626-7677; eiageev@itmo.ru

Sergej V. Koromyslov – ITMO University, Kronverkskiy, 49, St. Petersburg, 197101, Russia; sergej.koromyslov@metalab.ifmo.ru

Mikhail A. Gremilov – St. Petersburg Polytechnic University of Peter the Great, Polytechnicheskaya, 29, St. Petersburg, 195251, Russia; mihail.gremilov@mail.ru

Denis V. Danilov – St. Petersburg State University, Universitetskaya Emb., 7/9, St. Petersburg, 199034, Russia; ORCID 0000-0002-4422-0684; d.danilov@spbu.ru

Elena A. Petrova – ITMO University, Kronverkskiy, 49, St. Petersburg, 197101, Russia; elena.petrova@metalab.ifmo.ru

Ivan I. Shishkin – ITMO University, Kronverkskiy, 49, St. Petersburg, 197101, Russia; ORCID 0000-0002-2330-0159; i.shishkin@metalab.ifmo.ru

Dmitry A. Zuev – ITMO University, Kronverkskiy, 49, St. Petersburg, 197101, Russia; ORCID 0000-0001-9157-5683; d.zuev@metalab.ifmo.ru

Conflict of interest: the authors declare no conflict of interest.

Synthesis of $\text{PbFe}_{2.4}\text{X}_{2.4}\text{Y}_{2.4}\text{Ga}_{2.4}\text{In}_{2.4}\text{O}_{19}$ high-entropy oxides with the magnetoplumbite structure

Olga V. Zaitseva, Evgeny A. Trofimov, Vladimir E. Zhivulin, Ahmad Ostovari Mogaddam, Olga V. Samoilova, Ksenia S. Litvinyuk, Alena R. Zykova, Dmitry V. Mikhailov, Svetlana A. Gudkova, Denis A. Vinnik

South Ural State University, Chelyabinsk, Russia

Corresponding author: Denis A. Vinnik, vinnikda@susu.ru

ABSTRACT The purpose of this study is to obtain high-entropy oxides with the magnetoplumbite structure, in which the Pb cation is used as a divalent metal cation. The synthesis conditions were optimized, and a technique was developed to avoid the evaporation of lead oxide. For the first time, single-phase samples of high-entropy oxides with the magnetoplumbite structure were obtained, its chemical composition is reflected by the formula $\text{PbFe}_{2.4}\text{X}_{2.4}\text{Y}_{2.4}\text{Ga}_{2.4}\text{In}_{2.4}\text{O}_{19}$. The particle size of the high-entropy phase is about 100 nm, which makes it promising for a number of applications. The effect of preliminary grinding of the initial components on the results of synthesis was studied. A synthesis mechanism is proposed. The results pave the way to synthesis and study of the properties of a new large subgroup of high-entropy oxides with the magnetoplumbite structure, which expands the possibilities of controlling the properties of ceramic magnetic materials.

KEYWORDS high-entropy oxides, magnetoplumbite, lead, nanocrystals, structure, synthesis, magnetic materials

ACKNOWLEDGEMENTS This work was supported by the Russian Science Foundation (project No. 18-73-10049).

FOR CITATION Zaitseva O.V., Trofimov E.A., Zhivulin V.E., Ostovari Mogaddam A., Samoilova O.V., Litvinyuk K.S., Zykova A.R., Mikhailov D.V., Gudkova S.A., Vinnik D.A. Synthesis of $\text{PbFe}_{2.4}\text{X}_{2.4}\text{Y}_{2.4}\text{Ga}_{2.4}\text{In}_{2.4}\text{O}_{19}$ high-entropy oxides with the magnetoplumbite structure. *Nanosystems: Phys. Chem. Math.*, 2023, **14** (3), 354–362.

1. Introduction

Ferrites with the magnetoplumbite structure (with the space group $P6_3/mmc$) have been successfully used for a long time in the manufacturing of high-frequency transformers, fabricating of microwave electronic devices, and manufacturing of magnetic memory devices. They are also used in the manufacturing of functional sensors, as well as for the production of plastoferrites, magnetic fluids, permanent magnets, and multiferroics [1–14]. All these are possible due to the unique structural and magnetic properties of ferrites with the magnetoplumbite structure, as well as their mechanical, chemical and thermal resistance.

The level of development of modern technology imposes ever more stringent requirements on the materials used for manufacturing of devices. Such requirements for the performance of materials with the magnetoplumbite structure led to the idea of replacing some of the iron atoms in their structure with atoms of other elements. It was found that such a substitution leads to a change not only in the characteristics of the crystal lattice, but also in the properties of the resulting material, including changes in the magnitude of the coercive force, the Curie temperature, and the degree of uniaxial magnetic anisotropy. Thus, atomic substitution allows one to regulate the properties of materials in the required directions owing to the controlled changes in the qualitative and quantitative composition of dopants.

To date, a large number of works have been devoted to the study of the effect of Fe^{3+} ions substitution in the parent ferrites having a magnetoplumbite structure with the cations of other (most often, trivalent) metals. The elements acting as dopants include gallium [15], aluminum [16, 17], chromium [18], tin [4], indium [19], titanium [20], etc. Quite often, cobalt acts as a doping element [21].

However, the solubility of individual dopant elements in the ferrite structure and the ability of their atoms to occupy iron positions is, as a rule, limited. There are applications that require ceramics with a magnetoplumbite structure and a high (more than 50 at.%) degree of replacement of iron atoms by atoms of other elements. Obtaining such structures with one iron-replacing element is not feasible for all possible dopants. However, the formation of stable crystal structures with a high level of dopants can be facilitated by the high configurational entropy of mixing of the sublattice components, which is formed by iron atoms in magnetoplumbite and similar substances. High values of this quantity increase the entropy of the oxide phase as a whole, resulting in a decrease in its Gibbs free energy, and consequently, make the formation and existence of such a single-phase oxide more thermodynamically probable than the emergence of other substances from the same elements.

The concept of high-entropy phases arose in early 21st century, primarily in relation to metallic materials (such work is still relevant today, for example [22]), but since 2015 this concept has been actively and effectively developed for obtaining new nonmetallic phases (for example [23]) including ceramic phases. To date, high-entropy oxides (HEO) with various structures (such as spinel structure [24], perovskite structure [25], garnet structure [26], etc.) have been obtained. In our work, for the first time, stable high-entropy oxides with the magnetoplumbite structure were obtained [27–31], in which the iron ions were replaced mainly by ions of trivalent elements or pairs of bi- and tetravalent elements (to maintain electronic balance). An assessment is made of how the change in the entropy of mixing correlates with the changes in electrical and magnetic properties of a number of representatives of this new group of materials.

Previous studies [14] indicated that properties of oxide materials with the magnetoplumbite structure are determined not only by the qualitative and quantitative composition of the sublattice occupied by iron atoms and dopants, but also by the atom constituting a doubly charged cation outside this sublattice [14, 32]. To date, structures with Ba or Sr as such adoubly charged cation have been studied. Expanding the range of possible structures by increasing the number of such elements will increase the possibilities for expanding the range of variation in the magnetic and microwave properties of materials with the magnetoplumbite structure. An obvious candidate for such an element is Pb.

However, attempts to obtain and study high-entropy oxides with the magnetoplumbite structure, in which only lead would act as a divalent element, have so far been unsuccessful. Our attempts to obtain $(Ba,Sr,Pb)M_{12}O_{19}$ structures by solid-phase synthesis route at 1300 – 1400 °C ran into the fact that after calcination at these temperatures for 5 hours (the usual method for obtaining HEO with the magnetoplumbite structure with the participation of divalent metal Ba and Sr) magnetoplumbite structure was absent in the obtained Pb samples. At the same time, our results demonstrate that it is impossible to obtain single-phase HEOs with the magnetoplumbite structure with the participation of Ba or Sr during 5 hours at lower temperatures.

Therefore, the purpose of this study is to obtain HEO with the magnetoplumbite structure, in which Pb is used as a divalent metal cation. Considering the unsuccessful attempts to obtain magnetoplumbite phases at temperatures of 1300 – 1400 °C, it can be assumed that successful synthesis can be carried out at significantly lower temperatures and in a shorter time (to avoid evaporation of lead oxide). In this case, the success of the synthesis can be facilitated by more thorough grinding of the starting components.

A decrease in the synthesis temperature of HEO with the magnetoplumbite structure can facilitate the formation of the target phase in the form of smaller particles than that obtaining in the conventional process. Reducing the particle size down to nanosize, in turn, opens up the possibility of expanding the scope of possible applications of these substances not only as magnetic materials, but also as catalysts for oxidation/reduction processes.

Considering the phase diagram of $PbO-Fe_2O_3$ system [33] (Fig. 1), it can be assumed that during the synthesis, one should focus on the temperatures ranging from 886 – 1315 °C. The first temperature is the melting point of PbO and, at the same time, the minimum temperature at which the melt is in equilibrium with $PbFe_{12}O_{19}$. The second temperature is the temperature of the incongruent decomposition of $PbFe_{12}O_{19}$. Of course, it should be considered that, for high-entropy oxides, the temperatures of the last two processes can differ significantly from the temperatures in the $PbO-Fe_2O_3$ binary system, and that, in order to avoid losses of PbO, one should not increase the temperature above the minimum required for synthesis. Based on these considerations, the temperature regime used in the course of the experimental study was selected.

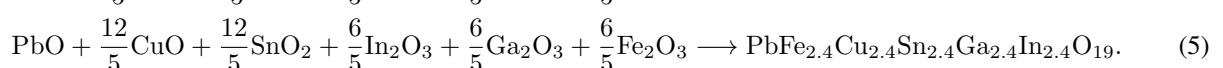
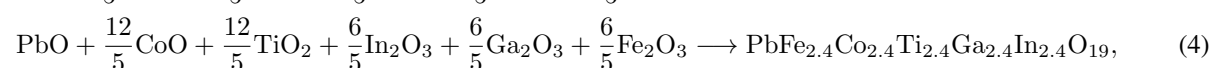
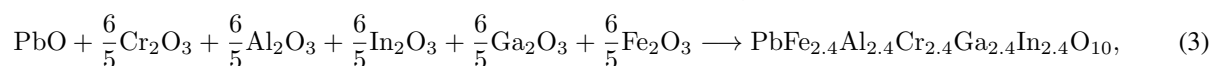
2. Methodology of experimental research

Oxides of iron Fe_2O_3 , aluminum Al_2O_3 , chromium Cr_2O_3 , cobalt CoO , copper CuO , titanium TiO_2 , tin SnO_2 , gallium Ga_2O_3 , indium In_2O_3 , and lead PbO were used as starting components. All components were chemically pure. Table1 shows the chemical formulas of the target compounds and the mass content of the starting components. The compositions are chosen in such a way to ensure the maximum configurational entropy of mixing at the magnetoplumbite sublattice occupied by iron atoms ($\Delta S_{mix(B)}$). According to the formula:

$$\Delta S_{mix(B)} = -R \sum (x_{(B)} \ln x_{(B)}), \quad (1)$$

where $x_{(B)}$ is the atomic ratio of various cations filling sublattice B in $AB_{12}O_{19}$ unit cell, for a sublattice with five components presented in equimolar concentrations, this value is $1.6094R \text{ J/(mol}\cdot\text{K)}$.

The expected chemical reactions can be represented as the following equations:



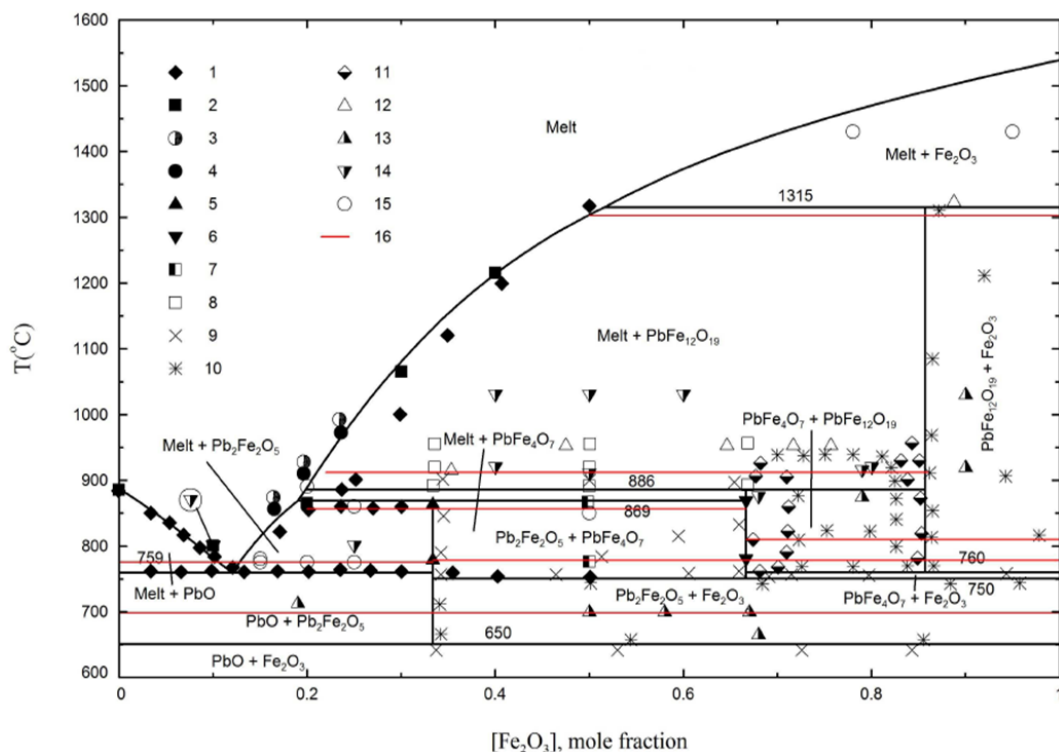


FIG. 1. Phase diagram of the PbO–Fe₂O₃ system [33]. 1 – DTA [34], 2 – DTA [35], 3 and 4 – liquidus temperature data [34], 5 – XRD (Pb₂Fe₂O₅) [34], 6 – XRD (PbFe₄O₇) [34], 7 – XRD (Pb₂Fe₂O₅+PbFe₄O₇) [34], 8 – XRD (PbO+PbFe₁₂O₁₉) [34], 9 and 10 – two solid phases [36], 11 – one solid phase [36], 12 – melt and solid phase [36], 13 – SEM, two solid phases [37], 14 – SEM, melt and solid phase [37], 15 – DTA, [33], 16 – average results DTA, obtained in the work [37]

TABLE 1. Compositions of initial mixtures

#	Chemical formula	Composition, wt. %					
		PbO	Al ₂ O ₃ /CoO/CuO	Cr ₂ O ₃ /TiO ₂ /SnO ₂	Ga ₂ O ₃	In ₂ O ₃	Fe ₂ O ₃
1	PbFe ₁₂ O ₁₉	18.894	—	—	—	—	81.106
2	PbFe _{2.4} Al _{2.4} Cr _{2.4} Ga _{2.4} In _{2.4} O ₁₉	17.736	9.722	14.493	17.874	24.948	15.227
3	PbFe _{2.4} Co _{2.4} Ti _{2.4} Ga _{2.4} In _{2.4} O ₁₉	16.842	13.570	14.466	16.973	23.690	14.460
4	PbFe _{2.4} Cu _{2.4} Sn _{2.4} Ga _{2.4} In _{2.4} O ₁₉	14.817	12.674	24.012	14.933	20.843	12.722

The initial components were weighed according to the stoichiometric ratio and processed in a planetary ball mill at 900 rpm for 5 hours and 10 hours using zirconia-jarand balls. The mixtures of oxides obtained after grinding were pressed into tablets 8 mm in diameter and 2 mm high on a hydraulic laboratory press in a metal mold with a force of 5 t/cm². The weight of the tablets averaged about 1 gram. The obtained samples were placed on a platinum substrate and sintered in a laboratory muffle furnace with ferrochromium heaters. Heating was carried out according to the following scheme: (i) heating to 150 °C and holding at this temperature for 30 minutes, (ii) heating up to 500 °C and holding at this temperature for 30 minutes, (iii) heating up to 800 °C and holding at this temperature for 30 minutes, (iv) heating up to 900 °C and holding at this temperature for 60 minutes, (v) heating up to 1000 °C and holding at this temperature for 120 minutes, (vi) heating up to 1150 °C, holding for 15 minutes and cooling the samples in air. Such a stepwise regime provides gradual access to the temperature range at which PbO melts, other oxides dissolve in the resulting microdroplets, and double oxides form. It was assumed that one-hour exposure at 900 °C allows all or most of the molten PbO to react with the formation of stable binary oxides and this will serve as an obstacle to the evaporation of PbO at higher temperatures. Despite the measures taken, the evaporation of the components of the reaction mixture could become a key problem in the synthesis, therefore, the samples were weighed with an accuracy of 1 mg before and after heat treatment in order to control the results of the synthesis.

The synthesized samples, as a result of the chemical reaction, were studied by X-ray diffraction (XRD), scanning electron microscopy (SEM) equipped with energy dispersive spectroscopy (EDS). X-ray patterns were recorded on a Rigaku Ultima IV powder diffractometer using Cu-K α radiation filtered by a Ni filter. The parameters of the elementary crystal lattice were also calculated from the data of powder X-ray diffraction patterns for samples 2. The calculation was made using the PDXL software package using a full profile analysis according to the Rietveld method. The chemical composition and microstructure were studied on JEOL JSM-7001F and JSM-6460LV scanning electron microscopes equipped with Oxford Instruments energy dispersive analyzers.

3. Results and discussion

The main results of studying the compositions (chemical composition obtained by EDS, and phase analysis determined by XRD) of the obtained samples are presented in Table 2. It also presents the values that characterize the process of obtaining samples: the processing time for the mixture of starting materials in a planetary mill and the weight loss of the samples during the firing process. Comparison of the data presented in Tables 1, 2, as well as X-ray diffraction patterns and SEM images of the obtained material, allows us to come to the following conclusions. In all cases, the obtained samples contain large amount of oxide phases with the magnetoplumbite structure. A correlation is observed between the mass loss of the sample during its calcination and the phase purity of the obtained samples. For compositions “1” and “4”, where the synthesis process was accompanied by maximum losses, PbO was clearly not enough to transform the entire substance into an oxide phase with the magnetoplumbite structure. This situation could be developed for three reasons (possibly different for samples “1” and “4”):

1. An oxide with magnetoplumbite structure could not be formed from composition “4”.
2. Oxides with a given structure of magnetoplumbite did not have time to form during the heat treatment, which facilitated the process of evaporation of unbound PbO.
3. The obtained phases turned out to be insufficiently resistant to the temperatures used and partly dissociated with the evaporation of PbO. In this case, the synthesis process would probably be more successful with a reduction in heat treatment time.

The effect of milling time on the synthesis of the samples is not obvious. Judging by the results of powder diffractometry (Figs. 2 and 3 show the results for compositions “2” and “3”, a similar picture is observed for other compositions), an increase in the milling time from 5 to 10 hours has practically no effect on the synthesis results. The same can be said by comparing the weight loss of the samples. There is no clear relationship between grinding time and weight loss.

TABLE 2. Chemical and phase compositions of the obtained samples

#	Mill time, h	Mass loss during synthesis, %	Composition of detectable phases according to EDS	Phase composition according to XRD (closest structures)
1	5	9.5	$PbFe_{12}O_{19}+Fe_2O_3$	$PbFe_{12}O_{19}+Fe_2O_3$
	10	11		
2	5	1	$PbFe_{2.4}Al_{2.6}Cr_{2.5}Ga_{2.3}In_{2.2}O_{19}$	$PbFe_{12}O_{19}$
	10	3	$PbFe_{2.4}Al_{2.6}Cr_{2.5}Ga_{2.2}In_{2.3}O_{19}$	
3	5	4.5	$PbFe_{2.3}Co_{2.6}Ti_{2.5}Ga_{2.3}In_{2.3}O_{19}$	$PbFe_{12}O_{19} + ?$
	10	3	$PbFe_{2.4}Co_{2.5}Ti_{2.5}Ga_{2.2}In_{2.4}O_{19}$	
4	5	7.5	$PbFe_{2.4-3.2}Cu_{2.0-3.5}Sn_{1.2-1.9}Ga_{2.1-3.3}In_{1.5-3.0}O_{19}+SnO_2$	$PbFe_{12}O_{19}+GaInO_3+SnO_2+Cu_{0.75}Fe_{2.25}O_4$
	10	6.5		

Judging by the X-ray diffraction data of $PbFe_{2.4}Al_{2.4}Cr_{2.4}Ga_{2.4}In_{2.4}O_{19}$ (Fig. 2), single-phase samples of high-entropy phases with the magnetoplumbite structure were obtained. For these samples, the unit cell parameters were calculated, it is presented in Table 3. These parameters can be compared with the literature data on the parameters for Pb, Ba, and Sr hexaferrites. It can be seen that the obtained data lie within the range of these values.

For the system, its composition is reflected by $PbFe_{2.4}Co_{2.4}Ti_{2.4}Ga_{2.4}In_{2.4}O_{19}$, samples with a predominance high-entropy magnetoplumbite phase were obtained, but a small amount of impurities is also present. Comparison of the data in Fig. 3 with the available XRD patterns of compounds that can be formed from the constituent elements of $PbFe_{2.4}Co_{2.4}Ti_{2.4}Ga_{2.4}In_{2.4}O_{19}$ suggests that the impurity is Pb_2O_3 . However, this contradicts to the detected mass

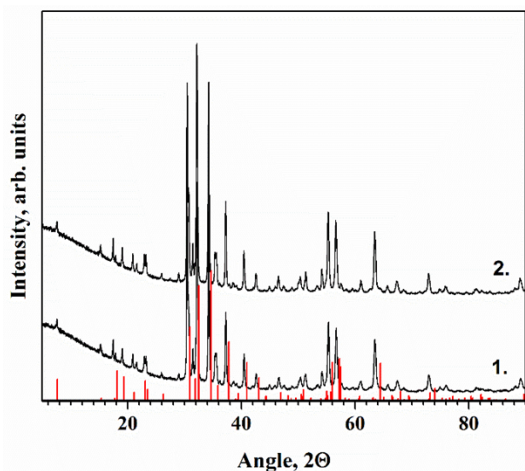


FIG. 2. Powder diffraction patterns for samples “2” at 300 K after 5 h (1) and 10 h (2) milling time. Red columns are reference data for $\text{PbFe}_{12}\text{O}_{19}$ [38]

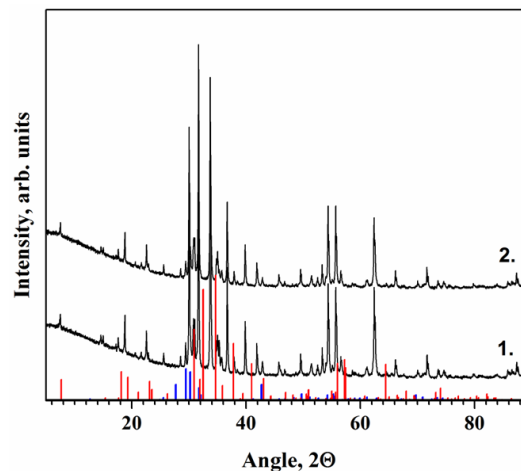


FIG. 3. Powder diffraction patterns for samples “3” at 300 K after 5 h (1) and 10 h (2) milling time. Red bars are reference data for $\text{PbFe}_{12}\text{O}_{19}$ [38], blue bars are for Pb_2O_3 [40]

TABLE 3. Unit cell parameters of samples of compositions “2”

Sample	a, Å	c, Å	V, Å ³
$\text{PbFe}_{2.4}\text{Al}_{2.4}\text{Cr}_{2.4}\text{Ga}_{2.4}\text{In}_{2.4}\text{O}_{19}$, 5 hours	5.858	23.227	690.4
$\text{PbFe}_{2.4}\text{Al}_{2.4}\text{Cr}_{2.4}\text{Ga}_{2.4}\text{In}_{2.4}\text{O}_{19}$, 10 hours	5.863	23.272	692.8
$\text{PbFe}_{12}\text{O}_{19}$ [38]	5.780	23.090	668.052
$\text{BaFe}_{12}\text{O}_{19}$ [39]	5.893	23.194	697.50
$\text{SrFe}_{12}\text{O}_{19}$ [39]	5.780	22.980	664.80

loss (Table 2), which indicates the samples lose PbO during heat treatment, as well as the data of electron microscopy did not allow detection of segregated Pb_2O_3 particles.

The available data (both those obtained in the course of the study and literature data on the properties of the substances involved in the ongoing processes) suggest that the synthesis mechanism includes the melting of PbO microparticles in the initial mixture and the dissolution of other oxides in the liquid phase with the formation of oxide particles (including multicomponent) with the structure of magnetoplumbite.

Figure 4 shows SEM images of the obtained samples at magnification $\times 25000$ (for samples “2”) and $\times 10000$ (for samples “3”). The samples have a porous typical structure of ceramics. In the presented images, particles with natural faceting are clearly visible. The particles have a hexagonal faceting typical of materials with the magnetoplumbite structure. The results of the electron microscopy study of samples “2” did not allow us to detect particles that differ significantly in composition and morphology from the main matrix phase. This testifies in favor of the conclusion that single-phase samples were obtained in this case. In samples “3”, there is a small number of small particles with a nearly cubic shape, but their size does not allow us to determine their composition using EDS.

The data presented in Fig. 4, among other things, demonstrate that relatively low temperatures made it possible to obtain crystallites whose dimensions for composition “2” are of the order of 100 nm or less (considering the thickness of hexagonal plates). In samples “1” and “4”, the size of crystallites of oxide phases with the magnetoplumbite structure are much larger. This can be judged by the images presented in Fig. 5.

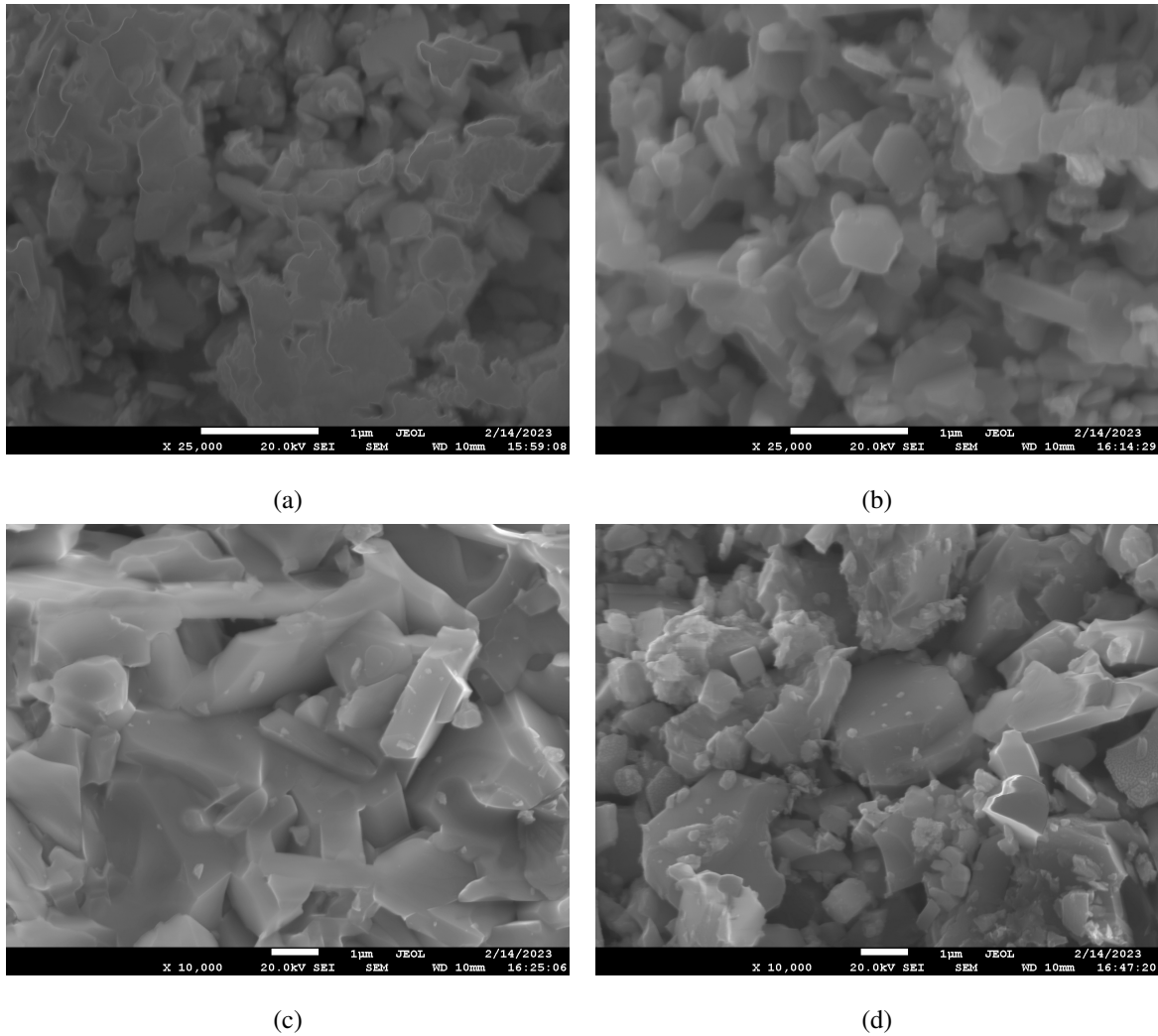


FIG. 4. SEM images of sample microstructures: (a) $\text{PbFe}_{2.4}\text{Al}_{2.4}\text{Cr}_{2.4}\text{Ga}_{2.4}\text{In}_{2.4}\text{O}_{19}$ (5 hours), (b) $\text{PbFe}_{2.4}\text{Al}_{2.4}\text{Cr}_{2.4}\text{Ga}_{2.4}\text{In}_{2.4}\text{O}_{19}$ (10 hours), (c) $\text{PbFe}_{2.4}\text{Co}_{2.4}\text{Ti}_{2.4}\text{Ga}_{2.4}\text{In}_{2.4}\text{O}_{19}$ (5 hours), (d) $\text{PbFe}_{2.4}\text{Co}_{2.4}\text{Ti}_{2.4}\text{Ga}_{2.4}\text{In}_{2.4}\text{O}_{19}$ (10 hours)

4. Conclusions

1. For the first time, single-phase samples of high-entropy phases with the magnetoplumbite structure were obtained, the composition of which is reflected by the formula $\text{PbFe}_{2.4}\text{Al}_{2.4}\text{Cr}_{2.4}\text{Ga}_{2.4}\text{In}_{2.4}\text{O}_{19}$. The particle size of the high-entropy phase is about 100 nm, which makes them promising for a number of applications. For the composition, which is reflected by the formula $\text{PbFe}_{2.4}\text{Co}_{2.4}\text{Ti}_{2.4}\text{Ga}_{2.4}\text{In}_{2.4}\text{O}_{19}$, samples were obtained in which the high-entropy phase with the magnetoplumbite structure predominates.
2. The conditions for the synthesis of the resulting phases have been established. The effect of preliminary ball milling of the initial components has been studied. A synthesis mechanism is proposed.
3. The results of the study pave the way to synthesis and study of the properties of a new large subgroup of high-entropy oxides with the magnetoplumbite structure, which expands the possibilities of controlling the properties of ceramic functional materials.

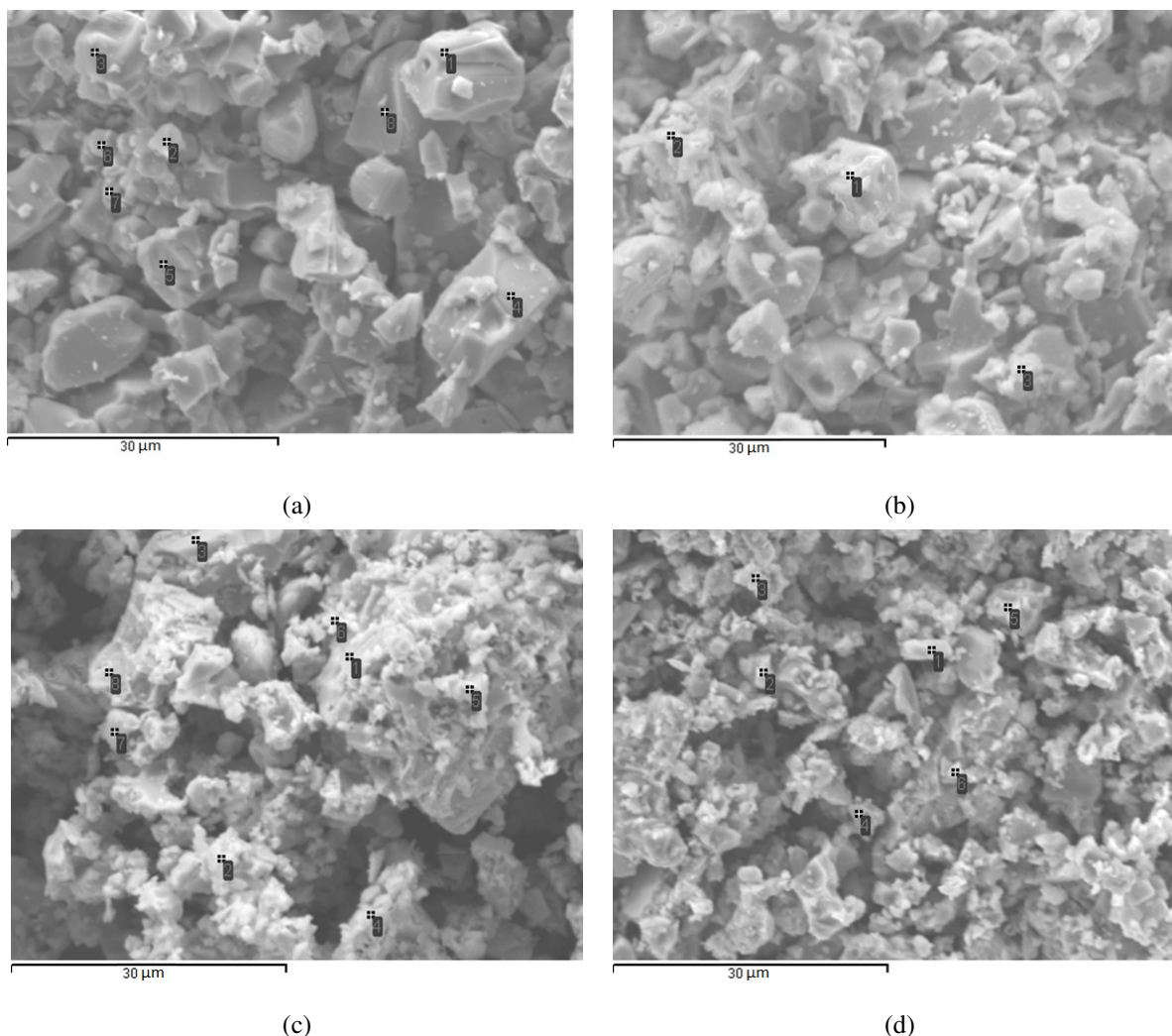


FIG. 5. SEM images showing the microstructures of (a) $\text{PbFe}_{12}\text{O}_{19}$ (5 hours), (b) $\text{PbFe}_{12}\text{O}_{19}$ (10 hours), (c) $\text{PbFe}_{2.4}\text{Cu}_{2.4}\text{Sn}_{2.4}\text{Ga}_{2.4}\text{In}_{2.4}\text{O}_{19}$ (5 hours), (d) $\text{PbFe}_{2.4}\text{Cu}_{2.4}\text{Sn}_{2.4}\text{Ga}_{2.4}\text{In}_{2.4}\text{O}_{19}$ (10 hours)

References

- [1] Wang C., Ma X., Xu C., Chen H., Chen Y., Chen F., Kang B., Lu W., Zhang J., Cao S. Magnetic field-induced polarization reversal in Y-type hexaferrites single crystals. *Ceram. Int.*, 2021, **47**, P. 19356–19361.
- [2] Huang K., Yu J., Zhang L., Xu J., Yang Z., Liu C., Wang W., Kan X. Structural and magnetic properties of Gd–Zn substituted M-type Ba–Sr hexaferrites by sol-gel auto-combustion method. *J. Alloys Compd.*, 2019, **803**, P. 971–980.
- [3] Zhang W., Li J., Yi S., Zu P., Wu J., Lin J., Li M., Su W. Influence of La–Nb co-substituted Sr ferrite on microstructure, spectrum and magnetic properties of hexaferrites. *J. Alloys Compd.*, 2021, **871**, 159563.
- [4] Almessiere M.A., Slimani Y., Algarou N.A., Gondal M.A., Wudil Y.S., Younas M., Auwal I.A., Baykal A., Manikandan A., Zubar T.I., Kostishin V.G., Trukhanov A.V., Ercan I. Electronic, magnetic, and microwave properties of hard/soft nanocomposites based on hexaferrite $\text{SrNi}_{0.02}\text{Zr}_{0.02}\text{Fe}_{11.96}\text{O}_{19}$ with variable spinel phase MFe_2O_4 (M=Mn, Co, Cu and Zn). *Ceram. Int.*, 2021, **47**, P. 35209–35223.
- [5] Darwish M.A., Turchenko V.A., Morchenko A.T., Kostishyn V.G., Timofeev A.V., Sayyed M.I., Sun Z., Podgornaya S.V., Trukhanova E.L., Kaniukov E.Y., Trukhanov S.V., Trukhanov A.V. Heterovalent substituted $\text{BaFe}_{12-x}\text{Sn}_x\text{O}_{19}$ ($0.1 \leq x \leq 1.2$) M-type hexaferrite: Chemical composition, phase separation, magnetic properties and electrodynamic features. *J. Alloys Compd.*, 2022, **896**, 163117.
- [6] Shams M.H., Salehi S.M.A., Ghasemi A. Electromagnetic wave absorption characteristics of Mg–Ti substituted Ba-hexaferrite. *Mater. Lett.*, 2008, **62** (10–11), P. 1731–1733.
- [7] Millimetre wave and terahertz sensors and technology XIII. Salmon N.A., Gumbmann F. (ed.) *Proc. SPIE – Int. Soc. Opt. Eng.*, 2020, **11541**, 121 p.
- [8] Bhaduri A., Singh S., Thapa K.B., Yadav B.C. Visible light-induced, highly responsive, below lower explosive limit (LEL) LPG sensor based on hydrothermally synthesized barium hexaferrite nanorods. *Sensors Actuators B Chem.*, 2021, **348**, 130714.
- [9] Rajaji U., Chinnapaiyan S., Chen T.-W., Chen S.-M., Mani G., Mani V., Ali M.A., Al-Hemaid F.M.A., El-Shikh M.S. Rational construction of novel strontium hexaferrite decorated graphitic carbon nitrides for highly sensitive detection of neurotoxic organophosphate pesticide in fruits. *Electrochim. Acta*, 2021, **371**, 137756.
- [10] Rai G.M., Iqbal M.A., Kubra K.T. Effect of Ho^{3+} substitutions on the structural and magnetic properties of $\text{BaFe}_{12}\text{O}_{19}$ hexaferrites. *J. Alloys Compd.*, 2010, **495**, P. 229–233.

- [11] Jacobo S.E., Hermea C., Bercoff P.G. Influence of the iron content on the formation process of substituted Co–Nd strontium hexaferrite prepared by the citrate precursor method. *J. Alloys Compd.*, 2010, **495**, P. 513–515.
- [12] Thakur A., Singh R.R., Barman P.B. Structural and magnetic properties of La^{3+} substituted strontium hexaferrite nanoparticles prepared by citrate precursor method. *J. Magn. Magn. Mater.*, 2012, **326**, P. 35–40.
- [13] Kostishyn V.G., Panina L.V., Timofeev A.V., Kozhitov L.V., Kovalev A.N., Zyuzin A.K. Dual ferroic properties of hexagonal ferrite ceramics $BaFe_{12}O_{19}$ and $SrFe_{12}O_{19}$. *J. Magn. Magn. Mater.*, 2016, **400**, P. 327–332.
- [14] Pullar R.C. Hexagonal ferrites: A review of the synthesis, properties and applications of hexaferrite ceramics. *Prog. Mater. Sci.*, 2012, **57** (7), P. 1191–1334.
- [15] Gorbachev E.A., Trusov L.A., Wu M., Vasiliev A.V., Svetogorov R.D., Alyabyeva L.N., Lebedev V.A., Slepsova A.E., Karpov M.A., Mozharov Y.M., Gorshunov B.P., Kazin P.E. Submicron particles of Ga-substituted strontium hexaferrite obtained by a citrate auto-combustion method. *J. Mater. Chem. C*, 2021, **9**, P. 13832–13840.
- [16] Choi J.-Y., Baek Y.-K., Lee J.-G., Kim Y.-K. Effect of sodium addition on structural and magnetic properties of solid state processed $SrFe_{12-x}Al_xO_{19}$ ($x \leq 4$). *Appl. Phys. A: Mater. Sci. and Proces.*, 2022, **128** (12).
- [17] Wu C., Liu Q., Yin Q., Chen J., Zhang H., Liu Y. Room-temperature multiferroic properties of Al-doped hexaferrites sintered at high oxygen atmospheric concentrations. *Ceram. Int.*, 2021, **47** (15), P. 21398–21403.
- [18] Sözeri H., Genç F., Almessiere M.A., Ünver İ.S., Korkmaz A.D., Baykal A. CR^{3+} -substituted Ba nano-hexaferrites as high-quality microwave absorber in X band. *J. Alloys Compd.*, 2019, **779**, P. 420–426.
- [19] Turchenko V., Kostishin V.G., Trukhanov S., Damay F., Balasoiu M., Bozzo B., Fina I., Burkhovetsky V.V., Polosan S., Zdorovets M.V., Kozlovskiy A.L., Astapovich K.A., Trukhanov A. Structural features, magnetic and ferroelectric properties of $SrFe_{10.8}In_{1.2}O_{19}$ compound. *Mater. Res. Bull.*, 2021, **138**, 111236.
- [20] Huang, K., Yu, J., Zhang, L., Xu, J., Li, P., Yang, Z., Kan, X. Synthesis and characterizations of magnesium and titanium doped M-type barium calcium hexaferrites by a solid state reaction method. *J. Alloys Compd.*, 2020, **825**, 154072.
- [21] Vinnik D. A., Gudkova S.A., Zhivulin V.E., Trofimov E.A. Ferrite-based solid solutions: Structure types, preparation, properties, and potential applications. *Inorg. Mater.*, 2021, **57** (11), P. 1109–1118.
- [22] Zhilina E.M., Russkikh A.S., Krasikov S.A., Osinkina T.V., Rempel A.A. Synthesis of High-Entropy Alloy $AlTiZrVNb$ by Aluminothermic Reaction. *Inorg. Chem.*, 2022, **61** (6), P. 825–828.
- [23] Teplonogova M.A., Yapryntsev A.D., Baranchikov A.E., Ivanov V.K. High-entropy layered rare earth hydroxides. *Inorg. Chem.*, 2022, **61** (49), P. 19817–9827.
- [24] Wang B., Yao J., Wang J., Chang A. Spinel-type high-entropy $(Co_{0.2}Mn_{0.2}Fe_{0.2}Zn_{0.2}Ti_{0.2})_3O_4$ oxides constructed from disordered cations and oxygen vacancies. *J. Alloys Compd.*, 2022, **897**, 163188.
- [25] Vinnik D.A., Zhivulin V.E., Trofimov E.A., Gudkova S.A., Punda A.Y., Valiulina A.N., Gavrilyak M., Zaitseva O.V., Taskaev S.V., Khandaker M.U., Alqahtani A., Bradley D.A., Sayyed M.I., Turchenko V.A., Trukhanov A.V., Trukhanov S.V. A-site cation size effect on structure and magnetic properties of $Sm(Eu,Gd)Cr_{0.2}Mn_{0.2}Fe_{0.2}Co_{0.2}Ni_{0.2}O_3$ high-entropy solid solutions. *Nanomaterials*, 2022, **12** (1), 36.
- [26] Dabrowa J., Cieślak J., Zajusz M., Możdzierz M., Berent K., Mikula A., Stepień A., Świerczek K. Structure and transport properties of the novel $(Dy,Er,Gd,Ho,Y)_3Fe_5O_{12}$ and $(Dy,Er,Gd,Ho,Y)_3Fe_5O_{12}$ high entropy garnets. *J. Eur. Ceram. Soc.*, 2021, **41**, P. 3844–3849.
- [27] Vinnik D.A., Trofimov E.A., Zhivulin V.E., Zaitseva O.V., Gudkova, S.A., Starikov A.Y., Zherebtsov D.A., Kirsanova A.A., Hässner M., Niewa R. High-entropy oxide phases with magnetoplumbite structure. *Ceram. Int.*, 2019, **45** (10), P. 12942–12948.
- [28] Vinnik D.A., Trofimov E.A., Zhivulin V.E., Zaitseva O.V., Zherebtsov D.A., Starikov A.Y., Sherstyuk D.P., Gudkova S.A., Taskaev S.V. The new extremely substituted high entropy $(Ba,Sr,Ca,La)Fe_{6-x}(Al,Ti,Cr,In,Cu,W)_xO_{19}$ microcrystals with magnetoplumbite structure. *Ceram. Int.*, 2020, **46** (7), P. 9656–9660.
- [29] Vinnik D.A., Zhivulin V.E., Trofimov E.A., Starikov A.Y., Zherebtsov D.A., Zaitseva O.V., Gudkova S.A., Taskaev S.V., Klygach D.S., Vakhitov M.G., Sander E.E., Sherstyuk D.P. Trukhanov A.V. Extremely polysubstituted magnetic material based on magnetoplumbite with a hexagonal structure: Synthesis, structure, properties, prospects. *Nanomater.*, 2019, **9** (4).
- [30] Trukhanov A.V., Vinnik D.A., Trofimov E.A., Zhivulin V.E., Zaitseva O.V., Taskaev S.V., Zhou D., Astapovich K.A., Trukhanov S.V., Yang Y. Correlation of the Fe content and entropy state in multiple substituted hexagonal ferrites with magnetoplumbite structure. *Ceram. Int.*, 2021, **47**, P. 17684–17692.
- [31] Zhivulin V.E., Trofimov E.A., Zaitseva O.V., Sherstyuk D.P., Cherkasova N.A., Taskaev S.V., Vinnik D.A., Alekhina Yu.A., Perov N.S., Tishkevich D.I., Zubar T.I., Trukhanov A.V., Trukhanov S.V. Effect of configurational entropy on phase formation, structure, and magnetic properties of deeply substituted strontium hexaferrites. *Ceram. Int.*, 2023, **49** (1), P. 1069–1084.
- [32] Obradors X., Solans X., Collomb A., Samaras D., Rodriguez J., Pernet M., Font-Altaba M. Crystal structure of strontium hexaferrite $SrFe_{12}O_{19}$. *J. Sol. St. Chem.*, 1988, **72** (2), P. 218–224.
- [33] Vinnik D.A., Trofimov E.A., Zherebtsov D.A. Experimental Study and Thermodynamic Modeling of Phase Equilibria in $PbO-Fe_2O_3$ System. In *Materials Science Forum Trans Tech Publications, Ltd.*, 2016, **870**, P. 282–285.
- [34] Nevřiva M., Fischer K. Contribution to the binary phase diagram of the system $PbO-Fe_2O_3$. *Mater. Res. Bull.*, 1986, **21**, P. 1285–1290.
- [35] Jonker H.D. Investigation of the phase diagram of the system $PbO-B_2O_3-Fe_2O_3-Y_2O_3$ for the growth of single crystals of $Y_3Fe_5O_{12}$. *J. Cryst. Growth.*, 1975, **28**, P. 231–239.
- [36] Mountvala A.J., Ravitz S.F. Phase Relations and Structures in the System $PbO-Fe_2O_3$. *J. Am. Ceram. Soc.*, 1962, **45**, P. 285–288.
- [37] Diop I., David N., Fiorani J.M., Podor R., Vilasi M. Experimental investigations and thermodynamic description of the $PbO-Fe_2O_3$ system. *Thermochimica Acta*, 2010, **510**, P. 202–212.
- [38] Aleshko-Ozhevskii O.P., Faek M.K., Yamzin I.I. A neutron diffraction study of the structure of magnetoplumbite. *Soviet Physics – Crystallography*, 1969, **14**, P. 367–369.
- [39] Obradors X., Collomb A., Pernet M., Samaras D., Joubert J.C. X-ray analysis of the structural and dynamic properties of $BaFe_{12}O_{19}$ hexagonal ferrite at room temperature. *J. Solid State Chem.*, 1985, **56** (2), P. 171–181.
- [40] Bouvaist J., Weigel D. Sesquioxide de plomb, Pb_2O_3 . I. Determination de la structure. *Acta Crystallogr. A*, 1970, **26**, P. 501–510.

Information about the authors:

Olga V. Zaitseva – South Ural State University, Lenin Av., 76, Chelyabinsk, 454080, Russia;
ORCID 0000-0001-5888-3297; zaitcevaov@susu.ru

Evgeny A. Trofimov – South Ural State University, Lenin Av., 76, Chelyabinsk, 454080, Russia;
ORCID 0000-0001-8073-3244; trofimizea@susu.ru

Vladimir E. Zhivulin – South Ural State University, Lenin Av., 76, Chelyabinsk, 454080, Russia;
ORCID 0000-0002-4389-8936; zhivulinve@mail.ru

Ahmad Ostovari Mogaddam – South Ural State University, Lenin Av., 76, Chelyabinsk, 454080, Russia;
ORCID 0000-0002-5316-3773; ostovarim@susu.ru

Olga V. Samoiloova – South Ural State University, Lenin Av., 76, Chelyabinsk, 454080, Russia;
ORCID 0000-0002-9514-3201; samoylova_o@mail.ru

Ksenia S. Litvinyuk – South Ural State University, Lenin Av., 76, Chelyabinsk, 454080, Russia;
ORCID 0009-0002-4773-1372; xenialitvinyuk@gmail.com

Alena R. Zykova – South Ural State University, Lenin Av., 76, Chelyabinsk, 454080, Russia;
ORCID 0000-0001-6333-5551; zykovaar@susu.ru

Dmitry V. Mikhailov – South Ural State University, Lenin Av., 76, Chelyabinsk, 454080, Russia;
ORCID 0000-0003-2484-8076; a_b_c81@mail.ru

Svetlana A. Gudkova – South Ural State University, Lenin Av., 76, Chelyabinsk, 454080, Russia;
ORCID 0000-0002-3028-947X; svetlanagudkova@yandex.ru

Denis A. Vinnik – South Ural State University, Lenin Av., 76, Chelyabinsk, 454080, Russia;
ORCID 0000-0002-5190-9834; vinnikda@susu.ru

Conflict of interest: the authors declare no conflict of interest.

Influence of the composition of the BiPO₄–BiVO₄ system on the phase formation, morphology, and properties of nanocrystalline composites obtained under hydrothermal conditions

Olga V. Proskurina^{1,2,a}, Ilke Diana Chetinel^{2,b}, Anna S. Seroglazova^{1,2,c}, Victor V. Gusarov^{1,d}

¹Ioffe Institute, 194021 St. Petersburg, Russia

²St. Petersburg State Institute of Technology, 190013 St. Petersburg, Russia

^aproskurinaov@mail.ru, ^bdiana03ridak@gmail.com, ^cannaseroglazova@yandex.ru,

^dvictor.v.gusarov@gmail.com

Corresponding author: Olga V. Proskurina, proskurinaov@mail.ru

ABSTRACT BiPO₄/BiVO₄ nanocrystalline composites were synthesized under hydrothermal conditions. The influence of the initial composition of the system on the phase state, the size of crystallites, and the morphology of the formed particles was determined. The photocatalytic activity of the nanocomposite was studied using the decomposition of methyl violet as an example.

KEYWORDS hydrothermal synthesis, phase formation, nanocrystals, bismuth orthophosphate, bismuth orthovanadate

ACKNOWLEDGEMENTS X-ray diffraction studies were performed employing the equipment of the Engineering Center of the St. Petersburg State Institute of Technology. The research was supported by the Russian Science Foundation Grant 21-13-00260.

FOR CITATION Proskurina O.V., Chetinel I.D., Seroglazova A.S., Gusarov V.V. Influence of the composition of the BiPO₄–BiVO₄ system on the phase formation, morphology, and properties of nanocrystalline composites obtained under hydrothermal conditions. *Nanosystems: Phys. Chem. Math.*, 2023, **14** (3), 363–371.

1. Introduction

Bismuth vanadate BiVO₄ is known as the following crystalline modifications: monoclinic (with the structure of the mineral *clinobiswanite*), tetragonal (with the structure of the mineral *dreyerite*) and rhombic (with the structure of the mineral *pucherite*). Materials based on BiVO₄ with a monoclinic structure exhibit photocatalytic properties when irradiated with visible light [1–3]. The band gap of monoclinic BiVO₄ phase is about 2.4 eV, and that of the tetragonal phase is 2.9 eV [4]. In addition, monoclinic bismuth vanadate is characterized by low toxicity and a high chemical stability under the influence of radiation [5]. Nevertheless, bismuth vanadate in the monoclinic system has rather low charge transfer rate and surface adsorption [6]. The structure of monoclinic bismuth vanadate is modified using various additives for achieving the maximum efficiency of the photocatalyst, and can interfere with the recombination of the generated electron-hole pairs [7–9]. Compounds containing PO₄³⁻ anions are able to improve photocatalytic properties, despite the fact that there are quite wide band gap. Due to the formation of a heterojunction between semiconductors, electrostatic interactions of phosphate anions with positively charged holes, and to inertness with respect to the resulting free electrons, the improvement of photocatalytic properties occurs.

Bismuth phosphate BiPO₄ has three polymorphic crystal structures such as hexagonal (the mineral *xymengite*) with space group P3₁21 and two monoclinic, one of which is unstable at low temperatures and exists only at high temperatures. The low-temperature modification has the space group P2₁/n [10]. The band gap in a xymengite crystal is ~ 4.6 eV, whereas, in the case of a monoclinic structure, it is about 3.8 eV [11]. The review [12] considers methods for the synthesis of BiPO₄ with emphasis on its crystal microstructure, optical and photocatalytic properties, as well as a way to create composites based on BiPO₄ for improving a photocatalytic activity.

Bismuth vanadate of the monoclinic modification can be obtained by several methods, that differ from each other in sets of precursors, synthesis conditions, and the complexity of its implementation. The phase formation for systems containing bismuth and vanadium oxides always proceeds in several sequential-parallel stages with the formation of intermediate products [13]. Bismuth vanadate with the *clinobiswanite* structure can be obtained by flame pyrolysis [14], a high-temperature heat treatment [15], solution combustion [16, 17], soft chemistry methods [18, 19], including solvothermal [5] and hydrothermal methods [20–23]. In some cases, the product is subjected to additional firing at a high temperature in order to completely remove moisture and improve the properties of the material: increase porosity and crystallinity and increase the charge transfer rate. According to [24], the best photocatalytic properties of BiVO₄ appear when the synthesis is completed by heat treatment of the product for 3 hours at a temperature of 500 °C.

Recently, a large number of works have appeared devoted to the creation of semiconductor materials as photocatalysts with heterojunctions that limit electron-hole recombination. From this point of view, investigations of solid solution open a prospect to control the energy band structure of a semiconductor and, at the same time, to build an efficient interface for photocatalysis.

The preparation of heterostructures in the $\text{BiVO}_4\text{-BiPO}_4$ system and the study of their photocatalytic characteristics were considered to [25], where compounds of the $\text{BiVO}_4/\text{BiPO}_4$ system were obtained by growing bismuth vanadate nanoparticles on the surface of bismuth phosphate. In [26], a hollow $\text{BiVO}_4/\text{BiPO}_4$ nanocomposite has been obtained under hydrothermal conditions, and showed great potential for use as a photocatalyst. To improve the photocatalytic characteristics, more complex doped or ternary composites based on $\text{BiVO}_4/\text{BiPO}_4$ are also considered [8, 9].

It is of interest to determine the mutual influence of BiVO_4 and BiPO_4 on the formation of nanocrystalline materials in the $\text{BiVO}_4\text{-BiPO}_4$ system, the possibility of the formation of solid solutions in the system, and also to study the photocatalytic properties of composites in this system.

2. Experimental

Bismuth nitrate $\text{Bi}(\text{NO}_3)_3 \cdot 5\text{H}_2\text{O}$ (analytical grade) in an amount of 4 mmol was dissolved in 10 ml of 6 M nitric acid HNO_3 (chemically pure) with stirring with a magnetic stirrer (solution "A"). An ammonium metavanadate solution was prepared by dissolving an appropriate amount of NH_4VO_3 (analytical grade) in 40 ml of distilled water (solution "B"). To increase the solubility of the salt, the solution was heated to 70 °C. For the synthesis of samples containing bismuth phosphate, solution "C" was prepared by dissolving an appropriate amount of $(\text{NH}_4)_2\text{HPO}_4$ (chemically pure) in cold distilled water.

Solution B was added dropwise to solution A with continuous stirring, resulting in an orange precipitate. After 10 minutes of vigorous stirring, solution C was also added dropwise to the reaction mixture.

The resulting suspension was stirred for 1 hour. At the same time, a 4 M solution of sodium hydroxide NaOH (analytical grade) was added to maintain pH=1. The reaction mixtures were subjected to hydrothermal treatment at 200 °C and a pressure of ~7 MPa for 4 hours. After 4 hours of isothermal exposure, the autoclave was removed from the furnace and cooled at room temperature. The result of precipitate was washed several times with distilled water until a neutral value pH, centrifuged, and dried at 80 °C for 12 hours for removing of moisture from the sample.

Samples of BiVO_4 , BiPO_4 , and $\text{BiVO}_4/\text{BiPO}_4$ compositions with different molar ratios were synthesized.

Determination of the elemental composition of samples, sizes and shapes of particles was carried out using a scanning electron microscope Tescan Vega 3 SBH (Tescan Orsay Holding, Czech Republic) with an attachment for energy dispersive X-ray spectroscopy Oxford Instruments INCA x-act (Oxford Instruments, Oxford, UK). The size characteristics of particles according to electron microscopy data were analyzed using the ImageJ program.

X-ray diffraction patterns were taken at 25 °C on a Rigaku SmartLab 3 diffractometer (Rigaku Corporation, Japan). Diffractograms were recorded in the Bragg-Brentano geometry in the angle range $2\theta = 10 - 60^\circ$ with a step of 0.01° , a shooting rate of $4^\circ/\text{min}$, and using a $K\beta$ filter ($\text{CuK}\alpha$ is radiation). The phase analysis of the samples was determined using the ICSD PDF-2 database. Full profile phase analysis was performed using the *SmartLab Studio IV* program (Rigaku Corporation, Japan). The average crystallite size was determined from non-overlapping reflections of each phase using the Halder-Wagner method [27]. The instrumental broadening of reflections of the samples was taken into account using a standard, which was a SrTiO_3 single crystal in the form of a polished thin plate.

The photocatalytic activity of the samples was studied in the process of catalytic photodegradation of methyl violet (MV) using xenon lamps to simulate visible light with a power of 100 W with a UV filter $\lambda \geq 420$ nm. The dye oxidation process was carried out in an isolated photochemical reactor [28], which included 50 ml beakers with a reaction solution, a magnetic stirrer, and two xenon lamps.

Before starting photocatalytic experiments, colloidal solutions of the corresponding samples with concentration of 0.045 g/L were preliminarily prepared. Then, 3 ml of a 0.1 g/L methyl violet dye solution and 22 ml of distilled water were added to each of the beakers. Thus prepared reaction solutions were kept in the dark for 15 minutes to achieve adsorption-desorption equilibrium. After this time, the reaction mixture was irradiated with visible light with constant stirring for 60 minutes with sampling of 5 ml every 10 minutes to build kinetic dependences and determine the rate constant of the photocatalytic process. The degree of efficiency of photocatalytic degradation was assessed by changing the concentration of MV using an AvaSpec-ULS2048 spectrometer with an AvaLight-XE light source.

A pseudo first order kinetic model was used to describe dye degradation data by the equation:

$$\ln(C_0/C) = K \cdot \tau,$$

where K is the apparent rate constant of the reaction, C_0 and C are the initial dye concentration after adsorption and the current dye concentration at time τ .

3. Results and discussion

The results of the elemental analysis of the samples are presented in Table 1. The designation of the samples in the work corresponds to their numbering in the table. In all samples, the bismuth content slightly exceeded that specified

for the synthesis. This seems to be related to the measurement error. The content of vanadium in samples turned out to be lower than that specified during synthesis. Probably, at $\text{pH}=1$, a part of vanadium did not crystallize in the form of bismuth orthovanadate, but remained in the hydrothermal solution and was washed out by washing the precipitate.

Diffraction patterns of the obtained samples are shown in Fig. 1. Sample 1 after hydrothermal treatment consists of the BiVO_4 monoclinic phase with the clinobiswanite structure (PDF #00-014-0688). Sample 5 is monoclinic BiPO_4 (PDF #00-015-0767). All samples containing both vanadium and phosphorus are two-phase, containing a BiVO_4 monoclinic phase and a BiPO_4 monoclinic phase. Since the content of vanadium in all samples turned out to be lower than that specified for synthesis, the reflections of the phase of monoclinic BiVO_4 are weakly expressed in diffraction patterns of the samples containing vanadium and phosphorus. Analysis of diffraction patterns of the samples shows that monoclinic modifications of vanadate and bismuth phosphate can be obtained by the hydrothermal method under these conditions (4 hours, $200\text{ }^\circ\text{C}$, 7 MPa) (Fig. 1). Data on the phase ratio in the samples were determined using the Rietveld method and are presented in Table 1.

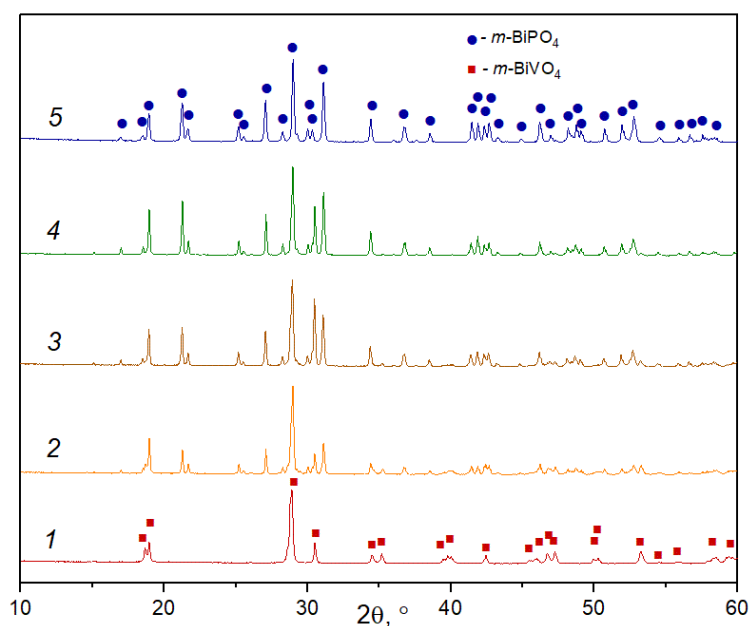


FIG. 1. X-ray diffraction patterns of samples

TABLE 1. Composition of samples

Designation of samples	Composition by synthesis	Composition by analysis (EDX)	Phase composition $m\text{-BiVO}_4 : m\text{-BiPO}_4$ (XRD)
1	BiVO_4	BiVO_4	100 : 0
2	$\text{BiV}_{0.67}\text{P}_{0.33}\text{O}_4$	$\text{BiV}_{0.40}\text{P}_{0.60}\text{O}_4$	41.2 : 58.8
3	$\text{BiV}_{0.50}\text{P}_{0.50}\text{O}_4$	$\text{BiV}_{0.16}\text{P}_{0.84}\text{O}_4$	25.2 : 74.8
4	$\text{BiV}_{0.33}\text{P}_{0.67}\text{O}_4$	$\text{BiV}_{0.12}\text{P}_{0.88}\text{O}_4$	7.3 : 92.7
5	BiPO_4	BiPO_4	0 : 100

The comparison of the data of elemental analysis and X-ray phase analysis showed that for sample 2, the elemental composition coincided with the phase composition of compound according to the analysis almost. For samples 3 and 4, it's shown that there is a decrease and an increase in the proportion of bismuth phosphate compared to elemental analysis, respectively. Further in the work, the composition of the samples will be given according to the data of X-ray phase analysis.

The dependence of the unit cell parameters of both phases on the content of BiPO_4 in the samples allows us to conclude that there is a limited region of the solid solution based on the phase of monoclinic bismuth orthophosphate $\text{BiP}_{1-x}\text{V}_x\text{O}_4$. The unit cell parameters of monoclinic bismuth orthovanadate do not change within the error, which indicates the absence or extremely low solubility of BiPO_4 in the phase based on BiVO_4 . As an example, Fig. 2 shows the dependence of the parameter a of monoclinic phases based on BiPO_4 and BiVO_4 on the $\text{BiVO}_4 : \text{BiPO}_4$ ratio.

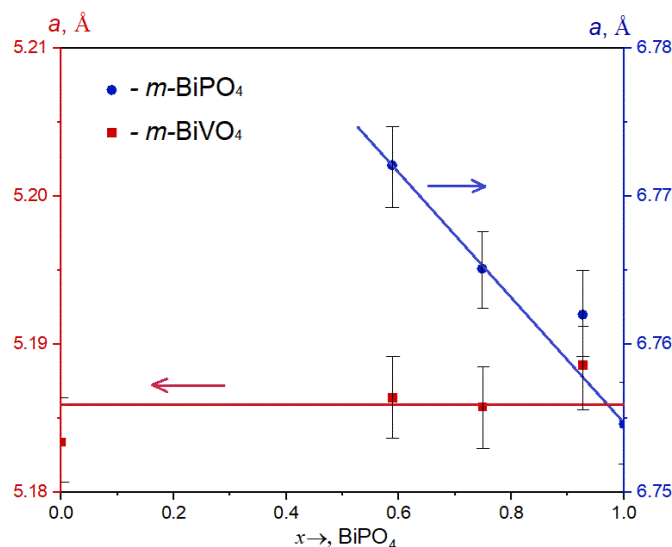


FIG. 2. Dependence of the unit cell parameter a of monoclinic bismuth orthophosphate and orthovanadate on the content of bismuth phosphate in the sample (x)

Graphs of the dependence of the average crystallite size of the coexisting phases on the $\text{BiVO}_4 : \text{BiPO}_4$ ratio are shown in Fig. 3.

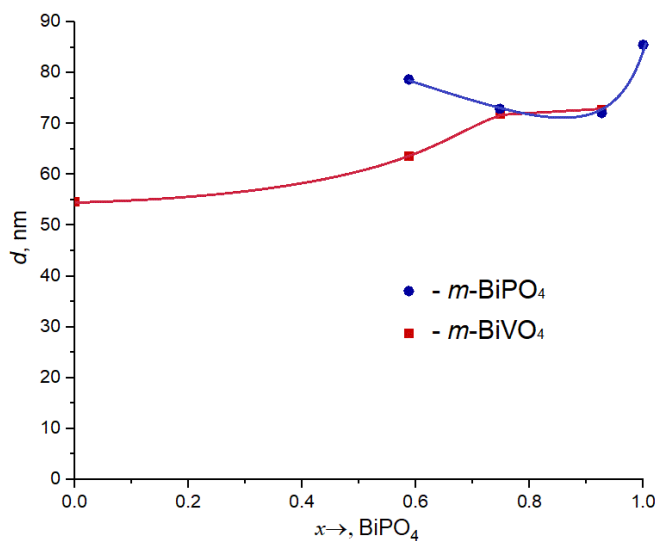


FIG. 3. Dependence of the average crystallite size of the phases of monoclinic bismuth phosphate and bismuth vanadate on the content of bismuth phosphate in the sample (x)

An increase in the amount of bismuth orthophosphate in the system leads to a slight increase in the average size of bismuth orthovanadate crystallites. The size of bismuth orthovanadate crystallites varies within 72 – 85 nm. The crystallites of the $m\text{-BiPO}_4$ phase have the smallest sizes in samples 3 and 4. In addition, in these samples, the average sizes of the crystallites of the $m\text{-BiVO}_4$ phase were closest to the sizes of crystallites of the accompanying $m\text{-BiPO}_4$ phase, and amounted to about 70 nm.

Microphotographs of the samples are shown in Fig. 4. Spot elemental analysis showed that the large particles in the samples are particles of the $m\text{-BiVO}_4$ phase (as an example, a snapshot of sample 3 in Fig. 4c is shown). Smaller particles belong to the $m\text{-BiPO}_4$ phase.

Particle size distributions obtained on the basis of the electron microscopy data are given as an example for sample 4 and are presented in Fig. 5.

On Fig. 6 shows plots of the particle length versus the $\text{BiVO}_4 : \text{BiPO}_4$ ratio in obtained samples.

It can be noted that the particle size of each phase in two-phase samples increases in comparison with single-phase samples with a decrease in the proportion of this phase. Moreover, the average particle length of bismuth orthovanadate increases from 4 to 21 μm with an increasing the proportion of bismuth orthophosphate from 0 to 0.927. Smaller-sized

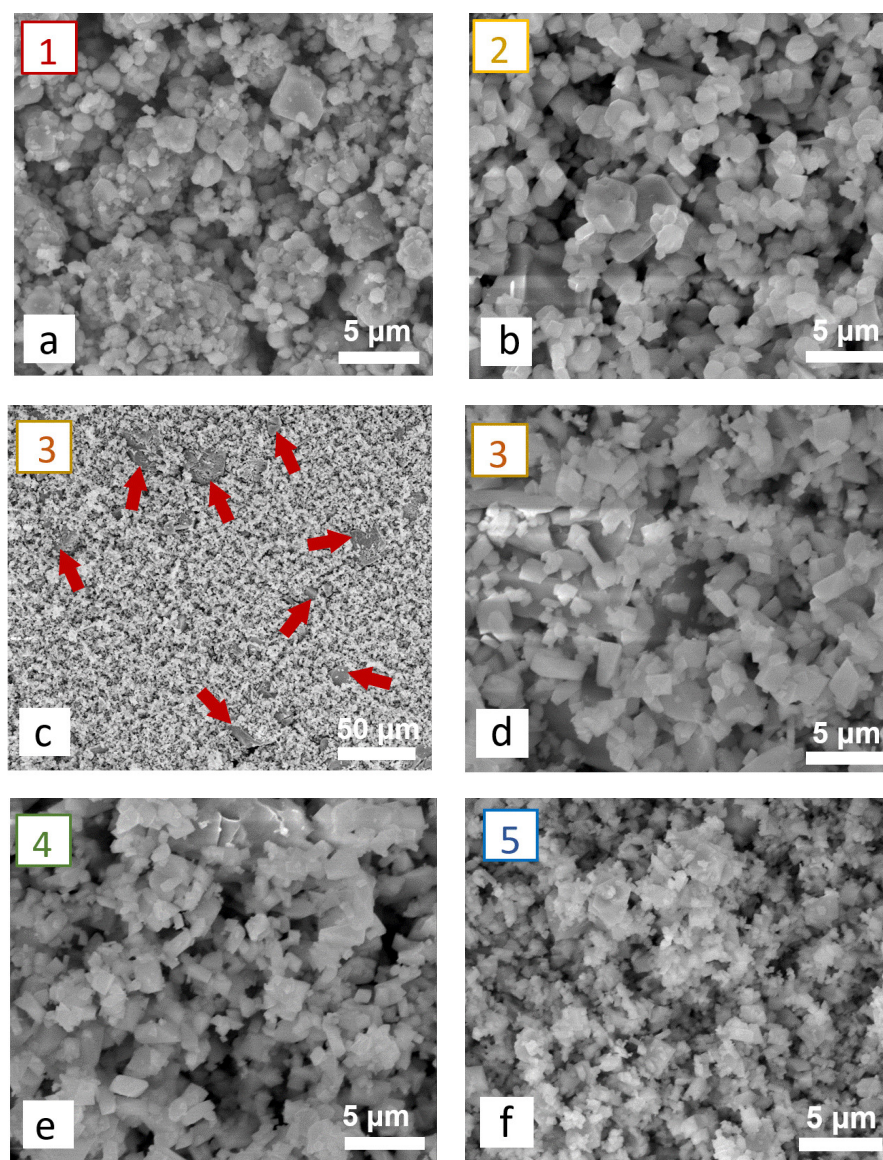


FIG. 4. Micrographs of samples: 1 (a); 2 (b); 3 (c, d); 4 (e), 5 (d) (Arrows point to $m\text{-BiVO}_4$ particles)

particles, have larger the surface area on which photons are absorbed. As a result, there are better photocatalytic properties of substances.

Photocatalytic characteristics of the samples were studied during the decomposition of methyl violet under the action of visible light (Fig. 7). The obtained UV-visible absorption spectra of MV demonstrate the effective destruction of dye molecules over time in the presence of all potential catalysts, as evidenced by the regular decrease in the characteristic peak of MV observed at 578 nm. From the analysis of the obtained spectra, it can be concluded that pure bismuth orthovanadate exhibits the highest photocatalytic activity (sample 1).

Depending on the amount of the bismuth vanadate phase in the samples, the catalytic ability of the samples changes in the following order: $5 > 4 > 3 > 2 > 1$. It can be affected by the morphology of the particles, the size of the crystallites, and the method of catalyst synthesis, its doping, and other factors.

To study the kinetic characteristics of all samples, kinetic curves were constructed, which are the ratio of the concentrations of the reaction solution to the concentration of the initial solution as a function of time (Fig. 8). The resulting curves show the photocatalytic activity of each sample as the exposure time increases and demonstrate a regular decrease in the relative concentration of the dye.

The rate constant of the catalytic reaction was calculated using the linearization of the graph of the dependence of the kinetic curves in pseudo-first-order logarithmic coordinates of the reaction (Fig. 9) and varies from 0.018 to 0.007 min^{-1} depending on the content of bismuth orthophosphate in the samples (Fig. 10).

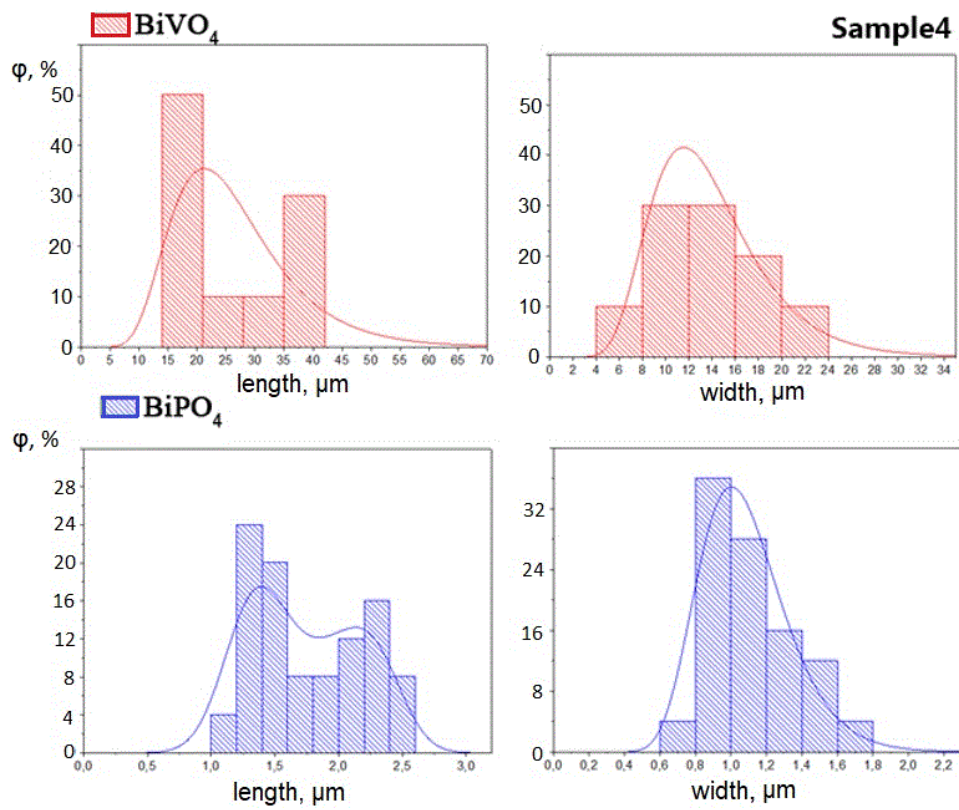
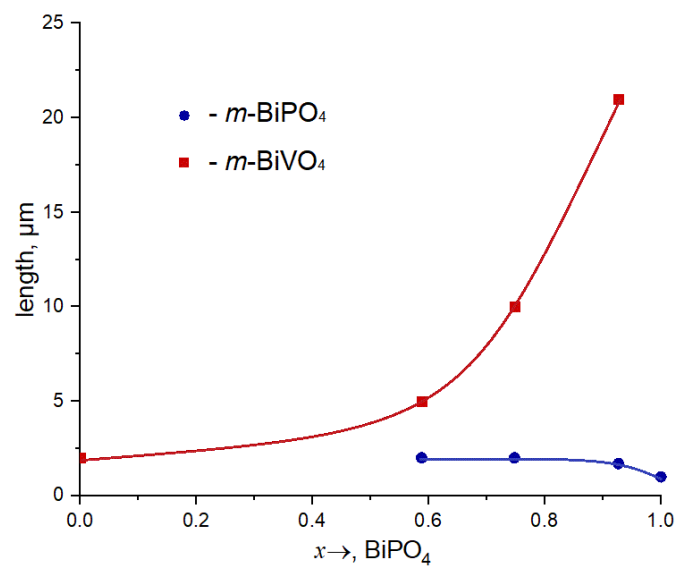
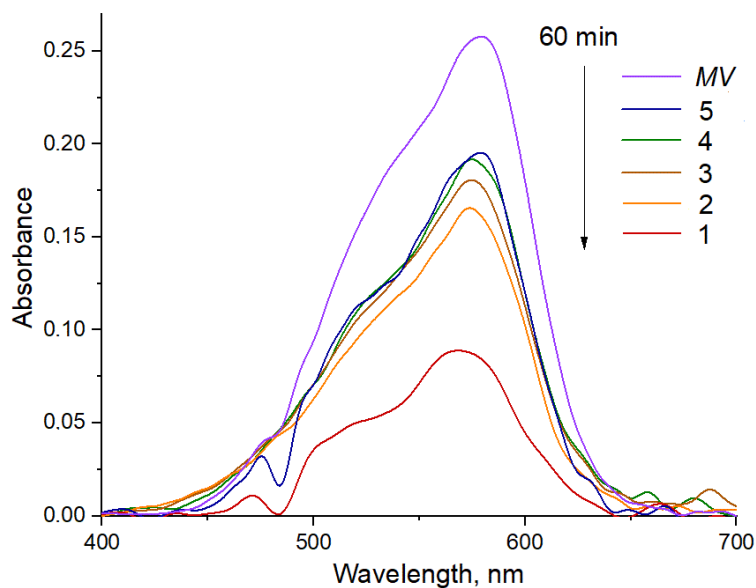
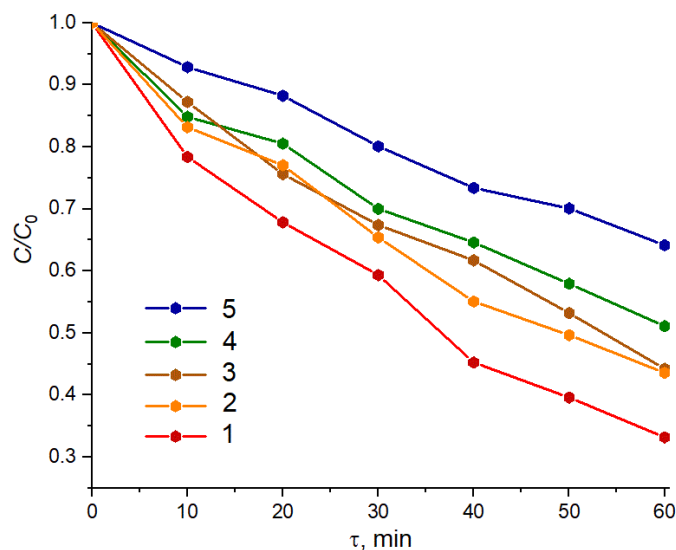


FIG. 5. Particle size distribution in sample 4

FIG. 6. Graph of average particle length versus bismuth phosphate content in a sample (x)


 FIG. 7. UV-Visible *MV* absorption spectra in the presence of a catalyst under the influence of visible light

 FIG. 8. *MV* degradation profiles of all photocatalysts

4. Conclusion

In the $\text{BiPO}_4\text{-BiVO}_4$ system obtained under hydrothermal conditions (4 hours of isothermal exposure at $200\text{ }^\circ\text{C}$), binary two-phase samples were obtained, which consist of nanocrystalline monoclinic modifications of bismuth vanadate and bismuth phosphate. The bismuth phosphate phase crystallized as a limited solid solution.

It was found that the sizes of crystallites of monoclinic bismuth orthovanadate and the sizes of its particles increased with a decrease in its content in the sample. Sizes of crystallites and particles in the phase based on monoclinic bismuth phosphate BiPO_4 are practically independent of the ratio of coexisting phases in the system.

The photocatalytic activity of obtained nanocrystalline powders in the $\text{BiPO}_4\text{-BiVO}_4$ system was studied during the oxidation of methyl violet. The sample of single-phase bismuth orthovanadate demonstrates a higher catalytic activity. Obtained results can be considered as intermediate for the search of methods for synthesis promising photocatalysts for the oxidation of organic water pollutants.

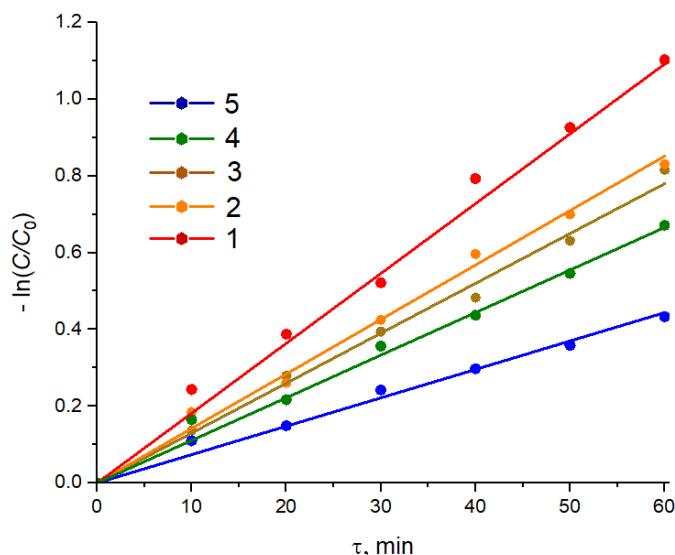


FIG. 9. Kinetic profiles (C/C_0) in logarithmic coordinates for all samples

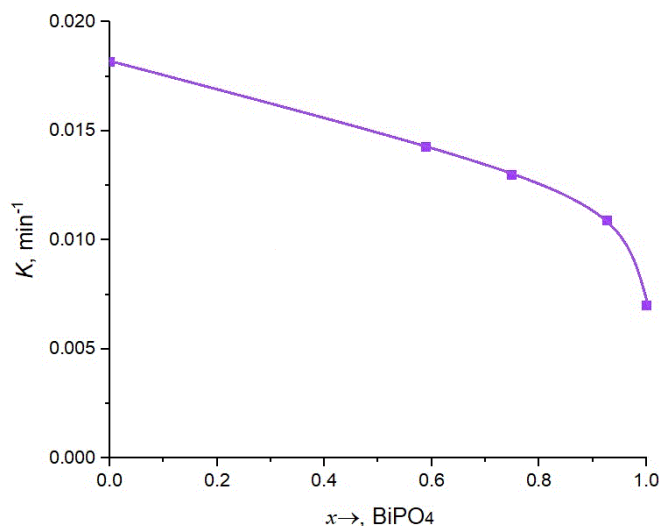


FIG. 10. Dependence of the rate constant of the catalytic reaction on the content of bismuth phosphate in the sample (x)

References

- [1] Malathi A., Madhavan J., Muthupandian Ashokkumar, Prabhakarn Arunachalam. A review on BiVO_4 photocatalyst: Activity enhancement methods for solar photocatalytic applications. *Applied Catalysis A: General*, 2018, **555**, P. 47–74.
- [2] Lin Y.-Y., Chi H.-T., Lin J.-H., Chen F.-H., Chen C.-C., Lu C.-S. Eight crystalline phases of bismuth vanadate by controllable hydrothermal synthesis exhibiting visible-light-driven photocatalytic activity. *Molecular Catalysis*, 2021, **506**, 111547.
- [3] Abdullah A.H., Ali N.M., Tahir M.I.M. Synthesis of bismuth vanadate as visible-light photocatalyst. *Malaysian J. of Analytical Sciences*, 2009, **13** (2), P. 151–157.
- [4] Dolić S.D., Jovanović D.J., Smits K., Babić B., Marinović-Cincović M., Porobić S., Dramićanin M.D. A comparative study of photocatalytically active nanocrystalline tetragonal zircon-type and monoclinic scheelite-type bismuth vanadate. *Ceramics Int.*, 2018, **44** (15), P. 17953–17961.
- [5] Nguyen T.D., Hong S.S. Facile solvothermal synthesis of monoclinic-tetragonal heterostructured BiVO_4 for photodegradation of rhodamine B. *Catalysis Communications*, 2020, **136**, 105920.
- [6] Abdi F.F., Savenije T.J., May M.M., Dam B., van de Krol R. The origin of slow carrier transport in BiVO_4 thin film photoanodes: a time-resolved microwave conductivity study. *The J. of Physical Chemistry Letters*, 2013, **4** (16), P. 2752–2829.
- [7] Jo W. J., Jang J.-W., Kong K., Kang H. J., Kim J. Y., Jun H., Parmar K.P.S., Lee J. S. Phosphate doping into monoclinic BiVO_4 for enhanced photoelectrochemical water oxidation activity. *Angewandte Chemie*, 2012, **124** (13), P. 3201–3205.
- [8] Ganguli S., Hazra C., Chatti M., Samanta T., Mahalingam V. A highly efficient UV–Vis–NIR active Ln^{3+} -doped $\text{BiPO}_4/\text{BiVO}_4$ nanocomposite for photocatalysis application. *Langmuir*, 2016, **32** (1), P. 247–253.
- [9] Shi L., Xue J., Xiao W., Wang P., Long M., Bi Q. Efficient degradation of VOCs using semi-coke activated carbon loaded ternary Z-scheme heterojunction photocatalyst $\text{BiVO}_4\text{-BiPO}_4\text{-}g\text{-C}_3\text{N}_4$ under visible light irradiation. *Physical Chemistry Chemical Physics*, 2022, **24** (37), P. 22987–22997.

- [10] Yang L., Peng S., Yu L., Zhao M. Microstructural, crystallographic, and luminescent analysis after grinding high-temperature monoclinic bismuth phosphate. *J. of Luminescence*, 2020, **225**, P. 117345.
- [11] Zhu Y., Ling Q., Liu Y., Wang H., Zhu Y. Photocatalytic performance of BiPO₄ nanorods adjusted via defects. *Applied Catalysis B: Environmental*, 2016, **187**, P. 204–211.
- [12] Naciri Y., Hsini A., Ajmal Z., Navío J.A., Bakiz B., Albourine A., Ezahri M., Benhachemi A. Recent progress on the enhancement of photocatalytic properties of BiPO₄ using p-conjugated materials. *Advances in Colloid and Interface Science*, 2020, **280**, 102160.
- [13] Buyanova E.S., Emelyanova Yu.V., Morozova M.V., Mikhailovskaya Z.A., Kaymieva O.S., Zhukovskiy V.M., Petrova S.A. Crystal structure and conductivity of bismuth-containing complex oxides. *Chimica Techno Acta*, 2015, **2** (4), P. 306–315.
- [14] Strobel R., Metz H.J., Pratsinis S.E. Brilliant yellow, transparent pure, and SiO₂-coated BiVO₄ nanoparticles made in flames. *Chemistry of Materials*, 2008, **20** (20), P. 6346–6351.
- [15] Gotić M., Musić S., Ivanda M., Šoufek M., Popović S. Synthesis and characterisation of bismuth (III) vanadate. *J. of Molecular Structure*, 2005, **744–747**, P. 535–540.
- [16] Jiang H.-q., Endo H., Natori H., Nagai M., Kobayashi K. Fabrication and photoactivities of spherical-shaped BiVO₄ photocatalysts through solution combustion synthesis method. *J. of the European Ceramic Society*, 2008, **28** (15), P. 2955–2962.
- [17] Manjunatha A.S., Pavithra N.S., Marappa S., Prashanth S.A., Nagaraju G., Puttaswamy Green synthesis of flower-like BiVO₄ nanoparticles by solution combustion method using lemon (Citrus Limon) juice as a fuel: Photocatalytic and electrochemical study. *Chemistry Select*, 2018, **3** (47), P. 13456–13463.
- [18] Kudo A., Omori K., Kato H. A novel aqueous process for preparation of crystal form-controlled and highly crystalline BiVO₄ powder from layered vanadates at room temperature and its photocatalytic and photophysical properties. *J. of the American Chemical Society*. 1999, **121** (49), P. 11459–11467.
- [19] Neves M.C., Trindade T. Chemical bath deposition of BiVO₄. *Thin solid films*, 2002, **406** (1–2), P. 93–97.
- [20] Packiaraj R., Devendran P., Bahadur S.A., Nallamuthu N. Structural and electrochemical studies of Scheelite type BiVO₄ nanoparticles: synthesis by simple hydrothermal method. *J. of Materials Science: Materials in Electronics*, 2018, **29** (15), P. 13265–13276.
- [21] Lin H., Ye H., Chen S., Chen Y. One-pot hydrothermal synthesis of BiPO₄/BiVO₄ with enhanced visible-light photocatalytic activities for methylene blue degradation. *RSC Advances*, 2014, **4** (21), P. 10968–10974.
- [22] Trinh N.D., Hoang H.H., Linh N.X., Vinh N.H., Vu H.T., Nguyen H.T., Vo D.-V.N., Do S.T., Duc L.T. A Facile Synthesis and Properties of Bismuth Vanadate (BiVO₄) Photocatalyst by Hydrothermal Method. *IOP Conference Series: Materials Science and Engineering*, 2019, **542** (1), 012059.
- [23] Zhang A., Zhang J., Cui N., Tie X., An Y., Li L. Effects of pH on hydrothermal synthesis and characterization of visible-light-driven BiVO₄ photocatalyst. *J. of Molecular Catalysis A: Chemical*, 2009, **304** (1–2), P. 28–32.
- [24] Samsudin M.F.R., Sufian S., Bashiri R., Mohamed N.M., Ramli R.M. Synergistic effects of pH and calcination temperature on enhancing photodegradation performance of m-BiVO₄. *J. of the Taiwan Institute of Chemical Engineers*, 2017, **81**, P. 305–315.
- [25] Yan Y., Li X., Ni T., Chang K., Li K., Guo Q. In-situ grafting BiVO₄ nanocrystals on a BiPO₄ surface: Enhanced metronidazole degradation activity under UV and visible light. *J. of the Taiwan Institute of Chemical Engineers*, 2019, **99**, P. 82–92.
- [26] Yan Y., Ni T., Du J., Li L., Fu S., Li K., Zhou J. Green synthesis of balsam pear-shaped BiVO₄/BiPO₄ nanocomposite for degradation of organic dye and antibiotic metronidazole. *Dalton Transactions*, 2018, **47** (17), P. 6089–6101.
- [27] Halder N.C., Wagner C.N.J. Separation of Particle Size and Lattice Strain in Integral Breadth Measurements. *Acta Crystallographica*, 1966, **20** (2), P. 312–313.
- [28] Seroglazova A.S., Popkov V.I. Synthesis of highly active and visible-light-driven PrFeO₃ photocatalyst using solution combustion approach and succinic acid as fuel. *Nanosystems: Phys. Chem. Math.*, 2022, **13** (6), P. 649–654.

Submitted 12 October 2022; revised 12 November 2022; accepted 24 November 2022

Information about the authors:

Olga V. Proskurina – Ioffe Institute, 194021 St. Petersburg, Russia; St. Petersburg State Institute of Technology, 190013, St. Petersburg, Russia; ORCID 0000-0002-2807-375X; proskurinaov@mail.ru

Ilke Diana Chetinel – St. Petersburg State Institute of Technology, 190013, St. Petersburg, Russia; ORCID 0009-0008-7287-298X; diana03ridak@gmail.com

Anna S. Seroglazova – Ioffe Institute, 194021 St. Petersburg, Russia; St. Petersburg State Institute of Technology, 190013, St. Petersburg, Russia; ORCID 0000-0002-3304-9068; annaseroglazova@yandex.ru

Victor V. Gusarov – Ioffe Institute, Politekhnikeskaya St. 26, St. Petersburg, 194021, Russia; ORCID 0000-0003-4375-6388; victor.v.gusarov@gmail.com

Conflict of interest: the authors declare no conflict of interest.

Stable hydrosol prepared by deaggregation from laser synthesis nanodiamond

Aleksandr E. Aleksenskii, Marina V. Baidakova, Andrey D. Trofimuk, Biligma B. Tudupova, Anastasia S. Chizhikova, Aleksandr V. Shvidchenko

Division of Solid State Electronics, Ioffe Institute, St. Petersburg, Russia

Corresponding author: Aleksandr E. Aleksenskii, blin@mail.ioffe.ru

PACS 82.70.Dd, 76.30.-v

ABSTRACT The new applications of nanodiamond in biology and nuclear physics require the use of products with a low content of impurities. One of the possible methods for obtaining a high-purity nanodiamond is the recently developed laser synthesis method. The aim of this work was to study the state of aggregation of laser synthesis nanodiamond particles in aqueous suspensions and to test the possibility of deaggregation of laser nanodiamond. The process of deaggregation of a laser synthesis nanodiamond is investigated. It was shown that the previously described process of deaggregation by milling with baking soda and the usual process of deaggregation give almost the same results. A solid phase from a colloidal solution of a laser synthesis nanodiamond has been isolated and investigated. The low content of impurities in the studied product was confirmed (less than 0.1% at.), the Raman, IR, and EPR spectra were studied.

KEYWORDS nanodiamonds, nanoparticles, optical properties, surface groups, EPR

ACKNOWLEDGEMENTS The authors thank O. Levinson and B. Zusman (Ray Techniques Ltd, Jerusalem, Israel) for providing the source material (LND) for this research. X-ray diffraction patterns were obtained on the equipment of the Joint Research Center “Material science and characterization in advanced technology” (Ioffe Institute, St. Petersburg, Russia). EDS measurements were performed using equipment of Engineering Center of St. Petersburg State Institute of Technology. Authors sincerely thank D. P. Danilovich for the extremely useful help in carrying out measurements and comprehensive methodological assistance and A. Ya Vul for useful discussion and support of the research. This research was carried out in the frame of the Government Topical Program for Ioffe Institute (project FFUG-2022-0012).

FOR CITATION Aleksenskii A.E., Baidakova M.V., Trofimuk A.D., Tudupova B.B., Chizhikova A.S., Shvidchenko A.V. Stable hydrosol prepared by deaggregation from laser synthesis nanodiamond. *Nanosystems: Phys. Chem. Math.*, 2023, **14** (3), 372–379.

1. Introduction

It is well known that nanodiamond is a product with a very wide range of applications [1]. However, in recent years, several new products based on nanodiamonds have appeared.

First of all, in the field of medical technology development, the possibility of using a detonation nanodiamond (DND) in MRI as a contrast agent has been practically demonstrated [2, 3] and as a component of the intracellular delivery system of the antiviral agent si-RNA (including in vivo) [4]. For such applications, the issue of developing a technology for obtaining a pharmaceutical-grade nanodiamond that meets Good Manufacturing Practice (GMP) requirements has become relevant. For injectable forms of medication, the content of metal contaminants should be no more than $1 \cdot 10^{-4} - 1 \cdot 10^{-8}$ at. %.

The use of nanodiamond for cooling and neutron reflection looks rather unexpected [5–7]. To be used as a special material in the atomic field, a product with zero content of impurities which absorb neutrons (B, Cd, Gd and other lanthanides, Co) is required.

Traditionally, the most commonly used type of nanodiamonds is detonation nanodiamond. This product is obtained by detonating explosive charges under special conditions and then separating the product from the detonation soot by the oxidizing method. Upon production of detonation nanodiamond, detonation soot is contaminated by erosion products of the explosive chamber material [12], the process of oxidative cleaning of nanodiamond is associated with contamination of the final product with heavy metals or corrosion products of reaction equipment. For this reason, conventional industrial detonation nanodiamond contains 0.5 – 1.0 % of ash-forming impurities. The most advanced cleaning methods make it possible to obtain an almost ash-free product, however, such processes are technologically quite complex and require the consumption of a large number of chemical reagents of a high degree of purification (Electronic Grade).

As a result, the question of the possibility of developing new methods for the synthesis of nanodiamonds that ensure the production of a high purity product directly in the synthesis process is relevant. One of such promising methods is recently developed method for obtaining nanodiamonds by inertial (laser) synthesis [13]. The method is based on laser ablation of a specially prepared target that containing soot and a hydrocarbon binder under a layer of optically transparent

liquid. Synthesized nanodiamond (laser nanodiamond, LND) was separated by flotation in deionized water [14, 15]. This method does not require the removal of the non-diamond component, since the resulting product does not contain a significant amount of non-diamond carbon. Recently, information has also been published on the synthesis of nanodiamonds directly in a deaggregated form when irradiated with a femtosecond laser with ethanol [16] and liquid carbon monoxide CO [17], but at present these technologies seem not might to be used for industrial scale production.

A serious advantage of the laser synthesis process is the exclusion of the use of explosives, which are not freely available reagents and require special permits, equipped facilities for storage and processing, as well as a special order of transportation.

For many applications, it is extremely important to obtain nanodiamond in the form of a colloidal solution containing individual free particles. In the form of a colloidal solution, nanodiamonds can be relatively easily cleaned and subjected to various chemical modifications.

In recent paper [18], Stehlik and co-authors reported successful deaggregation of a laser nanodiamond by obtaining a colloidal solution of free particles with a negatively charged surface by a method developed by Mochalin [19]. The method is based on ultrasonic processing of the initial nanodiamond in a NaCl or NaHCO₃ slurry. At the same time, before ultrasonic treatment, the source material is processed in the same way as previously described [9] or [10]. For this reason, there are reasonable doubts about the need to use salt slurry.

The aim of this work was to study the state of nanodiamond particles obtained by laser synthesis in aqueous suspensions and to test the possibility of obtaining nanodiamond colloids of this type consisting of free particles without the use of slurry of soluble salts and operations associated with this method. We also investigated the properties of such solutions, isolated a solid product from a colloidal solution, conducted a primary assessment of the purity of the resulting product and investigated some practically important physical properties.

2. Experimental

The laser nanodiamond (LND) sample was obtained by laser ablation of a target containing industrial carbon black and a hydrocarbon binder with the addition of stearic acid under a layer of water. A pulsed solid-state YAG laser with a wavelength of 1064 nm was used for irradiation. The synthesized LND was separated by flotation, additionally washed and dried. A more complete description of the synthesis is given in [13].

We used the deaggregation procedure similar to that previously described in [9]. The powder of the LND 7.5 g mass was placed in a graphite boat, which was installed in a quartz tube with a heater blown by a flow of hydrogen. The treatment temperature was 600 °C, the hydrogen treatment time was 6 hours. After cooling the product was mixed with 200 ml of deionized water and sonicated for 15 minutes (the temperature increase was 30 °C). After sonication, the product was separated by centrifugation (RCF $1.8 \cdot 10^4$ g), while a gray (sometimes bright blue or light blue, the origin of this color is the subject of discussion) precipitate and a black color supernatant were formed. Sonication of precipitate in water and centrifugation of obtained colloidal solution were repeated three times, as a result, 500 ml of a black supernatant were obtained.

The DND sample for ESR measurement was obtained from an industrial nanodiamond manufactured by SKTB "Technolog". The product was purified by washing with hydrochloric and hydrofluoric acid, annealed in hydrogen at 600 °C, sonicated and separated by centrifugation in accordance with [9]. The solid phase was separated by a vacuum rotary evaporator.

LND particle sizes were measured using a Mastersizer 2000 laser diffraction analyzer (Malvern Instruments, UK) and a LiteSizer 500 nanoparticle analyzer (Anton Paar, Au). The same device was used to measure the electrokinetic potential (PALSE).

X-ray diffraction (XRD) data were obtained using a powder diffractometer D2 Phaser (Bruker AXS, Germany) designed in vertical Bragg–Brentano θ – θ geometry and equipped with semiconductor linear position-sensitive detector LYNXEYE with opening angle of 5°. The measurements were performed in symmetric θ – 2θ scan mode using Cu-K α radiation monochromatized by Ni filter. To average the effect of preferred crystallite orientation, the sample was rotated around the sample holder axis coinciding with the axis of the diffractometer goniometer. To avoid the diffraction contribution of the sample holder and the adhesive, the samples were mounted on a background-free holder in the form of the Si(119) single crystal wafer. XRD patterns were analyzed using the TOPAS-5 program using the Scherrer model.

The Raman spectra were obtained using the Ntegra Spectra spectrometer (SOL Instruments, NT-MDT, Ru). A 532.01 nm diode laser (Integrated Optics) was used. To prevent heating of the sample, the radiation power density did not exceed $2 \cdot 10^3$ W/cm⁻². Diffraction gratings 600/600 bar/mm were used. All measurements were carried out at room temperature.

IR spectra were recorded using an Infracum FT-08 Fourier spectrometer (Lumex, Ru). To register the spectrum, 200 measurements were made with a resolution of 2 cm⁻¹.

Elemental analysis was performed using TESCAN VEGA-3 SBH SEM with an INCA X-act X-ray energy analyzer (Oxford Instruments, UK). The average variation for each channel is no more than 0.5 %.

EPR spectra were obtained using the ESR 70-03 XD/2 (KBS, Be) 9 GHz band (X-band) with a maximum generator power of 0.8 W. (microwave attenuation of 22 dB), modulation amplitude of 0.1 mT, number of signal accumulations

of 1, total spectrum recording time for one pass was 100 s. For quantitative measurements, short quartz tubes on a Teflon holder were used.

Sonication was performed using a UZG4-1.0/22 generator with magnetostrictive transducer with titanium alloy horn on frequency of 22 kHz. The acoustic power measured by the calorimetric method was 35 W.

Particle separation was performed on a Sigma 6-16 centrifuge with a 12169 rotor equipped with a set of Sarstedt capsules #0037-109.4827.

3. Results and discussion

The studied sample of nanodiamond looked initially as a gray powder. Its properties are described in more detail in [15]. To study the particle size distribution, the sample of the initial powder weighing 15 mg was mixed with 150 ml of water and sonicated for 15 minutes with 5 Wt power. The particle size distribution measured after cooling the sample is shown in Fig. 1.

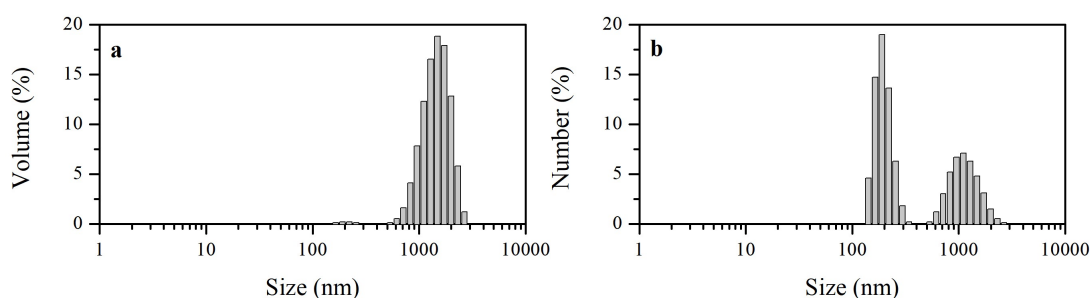


FIG. 1. The distribution of LND particles in water suspension after sonication by volume (a) and by the number of particles (b). Data was determined by the DLS

According to the results of measurements using DLS, it was found that most of the particles have a size of about 1 micron, but there is a significant proportion of particles with a smaller diameter (200 nm). Similar results were obtained when measuring the particle distribution by laser diffraction (Fig. 2). The distribution peaks are slightly shifted relative to the results of DLS measurements (220 and 2000 nm, respectively).

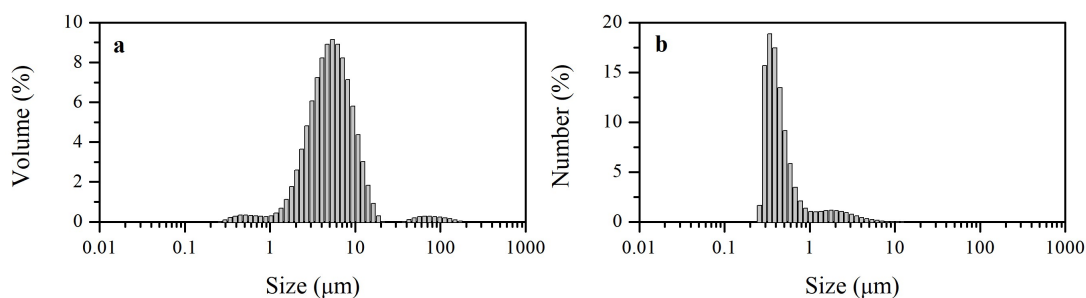


FIG. 2. The distribution of LND particles in water suspension after sonication by volume (a) and by the number of particles (b). Data was determined by the laser diffraction (Mastersizer 2000)

To explore the possibility of obtaining a colloidal solution containing single nanodiamond particles, we used the deaggregation procedure similar to that previously described by Williams et al [9].

The particles size distribution by volume in the obtained black colloidal solution, determined by the DLS, is shown in Fig. 3. Based on these results, we can conclude that the formation of a colloidal solution of LND is similar to the previously described [9].

When the produced solution was evaporated, it was possible to obtain a solid phase. The concentration of produced suspension was approximately 0.8 % by weight. Thus, the total yield of the solid phase was about 50 % of the initial mass of nanodiamond, which is quite close to that claimed by Stehlik [18].

An XRD pattern of the isolated solid product confirmed that the dispersed phase is the diamond (Fig. 4). According to the phase analysis, all the intense reflections observed in the XRD patterns of all samples correspond to the C cubic crystal (diamond phase, space group Fm3 (227), $a = 3.56637 \text{ \AA}$ at room temperature) [19]. All possible diamond reflections are observed; therefore, the samples are polycrystalline with crystallites about 4 nm in size (the crystallite sizes D obtained in the model without microstrains ($\varepsilon_s = 0$)). A thorough analysis of the XRD reflection profiles of the sample by the TOPAS methods has shown that the broadening of reflections is caused not only by the crystallite size D but also arises

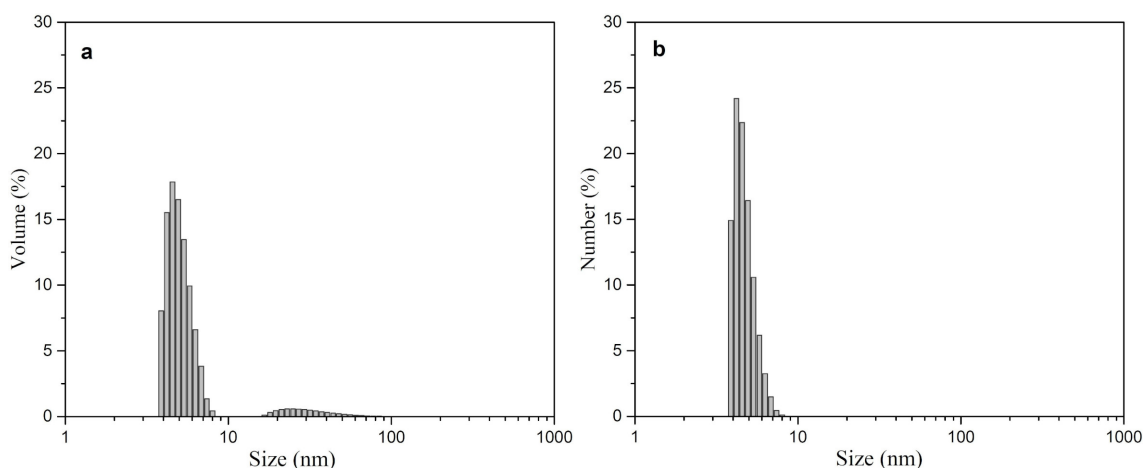


FIG. 3. The particle size distribution by volume (a) and by the number (b) of LND particles in supernatant water after deaggregation procedure. Data was determined by the DLS

due to microdeformations εs in them. The mean values of D obtained in the model with non-zero εs are characterized by slightly lower standard deviations than those calculated using the $\varepsilon s = 0$, but both methods give comparable values that agree well within one e.s.d. ($D = 4.50(4)$ and $4.34(4)$ nm, respectively). Also it should be noted the change of the observed preferred orientation along the (111) direction, which is typical for a powder of isolated diamond nanoparticles and was previously mentioned in the literature [10].

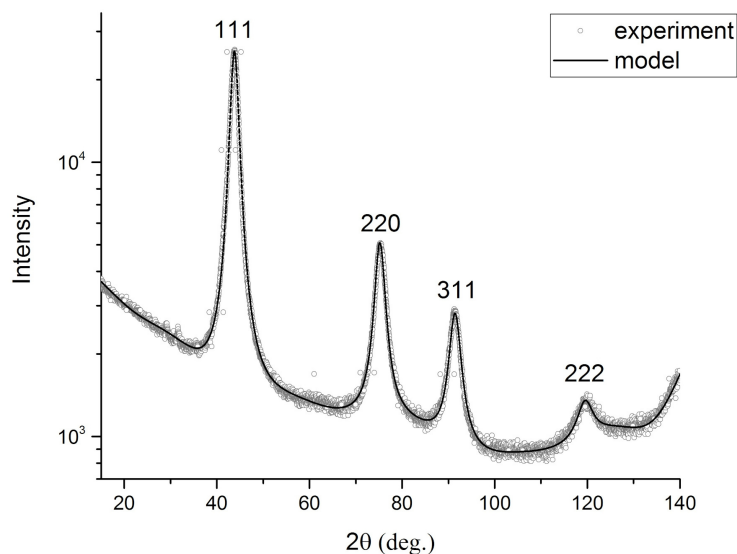


FIG. 4. Model and experimental XRD patterns of the isolated solid product. The Miller indices hkl of the reflections of the observed crystalline diamond phases are indicated

The results of particle size measurements performed by the DLS method and the value of the crystal size obtained by processing X-ray diffraction data coincide well. This suggests that we have produce a colloidal solution containing free nanodiamond particles.

The Raman spectrum of the isolated solid product (Fig. 5) has a form similar to that of the Raman spectrum of a deaggregated DND obtained by similar procedure described in [9]. It has the same characteristic features: some displacement of the peak center relative to a massive diamond and broadening of the spectrum lines. Moreover, the diamond peak maximum located at 1326 cm^{-1} , which corresponds to 4 nm particles by phonon confinement model (described at [23]). Note that there is some discrepancy between the X-ray data and the Raman spectrum. While there are no signs of the presence of graphite phase residues on the X-ray of the LND, in the Raman spectrum of the LND, the ratio of the diamond and G-peak is noticeably smaller compared to the spectrum of the DND.

Figure 6 shows the IR spectra of the sample of deaggregated LND in comparison with a sample of a deaggregated DND. The structure of the spectra is repeated, except for a narrow peak of 1394 cm^{-1} , which is absent in the spectrum of the LND.

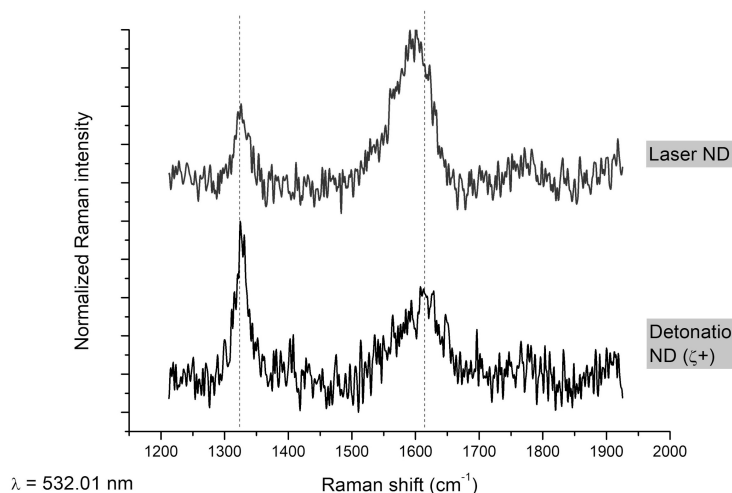


FIG. 5. The Raman spectrum of a deaggregated LND. For comparison, the Raman spectrum of a deaggregated DND is given

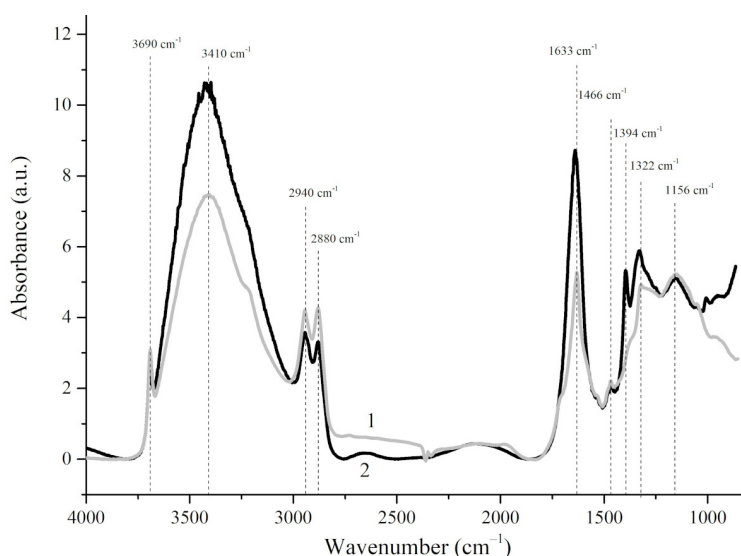


FIG. 6. IR spectra of deaggregated LND (1) and deaggregated DND (2)

The presence of a wide band with a maximum at 3410 cm^{-1} and a narrow band with a maximum at 3690 cm^{-1} corresponds to the valence vibrations of the O–H bond, mainly water sorbed by the sample itself. A narrow band with a peak in the region of 1636 cm^{-1} refers to deformation vibrations of O–H. Bands in the regions of 2960 , 2880 , 1466 cm^{-1} correspond to valence vibrations of methyl and methylene groups ($-\text{CH}_3$, $-\text{CH}_2$). The peak in the region of 1322 cm^{-1} characterizes the valence oscillations of C–C in diamond. Fluctuations of C–O belonging to lactones or esters are manifested in the region of 1156 cm^{-1} .

Comparison of the spectra shows that samples of diamond nanoparticles by the laser and the detonation synthesis have similar composition of functional groups on the surface. The main difference is that the peak in the 1394 cm^{-1} region corresponding to the C–O valence oscillations is not presented in the spectrum of the laser synthesis sample.

As has been repeatedly noted, the deaggregated DND, which after hydrogen treatment contains methyl and other groups with C–H bonds, is characterized by a positive surface charge with an electrokinetic potential of $40 - 50\text{ mV}$. A similar pattern is observed for laser synthesis nanodiamond after treatment in hydrogen. The measured value of the electrokinetic potential was about $+45\text{ mV}$.

The elemental composition of the LND was studied by the energy-dispersive X-ray spectroscopy (EDS) method. A typical EDS spectrum is shown in Fig. 7, the corresponding impurity content estimate is given in the upper right. A more accurate analysis result is shown in Table 1.

The content of the most impurity elements in the studied sample is at the noise level and corresponds to well-purified samples of DND. Attention is drawn to the low nitrogen content, which is usually much higher for DND – about 4% or more [20]. However it is not zero at all as expected. This fact is presumably due to the laser synthesis in the air

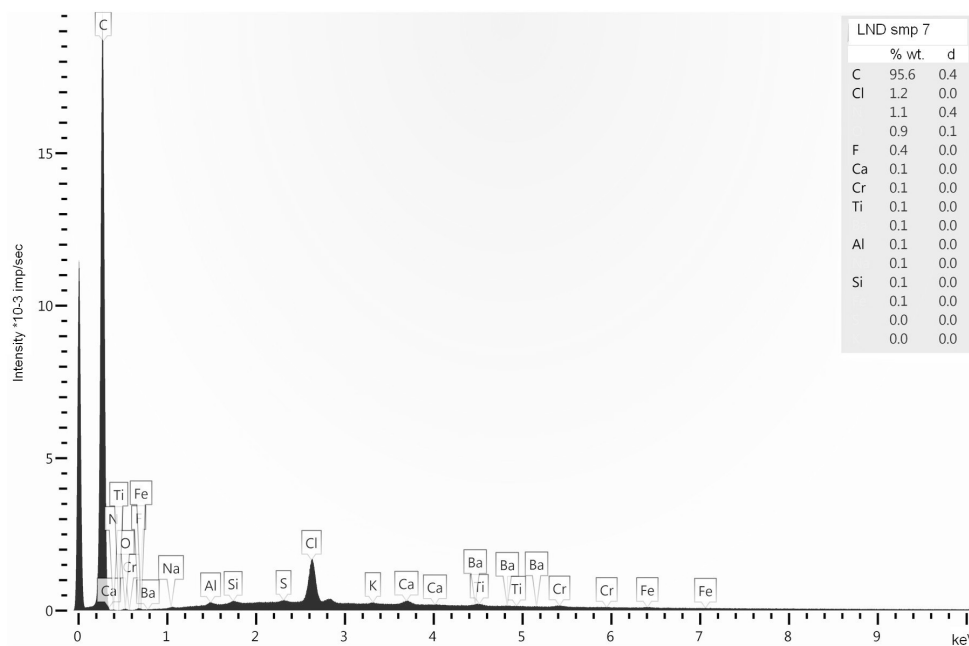


FIG. 7. Results of EDS analysis of deaggregated LND

TABLE 1. Element composition of LND sample

	C	N	O	F	Na	Al	Si	S	Cl	K	Ca	Ti	Cr	Fe	Ba
mass.%	95.59	1.15	0.91	0.44	0.06	0.07	0.05	0.05	1.23	0.04	0.13	0.08	0.09	0.05	0.08
at.%	97.38	1.00	0.69	0.29	0.03	0.03	0.02	0.02	0.42	0.01	0.04	0.02	0.02	0.01	0.01

atmosphere. In this case the air dissolved in the water used is captured. It is also possible to capture atmospheric nitrogen directly during synthesis due to the intensive mixing. Obviously the result can be improved by blowing of the argon and providing the laser synthesis in a nitrogen-free atmosphere. We should also hope for a significant reduction in the content of impurities during laser synthesis under conditions corresponding to GMP.

The measured EPR spectrum has no significant differences from the EPR spectrum of the detonation nanodiamond (Figs. 8, 9). There is no splitting of the single intense line. The concentration of paramagnetic centers in the LND sample is slightly higher (approximately 105 %) of the concentration of paramagnetic centers ($5.0 \cdot 10^{18}$ units/g) in the reference sample of detonation nanodiamond.

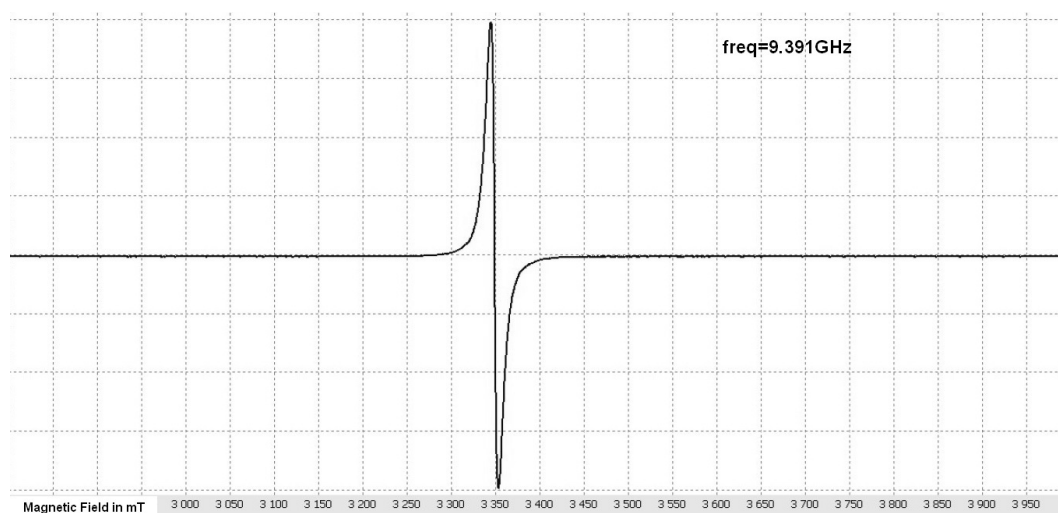


FIG. 8. EPR spectrum of deaggregated LND. Sample mass is 5.9 mg



FIG. 9. EPR spectrum of deaggregated DND with positive surface charge. Sample mass is 6.2 mg

For the purpose of preliminary evaluation of the relaxivity of the resulting product spectra with high power input 200 and 400 mW were measured. There was not found the significant change in the shape of the lines or signal suppression. This suggests a potentially high spin-spin interaction constant, which is needed for the use of nanodiamond in contrast agents for MRI. Of course, the correct measurement of the relaxivity of a deaggregated LND will be the subject of the next article.

4. Conclusions

1. The aggregation of nanodiamond particles by laser synthesis in aqueous suspensions is investigated. It has been established that nanodiamonds are contained in aggregates ranging in size from 200 nm to 1 μm depending on modifications of the synthesis conditions. Nanometer particles of the laser nanodiamond were not detected in the pristine product.
2. The process of deaggregation of the laser synthesis nanodiamond is investigated. The colloidal solution of LND with a positive surface charge containing free nanodiamond particles of about 5 nm in size was obtained.
3. The output of the deaggregated product is nearly to the previously described process using salt slurry. The need for its use is not obvious, thus the use of salt slurry is, apparently, a “successful complication” of the deaggregation procedure, because of the fact that the use of additional reagents of inadequate quality can cause contamination of the final product.
4. The solid phase from the colloidal solution of laser nanodiamond is isolated and investigated, its diamond nature is confirmed. The low content of impurities in the investigated product was confirmed.
5. The EPR spectra of the deaggregated laser synthesis nanodiamond has been studied. The parameters of the EPR signal are close to those for the detonation synthesis nanodiamond, which suggests the possibility of its use in relaxation agent for MRI.

References

- [1] Dideikin A. *Applications of Detonation Nanodiamonds in Detonation Nanodiamonds: Science and Applications*. Jenny Stanford Publishing, Singapore, 2014, 346 p.
- [2] Panich A., Salti M., Prager O., Swissa E., Kulvelis Yu., Yudina E., Aleksenskii A., Goren Sh., Vul' A., Shames A. PVP-coated Gd-grafted nanodiamonds as a novel and potentially safer contrast agent for in vivo MRI. *Magn Reson Med.*, 2021, 8, P. 1–8.
- [3] Panich A., Shames A., Aleksenskii A., Yudina E., Vul A.Ya. Manganese-grafted detonation nanodiamond, a novel potential MRI contrast agent. *Diamond & Related Materials*, 2021, 119, 108590
- [4] Jingru Xu, Mengjie Gu, Lissa Hooi, Tan Boon Toh, Dexter Kai Hao Thng, Jhin Jieh Limb, Edward Kai-Hua Chow. Enhanced penetrative siRNA delivery by a nanodiamond drug delivery platform against hepatocellular carcinoma 3D models. *Nanoscale*, 2021, 13, 16131
- [5] Artem'ev V. Estimation of neutron reflection from nanodispersed materials. *At. Energy*, 2006, 101, P. 901–904.
- [6] Nesvizhevsky V., Lychagin E., Muzychka A., Strelkov A., Pignol G., Protasov K. The reflection of very cold neutrons from diamond powder nanoparticles. *Nucl. Instrum. Methods*, 2008, 595, P. 631–636.
- [7] Aleksenskii A., Bleuel M., Bosak A., Chumakova A., Dideikin A., Dubois M., Korobkina E., Lychagin E., Muzychka A., Nekhaev G., et al. Clustering of Diamond Nanoparticles. Fluorination and Efficiency of Slow Neutron Reflectors. *Nanomaterials*, 2021, 11, 1945.
- [8] Kruger A., Kataoka F., Ozawa M., Fujino T., Suzuki Y., Aleksenskii A., Vul' A., Osawa E. Unusually tight aggregation in detonation nanodiamond: Identification and disintegration. *Carbon*, 2005, 43 (8), P. 1722–1730.
- [9] Williams O., Hees J., Dieker C., Jager W., Kirste L., Nebel C. Size-Dependent Reactivity of Diamond Nanoparticles. *ACS Nano*, 2010, 4 (8), P. 4824–4830.
- [10] Aleksenskiy A., Eydelman E., Vul' A. Deaggregation of Detonation Nanodiamonds. *Nanosci. Nanotechnol. Lett.*, 2011, 3, P. 68–74.

- [11] Aleksenskii A., Kirilenko D., Trofimuk A., Shvidchenko A., Yudina E. Deaggregation of polycrystalline diamond synthesized from graphite by shock-compression. *Fullerenes, Nanotubes and Carbon Nanostructures*, 2021, 29 (10), P. 779–782.
- [12] Aleksenskii A. *Technology of preparation of detonation nanodiamond in Detonation Nanodiamonds: Science and Applications*, Jenny Stanford Publishing, Singapore, 2014, 346 p.
- [13] Perevedentseva E., Peer D., Uvarov V., Zousman B., Levinson O. Nanodiamonds of Laser Synthesis for Biomedical Applications. *J. of Nanoscience and Nanotechnology*, 2015, 15, P. 1045–1052.
- [14] Panich A., Shames A., Zousman B., Levinson O. Magnetic resonance study of nanodiamonds prepared by laser-assisted technique. *Diamond & Related Materials*, 2012, 23, P. 150–153
- [15] Baidakova M., Kukushkina Yu., Sitnikova A., Yagovkina M., Kirilenko D., Sokolov V., Shestakov M., Vul' A., Zousman B., Levinson O. Structure of Nanodiamonds Prepared by Laser Synthesis. *Physics of the Solid State*, 2013, 55 (8), P. 1747–1753.
- [16] Nee C.-H., et al. Direct synthesis of nanodiamonds by femtosecond laser irradiation of ethanol. *Nature Sci. Rep.*, 2016, 6, 33966.
- [17] Armstrong M., Lindsey R., Goldman N., Nielsen H., Stavrou E., Fried L., Zaugg J., Bastea S. Ultrafast shock synthesis of nanocarbon from a liquid precursor. *Nature Comm.*, 2020, 11, 353.
- [18] Stehlik S., Henych J., Stenclova P., Kral R., Zemenova P., Pangrac J., Vanek O., Kromka A., Rezek B. Size and nitrogen inhomogeneity in detonation and laser synthesized primary nanodiamond particles revealed via salt-assisted deaggregation. *Carbon*, 2021, 171, P. 230–239.
- [19] Mochalin V., Turcheniuk K., Trecuzzi C., Deeleepojananan C. Salt-Assisted Ultrasonic Deaggregation of Nanodiamond. *ACS Appl. Mater. Interfaces*, 2016, 8, P. 25461–25468.
- [20] Topas Version 5. Technical reference. Bruker AXS, Karlsruhe, Germany, 2014. URL: <https://www.bruker.com/en/products-and-solutions/diffractometers-and-scattering-systems/x-ray-diffractometers/diffrac-suite-software/diffrac-topas.html>
- [21] Hom T., Kiszenik W., Post B. Accurate lattice constants from multiple reflection measurements. II. Lattice constants of germanium silicon, and diamond. *J. Appl. Cryst.*, 1975, 8, P. 457–458.
- [22] Shenderova O., Vlasov I., Turner S., Gustaaf Van Tendeloo, Orlinskii S., Shiryaev A., Khomich A., Sulyanov S., Jelezko F., Wrachtrup J. Nitrogen Control in Nanodiamond Produced by Detonation Shock-Wave-Assisted Synthesis. *J. Phys. Chem. C*, 2011, 115, P. 14014–14024.
- [23] Meilakhs A., Koniakhin S. New explanation of Raman peak redshift in nanoparticles. *Superlattices Microstruct.*, 2017, 110, P. 319–323.

Submitted 20 August 2022; revised 26 April 2023; accepted 16 June 2023

Information about the authors:

Aleksandr E. Aleksenskii – Division of Solid State Electronics, Ioffe Institute, Polytechnicheskaya 26, 194021 St. Petersburg, Russia; ORCID 0000-0002-5004-6993; blin@mail.ioffe.ru

Marina V. Baidakova – Centre of Nanoheterostructure Physics, Ioffe Institute, Polytechnicheskaya 26, 194021 St. Petersburg, Russia; ORCID 0000-0002-5524-7233; baidakova@mail.ioffe.ru

Andrey D. Trofimuk – Division of Solid State Electronics, Ioffe Institute, Polytechnicheskaya 26, 194021 St. Petersburg, Russia; ORCID 0000-0003-3140-0245; trofimuk.ad@mail.ioffe.ru

Biligma B. Tudupova – Division of Solid State Electronics, Ioffe Institute, Polytechnicheskaya 26, 194021 St. Petersburg, Russia; ORCID 0000-0002-7655-294X; biligma0201@gmail.com

Anastasia S. Chizhikova – Division of Solid State Electronics, Ioffe Institute, Polytechnicheskaya 26, 194021 St. Petersburg, Russia; ORCID 0000-0002-0120-5847; chizhikova@mail.ioffe.ru

Aleksandr V. Shvidchenko – Division of Solid State Electronics, Ioffe Institute, Polytechnicheskaya 26, 194021 St. Petersburg, Russia; ORCID 0000-0002-5417-7472; avshvid@mail.ioffe.ru

Conflict of interest: the authors declare no conflict of interest.

Synthesis and characterization of one pot electrochemical graphene for supercapacitor applications

R. Naresh Muthu

Department of Physics, J. P. College of Arts and Science, Tenkasi – 627852, Tamilnadu, India
(Affiliated to Manonmaniam Sundaranar University, Tirunelveli, Tamil Nadu, India)

rnaresh7708@gmail.com

ABSTRACT Graphene can be used to store energy as well as a supercapacitor material because of its unique physical and chemical properties, including high specific surface area, high chemical stability, high mechanical strength, and oxidation resistance. In this report, a facile, green, and cost-effective approach has been adopted to synthesize graphene sheets through an electrochemical exfoliation technique for supercapacitor applications. Graphene sheets were synthesized using aqueous electrolyte (Ag/AgCl, 0.1 M H₂SO₄) with four different exfoliation potentials such as 3, 5, 7 and 9 V. The prepared graphene sheets were subjected to characterization techniques such as Raman spectroscopy, X-ray photoelectron spectroscopy (XPS), X-ray diffraction (XRD), and atomic force microscopy (AFM). The Raman results revealed that the defect density and thickness of the graphene layers increased with increased in the exfoliation potential and then eventually decreased. Among all potentials, the maximum crystalline size of graphene was observed for the potential of 5 V, an intermediate crystalline size of 9 V, and minimum for 7 V, showing that the exfoliated graphene layer was sensitive to the exfoliation potential. XPS study shows the structural oxidation (relative percentage of carbon and oxygen) of the exfoliated graphene at different potentials. The results indicate that electrochemically exfoliated graphene (5 V) has been successfully produced. The behaviour of 5 V graphene has been examined using a charge-discharge (CD) curve and cyclic voltammetry (CV) for supercapacitor applications. The maximum value of specific capacitance obtained is 198 F·g⁻¹ at a current density of 0.14 A·g⁻¹ in 6 M KOH. The highest value obtained for energy density and power density is 17 W·h·kg⁻¹ and 1176 W·kg⁻¹.

KEYWORDS graphene, electrochemical exfoliation, supercapacitor, EDLC

FOR CITATION Naresh Muthu R. Synthesis and characterization of one pot electrochemical graphene for supercapacitor applications. *Nanosystems: Phys. Chem. Math.*, 2023, **14** (3), 380–389.

1. Introduction

Due to the continuous depletion of fossil fuels, we require an alternative source of energy. Batteries, fuel cells, and electrochemical supercapacitors are some of the alternative ways to store energy. Supercapacitors got attention because of their distinct features, like high power density, fast charging/discharging rates, high stability, and long-life duration compared to batteries and other electrochemical energy storage devices. Electrochemical supercapacitors can be classified as pseudo-capacitors, electrical double layer capacitors, and hybrid capacitors. Apart from lifetime, energy density and power density are the two parameters for the selection of supercapacitor materials [1, 2].

Graphene is a crystalline allotrope of carbon having a single atomic 2D layer with all carbon having sp² hybridization and the remaining electron in the p-orbital form large pi-bond [3]. Due to the presence of a sigma bond, graphene is flexible and stable, the presence of elastic corrugation can bear thermal fluctuation through the modulating bond length. Graphene is attractive due to its exceptional properties [4] including high thermal conductivity (~ 5000 W·m⁻¹·K⁻¹), high electron mobility (15000 cm²·V⁻¹·s⁻¹), high current density, high specific surface area (2620 m²·g⁻¹), high mechanical flexibility. The intrinsic capacitance of graphene single layer was found to be 21 μF·cm⁻² [5] i.e. the upper limit for electrical double-layer capacitance for carbon-based materials. This suggests that graphene is the ideal carbon electrode material for EDL supercapacitors because the maximum specific capacitance value achieved by graphene when the entire surface of 2675 m²·g⁻¹ is fully utilized is 550 F·g⁻¹.

There are various methods involved in the production of graphene such as Hummer's method, microwave method, chemical vapour deposition (CVD) method, dispersion method and electrochemical exfoliation method. Recently, electrochemical exfoliation of graphene from graphite has attracted researchers due to its easy, cheap and environmental friendly approach to produce high-quality graphene [6].

This report deals with electrochemical exfoliation of graphene from graphite rod in aqueous solution (sulfuric acid) [6–8]. Here SO₄²⁻ ions from sulfuric acid (H₂SO₄) acts as an exfoliating agent, it gets intercalate between graphite layer and increase the spacing between two consecutive graphite layers, results in graphene layer separation from the

graphite surface. By optimizing the applied potential for electrochemical process, the oxidation of graphene during exfoliation can be reduced. This result suggests that the 5 V exfoliated graphene were relatively higher C/O ratio (from XPS), less defect ratio (from Raman), multiyear graphene (from Raman and AFM) among the 7 and 9 V exfoliated graphene. Based on this, we have chosen 5 V prepared graphene for supercapacitor applications. The specific capacitance of the produced 5 V graphene has been calculated using cyclic voltammetry and charge-discharge curve. It has been found that the maximum specific capacitance value achieved from charging-discharging curve is $198 \text{ F}\cdot\text{g}^{-1}$, the maximum energy density and maximum power density calculated are $17.54 \text{ W}\cdot\text{h}\cdot\text{kg}^{-1}$ and $1178 \text{ W}\cdot\text{kg}^{-1}$ respectively.

2. Experimental section

2.1. Materials

Polyvinylidene fluoride (PVDF) membrane (220 nm pore size) and carbon black were supplied by Sigma-Aldrich. Sulfuric acid (H_2SO_4) 98 %, N-Methyl-2-pyrrolidone (NMP), and potassium hydroxide (KOH) were obtained from Merck. High-purity graphite rods (99.9995 %, 3.05 mm dia, and 305 mm long) and polyvinylidene fluoride (PVDF) were received from Alfa Aesar. All purchased reagents were of analytical grade and used without further purification. Double distilled water was used throughout this study.

2.2. Electrochemical exfoliation of graphene

Electrochemical exfoliation of graphite rods (working electrode) were performed using a three-electrode cell configuration with 0.1 M H_2SO_4 (0.449 ml of sulfuric acid by using a Sartorius Proline micro pipette to 80 ml of water) as an electrolyte (Ag/AgCl, 0.1 M H_2SO_4) [9]. The counter electrode was platinum mesh and the reference electrode was an Ag/AgCl. A constant potential of 3, 5, 7 and 9 V was applied for 1 h using Chronoamperometry technique (CHI 660E electrochemical workstation). After exfoliation, the product was collected by vacuum filtration on a polyvinylidene fluoride (PVDF) membrane (220 nm pore size) filter and washed sequentially with deionized water and ethanol until the PH attains 6 – 7 to remove the residual impurities of electrolytes (SO_4^{2-}). Then it was dried at 100°C for overnight in hot air oven. Finally, electrochemically exfoliated graphene was obtained as fine block powder.

2.3. Working electrode preparation for electrochemical supercapacitor applications

2.3.1. Chemicals and electrode: The 5 V prepared graphene was used as an active material, polyvinylidene fluoride (PVDF) as a binder, N-methyl-2-pyrrolidone (NMP) as solvent for active material dispersion, carbon black to provide high surface area and cylindrical platinum electrode.

2.3.2. Working electrode fabrication: The active material (40 mg), binder PVDF (5 mg) and carbon black (5 mg) are dispersed in 0.5 ml of NMP and mix properly to prepare a thick mixture. This mixture is coated over platinum electrode. Total mass loaded on electrode is 3.4 mg. The electrode then dried in an oven for approximately 24 hours at the temperature of 60°C . Binder makes the active material attached to the electrode in KOH electrolyte solution. The prepared electrode used for electrochemical characterization.

2.4. Characterization

As electrochemically synthesized graphene were subjected to structural, chemical bonding and functional group analysis using characterization techniques. Raman spectroscopy (Thermofischer, 532 nm Ar (green) Laser) was used to characterize the number of graphene layers. The functional groups and oxygen content of the exfoliated samples was determined by X-ray photoelectron spectroscopy (XPS). XPS analysis was performed using an AXIS Supra, Kratos Analytical, with a monochromatic Al K α radiation. High resolution spectra were collected at pass energy is 20 eV. The synthesized graphene sheets were dried at 120°C for 24 h before the XPS test to minimize the physically absorbed water. The deconvolution of the C 1 s peak was performed by using origin software. X-ray diffraction (XRD) patterns were recorded at room temperature PAN alytical EMPYREAN with Cu K α radiation ($\lambda = 1.5406 \text{ \AA}$) in the range from 10° to 80° . The electrochemical characterization of prepared electrode was performed by an electrochemical workstation (CHI 660 E). A three-electrode system constituting working electrode (graphene coated platinum electrode), counter electrode (platinum mesh) and reference electrode (saturated calomel electrode, SCE) were used to perform cyclic voltammetry and chronopotentiometry analysis. All experiments were performed at ambient temperature and 6 M KOH used as an electrolyte. The cyclic voltammetry (CV) analysis performed at the potential window ranging from -1 to 0 V at different scan rate varying from 10 to $200 \text{ mV}\cdot\text{s}^{-1}$. The chronopotentiometry charge-discharge analysis is carried out in potential window of 0.8 V at different current densities from 0.3 to $3 \text{ A}\cdot\text{g}^{-1}$. Specific capacitance values C_s from cyclic voltammetry curves were calculated using equation (1) [11]:

$$C_s = \frac{1}{vm(V_2 - V_1)} \int_{V_1}^{V_2} i(V)dv, \quad (1)$$

where C_s , V_1 , V_2 , i , v , m are specific capacitance ($\text{F}\cdot\text{g}^{-1}$), initial voltage (V), final voltage (V), current (A), scan rate ($\text{mV}\cdot\text{s}^{-1}$) and active mass (g), respectively. The value of integral in numerator was obtained by measuring area under the CVs. The specific capacitance (C_{sp}) from charge-discharge curve is calculated using equation (2) [12],

$$C_{sp} = \frac{I\Delta t}{m\Delta V}, \quad (2)$$

where I , Δt , m , ΔV are current, discharging time, active mass and potential window, respectively.

Energy density (E) and Power density (P) is calculated by using equations (3) and (4) [11]:

$$E = \frac{1}{2} \left[\frac{C_{sp} (V_f - V_i)^2}{3.6} \right] \quad (\text{W}\cdot\text{h}\cdot\text{kg}^{-1}), \quad (3)$$

$$P = \frac{3600 \cdot E}{\Delta t} \quad (\text{W}\cdot\text{kg}^{-1}), \quad (4)$$

V_f , V_i are final and initial potential respectively.

3. Results and discussion

The present work is to optimize the applied potential for getting high-quality graphene via an electrochemical route. During electrochemical exfoliation, the influence of the applied potential (3, 5, 7, and 9 V) was studied, while the rest of the conditions such as solution concentration (0.1 M H_2SO_4) and reaction time (1 h) were kept constant. There is no exfoliation visible on 3 V.

3.1. Structural and morphological analysis

Raman spectroscopy is a powerful tool for studying the structural quality of synthesized graphene. Fig. 1 depicts the Raman spectra of electrochemically synthesized graphene with 5, 7, and 9 V. For comparison, the Raman spectra of graphite rod is also included in Fig. 1. Raman spectra of graphite and synthesized graphene showed three characteristic peaks located at 1351, 1587, and $\sim 2698 \text{ cm}^{-1}$ that correspond to the D band, G band, and 2D band, respectively. The G band originates from the vibrations of the sp^2 hybridized carbon atoms (E_{2g} mode), whereas the D band arises from lattice distortion (structural defects) in sp^2 hybridized carbon. The 2D band is attributed to the second order of zone boundary phonons [7, 13]. Graphite shows a less intensity D band, whereas defect is well pronounced in the prepared graphene and indicates the presence of edges and/or topological defects in the basal plane.

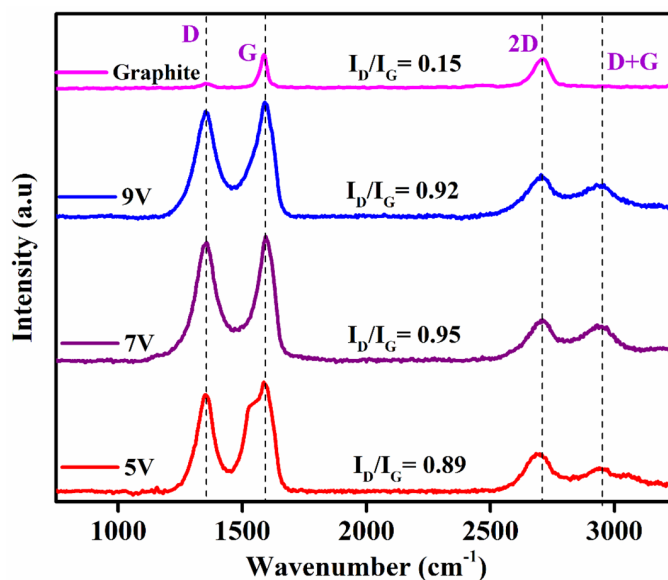


FIG. 1. Raman Spectra of graphite and electrochemically exfol

The intensity ratio of the D and G bands (I_D/I_G) gives the amount of defects in synthesized graphene [12]. The 9 V shows an I_D/I_G value of 0.92, which is larger than 5 V ($I_D/I_G = 0.8$) but smaller than that of 7 V ($I_D/I_G = 0.95$). The increase in I_D/I_G ratio value indicates the increase in the amount of defects present in the graphene structure when high potential (7 and 9 V) were used, suggesting that a higher defect density is induced by accelerating the oxidation at potential (7 V) as well as the sulphate ions directly forms the SO_2 gas without interaction at the high anodic potential of 9 V, yield of the exfoliated graphene is very low. The I_D/I_G ratio value of exfoliated graphene at 5 V was increased to

0.89 from 0.15 of pristine graphite because the sp^2 domains, which are newly formed, are smaller than those of graphite during electrochemical exfoliation.

It is known that the crystallite sizes (L_a) are inversely proportional to the I_D/I_G . The average crystallite size of graphene can be estimated (Table 1) from Tuinstra–Koenig (TK) formula [14].

$$L_a = 2.4 \cdot 10^{-10} \cdot \lambda^4 \cdot (I_D/I_G)^{-1}, \quad (5)$$

where λ is the Raman excitation wavelength. It is found that the crystallite size decreases with increased potential.

TABLE 1. The characteristics of Raman bands of electrochemically exfoliated graphene. The thickness and morphology of the prepared graphene were further examined by AFM

Sample Name	I_D Band	I_G Band	2D Band Peak Position (cm^{-1})	I_{2D} Band	I_D/I_G	I_{2D}/I_G	Average Crystallite Size (nm)
Graphite	605	4033	2711	162	0.15	0.04	120
5 V	2006	2251	2698	845	0.89	0.38	21.57
7 V	2401	2521	2710	879	0.95	0.35	20.19
9 V	2159	2334	2703	911	0.92	0.39	20.78

The 2D band of 7 and 9 V was located at 2710 cm^{-1} (red shift of 12 cm^{-1} compared to 5 V) and 2703 cm^{-1} (red shift of 5 cm^{-1} compared to 5 V), respectively (Fig. 2). The red shift of the 2D band is indicating the increase in the thickness of layer. From Fig. 2, the 2D band of graphite appears at 2711 cm^{-1} , exhibiting a red shift from exfoliated graphene at 5 V (2698 cm^{-1}), and the shape of the 2D band became more symmetrical for graphite in comparison with that of graphene. It suggests that the exfoliated graphene sheets are composed of thinned and multilayered.

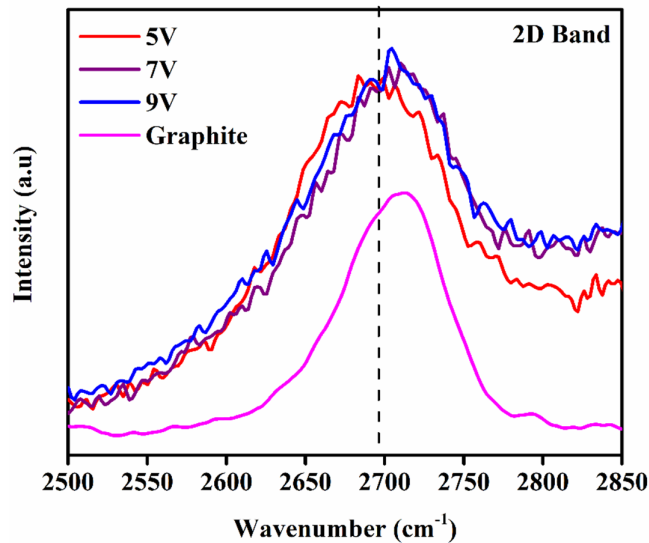


FIG. 2. 2D band spectra of the graphite and electrochemically exfoliated graphene

The intensity ratio of 2D and bands G (I_D/I_G) is used to determine the number of graphene layers. The ratio I_{2D}/I_G is around 2 – 3 for monolayer graphene, 2 – 1 for bi-layer graphene, and $I_{2D}/I_G \leq 1$ for multilayer graphene [15]. Table 1 summarizes the characteristic Raman G, D, and 2D bands, and their intensity ratio I_D/I_G , I_{2D}/I_G and crystallite size are given for synthesized graphene. The I_{2D}/I_G graphite is 0.15, and 5 V exfoliated graphene is 0.38. Based on the I_{2D}/I_G ratio of Raman spectra, it can be suggested that the produced graphene contains multilayers.

X-ray photoelectron spectroscopy (XPS) is used to investigate the nature of the chemical bonding of the graphene. The XPS survey spectra of electrochemically exfoliated graphene are shown in Fig. 3. It clearly shows the presence of C 1s and O 1s peaks at ~ 284 and ~ 532 eV, respectively. The high-resolution scan of C 1s band for 5 V could be fitted with three deconvoluted peaks, whereas 7 and 9 V could be fitted with four deconvoluted peaks (Fig. 4). The deconvoluted peaks at 284.28 ± 0.13 , 285.04 ± 0.28 , 286.41 ± 0.20 and 287.33 ± 0.24 eV corresponding to the binding energies of sp^2 Carbon, C–O, C=O and C–O–C, respectively [16, 17]. The major intense peak at ~ 284.28 eV in C 1s spectrum suggests that the presence of sp^2 carbon atoms (C=C) which informs that majority of carbon atoms were arranged in honeycomb structure during electrochemical exfoliation of graphene.

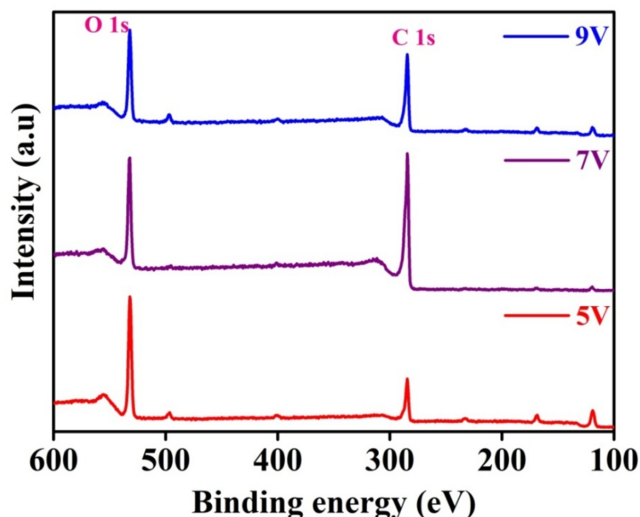


FIG. 3. Full range XPS spectra electrochemically exfoliated graphene

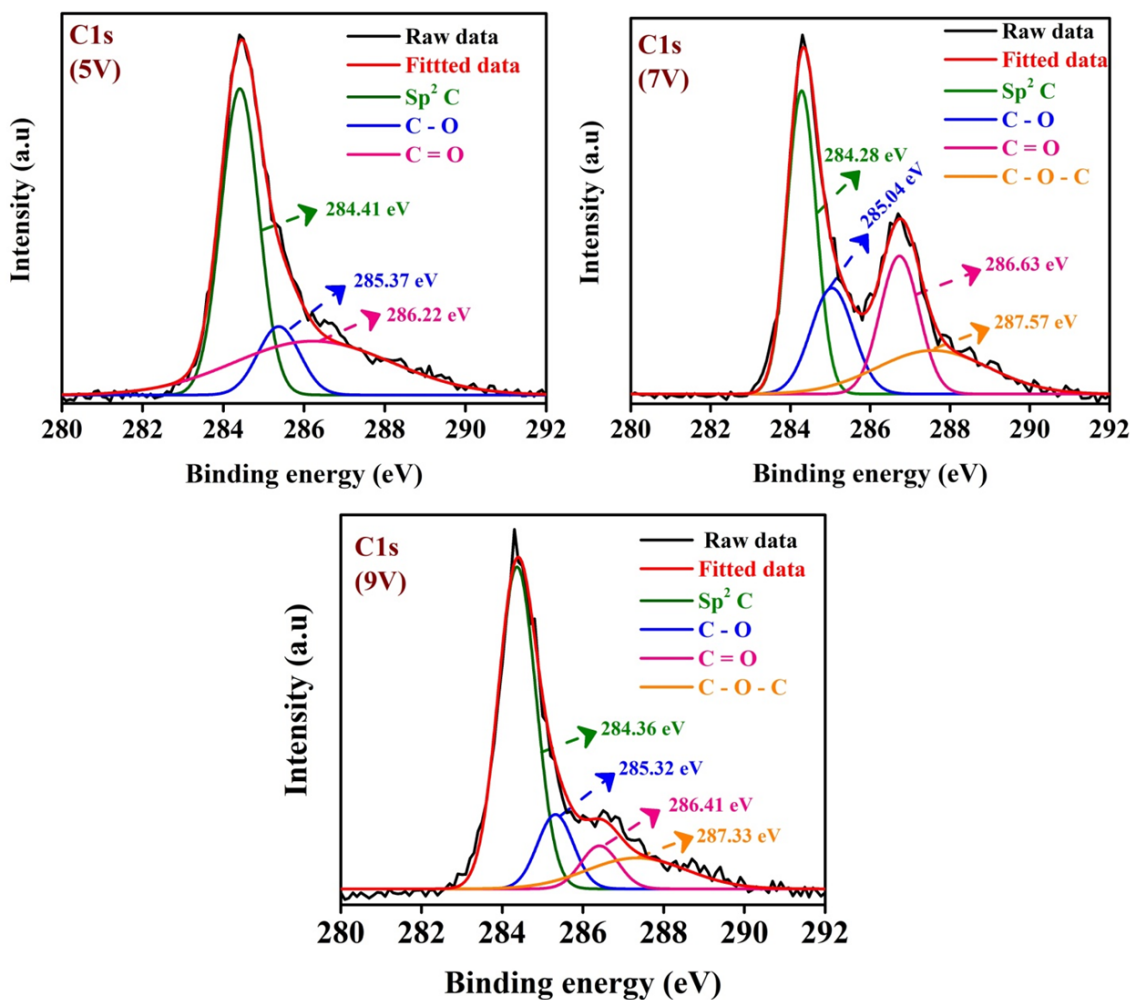


FIG. 4. High resolution XPS spectra of C 1 s for 5, 7, and 9 V

As shown in Table 2, the atomic percentage of carbon and oxygen elements of electrochemical exfoliated graphene. The sample from 5 to 7 V, oxygen element (O at. %) increased from 19 to 48 %. This implies that the oxidation has increased. This is due to increase in OH^- and SO_4^{2-} ions from 0.1 M H_2SO_4 . Interestingly, the amount of O at% in 9 V is (27 %) less than the 7 V but higher than the 5 V. The 5 V exfoliated graphene were relatively higher C/O ratio among the 7 and 9 V exfoliated graphene. This result suggests that during electrochemical exfoliation reaction, small amount of oxygen containing functional groups are formed onto the surface of graphene. It is to be noticed that less amount of oxygen functional groups are present in the electrochemically prepared graphene at 5 V as compared to the other chemical and thermal route, which was previously reported [2, 9, 18].

TABLE 2. Atomic percentages of C and O elements in the synthesized graphene

Sample Name	C 1 s Atomic (%)	O 1 s Atomic (%)	C/O ratio
5 V	81	19	4.23
7 V	52	48	1.09
9 V	73	27	2.66

The Atomic Force Microscopy (AFM) images of graphene prepared at 5, 7 and 9 V are shown in Fig. 5. The AFM images shows that the exfoliated graphene has average thickness of 5.7, 7.6 and 6.5 nm at 5, 7 and 9 V respectively. At the potential of 5 V, minimum thickness observed with 17 graphene layers (multiyear) superimposed on each other. From Fig. 5, it is clearly visible that the graphene sheets appear multilayer, and it is confirmed that some graphitic nanoparticles still need to be exfoliated.

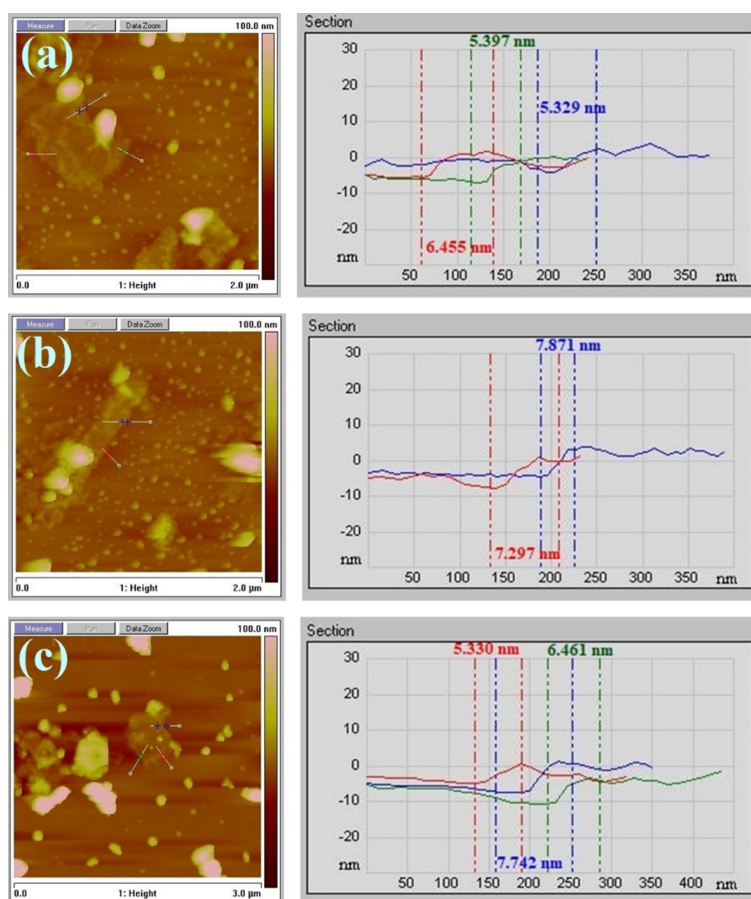


FIG. 5. AFM images (left) and line profile (right) of graphene prepared at 5 V (a), 7 V (b) and 9 V (c)

X-ray diffraction (XRD) analysis was performed to further characterize the synthesized graphene by electrochemical method and purchased graphite rod. Fig. 6 shows the XRD patterns of the graphite rod and synthesized graphene after applying a constant voltage of 5 V. In graphite rod, the peaks that appeared at $2\theta = 26.6^\circ$, 44.5° , and 54.8° correspond to (002), (100), and (004) planes, respectively. The XRD pattern of the synthesized graphene exhibits a much weaker and broader peak center at $\sim 24.78^\circ$ and 43.1° indexed as (002) and (100) plane, respectively. These two diffraction peaks

indicate the multilayer graphene, which further signifies the efficient exfoliation of graphene and well match with reported literature [2, 9, 18]. Further, the absence of a diffraction peak at $\sim 11^\circ$ in the prepared sample revealed the absence of graphene oxide, and it was only composed of graphene [18].

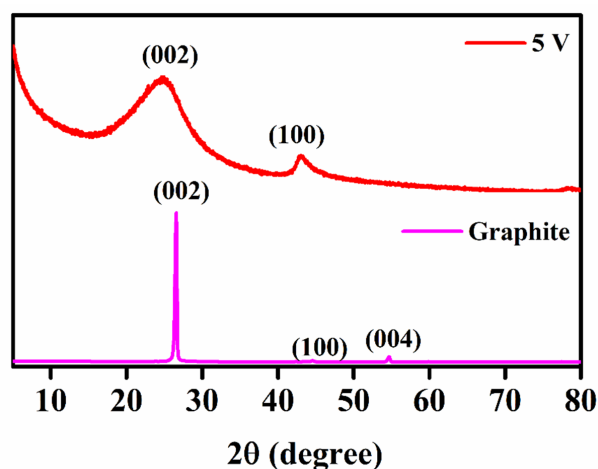


FIG. 6. XRD patterns of graphite rod and graphene prepared at 5 V

The inter-layer spacing at (002) plane of graphite rod and synthesized graphene were calculated by using Bragg's Law: $2d \sin \theta = n\lambda$, where $n = 1$, λ is the X-ray wavelength. The estimated inter-layer spacing of the graphite rod was 3.3484 Å, and the synthesized graphene was 3.5901 Å. Compared to graphite, the peak (002) shift with increased inter-layer spacing suggests the poor ordering of sheets along the stacking direction of c-axis. The obtained XRD patterns agree well with the Raman, XPS, and AFM analysis, which confirms the successful preparation of multilayer graphene sheets with low defects.

The present electrochemically exfoliated graphene is definitely feasible to the previously reported chemically prepared graphene. It is noted that our exfoliated graphene produced at 5 V exhibits the less degree of disorder I_D/I_G from Raman and low oxygen contents (19 %) from XPS and XRD indicates the high structural quality of multilayered graphene with efficiency of 26.3 % (yield) formed. Here, electrochemical exfoliation method, the graphene is attained through a simple intercalation process, so it validates a comparatively lower defect.

3.2. Electrochemical performance of 5 V prepared graphene electrode

The electrochemical performance of the synthesised graphene at 5 V was studied through CV and CD. Fig. 7(a) depicts the CV of graphene at a scan rate of $20 \text{ mV}\cdot\text{s}^{-1}$. The CVs almost featureless without redox peak and exhibiting rectangular shape indicates an electrical double layer capacitor (EDLC) behaviour between electrode-electrolyte interfaces via non-faradic charging / discharging process. The curves at a different scan rate from 10 to $200 \text{ mV}\cdot\text{s}^{-1}$ are shown in Fig. 7(b). The value of current density increases with increase in scan rate suggesting fast charging characteristics of electrode. The CVs at all the scan rate of synthesised graphene at 5 V are featureless (there is no peak observed), in the optimized potential range of -1.0 to 0 V vs SCE, indicating EDLC [19].

Upon scanning to more negative (cathodic) potentials, diffusion of K^+ from the electrolyte solution to the electrochemically exfoliated electrode surface was adsorbed through non-faradic reaction. When the scan direction is reversed, and the potential is scanned in the positive (anodic) direction, K^+ at the graphene electrode surface is depleted.

Figure 8 represent the value of specific capacitance (C_s) obtained from CVs, the higher value of specific capacitance observed at slow scan rate and vice-versa. At slow scan rate ions in the electrolyte gets sufficient time to get adsorb over graphene sheets but at high scan rate, charging and discharging process are too fast for the full adsorption and hence lesser surface of electrode used, resulting in low specific capacitance value for higher scan rates and high capacitance value for lower scan rates [19].

Figure 9 (a) depicts the chronopotentiometric charge-discharge (CD) curve of graphene at the current density of $0.6 \text{ A}\cdot\text{g}^{-1}$. Fig. 9(b) shows the chronopotentiometric charge-discharge curves at different current densities from 0.3 to $3 \text{ A}\cdot\text{g}^{-1}$ with the voltage ranges from -0.1 to -0.8 V for the same electrode used above for CV. The linear increase in charging curve with constant slope indicates the electrical double layer capacitor behaviour. This result well agrees with the CV studies and consistent with previous report.

Figure 10 shows the values of specific capacitance ranging from 198 to $37 \text{ F}\cdot\text{g}^{-1}$. Similar to CV, here also increase in current density leads to decrease in specific capacitance. As ion adsorptions over graphene layer reduces with increase in current density.

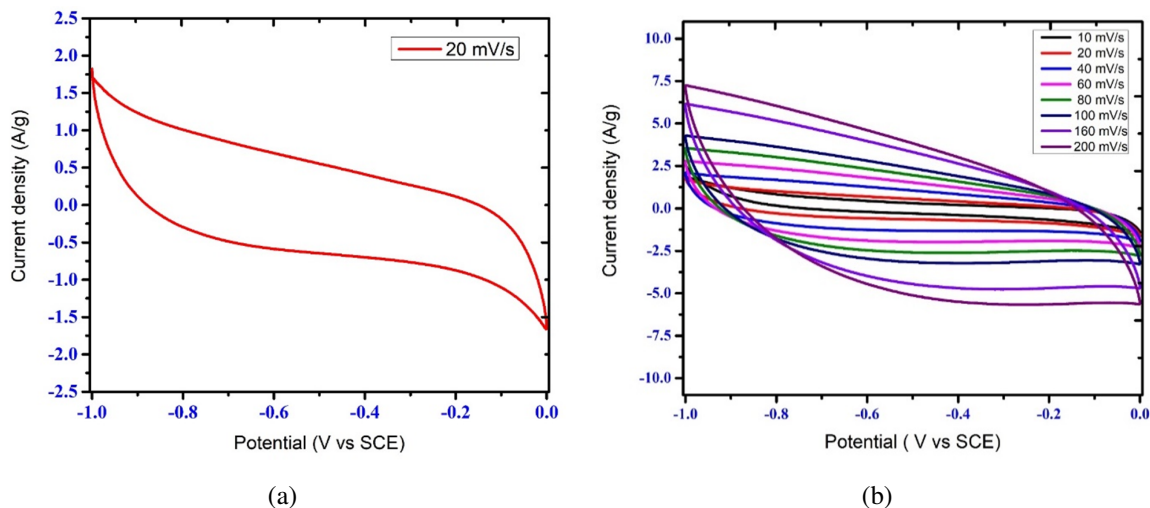


FIG. 7. (a) CV at scan rate of $20 \text{ mV}\cdot\text{s}^{-1}$; (b) CVs at different scan rates

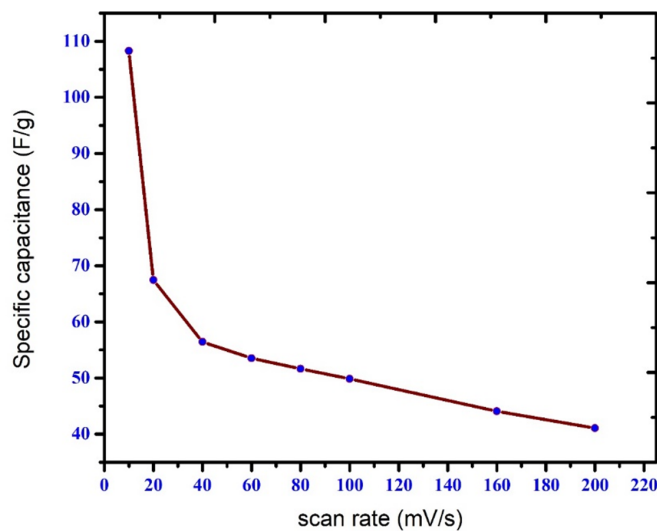


FIG. 8. Specific capacitance at various scan rates (10 to $200 \text{ mV}\cdot\text{s}^{-1}$)

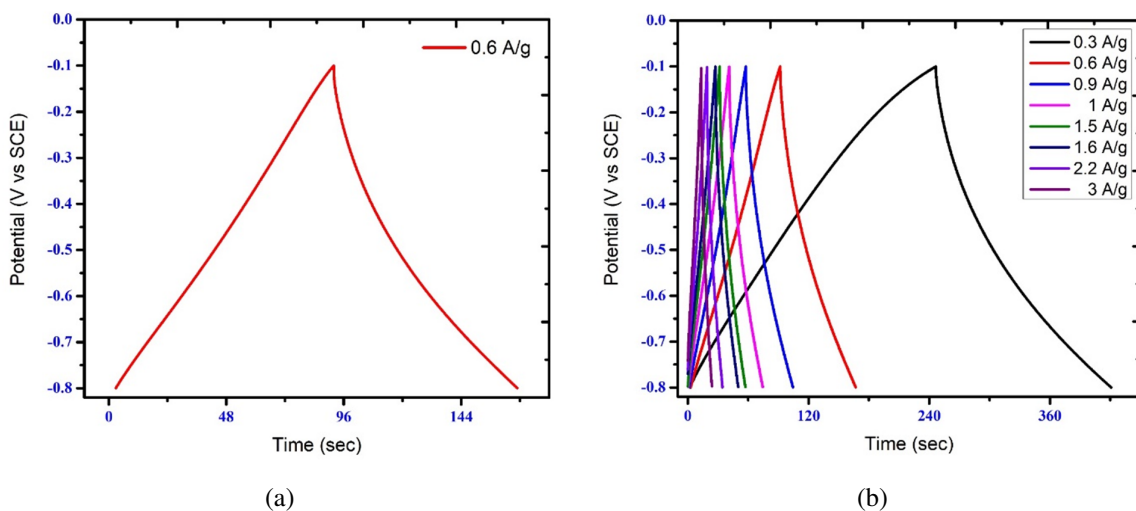


FIG. 9. (a) Charge-discharge curve at current density of $0.6 \text{ A}\cdot\text{g}^{-1}$; (b) Charge-discharge curve at current density varies from 0.3 to $3 \text{ A}\cdot\text{g}^{-1}$

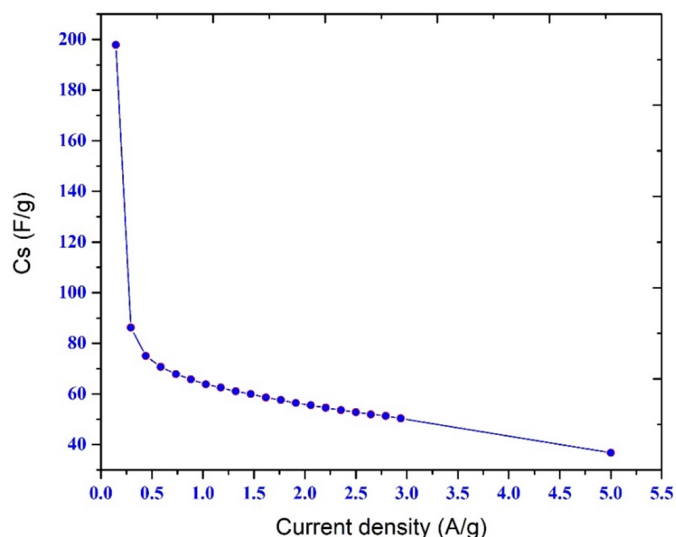


FIG. 10. Specific capacitance at different current density

The cyclic stability of electrode can be observed at a current density of $5 \text{ A}\cdot\text{g}^{-1}$ from Fig. 11, the value of specific capacitance for 1st and 500th cycle is 36.76 and $34.92 \text{ F}\cdot\text{g}^{-1}$ with the retention of 95 % of the specific capacitance value after 500 cycles, shows that prepared electrode shows excellent stability for supercapacitor behaviour.

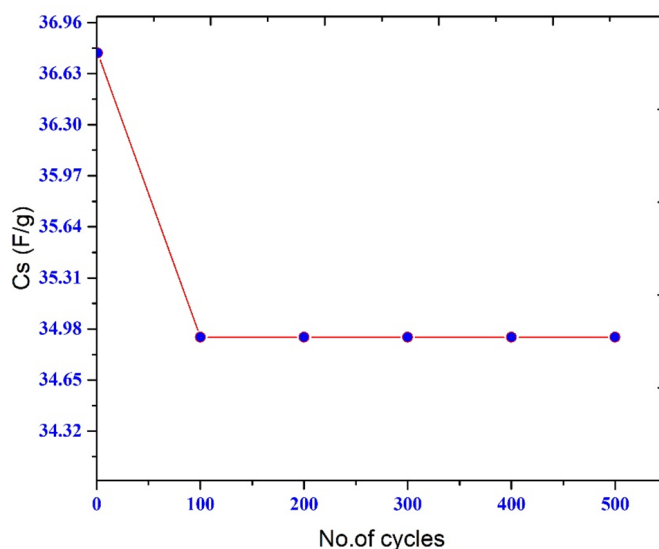


FIG. 11. Cyclic stability of graphene electrode at a current density of $5 \text{ A}\cdot\text{g}^{-1}$

Power density and Energy density values calculated from charge-discharge shown in Fig. 12. The maximum power density obtained is $1176 \text{ W}\cdot\text{kg}^{-1}$ at current density of $3 \text{ A}\cdot\text{g}^{-1}$. The maximum energy density obtained is $17 \text{ W}\cdot\text{h}\cdot\text{kg}^{-1}$.

4. Conclusion

The present study demonstrates that one-pot synthesis of graphene sheets was fabricated via electrochemical exfoliation with the optimization of applied potential in the presence of $0.1 \text{ M H}_2\text{SO}_4$ (Ag/AgCl , $0.1 \text{ M H}_2\text{SO}_4$). The graphene sheets were analysed by XPS, Raman, AFM and XRD. XPS results show the less oxygen content of $\sim 19.11 \text{ at}\%$ for 5 V . AFM exhibits the multi-layer graphene. Raman spectroscopy indicates the low defect density of as-synthesized multi-layer graphene sheets. The XRD result confirms the formation of multi-layer graphene sheets at applied potential of 5 V . Hence by using this graphene (prepared at potential of 5 V) to make electrode, by coated on platinum electrode gives specific capacitance of $198 \text{ F}\cdot\text{g}^{-1}$, energy density of $17 \text{ W}\cdot\text{h}\cdot\text{kg}^{-1}$ and power density of $1176 \text{ W}\cdot\text{kg}^{-1}$ which shows a good EDLC behaviour of electrode in 6 M KOH solution.

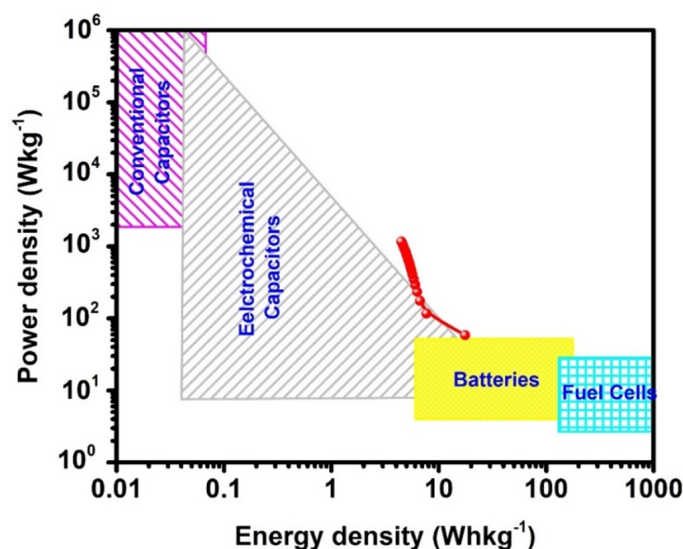


FIG. 12. Ragone plot of prepared graphene electrode compared with different electrochemical devices

References

- [1] Zhong C., Deng Y., Hu W., Qiao J., Zhang L., Zhang J. A review of electrolyte materials and compositions for electrochemical supercapacitors. *Chem. Soc. Rev.*, 2015, **44** (21), P. 7484–7539.
- [2] Muthu R.N., Tatiparti S.S.V. Electrochemical Behavior of Cobalt Oxide/Boron-Incorporated Reduced Graphene Oxide Nanocomposite Electrode for Supercapacitor Applications. *J. of Mater. Eng. and Perform.*, 2020, **29**, P. 6535–6549.
- [3] Zhong Y., Zhen Z., Zhu H. Graphene: Fundamental research and potential applications. *FlatChem*, 2017, **4**, P. 20–32.
- [4] Rodríguez-Pérez L., Herranz M.Á., Martín N. The chemistry of pristine graphene. *Chem. Commun.*, 2013, **49** (36), P. 3721–3735.
- [5] Liu C., Yu Z., Neff D., Zhamu A., Jang B.Z. Graphene-based supercapacitor with an ultrahigh energy density. *Nano Lett.*, 2010, **10** (12), P. 4863–4868.
- [6] Jibrael R.I., Mohammed M.K.A. Production of graphene powder by electrochemical exfoliation of graphite electrodes immersed in aqueous solution. *Optik (Stuttg.)*, 2016, **127** (16), P. 6384–6389.
- [7] Chen J., Li Y., Huang L., Li C., Shi G. High-yield preparation of graphene oxide from small graphite flakes via an improved Hummers method with a simple purification process. *Carbon N.Y.*, 2015, **81** (1), P. 826–834.
- [8] Pei S., Wei Q., Huang K., Cheng H.M., Ren W. Green synthesis of graphene oxide by seconds timescale water electrolytic oxidation. *Nat. Commun.*, 2018, **9** (1), P. 1–9.
- [9] Muthu R.N., Tatiparti S.S.V. Electrode and symmetric supercapacitor device performance of boron-incorporated reduced graphene oxide synthesized by electrochemical exfoliation. *Energy Storage*, 2020, **2**, e134.
- [10] Arunkumar M., Amit P. Importance of Electrode Preparation Methodologies in Supercapacitor Applications. *ACS Omega*, 2017, **2** (11), P. 8039–8050.
- [11] Pandit B., Dubal D.P., Sankapal B.R. Large scale flexible solid state symmetric supercapacitor through inexpensive solution processed V₂O₅ complex surface architecture. *Electrochim. Acta*, 2017, **242**, P. 382–389.
- [12] Roldán S., Barreda D., Granda M., Menéndez R., Santamaría R., Blanco C. An approach to classification and capacitance expressions in electrochemical capacitors technology. *Phys. Chem. Chem. Phys.*, 2015, **17** (2), P. 1084–1092.
- [13] Das A.K., et al. Iodide-mediated room temperature reduction of graphene oxide: A rapid chemical route for the synthesis of a bifunctional electrocatalyst. *J. Mater. Chem. A*, 2014, **2** (5), P. 1332–1340.
- [14] Kakaei K., Alidoust E., Ghadimi G. Synthesis of N- doped graphene nanosheets and its composite with urea choline chloride ionic liquid as a novel electrode for supercapacitor. *J. Alloys Compd.*, 2018, **735**, P. 1799–1806.
- [15] Nguyen V.T., Le H.D., Nguyen V.C., Ngo T.T.T., Le D.Q., Nguyen X.N., Phan N.M. Synthesis of multi-layer graphene films on copper tape by atmospheric pressure chemical vapor deposition method. *Adv. Nat. Sci. Nanosci. Nanotechnol.*, 2013, **4** (3), 035012.
- [16] Bindumadhavan K., Chang P-Y., Doong R-a. Silver nanoparticles embedded boron-doped reduced graphene oxide as anode material for high performance lithium ion battery. *Electrochimica Acta*, 2017, **243**, P. 282–290.
- [17] Pullamsetty A., Subbiah M., Sundara R. Platinum on boron doped graphene as cathode electrocatalyst for proton exchange membrane fuel cells. *Int. J. Hydrogen Energy*, 2015, **40** (32), P. 10251–10261.
- [18] Muthu R.N., Rajashabala S., Kannan R. Facile synthesis and characterization of a reduced graphene oxide/halloysite nanotubes/hexagonal boron nitride (RGO/HNT/h-BN) hybrid nanocomposite and its potential application in hydrogen storage. *RSC Adv.*, 2016, **6**, P. 79072.
- [19] Gong Y., Li D., Fu Q., Pan C. Influence of graphene microstructures on electrochemical performance for supercapacitors. *Progress in Natural Science: Materials International*, 2015, **25** (5), P. 379–385.

Submitted 8 February 2023; revised 2 April 2023; accepted 4 April 2023

Information about the authors:

R. Naresh Muthu – Department of Physics, J. P. College of Arts and Science, Tenkasi – 627852, Tamilnadu, India (affiliated to Manonmaniam Sundaranar University, Tirunelveli); ORCID 0000-0002-4998-7497; rnaresh7708@gmail.com



NANOSYSTEMS:

PHYSICS, CHEMISTRY, MATHEMATICS

INFORMATION FOR AUTHORS

The journal publishes research articles and reviews, and also short scientific papers (letters) which are unpublished and have not been accepted for publication in other magazines. Articles should be submitted in English. All articles are reviewed, then if necessary come back to the author to completion.

The journal is indexed in Web of Science Core Collection (Emerging Sources Citation Index), Chemical Abstract Service of the American Chemical Society, Zentralblatt MATH and in Russian Scientific Citation Index.

Author should submit the following materials:

1. Article file in English, containing article title, the initials and the surname of the authors, Institute (University), postal address, the electronic address, the summary, keywords, MSC or PACS index, article text, the list of references.
2. Files with illustrations, files with tables.
3. The covering letter in English containing the article information (article name, MSC or PACS index, keywords, the summary, the literature) and about all authors (the surname, names, the full name of places of work, the mailing address with the postal code, contact phone number with a city code, the electronic address).
4. The expert judgement on possibility of publication of the article in open press (for authors from Russia).

Authors can submit a paper and the corresponding files to the following addresses: nanojournal.ifmo@gmail.com, popov1955@gmail.com.

Text requirements

Articles should be prepared with using of text editors MS Word or LaTeX (preferable). It is necessary to submit source file (LaTeX) and a pdf copy. In the name of files the English alphabet is used. The recommended size of short communications (letters) is 4-6 pages, research articles– 6-15 pages, reviews – 30 pages.

Recommendations for text in MS Word:

Formulas should be written using Math Type. Figures and tables with captions should be inserted in the text. Additionally, authors present separate files for all figures and Word files of tables.

Recommendations for text in LaTeX:

Please, use standard LaTeX without macros and additional style files. The list of references should be included in the main LaTeX file. Source LaTeX file of the paper with the corresponding pdf file and files of figures should be submitted.

References in the article text are given in square brackets. The list of references should be prepared in accordance with the following samples:

- [1] Surname N. *Book Title*. Nauka Publishing House, Saint Petersburg, 2000, 281 pp.
- [2] Surname N., Surname N. Paper title. *Journal Name*, 2010, **1** (5), P. 17-23.
- [3] Surname N., Surname N. Lecture title. In: Abstracts/Proceedings of the Conference, Place and Date, 2000, P. 17-23.
- [4] Surname N., Surname N. Paper title, 2000, URL: <http://books.ifmo.ru/ntv>.
- [5] Surname N., Surname N. Patent Name. Patent No. 11111, 2010, Bul. No. 33, 5 pp.
- [6] Surname N., Surname N. Thesis Title. Thesis for full doctor degree in math. and physics, Saint Petersburg, 2000, 105 pp.

Requirements to illustrations

Illustrations should be submitted as separate black-and-white files. Formats of files – jpeg, eps, tiff.



NANOSYSTEMS:

PHYSICS, CHEMISTRY, MATHEMATICS

Журнал зарегистрирован

Федеральной службой по надзору в сфере связи, информационных технологий и массовых коммуникаций

(свидетельство ПИ № ФС 77 - 49048 от 22.03.2012 г.)

ISSN 2220-8054

Учредитель: федеральное государственное автономное образовательное учреждение высшего образования

«Национальный исследовательский университет ИТМО»

Издатель: федеральное государственное автономное образовательное учреждение высшего образования

«Национальный исследовательский университет ИТМО»

Отпечатано в Учреждении «Университетские телекоммуникации»

Адрес: 197101, Санкт-Петербург, Кронверкский пр., 49

Подписка на журнал НФХМ

На второе полугодие 2023 года подписка осуществляется через

ОАО «АРЗИ», подписной индекс Э57385